

AD-A187 663

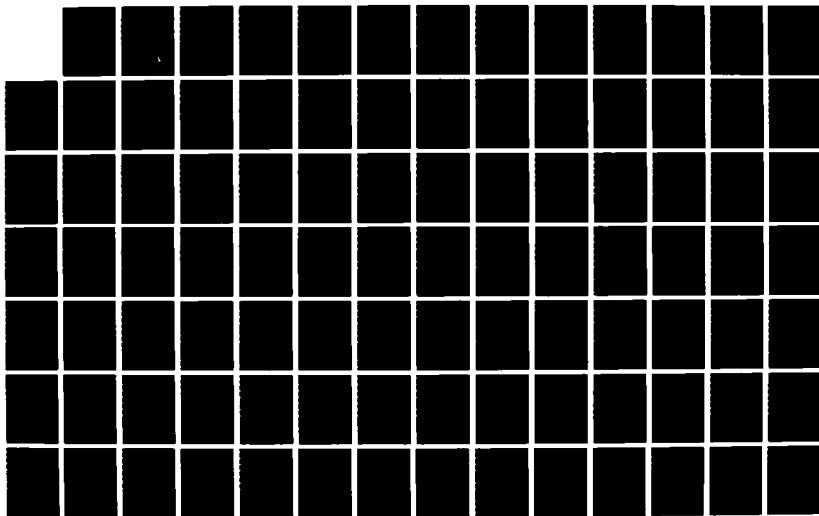
A SPECTRAL METHOD FOR COMPUTING COMPLETE SYNTHETIC  
SEISMOGRAMS(U) COLORADO UNIV AT BOULDER D J HARVEY  
MAR 87 AFGL-TR-87-0238 F19628-85-K-0016

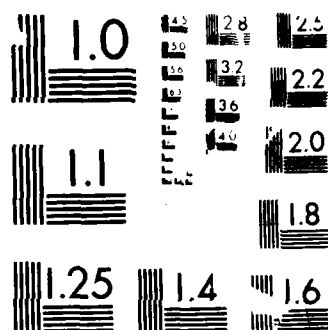
1/4

UNCLASSIFIED

F/G 8/11

NL





MICROCOPY RESOLUTION TEST CHART

10-100-1

AD-A187 663

AFGL-TR-87-0238

DTIC FILE COPY

12

A SPECTRAL METHOD FOR COMPUTING COMPLETE  
SYNTHETIC SEISMOGRAMS

DANNY J. HARVEY

UNIVERSITY OF COLORADO/CIRES  
CAMPUS BOX 449  
BOULDER, CO 80309

MARCH 1987

FINAL REPORT

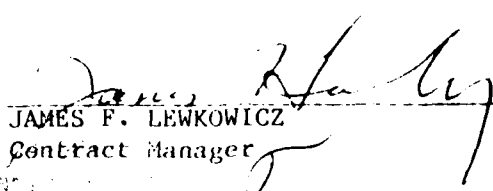
25 October 1984-31 December 1986

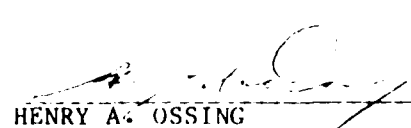
APPROVED FOR PUBLIC RELEASE, DISTRIBUTION UNLIMITED

DTIC  
ELECTE  
NOV 16 1987  
A

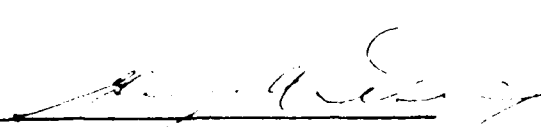
AIR FORCE GEOPHYSICS LABORATORY  
AIR FORCE SYSTEMS COMMAND  
UNITED STATES AIR FORCE  
HANSCOM AIR FORCE BASE, MASSACHUSETTS 01731

"This technical report has been reviewed and is approved for publication."

  
JAMES F. LEWKOWICZ  
Contract Manager

  
HENRY A. OSSING  
Chief, Solid Earth Geophysics Branch

FOR THE COMMANDER

  
HENRY A. OSSING  
Acting Director  
Earth Sciences Division

This report has been reviewed by the ESD Public Affairs Office (PA) and is releasable to the National Technical Information Service (NTIS).

Qualified requestors may obtain additional copies from the Defense Technical Information Center. All others should apply to the National Technical Information Service.

If your address has changed, or if you wish to be removed from the mailing list, or if the addressee is no longer employed by your organization, please notify AFGL/PAA, Hanscom AFB, MA 01731. This will assist us in maintaining a current mailing list.

Do not return copies of this report unless contractual obligations or notices on a specific document requires that it be returned.





Unclassified

SECURITY CLASSIFICATION OF THIS PAGE

## REPORT DOCUMENTATION PAGE

1a. REPORT SECURITY CLASSIFICATION Unclassified		1b. RESTRICTIVE MARKINGS													
2a. SECURITY CLASSIFICATION AUTHORITY		3. DISTRIBUTION/AVAILABILITY OF REPORT approved for public release, distribution unlimited													
2b. DECLASSIFICATION/DOWNGRADING SCHEDULE															
4. PERFORMING ORGANIZATION REPORT NUMBER(S)		5. MONITORING ORGANIZATION REPORT NUMBER(S) AFGL-TR-87-0238													
6a. NAME OF PERFORMING ORGANIZATION University of Colorado	6b. OFFICE SYMBOL (If applicable)	7a. NAME OF MONITORING ORGANIZATION Air Force Geophysics Laboratory													
6c. ADDRESS (City, State and ZIP Code) Campus Box B-19 Boulder, CO 80309		7b. ADDRESS (City, State and ZIP Code) Hanscom AFB Massachusetts 01731													
8a. NAME OF FUNDING/SPONSORING ORGANIZATION DARPA	8b. OFFICE SYMBOL (If applicable) STO/GSD	9. PROCUREMENT INSTRUMENT IDENTIFICATION NUMBER F19628-85-K-0016													
8c. ADDRESS (City, State and ZIP Code) 1400 Wilson Boulevard Arlington, VA 22209-2308		10. SOURCE OF FUNDING NOS. <table border="1"><tr><td>PROGRAM ELEMENT NO</td><td>PROJECT NO</td><td>TASK NO</td><td>WORK UNIT NO</td></tr><tr><td>61101E</td><td>5A10</td><td>DA</td><td>AY</td></tr></table>		PROGRAM ELEMENT NO	PROJECT NO	TASK NO	WORK UNIT NO	61101E	5A10	DA	AY				
PROGRAM ELEMENT NO	PROJECT NO	TASK NO	WORK UNIT NO												
61101E	5A10	DA	AY												
11. TITLE (Include Security Classification) A Spectral Method for Computing Complete Syn- thetic Seismograms															
12. PERSONAL AUTHOR(S) Danny J. Harvey															
13a. TYPE OF REPORT FINAL REPORT	13b. TIME COVERED FROM 10-25-84 TO 12-31-86	14. DATE OF REPORT (Yr., Mo., Day) March 1987	15. PAGE COUNT 304												
16. SUPPLEMENTARY NOTATION															
17. COSATI CODES <table border="1"><tr><td>FIELD</td><td>GROUP</td><td>SUB GR</td></tr><tr><td></td><td></td><td></td></tr><tr><td></td><td></td><td></td></tr><tr><td></td><td></td><td></td></tr></table>		FIELD	GROUP	SUB GR										18. SUBJECT TERMS (Continue on reverse if necessary and identify by block number) Synthetic Seismograms, Modal Synthesis, Propagation Methods	
FIELD	GROUP	SUB GR													
19. ABSTRACT (Continue on reverse if necessary and identify by block number) The efficient computation of complete solution synthetic seismograms for flat, plane layered, laterally homogeneous elastic media and for high frequency bandwidths is a problem which has received considerable attention in the field of solid-earth geophysics. The only available methods for computing complete synthetic seismograms are computationally expensive and, in many cases, suffer from numerical instabilities which limit their ranges of applicability. A new method is presented which is based upon a spectral representation of the solution of the elastic wave equation. The eigenvalue and eigenfunction computations are reformulated in a manner which avoids the numerical instabilities. A mode searching algorithm is developed which makes it possible to find large numbers of Rayleigh and Love dispersion curves in an efficient and reliable manner. The locked mode approximation is then presented which allows nearly complete synthetic seismograms to be computed using only the discrete part of the spectrum and using only normal modes with real eigenwavenumbers. This is achieved by adding a high velocity															
20. DISTRIBUTION/AVAILABILITY OF ABSTRACT UNCLASSIFIED/UNLIMITED <input type="checkbox"/> SAME AS RPT <input type="checkbox"/> DTIC USERS <input type="checkbox"/>		21. ABSTRACT SECURITY CLASSIFICATION Unclassified													
22a. NAME OF RESPONSIBLE INDIVIDUAL James Lewkowicz		22b. TELEPHONE NUMBER (Include Area Code) (617) 377-3028	22c. OFFICE SYMBOL AFGL/LWH												

Abstract (continued)

cap layer to the bottom of the elastic model and by using phase velocity filtering to attenuate the spurious scattering caused by the cap layer.

Comparisons of the results of the locked mode approximation with exact results obtained from other synthesis methods are presented and the limitations of the method are demonstrated and discussed. A number of examples of synthetic seismograms using the locked mode approximation are then given along with a comparison of observed and synthetic seismograms.

The locked mode approximation provides a new and efficient method for computing complete synthetic seismograms which extends the range of geophysical problems that can be treated with the aid of seismogram synthesis.

Danny J. Harvey (Ph.D., Geophysics)

A Spectral Method for Computing Complete Synthetic Seismograms

Thesis directed by Professor Charles B. Archambeau

The efficient computation of complete solution synthetic seismograms for flat, plane layered, laterally homogeneous elastic media and for high frequency bandwidths is a problem which has received considerable attention in the field of solid-earth geophysics. The only available methods for computing complete synthetic seismograms are computationally expensive and, in many cases, suffer from numerical instabilities which limit their ranges of applicability.

A new method is presented which is based upon a spectral representation of the solution of the elastic wave equation. The eigenvalue and eigenfunction computations are reformulated in a manner which avoids the numerical instabilities. A mode searching algorithm is developed which makes it possible to find large numbers of Rayleigh and Love dispersion curves in an efficient and reliable manner.

The locked mode approximation is then presented which allows nearly complete synthetic seismograms to be computed using only the discrete part of the spectrum and using only normal modes with real eigenwavenumbers. This is achieved by adding a high velocity cap layer to the bottom of the elastic model and by using phase velocity filtering to

attenuate the spurious scattering caused by the cap layer.

Comparisons of the results of the locked mode approximation with exact results and with results obtained from other synthesis methods are presented and the limitations of the method are demonstrated and discussed. A number of examples of synthetic seismograms using the locked mode approximation are then given along with a comparison of observed and synthetic seismograms.

The locked mode approximation provides a new and efficient method for computing complete synthetic seismograms which extends the range of geophysical problems that can be treated with the aid of seismogram synthesis.

The form and content of this abstract are approved.  
I recommend its publication.

Signed Charles B. Fuchsman  
Faculty member in charge of thesis

## TABLE OF CONTENTS

### CHAPTER

I.	INTRODUCTION . . . . .	1
II.	THE FUNDAMENTALS OF NORMAL MODE THEORY FOR FLAT LAYERED STRUCTURES . . . . .	13
2.1	Basic Assumptions . . . . .	15
2.2	Differential Equations, Coordinate Systems, and Boundary Conditions . . . . .	18
2.3	Separable Solutions of the Elastic Wave Equation in Cylindrical Coordinates . . . . .	24
2.4	Solutions of the Depth Dependent ODEs: The Propagator Matrix . . . . .	29
2.5	Integral and Spectral Representations for the Solutions of the Elastic Wave Equation . . . . .	48
2.6	The Branch Cut Integral Contributions . . . . .	74
III.	REFORMULATION OF THE NORMAL MODE PROBLEM TO AVOID NUMERICAL INSTABILITIES . . . . .	81
3.1	Computation of the Rayleigh Eigenvalues . . . . .	85
3.2	Computation of the Rayleigh Eigenfunctions: I - A Simple but Stable Numerical Algorithm . . . . .	98
3.3	Computation of the Rayleigh Eigenfunctions: II - A More Robust Method . . . . .	114
3.4	Computation of the Love and Acoustic Eigenvalues and Eigenfunctions . . . . .	133
3.5	Rayleigh Eigenfunctions: The Final Numerical Algorithm . . . . .	138

IV.	NORMAL MODE SEISMOGRAM SYNTHESIS: THE NUMERICAL ALGORITHMS . . . . .	148
4.1	Eigenvalue Computation: The Mode Searching Algorithm . . . . .	152
4.2	Eigenvalue Computation: Computing the Group Velocity, Normalizing the Eigenfunctions, and Accounting for Frequency Dependent Anelastic Attenuation . . . . .	187
4.3	Locked Mode Seismogram Synthesis: The Computer Programs . . . . .	197
4.4	Locked Mode Seismogram Synthesis: The Locked Mode Approximation . . . . .	206
4.5	The Locked Mode Approximation: Comparisons with Other Complete Solution Methods and a Discussion of Its Limitations . . . . .	216
V.	NUMERICAL EXAMPLES OF THE LOCKED MODE APPROXIMATION . . . . .	227
VI.	CONCLUDING REMARKS . . . . .	241
	REFERENCES . . . . .	248
	APPENDIX	
A.	A METHOD OF REDUCING THE DYNAMIC RANGE OF THE [R] MATRIX ELEMENTS . . . . .	252
B.	THE COMPUTATIONS OF THE CHARACTERISTIC FUNCTION PARTIAL DERIVATIVES . . . . .	260
C.	THE SOURCE JUMP VECTOR . . . . .	277

## TABLES

### Table

4-1.	Three Layer Crust and Upper Mantle Structure . . . . .	164
4-2.	Southern California Crust and Upper Mantle Structure East of the San Andreas Fault . . . . .	179
4-3.	A Structural Model with Three Similar Low Velocity Zones . . . . .	186
4-4.	A Simple Two Layer Structural Model . . . . .	221
5-1.	The Rulison Structural Model . . . . .	233
5-2.	The Rulison Q Model . . . . .	234
5-3.	The Gasbuggy Structural Model . . . . .	238

## FIGURES

### Figure

2-1.	Coordinate systems and layer numbering conventions . . . . .	21
2-2.	Wavenumber integration contour . . . . .	67
3-1.	Vertical displacement and normal stress eigenfunctions for an infinite homogeneous half space using the traditional Thomson-Haskell matrix method . . . . .	104
3-2.	Vertical displacement and normal stress eigenfunctions for an infinite homogeneous half space using a stabilized version of the Thomson-Haskell matrix method with one constraint at five km depth . . . . .	105
3-3.	Vertical displacement and normal stress eigenfunctions for an infinite homogeneous half space using a stabilized version of the Thomson-Haskell matrix method with constraints at 2.5, 5.0, and 7.5 km depth . . . . .	105
3-4.	Vertical displacement and normal stress eigenfunctions for a two layer structural model using the traditional Thomson-Haskell matrix method . . . . .	108
3-5.	Vertical displacement and normal stress eigenfunctions for a two layer structural model using a stabilized version of the Thomson-Haskell matrix method with constraints at five and ten km depth . . . . .	109
3-6.	Vertical displacement and normal stress eigenfunctions for a two layer structural model using a stabilized version of the Thomson-Haskell matrix method with constraints at 2.5, 5.0, 7.5, and 10.0 km depth . . . . .	110
3-7.	Vertical displacement and normal stress eigenfunctions for an infinite homogeneous half space using equations (3.3.53) . . . . .	139
3-8.	Vertical displacement and normal stress eigenfunctions for a two layer structural model using equations (3.3.53) . . . . .	141



3-9.	Vertical displacement eigenfunctions for a structural model with two buried low velocity layers using equations (3.3.53) . . . . .	145
4-1.	A plot of the Rayleigh characteristic function versus phase velocity at a single frequency . . . . .	163
4-2.	Interpole spacing ratios for the Rayleigh characteristic function shown in figure 4-1. . . . .	168
4-3.	Rayleigh dispersion curves for the three layer crust and upper mantle structure . . . . .	176
4-4.	Rayleigh dispersion curves for the southern California structural model . . . . .	178
4-5.	Rayleigh dispersion curves for a structural model with three similar low velocity zones . . . . .	185
4-6.	Computer programs used to compute locked mode synthetic seismograms . . . . .	199
4-7.	A comparison of the locked mode approximation solution of Lamb's problem with the exact solution . . . . .	209
4-8.	A comparison of synthetic surface displacements using the locked mode approximation for various phase velocity cutoffs and as the cap layer depth is changed . . . . .	214
4-9.	A comparison of synthetic seismograms produced by the locked mode approximation and the complete spectral method of Wang and Herrmann (1980) . . . .	218
4-10.	A comparison of synthetic seismograms produced by the locked mode approximation with those produced by two other synthesis methods . . . . .	223
5-1.	Vertical velocity ground motion produced by the locked mode approximation for the structural model given in table 4-4. . . . .	228
5-2.	Vertical ground motion produced by the locked mode approximation for the southern California structural model and for a strike slip relaxation source . . . . .	230
5-3.	Vertical component synthetic seismograms produced by the locked mode approximation for the southern California structural model and for an explosion source . . . . .	231

5-4.	Vertical velocity ground motion produced by the locked mode approximation for the Rulison structural model . . . . .	235
5-5.	Radial velocity ground motion produced by the locked mode approximation for the Rulison structural model . . . . .	236
5-6.	A comparison of synthetic and observed Gasbuggy particle velocity seismograms . . . . .	239

## CHAPTER I

### INTRODUCTION

Historically, normal mode theory has been restricted in its applications to low frequency bandwidths; namely to low frequency spherical earth normal modes and to Rayleigh and Love surface waves for flat layered structures. In this dissertation I will show how spectral solutions of the elastic wave equation can be used to compute complete, high frequency synthetic seismograms for flat, plane layered, and laterally homogeneous structural models in an efficient manner. The method which I developed is most useful for computing synthetic seismograms in the zero to ten Hertz frequency range and for source-receiver distances of 10 to 1000 km. I have also been able to successfully apply the method to exploration geophysics problems with frequency bandwidths of 100 Hertz and source-receiver distances of several km. By making a simple modification to the structural model I am able to use this method to compute the P and S body waves, in addition to the surface waves, using only normal modes with real eigenwavenumbers. I am thus able to approximate a complete solution of the elastic wave equation with a mode sum which makes this approach much more efficient than existing complete solution methods which are based upon direct numerical integration such as the reflectivity method.

A variety of approaches have been used to synthesize the P and S body waves for laterally homogeneous structures, and all of these approaches start with a doubly transformed version of the elastic wave equation which remove the derivatives of time and the horizontal space coordinates. The

methods differ by the solution of the transformed wave equation which is used and by the way in which the two inverse transform integrals are evaluated. The asymptotic methods evaluate either one or both of these integrals analytically by approximating the integrand function with suitable asymptotic expansions, and the resulting solution is a decomposition of the complete solution in terms of rays. These ray theories work well for synthesizing particular phases, but they can be cumbersome to use when trying to compute the complete solution, especially in certain distance ranges. For very near field distances (zero to ten km) and at teleseismic distances (greater than 1000 km) and for sources at typical earthquake depths, the elastic energy is propagating in a fundamentally vertical direction in the crust. This means that the scattering off of the large discontinuities in the P and S wave velocities that can occur in the crust and at the Mohorovicic discontinuity (Moho) can be represented by a relatively small number of ray paths, and so the major applications of ray theory have been in these distance ranges. In the 10 to 1000 km distance range however the crust acts as a waveguide and most of the elastic energy is contained within this waveguide and propagates in a fundamentally horizontal direction. In this distance range, when using a detailed crust and upper mantle model, ray theories require the a priori specification of a very large number of ray paths to synthesize the complete solution for the P and S body waves (a typical example of this is the  $P_g$  coda which is seen in the western United States).

Another category of seismogram synthesis techniques which have been used over the past fifteen years are the complete solution methods and these methods all differ from the ray theoretical methods by the solution of the doubly transformed elastic wave equation which is used. The complete

solution methods, as the name implies, use a complete solution of the doubly transformed elastic wave equation by allowing for all possible P and S wave propagation throughout the structural model and by treating this as a boundary value problem. When one uses a complete solution method it is only necessary to specify the structural model and frequency bandwidth to compute synthetic seismograms and these synthetics contain an infinity of rays. In contrast, ray theoretical methods require the user to specify ray paths and, based upon these specified ray paths, an incomplete solution is obtained. It is the use of this incomplete solution, in addition to certain other approximations which are usually made, that causes the ray theoretical methods to be much more efficient than complete solution methods and it is primarily this efficiency that has made ray theoretical methods so popular.

The complete solution methods are themselves broken down into two general categories which I refer to as the reflectivity method and the spectral method and these methods differ in the way in which the two inverse transform integrals are evaluated. I am using the reflectivity method to refer to all methods which compute both integrals in a direct numerical manner although the original reflectivity method, as developed by Fuchs and Muller (1971), is rather restrictive in terms of the horizontal phase velocity range over which it works. Owing to recent developments (Kind (1978), Kennett and Kerry (1979), Kennett (1980), Cormier (1980), Bouchon (1981)) the reflectivity method can now be used to compute complete seismic codas for arbitrary frequency bandwidths and source depths and for vertically inhomogeneous structural models. If the reflectivity method were also efficient, then the problem of computing complete synthetic seismograms for flat, laterally homogeneous earth models could be

considered to be solved however the reflectivity methods are very computationally expensive and this expense is proportional to the product of the frequency bandwidth and the maximum source-receiver distance. In fact the computational expense is so high that it limits the use of these methods to low frequency bandwidths for cases where the complete seismic coda is computed.

One obvious way of increasing the efficiency of complete solution methods is to analytically evaluate at least one of the inverse transform integrals as is done by most ray theoretical methods. Unfortunately the complexity of the complete solution integrand function, for generally complex structural models, frustrates efforts to apply the types of techniques which are used by ray theoretical methods to eliminate the numerical evaluation of the inverse transform integrals. There is one straightforward method however which we can always use to evaluate at least part of one of the inverse transform integrals analytically and this method makes use of the residue theorem. We can extend the integration path in the complex plane into a closed contour and then evaluate the original integral in terms of a sum of residues which are caused by the poles of the integrand function which are contained within the contour of integration. These poles correspond to flat earth normal modes and for structural models which have totally reflective top and bottom boundaries, one of the inverse integral transforms can be expressed as an infinite sum of normal modes. The cases of most interest in seismology are for structural models which have a free top boundary and an infinite homogeneous half space on the bottom and for these situations one of the inverse integral transforms can be expressed as a finite sum of normal modes along with branch cut integrals which come about due to the semi-infinite nature of the structural model.

I refer collectively to methods which use the residue theorem to evaluate one of the inverse transform integrals as the spectral method. Although this method has not been as popular as the reflectivity method for computing complete synthetic seismograms, it has undergone parallel developments and improvements with the reflectivity method. The first uses of the spectral method actually predate the reflectivity method since the spectral method is the basis behind the computation of synthetic, flat earth, Rayleigh and Love fundamental surface waves however, among the earliest uses of the spectral method for computing a substantial portion of the complete seismic coda, are those of Knopoff, et. al. (1973), Nakanishi, et. al. (1977), and Mantovani, et. al. (1977) who used a sum of SH normal modes to compute synthetic SH seismograms. More recently Swanger and Boore (1978) computed both SH and P-SV synthetic seismograms for near field strong motion studies using a normal mode sum. All of these uses of the spectral method had one thing in common which was that a small number of normal modes was included in the mode sum and this resulted in rather incomplete solutions to the elastic wave equation.

One fundamental difficulty, which had a large effect on both the development of the complete solution methods and their ranges of applicability, was a numerical instability which seemed to be inherent in the complete solution form of the P-SV integrand function. This numerical instability was always associated with the presence of inhomogeneous or evanescent waves within the elastic medium which exist at horizontal phase velocities that are less than the local P or S wave velocity. This problem was first recognized by Dorman, et. al. (1960) when the complete matrix solution formalism of Thomson (1950) and Haskell (1953) was applied to the problem of computing Rayleigh dispersion curves using an early digital computer.

Although the numerical problem was circumvented for the computation of the fundamental Rayleigh dispersion curve by the use of structural layer reduction, it wasn't until Knopoff (1964) applied Laplace's development by minors to the problem of computing the Rayleigh characteristic function that the numerical problem was formally addressed in an analytical manner. Knopoff's work was the seed for an area of research which was followed by Dunkin (1965), Watson (1970) and most recently by Abo-Zena (1979) and all of this research was aimed at streamlining Knopoff's original method and understanding why it worked as well as it did. The method completely solved the numerical instability problem, as related to computing the Rayleigh characteristic function and thus the Rayleigh dispersion curves, for all frequency bandwidths and structural models.

Although Knopoff's method works quite well for computing the Rayleigh characteristic function *it does not address the problem of numerical instabilities which are present in the computation of the depth dependent stress and displacement eigenfunctions*. Because of this it has not been possible to use the spectral method to compute P-SV synthetic seismograms for buried sources and at high frequencies when using the Knopoff modified version of the Thomson-Haskell matrix formalism. Thus we can see that there are actually two numerical instability problems which must be solved in order to use the spectral method to compute P-SV synthetic seismograms for arbitrary sources and frequencies, and my research has focused on extending Knopoff's method to solve the eigenfunction numerical problem.

The same numerical difficulties that plagued the spectral method were encountered with the reflectivity method. The original method as given by Fuchs and Muller was based directly on the original Thomson-Haskell matrix method and they avoided the numerical problems by



limiting the range of phase velocities to those for which there were no evanescent waves within the structure. This narrowed the range of applicability of the reflectivity method until Kind (1978) applied Knopoff's method to remove the numerical instabilities. Kind also reformulated the integrand function in a manner which he claimed eliminated the numerical instabilities associated with buried sources. A completely different and novel approach was taken by Kennett, et. al. (1978), Kennett and Kerry (1979) and Kennett (1980) to solve the numerical problems of the reflectivity method which was not an extension of Knopoff's original work. They showed how the doubly transformed complete solution of the elastic wave equation could be expressed in terms of a set of generalized reflection and transmission functions. They then showed how all growing exponential solutions could be eliminated in this ray-like representation of the complete solution and this eliminated the numerical instabilities for all source depths.

The most recent developments of the spectral method have focused on solving the numerical problems for arbitrary frequencies, source depths, and structural models and extending the completeness of the spectral solutions. All of the earlier uses of the spectral method used only a small number of normal modes and thus produced rather incomplete solutions. Harvey (1981) and Kerry (1981) were the first researchers to use all of the normal modes with real eigenwavenumbers and I refer to spectral synthetic seismograms produced in this manner as locked mode synthetics. The branch cut integral contributions are ignored when using the locked mode method which gives the most complete spectral solution possible without using numerical integration or without locating poles off of the real wavenumber axis. At about the same time Wang and Herrmann (1980) developed a truly complete spectral solution by including both a numerical

integration of the branch cuts along with all of the locked mode residues.

As with the reflectivity method, the development of numerically stable algorithms to use in the spectral method has followed two paths. Kerry (1981) directly applied the methods developed by Kennett, et. al. which reformulated the frequency-wavenumber solution of the elastic wave equation in terms of generalized reflection and transmission functions. I chose to extend Knopoff's method, which operates directly with the Thomson-Haskell matrix formalism and uses stress and displacement functions to describe the elastic propagation, and the numerical algorithms which I developed constitute a substantial portion of my research. Kerry's locked mode method comes the closest to my own both in terms of the basic way in which it works and its range of applicability and I will be comparing these two methods throughout this dissertation.

The research which I will be describing in the following chapters has as its basic objective the development of an optimally fast, accurate and complete spectral method for computing P-SV synthetic seismograms for flat, plane layered, laterally homogeneous structural models. An equally important criterion which I placed on the method is that it work for the widest possible range of frequency bandwidths and structural models. I adopted this last criterion to cover problems such as high frequency  $P_n$  and  $S_n$  wave propagation in oceanic structural models with liquid and near-liquid layers and very high frequency near surface wave propagation in structural models which have numerous strong low velocity zones for problems in earthquake hazards engineering and geophysical exploration.

Since eigensolutions of the elastic wave equation can be thought of as providing optimal sampling in the wavenumber domain, spectral methods should be able to provide the most efficient way to compute

complete synthetic seismograms. I feel that one of the fundamental reasons that the spectral has not seen the popularity of the reflectivity method has been the lack of an efficient and reliable normal mode searching algorithm. A substantial portion of my research has been devoted to developing a truly fast, accurate and completely reliable mode searching algorithm in order to realize the potential efficiency of the spectral method. Also, in order to maximize the efficiency, it was desirable to compute nearly complete synthetic seismograms without making numerical evaluations of the branch cut integrals. For normal structural models locked mode synthetic seismograms will not contain any P wave arrivals since they are typically part of the branch cut integral contribution however, by making a simple modification to the structural model, one can significantly extend the phase velocity range which will be represented in the locked mode synthetic seismograms while simultaneously insuring that a certain time window within the synthetic seismograms will be uncontaminated by the structural modification. When the locked method is applied to such modified structural models, I refer to this as the locked mode approximation which produces nearly complete synthetic seismograms while only using normal modes with real eigenwavenumbers.

In chapter two I review the basic theory for computing flat earth normal modes and the resulting displacements. Most of this draws upon previously published work however I will present a complete and consistent derivation starting with the elastic wave equation and ending with the spectral solution for flat, plane layered, isotropic and laterally homogeneous models. During this derivation I will indicate the departure points of the various seismogram synthesis methods and I will also point out the sources of the numerical instabilities. The final solution which I derive will be

expressed in terms of proper and improper eigenfunctions representing respectively the discrete normal modes and the continuous branch cut integrals.

In chapter three I will address the numerical instabilities which are inherent in the Thomson-Haskell matrix formulation and I will present two methods which overcome these instabilities. I start by reviewing Knopoff's method, along with the later work which was based upon it, and I give the derivation of a numerically stable computation of the Rayleigh characteristic function. I then describe a simple method for stabilizing the depth dependent stress and displacement eigenfunctions which works quite well for completely elastic structural models with monotonically increasing velocities with depth except for no more than one weak low velocity zone. The locked mode method when using this algorithm is functionally equivalent to the method developed by Kerry and I discuss the restrictions which these methods have in common. I then proceed to derive a much more robust method of computing numerically stable eigenfunctions which has virtually no restrictions. This method works for oceanic models as well as for complex elastic models with multiple strong low velocity zones and at arbitrary frequency bandwidths. I finally show numerical examples of depth dependent eigenfunctions using the two methods for several different structural models.

In chapter four I describe the numerical algorithms and computer programs which I developed to implement the computation of locked mode synthetic seismograms from a starting structural model to the final, three component time traces at specified receiver locations. The first step in this process is the normal mode searching algorithm which locates the Rayleigh and Love dispersion curves and I go into considerable detail to describe the

algorithm which I developed. The next step involves the computation of certain partial derivatives which are necessary for eigenfunction normalization and which I use in a first order perturbation approximation to account for the effects of frequency dependent anelastic attenuation in the structural model. I give analytic expressions for these derivatives and I show how the first order attenuation approximation can be computed and applied in a fast manner which does not require the use of complex arithmetic. In the next section I describe the actual computer programs which I wrote and the user interface with these programs. I discuss practical matters such as the algorithms which require the use of double precision arithmetic, the amount of core memory required by each program, the approximate run times of the programs, and the structure and size of the intermediate data files which link the programs together. I then formally present the locked mode approximation and show when the approximation breaks down. In this section I also show synthetic seismograms produced by the locked mode approximation and how spurious arrivals caused by the approximation can be controlled. Finally I show comparisons of synthetic seismograms produced by the locked mode approximation with synthetics for the same structural models which were generated using other complete solution methods.

Chapter five is devoted to showing examples of synthetic seismograms produced by the locked mode approximation for a variety of frequency bandwidths, structural models and source-receiver distances. In the first part of the chapter I show a number of examples which illustrate the characteristics of elastic wave propagation which can be seen when using a complete solution method. I then show an example in which theoretical seismograms using the locked mode approximation are compared to real observed data. This example involves modelling an underground nuclear

explosion which took place in northern New Mexico and for which receivers recorded seismograms in the 10 to 100 km distance range and the 0 to 10 Hertz frequency range. This is a well constrained example since both the source and the structure were known and since the structure was closely approximated by a flat layered half space.

In chapter six I conclude the dissertation by summarizing the relative advantages and disadvantages of the locked mode approximation when compared to other seismogram synthesis techniques. The possibility of future extensions of my research are discussed which would extend the range of applicability of the methods which I have developed while maintaining the efficiency.

## CHAPTER II

### THE FUNDAMENTALS OF NORMAL MODE THEORY FOR FLAT LAYERED STRUCTURES

Although the development of the theoretical basis for elastic wave propagation can be traced all the way back to Lord Rayleigh's time, the first occurrence of the complete solution of the elastic wave equation in cylindrical coordinates and for flat, plane layered, isotropic and laterally homogeneous elastic media is given by Sezawa (1931). He uses a transformed version of the elastic wave equation which eliminates all derivatives except for the depth derivatives and thus he reduces the problem of solving the elastic wave equation to one of solving several ordinary differential equations and evaluating inverse integral transforms. The form of the solution which Sezawa presents is identical to that used by all modern day seismologists who work in cylindrical coordinates.

Sezawa did not give solutions for the depth dependent ordinary differential equations for arbitrary vertical velocity distributions and the next major development was aimed at solving these equations. Thomson (1950) derived a solution for the depth dependent differential equations which was expressed in terms of recursive matrix multiplications. Thomson's method applied to elastic structures which were composed of planar, isotropic and completely homogeneous layers which were welded together along their top and bottom surfaces. Although each layer had to be homogeneous there was no restriction on the number of different layers that were welded together or on the thinness of each layer and so, in the limit of

an infinite number of infinitesimally thin layers, Thomson's method provided complete solutions of the depth dependent differential equations for arbitrary vertical velocity profiles. Haskell (1953) embraced Thomson's approach and basically streamlined it and applied it to produce numerical computations of the fundamental Rayleigh dispersion curve for several simple structural models. The Thomson-Haskell matrix method has provided a formalism for obtaining complete solutions of the elastic wave equation and, as with Sezawa's work, this has become one of the basic tenets of a large branch of subsequent research.

It wasn't until digital computers became generally available that the next major developments in the theory of seismic wave propagation in cylindrical coordinates took place. In the early sixties a number of researchers applied the Thomson-Haskell matrix method to write computer programs for locating Rayleigh dispersion curves (e.g. Dorman, et. al. (1960), Press, et. al. (1961)). Numerical instabilities in the Thomson-Haskell method were discovered at this time however these instabilities occurred at frequencies which were above the range of interest of the researchers. Harkrider (1964) made the next major contribution by showing how to compute time domain synthetic seismograms for Rayleigh and Love surface waves and for arbitrary point sources at arbitrary depths. This research was based directly on the Thomson-Haskell matrix method and it suffered an additional numerical instability associated with the source depth.

In the following chapter I give a condensed yet complete summary of linear elastic wave theory for flat, plane layered, laterally homogeneous structures. This treatment will draw primarily from the work of Harkrider (1964) and Ben-Menahem and Singh (1972 and 1981) who show how a complete solution of the elastic wave equation can be expressed in



terms of vector cylindrical harmonics, but in order to preserve continuity, I will use my own notation and layering conventions. I will show how normal mode solutions are derived from the general solutions of the elastic wave equation and to what extent these solutions are related to other types of solutions such as ray theoretical and reflectivity solutions. I will also point out both accuracy and efficiency problems which come up in the numerical implementation of the theory. These problems will be addressed in detail in subsequent chapters and constitute the major portion of my research.

## 2.1 Basic Assumptions

In order to obtain tractable solutions of the elastic wave equation it is necessary to make a number of assumptions. Most of the assumptions I have made fall in this category and are absolutely necessary in order to solve the problem at all. I have however made a few additional assumptions which were made primarily to narrow the range of the problem and I will outline the necessary steps which must be taken to remove these assumptions.

The first assumption is that of a linearized elastic wave equation. This is widely used and accepted by seismologists and is justified by the small amplitudes of differential strains that are produced globally by most seismic disturbances. The exception to this is in the near vicinity of a large, non-linear seismic source such as an earthquake or a nuclear explosion. Even in these cases we can consider the elastic wave field to be linear beyond some volume which encloses the non-linear source region and represent the source by an equivalent linear point source (e.g. Bache and Harkrider (1976)). In this case our solution will be invalid within the non-linear region but will be valid outside that region.

The second assumption is an earth structure which is laterally homogeneous. This is the most restrictive assumption and considering the attention that seismogram synthesis for laterally homogeneous structures has received in the past, some justification is deserved at this point. I justified the laterally homogeneous assumption based upon the following three premises:

1. A starting point for the solution of certain laterally inhomogeneous problems is an accurate, efficient and complete solution to the laterally homogeneous problem.
2. Although much work has been directed towards the laterally homogeneous problem, an accurate efficient and complete solution is yet to be realized.
3. Spectral solutions of the elastic wave equation promise the most efficient solution to the problem, at least when compared to the methods used presently.

The second premise can be justified by a quick review of existing methods for synthesizing seismograms for laterally homogeneous structures. These methods fall into two general categories: ray theoretical methods and complete solutions methods. Ray theoretical methods, although efficient and accurate, do not, in general, provide complete solutions (Hartzell and Helmburger (1982)). The complete solution methods are all closely related to the original reflectivity method (Fuchs and Muller, (1972)) and suffer from being rather inefficient. This is due to the direct numerical integration approach used by all of these methods to compute the inverse Hankel transform. Discrete spectral representations of the solution, however, allow for the inverse Hankel transform to be evaluated analytically in terms of a residue sum which, in addition to avoiding the accuracy problems associated

with direct numerical integration, also provides a more efficient solution as I will show later.

The third assumption is the flat earth approximation. This is not at all restrictive and can be easily justified for several reasons. First of all, as will be shown later, the major applicability of the spectral method will be for near field problems where the flat earth approximation is quite good on its own. If the source receiver distances become large, a flattening correction can be applied to the vertical structural dependence which will give very good solutions out to teleseismic distances. It should be pointed out that *all* ray theoretical solutions end up making the flat earth approximation implicitly by using the Poisson sum formula to convert discrete sum solutions in terms of spherical wave functions to continuous integral solutions in terms of cylindrical or Cartesian wave functions.

The fourth assumption is that the earth structure will be made up of homogeneous layers connected by flat plane interfaces. At first this may appear to be a restrictive assumption, but we can represent any arbitrary depth dependence for some finite wave length by specifying a large number of suitably thin layers. The question, then, is whether it is more efficient and accurate to use a large number of homogeneous layers or a smaller number of inhomogeneous layers and I will address this question in more detail in a later section.

The fifth assumption is that the earth structure will be isotropic. This restriction can be reduced to that of lateral isotropy without any fundamental change in the analytical development of the solution although with the expense of significantly increased algebraic complexity.

The sixth assumption is that the source of seismic energy will be a spatial point source. Once again this is not a restrictive assumption since any distributed source can be represented as either an equivalent point source or a linear superposition of a large number of point sources placed along the boundary of the distributed source.

## 2.2 Differential Equations, Coordinate Systems, and Boundary Conditions

The most general representation of the linearized elastic wave equation in Cartesian coordinates is:

$$\sigma_{ij,j} + \rho f_i = \rho \ddot{u}_i \quad (2.2.1)$$

where  $\sigma_{ij}$  is the space and time dependent stress tensor,  $f_i$  is the space and time dependent applied body forces,  $\rho$  is the space dependent density and  $u_i$  is the space and time dependent displacement vector. Integer indices range from one to three with the implied summation convention. Partial differentiation is indicated by  $,j = \partial/\partial x_j$  and  $\ddot{\phantom{u}} = \partial^2/\partial t^2$ .

The stress tensor is related to the displacements through the constitutive tensor,  $C_{ijkl}$ :

$$\sigma_{ij} = C_{ijkl} u_{k,l} \quad (2.2.2)$$

Using the first law of thermodynamics and assuming adiabatic elastic deformations, one can show:

$$C_{ijkl} = C_{klij} \quad (2.2.3)$$

and since the stress and strain tensors are symmetric,

$$C_{ijkl} = C_{jikl} = C_{ijlk} = C_{jilk} \quad (2.2.4)$$

Equations (2.2.3) and (2.2.4) reduce the number of independent components

in  $C_{ijkl}$  to 21 and this is the number of elastic constitutive parameters which must be specified for a general anisotropic material. Since we have assumed a linearized elastic wave equation, each of these parameters depend only on the spatial coordinates and not on the displacement or any of its derivatives. Also, since we assumed a laterally homogeneous structure, the elastic constitutive parameters (along with the density) will only be dependent on one spatial coordinate,  $x_3$ .

If we assume lateral isotropy about the  $x_3$  axis, the number of independent elastic constitutive parameters reduces from 21 to 5 and following the notation of Takeuchi and Saito (1972) we represent these parameters with the coefficients A, C, F, L and N in expression (2.2.2).

$$\sigma_{11} = A(u_{1,1} + u_{2,2}) - 2Nu_{2,2} - Fu_{3,3} \quad (2.2.5)$$

$$\sigma_{22} = A(u_{1,1} + u_{2,2}) - 2Nu_{1,1} - Fu_{3,3}$$

$$\sigma_{33} = F(u_{1,1} + u_{2,2}) + Cu_{3,3}$$

$$\sigma_{23} = L(u_{2,3} + u_{3,2}) = \sigma_{32}$$

$$\sigma_{31} = L(u_{3,1} + u_{1,3}) = \sigma_{13}$$

$$\sigma_{12} = N(u_{1,2} + u_{2,1}) = \sigma_{21}$$

For the case of a completely isotropic material,

$$A = C = \lambda + 2\mu, L = N = \mu, F = \lambda \quad (2.2.6)$$

where  $\lambda$  and  $\mu$  are the Lamé elastic parameters and we can rewrite equation (2.2.2) in the following familiar form:

$$\sigma_{ij} = \lambda \delta_{ij} u_{k,k} + \mu (u_{i,j} + u_{j,i}) \quad (2.2.7)$$

Typically the elastic parameters are redefined in terms of the P and S wave

velocities in a homogeneous isotropic material

$$\alpha = \sqrt{(\lambda + 2\mu)/\rho}, \quad \beta = \sqrt{\mu/\rho} \quad (2.2.8)$$

For the case of a laterally isotropic material we can also define the elastic parameters in terms of horizontal and vertical propagating P and S wave velocities.

$$\begin{aligned} \alpha_H &= \sqrt{A/\rho}, \quad \alpha_V = \sqrt{C/\rho}, \\ \beta_H &= \sqrt{N/\rho}, \quad \beta_V = \sqrt{L/\rho} \end{aligned} \quad (2.2.9)$$

and we are left over with a fifth coefficient, F.

The constitutive relations (2.2.5) and (2.2.7) along with the elastic parameters allow us to model either a full elastic material or an acoustic liquid material by setting  $\beta = 0$ . We can also model an anelastic material by allowing the elastic moduli to have non-zero imaginary components and this will be addressed in more detail in a later chapter.

In order to easily represent the radiation field from point sources and to match boundary conditions at horizontal layer interfaces, the coordinates will be changed from Cartesian to a cylindrical coordinate system and all of the following analytical developments will be done in cylindrical coordinates. The cylindrical coordinate system is shown in Figure 2-1 along with layer numbering conventions. At a later point in the theoretical development the assumption of a layered structure will be made and since I will be writing solutions of the wave equation in each individual layer and then matching boundary conditions throughout the stack, I employ both a global coordinate system and a set of local coordinates, each relative to an individual layer. The origin of the global coordinate system will be at the free surface with the positive z-axis pointing down. The origin of a local



coordinate system will be at the top of the layer, with the radial and azimuthal coordinates being the same for all of the coordinate systems.

I distinguish between the global and local vertical coordinates by using an unsubscripted or unsuperscripted  $z$  for the global coordinate and a superscripted  $\zeta^{(p)}$  for local coordinates where  $p$  is the layer index. The depth of the bottom of the  $p^{\text{th}}$  layer in global coordinates is  $z = h^{(p)}$  whereas the thickness of the  $p^{\text{th}}$  layer is  $\xi^{(p)}$ , ( $\xi^{(p)} = h^{(p)} - h^{(p-1)}$ ). This dual representation is used for all of the functions of  $z$  as well. Whenever a function of  $z$  appears without a layer superscript it is understood that the argument will be in global coordinates and whenever a layer superscript does appear, then the argument of the function will be in local coordinates. Thus for some function,  $f(z)$

$$f(z) \Big|_{z = h^{(p-1)} + \zeta^{(p)}} = f^{(p)}(\zeta^{(p)}) \quad (2.2.10)$$

By making the flat earth and laterally homogeneous assumptions, the elastic moduli and density will be dependent only on the  $z$  coordinate and the lateral isotropy assumption will imply isotropy about the  $z$ -axis.

The boundary conditions will be specified either in terms of displacements and tractions, or in terms of wave field functions (radiation condition). The displacements are denoted by  $u_r(r, \theta, z, t)$ ,  $u_\theta(r, \theta, z, t)$ ,  $u_z(r, \theta, z, t)$ , and the tractions across a horizontal plane are  $T_r(r, \theta, z, t)$ ,  $T_\theta(r, \theta, z, t)$ , and  $T_z(r, \theta, z, t)$ . The boundary conditions are as follows

1. A traction-free surface will exist at the top of the structure ( $z = 0$ ).

$$\begin{aligned} T_r(r, \theta, 0, t) - T_\theta(r, \theta, 0, t) &= \\ &= T_z(r, \theta, 0, t) = 0 \quad \text{for all } r, \theta, t \end{aligned} \quad (2.2.11)$$

2. Either a radiation condition will exist for a semi-infinite bottom layer,

$$\text{no sources at } z \rightarrow \infty, \quad (2.2.12)$$



or a plate boundary condition will exist for the underside of the bottom layer at  $z = H$  which can be specified in several ways; either

$$T_r(r, \theta, H; t) = T_\theta(r, \theta, H; t) = T_z(r, \theta, H; t) = 0 \text{ for all } r, \theta, t, \quad (2.2.13)$$

or

$$u_r(r, \theta, H; t) = u_\theta(r, \theta, H; t) = u_z(r, \theta, H; t) = 0 \text{ for all } r, \theta, t, \quad (2.2.14)$$

or

$$T_r(r, \theta, H; t) = T_\theta(r, \theta, H; t) = u_z(r, \theta, H; t) = 0 \text{ for all } r, \theta, t. \quad (2.2.15)$$

The mixed boundary condition given by (2.2.15) insures no conversion of P to S energy at the plate bottom or vice versa.

3. Tractions and displacements will be continuous along the  $z$ -axis for all  $r, \theta$ , and  $t$  as long as the elastic moduli are continuous except at the source location.
4. For a horizontal interface at  $z = h$  where the elastic moduli change discontinuously, the boundary conditions will be specified according to the type of discontinuity. For a solid-solid discontinuity,

$$T_r(r, \theta, h^+; t) = T_r(r, \theta, h^-; t),$$

$$T_\theta(r, \theta, h^+; t) = T_\theta(r, \theta, h^-; t),$$

$$T_z(r, \theta, h^+; t) = T_z(r, \theta, h^-; t), \quad (2.2.16)$$

$$u_r(r, \theta, h^+; t) = u_r(r, \theta, h^-; t),$$

$$u_\theta(r, \theta, h^+; t) = u_\theta(r, \theta, h^-; t),$$

$$\text{and } u_z(r, \theta, h^+; t) = u_z(r, \theta, h^-; t),$$

for all  $r, \theta$ , and  $t$ , where  $h^+$  is just below the interface and  $h^-$  is just above the interface.

For a solid-liquid and liquid-liquid discontinuity

$$T_r(r, \theta, h^+; t) = T_\theta(r, \theta, h^+; t) = 0,$$

$$T_r(r, \theta, h^-; t) = T_\theta(r, \theta, h^-; t) = 0,$$

$$T_z(r, \theta, h^+; t) = T_z(r, \theta, h^-; t), \quad (2.2.17)$$

$$u_z(r, \theta, h^+; t) = u_z(r, \theta, h^-; t),$$

for all  $r, \theta$ , and  $t$ .

### 2.3 Separable Solutions of the Elastic Wave Equation in Cylindrical Coordinates

The elastic wave equation (2.2.1), can be written in cylindrical coordinates as follows:

$$\rho \ddot{u}_r = \rho f_r + \frac{1}{r} \frac{\partial}{\partial r} (r \sigma_{rr}) - \frac{1}{r} \frac{\partial \sigma_{r\theta}}{\partial \theta} + \quad (2.3.1)$$

$$+ \frac{\partial \sigma_{rz}}{\partial z} - \frac{1}{r} \sigma_{\theta\theta}$$

$$\rho \ddot{u}_\theta = \rho f_\theta + \frac{1}{r} \frac{\partial}{\partial r} (r \sigma_{r\theta}) + \frac{1}{r} \frac{\partial \sigma_{\theta\theta}}{\partial \theta} +$$

$$+ \frac{\partial \sigma_{\theta z}}{\partial z} + \frac{1}{r} \sigma_{r\theta}$$

$$\rho \ddot{u}_z = \rho f_z + \frac{1}{r} \frac{\partial}{\partial r} (r \sigma_{rz}) - \frac{1}{r} \frac{\partial \sigma_{\theta z}}{\partial \theta} + \frac{\partial \sigma_{zz}}{\partial z}$$

Likewise, the constitutive equations (2.2.5) can also be written in cylindrical coordinates for the case of lateral isotropy.

$$\sigma_{rr} = A \frac{\partial u_r}{\partial r} + (A - 2N) \left( \frac{1}{r} \frac{\partial u_\theta}{\partial \theta} - \frac{1}{r} u_r \right) + F \frac{\partial u_z}{\partial z} \quad (2.3.2)$$

$$\sigma_{\theta\theta} = (\Lambda - 2N) \frac{\partial u_r}{\partial r} + \Lambda \left( \frac{1}{r} \frac{\partial u_\theta}{\partial \theta} + \frac{1}{r} u_r \right) + F \frac{\partial u_z}{\partial z}$$

$$\sigma_{zz} = F \frac{\partial u_r}{\partial r} + F \left( \frac{1}{r} \frac{\partial u_\theta}{\partial \theta} + \frac{1}{r} u_r \right) + C \frac{\partial u_z}{\partial z}$$

$$\sigma_{\theta z} = L \left( \frac{1}{r} \frac{\partial u_z}{\partial \theta} + \frac{\partial u_\theta}{\partial z} \right) = \sigma_{z\theta}$$

$$\sigma_{rz} = L \left( \frac{\partial u_r}{\partial z} + \frac{\partial u_z}{\partial r} \right) = \sigma_{zr}$$

$$\sigma_{r\theta} = N \left( \frac{\partial u_\theta}{\partial r} - \frac{1}{r} u_\theta + \frac{1}{r} \frac{\partial u_r}{\partial \theta} \right) = \sigma_{\theta r},$$

where the coefficients  $\Lambda$ ,  $C$ ,  $L$ ,  $N$ , and  $F$  are functions only of  $z$ . For the case of a completely isotropic structure equations (2.3.2) reduce to the following:

$$\sigma_{rr} = (\lambda + 2\mu) \frac{\partial u_r}{\partial r} + \lambda \left( \frac{1}{r} u_r + \frac{1}{r} \frac{\partial u_\theta}{\partial \theta} + \frac{\partial u_z}{\partial z} \right) \quad (2.3.3)$$

$$\sigma_{\theta\theta} = (\lambda + 2\mu) \left( \frac{1}{r} u_r + \frac{1}{r} \frac{\partial u_\theta}{\partial \theta} \right) + \lambda \left( \frac{\partial u_r}{\partial r} + \frac{\partial u_z}{\partial z} \right)$$

$$\sigma_{zz} = (\lambda + 2\mu) \frac{\partial u_z}{\partial z} + \lambda \left( \frac{1}{r} u_r + \frac{1}{r} \frac{\partial u_\theta}{\partial \theta} + \frac{\partial u_r}{\partial r} \right)$$

$$\sigma_{\theta z} = \mu \left( \frac{1}{r} \frac{\partial u_z}{\partial \theta} + \frac{\partial u_\theta}{\partial z} \right) = \sigma_{z\theta}$$

$$\sigma_{rz} = \mu \left( \frac{\partial u_r}{\partial z} + \frac{\partial u_z}{\partial r} \right) = \sigma_{zr}$$

$$\sigma_{r\theta} = \mu \left( \frac{\partial u_\theta}{\partial r} - \frac{1}{r} u_\theta + \frac{1}{r} \frac{\partial u_r}{\partial \theta} \right) = \sigma_{\theta r},$$

where once again  $\lambda$  and  $\mu$  are functions only of  $z$ .

Equations (2.3.2) or (2.3.3) could be substituted back into equations (2.3.1) to eliminate the stress variables and produce a system of three coupled, second order, partial differential equations in the three displacement unknowns,  $u_r$ ,  $u_\theta$ , and  $u_z$ . The next step, normally, would be to define three potential functions of the displacements in order to decouple the system of equations (2.3.1). The P wave dilatational potential and the SV and SH wave shear potential functions will only decouple equations (2.3.1) when the structure is completely homogeneous and, in the case of an arbitrarily inhomogeneous material, the representation of equations (2.3.1) in terms of the potential functions would be completely coupled. Ben-Menahem and Singh (1981) have shown, however, how separable solutions of the elastic wave equation in cylindrical coordinates for the case of an arbitrary vertically inhomogeneous structure can be represented in terms of vector cylindrical harmonics. When these separable functions are substituted into equations (2.3.1), the  $t$ ,  $r$  and  $\theta$  dependence are eliminated and we are left with a set of coupled ordinary differential equations (ODE) in the depth variable,  $z$ .

I will thus assume the following solutions for the displacements,

$$\mathbf{u} = (u_r, u_\theta, u_z).$$

$$\begin{aligned} \mathbf{u} = e^{i\omega t} \left( u_P(\omega, k, m, z) \mathbf{P}_k^m(r, \theta) + \right. \\ \left. + u_B(\omega, k, m, z) \mathbf{B}_k^m(r, \theta) + u_C(\omega, k, m, z) \mathbf{C}_k^m(r, \theta) \right) \end{aligned} \quad (2.3.4)$$

where  $\omega$  is the constant angular frequency,

$k$  is the constant horizontal wavenumber,

$m$  is the constant integer azimuthal order,

and  $P$ ,  $B$  and  $C$  are the vector cylindrical harmonics and are given by

$$P_k^m(r, \theta) = e_z Y_k^m(r, \theta)$$

$$B_k^m(r, \theta) = \left( e_r \frac{\partial}{\partial(kr)} + e_\theta \frac{1}{kr} \frac{\partial}{\partial \theta} \right) Y_k^m(r, \theta) \quad (2.3.5)$$

$$C_k^m(r, \theta) = \left( e_r \frac{1}{kr} \frac{\partial}{\partial \theta} - e_\theta \frac{\partial}{\partial(kr)} \right) Y_k^m(r, \theta),$$

where  $e_r$ ,  $e_\theta$  and  $e_z$  are unit vectors in the  $r$ ,  $\theta$  and  $z$  directions and  $Y_k^m(r, \theta)$  is the scalar horizontal wavefunction and is

$$Y_k^m(r, \theta) = J_m(kr) e^{im\theta}. \quad (2.3.6)$$

$J_m(kr)$  is the integer order Bessel function of the first kind.

In order to satisfy the boundary conditions it will be necessary to compute the tractions across the  $z=\text{constant}$  plane as well as the displacements. Separable solutions for the tractions in terms of vector cylindrical harmonics will also be used.

$$T = e^{i\omega t} \left( T_P(\omega, k, m, z) P_k^m(r, \theta) + \right. \quad (2.3.7)$$

$$\left. + T_B(\omega, k, m, z) B_k^m(r, \theta) + T_C(\omega, k, m, z) C_k^m(r, \theta) \right)$$

where  $T = (T_r, T_\theta, T_z)$  and

$$T_r = \sigma_{rr}$$

$$T_\theta = \sigma_{\theta z}$$

$$T_z = \sigma_{zz}.$$

Finally, I will represent the body forces,  $\rho f = (\rho f_r, \rho f_\theta, \rho f_z)$ , in the same manner as the displacements and tractions.

$$\rho f = e^{i\omega t} \left( f_P(\omega, k, m, z) P_1^m(r, \theta) + \right. \\ \left. + f_B(\omega, k, m, z) B_1^m(r, \theta) + f_C(\omega, k, m, z) C_1^m(r, \theta) \right) \quad (2.3.8)$$

If we substitute equations (2.3.4), (2.3.7), and (2.3.8) into equations (2.3.1) and (2.3.2) and use relations (2.3.5) and (2.3.6) along with various properties of integer order Bessel functions, the  $t$ ,  $r$  and  $\theta$  dependences can be factored out leaving a system of six coupled ordinary differential equations of  $z$ , in the dependent variables  $u_P$ ,  $u_B$ ,  $u_C$ ,  $T_P$ ,  $T_B$ , and  $T_C$ . The resulting  $z$ -dependent ODEs can be written as follows:

$$\frac{d}{dz} \begin{Bmatrix} u_P \\ u_B \\ T_P \\ T_B \\ u_C \\ T_C \end{Bmatrix} = \begin{bmatrix} 0 & k \frac{F}{C} & \frac{1}{C} & 0 & 0 & 0 \\ -k & 0 & 0 & \frac{1}{L} & 0 & 0 \\ -\omega^2 \rho & 0 & 0 & k & 0 & 0 \\ 0 & \left[ k^2 \left( A - \frac{F^2}{C} \right) - \omega^2 \rho \right] & -\frac{kF}{C} & 0 & 0 & 0 \\ 0 & 0 & 0 & 0 & 0 & \frac{1}{L} \\ 0 & 0 & 0 & 0 & (k^2 N - \omega^2 \rho) & 0 \end{bmatrix} \begin{Bmatrix} u_P \\ u_B \\ T_P \\ T_B \\ u_C \\ T_C \end{Bmatrix} \\ - \begin{Bmatrix} 0 \\ 0 \\ f_P \\ f_B \\ 0 \\ f_C \end{Bmatrix} \quad (2.3.9)$$

Once again the elastic moduli  $A$ ,  $C$ ,  $L$ ,  $N$ , and  $F$  are arbitrary functions of  $z$  and at this point we have made no approximations or assumptions other than linearity, laterally homogeneous structure and laterally isotropic structure.

Because of the separable form of the solutions expressed by equations (2.3.4) and (2.3.7), equations (2.3.7) must hold at a fixed  $\omega$ ,  $k$  and  $m$  for all  $t$ ,  $r$  and  $\theta$ . Thus the boundary conditions expressed by equations (2.2.11) through (2.2.17) will be insured by applying them to the depth dependent spectral functions in equations (2.3.9).

#### 2.4 Solutions of the Depth Dependent ODEs: The Propagator Matrix

We can write equations (2.3.9) in a more convenient form as follows:

$$\frac{d}{dz} \{y(z)\} = [U(z)] \{y(z)\} - \{w(z)\}, \quad (2.4.1)$$

where  $\{y(z)\}$  is the six component displacement-stress vector, and is given by

$$\begin{pmatrix} y_1(z) \\ y_2(z) \\ y_3(z) \\ y_4(z) \\ y_5(z) \\ y_6(z) \end{pmatrix} = \begin{pmatrix} u_P \\ u_B \\ T_P \\ T_B \\ u_C \\ T_C \end{pmatrix}, \quad (2.4.2)$$

$\{w(z)\}$  is the six component forcing function vector and for a time and space distribution of simple body forces is given by

$$\begin{pmatrix} w_1(z) \\ w_2(z) \\ w_3(z) \\ w_4(z) \\ w_5(z) \\ w_6(z) \end{pmatrix} = \begin{pmatrix} 0 \\ 0 \\ f_P \\ f_B \\ 0 \\ f_C \end{pmatrix}, \quad (2.4.3)$$

and  $[U(z)]$  is a six by six matrix whose element are functions only of  $\omega, k$  and depth dependent elastic moduli.

It is obvious from equations (2.3.9) that we can partition equations (2.4.1) as follows,

$$\frac{d}{dz} \{Ry(z)\} = [R U(z)] \{Ry(z)\} - \{Rw(z)\}, \quad (2.4.4)$$

and

$$\frac{d}{dz} \{Ly(z)\} = [L U(z)] \{Ly(z)\} - \{Lw(z)\}. \quad (2.4.5)$$

Where

$$\{Ry(z)\} = \begin{Bmatrix} y_1(z) \\ y_2(z) \\ y_3(z) \\ y_4(z) \end{Bmatrix}, \{Rw(z)\} = \begin{Bmatrix} w_1(z) \\ w_2(z) \\ w_3(z) \\ w_4(z) \end{Bmatrix},$$

$$[R U(z)] = \begin{bmatrix} 0 & \frac{kF}{\alpha_V^2 \rho} & \frac{1}{\alpha_V^2 \rho} & 0 \\ -k & 0 & 0 & \frac{1}{\beta_V^2 \rho} \\ -\omega^2 \rho & 0 & 0 & k \\ 0 & \left[ k^2 \left( \alpha_H^2 \rho - \frac{F^2}{\alpha_V^2 \rho} \right) - \omega^2 \rho \right] & -\frac{kF}{\alpha_V^2 \rho} & 0 \end{bmatrix}, \quad (2.4.6)$$

and

$$\{Ly(z)\} = \begin{Bmatrix} y_5(z) \\ y_6(z) \end{Bmatrix}, \{Lw(z)\} = \begin{Bmatrix} w_5(z) \\ w_6(z) \end{Bmatrix}, \quad (2.4.7)$$

$$[L U(z)] = \begin{bmatrix} 0 & \frac{1}{\beta_V^2 \rho} \\ (k^2 \beta_H^2 \rho - \omega^2 \rho) & 0 \end{bmatrix}.$$



and where the R subscript denotes Rayleigh or P-SV wave motion, the L subscript denotes Love or SH wave motion, and the elastic moduli A, C, L and N have been replaced by the P and S wave vertical and horizontal velocities,  $\alpha_v$ ,  $\beta_v$ ,  $\alpha_H$ , and  $\beta_H$  from equations (2.2.9). We can easily determine  $[{}_R U]$  and  $[{}_L U]$  for a completely isotropic structure by setting  $\alpha_v = \alpha_H = \alpha$ ,  $\beta_v = \beta_H = \beta$  and  $F = \lambda$ .

Consider the homogeneous or unforced part of equation (2.4.1), namely,

$$\frac{d}{dz} \{y\} = [U] \{y\}. \quad (2.4.8)$$

Gilbert and Backus (1966) studied solutions to this equation and popularized and generalized the propagator matrix method which was first employed by Thomson (1950) and Haskell (1953) for the case of a plane homogeneous layered structure. In order to solve (2.4.8) the matrizant of  $[U]$  is defined as follows,

$$\begin{aligned} [A(z, z_0)] &= [I] + \int_{z_0}^z [U(\zeta_1)] d\zeta_1 - \\ &+ \int_{z_0}^z [U(\zeta_1)] \int_{z_0}^{\zeta_1} [U(\zeta_2)] d\zeta_2 d\zeta_1 + \dots \end{aligned} \quad (2.4.9)$$

where  $[I]$  is the unit matrix. Differentiating the matrizant with respect to  $z$  gives,

$$\frac{d}{dz} [A(z, z_0)] = [U(z)] + [U(z)] \int_{z_0}^z [U(\zeta_1)] d\zeta_1 + \dots$$

or

$$\frac{d}{dz} [A(z, z_0)] = [U(z)] [A(z, z_0)]. \quad (2.4.10)$$

If we post multiply (2.4.10) by  $\{y(z_0)\}$  we arrive at,

$$\frac{d}{dz} [A(z, z_0)] \{y(z_0)\} = [U(z)] [A(z, z_0)] \{y(z_0)\} , \quad (2.4.11)$$

and comparing this to equation (2.4.8) it follows that,

$$\{y(z)\} = [A(z, z_0)] \{y(z_0)\} . \quad (2.4.12)$$

When we include the forcing function vector  $\{w\}$ , equation (2.4.12) becomes

$$\{y(z)\} = [A(z, z_0)] \{y(z_0)\} - \int_{z_0}^z [A(z, \zeta)] \{w(\zeta)\} d\zeta . \quad (2.4.13)$$

The matrizant of  $[U]$  given by equation (2.4.9) allows us to propagate the solution for  $\{y\}$  from some initial depth,  $z_0$ , to some other depth,  $z$ , and thus the matrizant is usually called the propagator matrix. One obvious property of the propagator matrix which must be true in order for relation (2.4.12) to be valid is that,

$$[A(z, z)] = [I] . \quad (2.4.14)$$

Another important property of the propagator matrix is that it is only dependent on  $\omega$ ,  $k$ ,  $z$ , and the depth dependent elastic moduli, and is independent of  $r$ ,  $\theta$  and the azimuthal order  $m$ . The major difficulty, then in determining spectral solutions of the elastic wave equation for a laterally homogeneous structure, is in computing the propagator matrix.

Consider the  $\{y\}$  vector at three depths,  $z_0$ ,  $z_1$ , and  $z_2$ , such that  $z_2 > z_1 > z_0$ . From equation (2.4.13),

$$\{y(z_1)\} = [A(z_1, z_0)] \{y(z_0)\} - \int_{z_0}^{z_1} [A(z_1, \zeta)] \{w(\zeta)\} d\zeta$$

and

$$\{y(z_2)\} = [A(z_2, z_1)] \{y(z_1)\} - \int_{z_1}^{z_2} [A(z_2, \zeta)] \{w(\zeta)\} d\zeta .$$

or

$$\begin{aligned} \{y(z_2)\} &= [A(z_2, z_1)] [A(z_1, z_0)] \{y(z_0)\} \\ &\quad - [A(z_2, z_1)] \int_{z_0}^{z_1} [A(z_1, \zeta)] \{w(\zeta)\} d\zeta \\ &\quad - \int_{z_1}^{z_2} [A(z_2, \zeta)] \{w(\zeta)\} d\zeta, \end{aligned}$$

but since

$$\{y(z_2)\} = [A(z_1, z_0)] \{y(z_0)\} - \int_{z_0}^{z_1} [A(z_2, \zeta)] \{w(\zeta)\} d\zeta,$$

$$[A(z_2, z_0)] = [A(z_2, z_1)] [A(z_1, z_0)]. \quad (2.4.15)$$

Equation (2.4.15) expresses an important property of the propagator matrix which is especially useful when dealing with layered structures. The depth restriction,  $z_2 > z_1 > z_0$ , is actually not necessary and as a corollary to (2.4.15),

$$[A(z_0, z_0)] = [I] = [A(z_0, z_1)] [A(z_1, z_0)],$$

or

$$[A(z_0, z_1)] = [A(z_1, z_0)]^{-1}. \quad (2.4.16)$$

Thus the upward propagator matrix between two depths is the inverse of the downward propagator matrix between the same two depths.

For the case of a general heterogeneous structure with depth, equation (2.4.9) cannot be solved analytically and the only method presently available is that of numerical integration. In practice equation (2.4.1) is integrated with respect to  $z$  so that,

$$\{y(z)\} = \{y(z_0)\} + \int_{z_0}^z [U(\zeta)] \{y(\zeta)\} d\zeta - \int_{z_0}^z \{w(\zeta)\} d\zeta.$$

(2.4.17)

The six by six propagator matrix can be determined by ignoring the forcing function contribution in (2.4.17) and then numerically integrating  $[U(z)]$   $\{y(z)\}$  six times with each element of the starting value of  $\{y(z_0)\}$  set consecutively to unity, the other elements being zero. The resulting six values of the vector  $\{y(z)\}$  will constitute the six columns of  $[A(z, z_0)]$ . It should be pointed out at this time that *all* solutions of the depth dependent ODEs for an arbitrary heterogeneous medium are in fact approximations to the exact solution. Thus we should evaluate candidate approximations according to accuracy, efficiency and ease of implementation.

One candidate approximation which is very popular and relatively easy to implement is to assume the structure is made up of a number of plane layers, each layer being completely homogeneous. It is obvious that any arbitrary depth dependence can be approximated by a large number of sufficiently thin homogeneous layers welded together. The approximation would then break down at wavelengths less than or equal to the individual layer thicknesses, and the approximation could be made arbitrarily accurate by decreasing the layer thicknesses.

In order to see why the homogeneous layered structure approximation is easy to implement let us first consider the case of a completely homogeneous structure. In this case  $[U]$  is independent of  $z$  and can be taken outside of the integrals in (2.4.9) which then gives

$$\begin{aligned} [A(z, z_0)] &= [I] + (z - z_0)[U] + \frac{1}{2} (z - z_0)^2 [U][U] + \dots \\ &= \exp\left((z - z_0)[U]\right). \end{aligned} \quad (2.2.18)$$

We can apply Sylvester's formula (Hildebrand (1952)) to compute any func-

tion of a matrix in terms of the eigenvalues of that matrix.

$$f([U]) = \sum_{k=1}^n f(\lambda_k) \frac{\prod_{m \neq k} ([U] - \lambda_m I)}{\prod_{m \neq k} (\lambda_k - \lambda_m)} \quad (2.4.19)$$

where  $[U]$  is a square  $n \times n$  matrix with distinct eigenvalues,  $\lambda_i$ ,  $i = 1, 2, \dots, n$ . We now have an explicit analytical solution for the propagator matrix in terms of the eigenvalues of  $(z - z_0)[U]$ . From equations (2.4.18) and (2.4.19) we can see right away that the solutions for the propagator matrix will be exponential functions in  $z$  which is what we might have expected for a homogeneous structure. It is the exact solution for the propagator matrix given by (2.4.19) along with the simple functional dependence with depth that makes the homogeneous layered approximation easy to implement, relatively efficient and arbitrarily accurate. As far as I can determine, there is no other structural approximation for which an exact analytical solution for the propagator matrix can be obtained.

The eigenvalues of  $(z - z_0)[U]$  for SH waves are easy to compute and from equation (2.4.7) are

$$\begin{aligned} \lambda_1 &= + (z - z_0) \left( \frac{\beta_H^2}{\beta_V^2} k^2 - \frac{\omega^2}{\beta_V^2} \right)^{1/2} \\ \lambda_2 &= - (z - z_0) \left( \frac{\beta_H^2}{\beta_V^2} k^2 - \frac{\omega^2}{\beta_V^2} \right)^{1/2} \end{aligned} \quad (2.4.20)$$

The Love wave propagator matrix can now be expressed as follows for a solid laterally isotropic homogeneous material

$$\begin{aligned} {}_L A(z, z_0) &= \exp \left[ (z - z_0) {}_L U \right] \\ &= \exp(\lambda_1) \frac{({}_L U - \lambda_2 I)}{(\lambda_1 - \lambda_2)} \end{aligned} \quad (2.4.21)$$

$$= \exp(\lambda_2) \frac{({}_1U - \lambda_1 I)}{(\lambda_1 - \lambda_2)},$$

$${}_1A(z, z_0) = {}_1U - \frac{1}{{}_1L^2} \sinh\left(i(z - z_0) {}_1L\right)$$

$$+ I \cosh\left(i(z - z_0) {}_1L\right),$$

$${}_1A(z) = {}_1U - \frac{1}{{}_1L^2} \cos\left((z - z_0) {}_1L\right)$$

$$+ I \cos\left((z - z_0) {}_1L\right), \quad (2.4.22)$$

where  ${}_1L$  is the Love wave vertical wavenumber and is given by,

$${}_1L = -i \left( \frac{\beta_H^2}{\beta_V^2} k^2 - \frac{\omega^2}{\beta_V^2} \right)^{1/2}. \quad (2.4.23)$$

I have chosen the vertical wavenumber by analogy with the horizontal wavenumber so that when  ${}_1L$  is real, propagating solutions occur in the  $z$ -direction and when  ${}_1L$  is imaginary, inhomogeneous or evanescent solutions exist. The propagator matrix, however, remains real for all real values of  $\omega$ ,  $k$ ,  $\beta_H$ ,  $\beta_V$  and  $\rho$ . Also, even though  ${}_1L$  is a dual valued function due to the square root, the propagator matrix itself is single valued. This is because both values of  ${}_1L$  are included in the propagator matrix which can be more easily seen in equation (2.4.21) where  $\lambda_1 = +i(z - z_0) {}_1L$  and  $\lambda_2 = -i(z - z_0) {}_1L$ .

Consider the transformation matrix,  $[B]$ , which diagonalizes  $[U]$

$$B^{-1} U B = \begin{bmatrix} \lambda_1 & 0 & 0 \\ 0 & \lambda_2 & 0 \\ 0 & 0 & \lambda_1 \end{bmatrix} = A \quad (2.4.24)$$

Obviously, the diagonalized version of  $[U]$  will consist of diagonal elements equal to the eigenvalues of  $[U]$  and the columns of  $[B]$  will be equal to the  $n$  eigenvectors of  $[U]$ . Let us use  $[B]$  to transform the stress-displacement vector,  $\{y\}$ , also.

$$\{v\} = [B]^{-1} \{y\},$$

or

$$\{y\} = [B] \{v\} \quad (2.4.25)$$

Substituting into equation (2.4.8) and assuming a completely homogeneous material,

$$[B] \frac{d}{dz} \{v\} = [U][B]\{v\},$$

$$\frac{d}{dz} \{v\} = [B]^{-1} [U][B]\{v\},$$

or

$$\frac{d}{dz} \{v\} = [A] \{v\}. \quad (2.4.26)$$

defining the propagator matrix for the transformed vector,  $\{v\}$ , as  $[V(z, z_0)]$  and applying Sylvester's formula we get,

$$\{v(z)\} = [V(z, z_0)] \{v(z_0)\}, \quad (2.4.27)$$

$$[V(z, z_0)] = \exp\left((z - z_0)[A]\right).$$

$$[V(z, z_0)] = \begin{bmatrix} \exp((z - z_0)\lambda_1) & & & \\ & \exp((z - z_0)\lambda_2) & 0 & \\ & & 0 & \\ & & & \exp((z - z_0)\lambda_n) \end{bmatrix} \quad (2.4.28)$$

This transformed version of the stress-displacement vector has been used extensively by Kennett, Kerry and Woodhouse (1978) and Kennett and Kerry (1979) who show how complete, numerically stable solutions to the elastic wave equation for plane homogeneous layered structures can be expressed in terms of a generalized ray expansion. They refer to the vector,  $\{v\}$ , as the wave or wavefield vector and its elements are decoupled from each other in a homogeneous material due to the diagonal form of the wavefield propagator matrix,  $[V]$ . The six elements of  $\{v\}$  are, in fact, the  $\omega$ ,  $k$  and  $z$  dependent factors in the P, SV and SH potential functions for upward and downward propagating waves. Thus the elements of the wavefield vector are the  $\omega$ ,  $k$  and  $z$  dependent complex amplitudes of P, SV and SH rays travelling either upward or downward through the homogeneous material. The matrix  $[B]$ , then, transforms the  $z$ -dependent solutions from a ray representation to a stress-displacement representation. Using  $[B]$  we can easily relate the stress-displacement propagator matrix directly to the wave field propagator matrix.

$$[A(z, z_0)] = [B] [V(z, z_0)] [B]^{-1} \quad (2.4.29)$$

The  $[B]$  matrix also proves useful in computing reflection and transmission coefficients across layer interfaces. Because of the usefulness of  $[B]$ , I will compute the P-SV propagator matrix using (2.4.29) instead of Sylvester's formula. The first step is to compute the eigenvalues of  $[{}_R U]$  given by equation (2.4.6). This reduces to solving for the roots of the following characteristic equation:

$${}_R \lambda^4 + {}_R \lambda^2 \left( {}_R V_{\beta\beta}^2 - {}_R V_{\beta\beta}^2 - \frac{k^2}{\beta^2} (\alpha^2(1 - \eta^2) + \xi) \right) + \left( {}_R V_{\beta\beta}^2 {}_R V_{\beta\beta}^2 + k^2 {}_R V_{\beta\beta}^2 (1 - \eta^2) \right) = 0 \quad (2.4.30)$$



where  ${}_R\lambda$  is an eigenvalue of  $[{}_RU]$ , and

$$\alpha = \alpha_V, \beta = \beta_V, \eta = \frac{\alpha_H}{\alpha_V}, \xi = \frac{F}{\rho} - \alpha_V^2 + 2\beta_V^2 \quad (2.4.31)$$

$$k_\alpha = \frac{\omega}{\alpha_V}, k_\beta = \frac{\omega}{\beta_V},$$

$${}_R\nu_\alpha^2 = k_\alpha^2 - k^2, {}_R\nu_\beta^2 = k_\beta^2 - k^2.$$

${}_R\nu_\alpha$  and  ${}_R\nu_\beta$  are P and S wave vertical wavenumbers and when they are real, the z-dependent solutions are propagating and when they are imaginary, the z-dependent solutions are evanescent as with  ${}_L\nu$ . For a completely isotropic material,

$$\eta = 1, \xi = 0,$$

and we can write equation (2.4.30) as follows:

$${}_R\lambda^4 + {}_R\lambda^2 ({}_R\nu_\alpha^2 + {}_R\nu_\beta^2) + {}_R\nu_\alpha^2 {}_R\nu_\beta^2 = 0, \quad (2.4.32)$$

which can be factored as,

$$\left( {}_R\lambda^2 + {}_R\nu_\alpha^2 \right) \left( {}_R\lambda^2 + {}_R\nu_\beta^2 \right) = 0,$$

so that

$${}_R\lambda^2 = -{}_R\nu_\alpha^2 \quad (2.4.33)$$

or

$${}_R\lambda^2 = -{}_R\nu_\beta^2.$$

This then gives the following four solutions for  ${}_R\lambda$  which corresponds to upward and downward travelling P and SV waves.

$${}_R\lambda_1 = +i\nu_\alpha = +i\sqrt{k_\alpha^2 - k^2} = +{}_R\lambda_\alpha \quad (2.4.34)$$

$${}_R\lambda_2 = -i\nu_\alpha = -i\sqrt{k_\alpha^2 - k^2} = -{}_R\lambda_\alpha$$

$${}_R\lambda_3 = +i\nu_\beta = +i\sqrt{k_\beta^2 - k^2} = +{}_R\lambda_\beta$$

$${}_R\lambda_4 = -i\nu_\beta = -i\sqrt{k_\beta^2 - k^2} = -{}_R\lambda_\beta$$

We can certainly obtain an explicit algebraic solution for  ${}_R\lambda^2$  even for the anisotropic case, however, the form of the solution will generally be complicated. For the isotropic case the roots  ${}_R\lambda^2$ , are always real and distinct for real  $\omega$ ,  $k$ ,  $\alpha$ ,  $\beta$  and  $\rho$  and as long as  $\alpha \neq \beta$ . For the anisotropic case the roots,  ${}_R\lambda^2$ , may be either real or complex depending on the sign of the discriminant of equation (2.4.30). As long as  $\eta$  is close to one and  $\xi$  is close to zero (weak anisotropy) we would expect the roots to remain real and distinct and the resulting wave motion would correspond approximately to P and SV type wave motion. There will be values of  $\eta$  and  $\xi$ , however, for which the roots,  ${}_R\lambda^2$ , will be complex, but since the coefficients in equation (2.4.30) are always real, complex values of  ${}_R\lambda^2$  will occur as complex conjugate pairs.

In order to compute  $[_RB]$  we need to compute the eigenvectors of  $[_RU]$ . We will compose  $[_RB]$  from the four eigenvectors of  $[_RU]$  as follows:

$$[_RB] = \left[ \{{}_Rb\}_1 \mid \{{}_Rb\}_2 \mid \{{}_Rb\}_3 \mid \{{}_Rb\}_4 \right], \quad (2.4.35)$$

where  $\{{}_Rb\}$  is a column vector with four components equal to the  $i^{\text{th}}$  eigenvector of  $[_RU]$ , and

$$\left[ [_RU] - {}_R\lambda_i I \right] \{{}_Rb\}_i = \{0\}, \quad i = 1, 2, 3, 4. \quad (2.4.36)$$

The normalization of the eigenvectors is arbitrary and so we will chose the first component in each eigenvector to be unity so that  ${}_RB_{11} = {}_RB_{12} = {}_RB_{13} = {}_RB_{14} = 1$ . Solving for the remaining components of the eigenvectors in (2.4.36) we get

$${}_RB_{1i} = 1 \quad (2.4.37)$$

$${}_R B_{2i} = \frac{1}{\delta_i} \left( \frac{\omega^2}{\alpha_V^2 \beta_V^2 \rho} - \frac{{}_R \lambda_i^2}{\beta_V^2 \rho} - \frac{k^2}{\alpha_V^2 \rho} \right)$$

$${}_R B_{3i} = \frac{1}{\delta_i} \left( - \frac{kF\omega^2}{\alpha_V^2 \beta_V^2 \rho} + {}_R \lambda_i^2 k + \frac{k^3 F}{\alpha_V^2 \rho} \right)$$

$${}_R B_{4i} = \frac{1}{\delta_i} \left( \frac{{}_R \lambda_i \omega^2}{\alpha_V^2} + {}_R \lambda_i^3 + \frac{{}_R \lambda_i k^2 F}{\alpha_V^2 \rho} \right)$$

where  $\delta_i = \frac{k {}_R \lambda_i}{\alpha_V^2} \left( \frac{F}{\beta_V^2 \rho} + 1 \right)$ , and  $i = 1, 2, 3, 4$ .

Since  ${}_R \lambda_2 = -{}_R \lambda_1$  and  ${}_R \lambda_4 = -{}_R \lambda_3$ , we can see that,

$${}_R B_{22} = -{}_R B_{21}, {}_R B_{24} = -{}_R B_{23}, \quad (2.4.38)$$

$${}_R B_{32} = -{}_R B_{31}, {}_R B_{34} = -{}_R B_{33},$$

$${}_R B_{42} = {}_R B_{41}, {}_R B_{44} = {}_R B_{43}.$$

We can obviously compute  $[{}_R B]^{-1}$  and from equation (2.4.29) obtain an explicit solution for the stress-displacement propagator matrix for the anisotropic case.

At this point I am going to assume a completely isotropic structure. This assumption is being made primarily to simplify the form of the solutions for  $[B]$  and  $[A]$  which will result in a computationally efficient algorithm, however, there is no fundamental reason why the anisotropic case cannot be handled in the same manner as the isotropic case. I am also going to redefine the stress-displacement vector,  $\{y\}$ , as,

$$\{ {}_R \bar{y} \}(z) = \begin{Bmatrix} y_1(z) \\ y_2(z) \\ y_3(z) \quad k \\ y_4(z) \quad k \end{Bmatrix}, \quad (2.4.39)$$

and

$$\{\bar{y}(z)\} = \begin{Bmatrix} y_5(z) \\ y_6(z)/k \end{Bmatrix}.$$

Similarly, I redefine the forcing function vector,  $\{w\}$ , as

$$\{\bar{w}(y)\} = \begin{Bmatrix} w_1(z) \\ w_2(z) \\ w_3(z)/k \\ w_4(z)/k \end{Bmatrix}, \{\bar{w}(z)\} = \begin{Bmatrix} w_5(z) \\ w_6(z)/k \end{Bmatrix}. \quad (2.4.46)$$

I will drop the overbar in the following development in order to simplify the notation. From the definition of the matrix,  $[{}_R B]$ , and assuming an isotropic homogeneous structure we arrive at

$$[{}_R B] = \begin{bmatrix} i\phi_0 & -i\phi_0 & 1 & 1 \\ 1 & 1 & i\phi_0 & -i\phi_0 \\ \rho c^2(\gamma-1) & \rho c^2(\gamma-1) & \rho c^2\gamma i\phi_0 & -\rho c^2\gamma i\phi_0 \\ \rho c^2\gamma i\phi_0 & -\rho c^2\gamma i\phi_0 & \rho c^2(\gamma-1) & \rho c^2(\gamma-1) \end{bmatrix},$$

where we have changed the normalization from that defined by (2.4.37) and,

$$c = \frac{\omega}{k} \text{ is the horizontal phase velocity,} \quad (2.4.42)$$

$\phi_0 = \sqrt{(c/\alpha)^2 - 1}$ ,  $\phi_0 = \sqrt{(c/\beta)^2 - 1}$  are the cotangents of the incidence angles for plane propagating P and S waves,

$$\text{and } \gamma = 2(\beta/c)^2.$$

Note that  $\nu_0 = k\phi_0$  and  $\nu_\beta = k\phi_\beta$  and that by redefining the stress-displacement vector with equation (2.4.39) we have eliminated  $\omega$  dependence from  $[{}_R B]$ . We can easily compute  $[{}_R B]^{-1}$  from (2.4.41)

$$[{}^R B]^{-1} = \frac{1}{2} \begin{bmatrix} \frac{-(\gamma-1)}{i\phi_a} & \gamma & -\frac{1}{\rho c^2} & \frac{1}{\rho c^2 i\phi_a} \\ \frac{(\gamma-1)}{i\phi_a} & \gamma & -\frac{1}{\rho c^2} & -\frac{1}{\rho c^2 i\phi_a} \\ \gamma & -\frac{(\gamma-1)}{i\phi_\beta} & \frac{1}{\rho c^2 i\phi_\beta} & -\frac{1}{\rho c^2} \\ \gamma & \frac{(\gamma-1)}{i\phi_\beta} & -\frac{1}{\rho c^2 i\phi_\beta} & -\frac{1}{\rho c^2} \end{bmatrix} \quad (2.4.43)$$

Using equations (2.4.28), (2.4.34), (2.4.41), (2.4.43), and (2.4.29) we can solve for the Rayleigh wave stress-displacement propagator matrix for a solid material.

$${}^R A_{11}(z, z_0) = -(\gamma-1) \cos(\theta_a) + \gamma \cos(\theta_\beta) \quad (2.4.44)$$

$${}^R A_{12}(z, z_0) = -\gamma \phi_a \sin(\theta_a) - \frac{(\gamma-1)}{\phi_\beta} \sin(\theta_\beta)$$

$${}^R A_{13}(z, z_0) = \frac{\phi_a}{\rho c^2} \sin(\theta_a) + \frac{1}{\rho^2 \phi_\beta} \sin(\theta_\beta)$$

$${}^R A_{14}(z, z_0) = \frac{1}{\rho c^2} \cos(\theta_a) - \frac{1}{\rho c^2} \cos(\theta_\beta)$$

$${}^R A_{21}(z, z_0) = -\frac{(\gamma-1)}{\phi_a} \sin(\theta_a) - \gamma \phi_\beta \sin(\theta_\beta)$$

$${}^R A_{22}(z, z_0) = \gamma \cos(\theta_a) - (\gamma-1) \cos(\theta_\beta)$$

$${}^R A_{23}(z, z_0) = -{}^R A_{14}(z, z_0)$$

$${}^R A_{24}(z, z_0) = \frac{1}{\rho c^2 \phi_a} \sin(\theta_a) - \frac{\phi_\beta}{\rho c^2} \sin(\theta_\beta)$$

$${}^R A_{31}(z, z_0) = -\frac{\rho c^2 (\gamma-1)^2}{\phi_a} \sin(\theta_a) - \rho c^2 \gamma^2 \phi_\beta \sin(\theta_\beta)$$

$${}_R A_{32}(z, z_0) = \rho c^2 \gamma (\gamma - 1) \cos(\theta_\alpha) - \rho c^2 \gamma (\gamma - 1) \cos(\theta_\beta)$$

$${}_R A_{33}(z, z_0) = {}_R A_{11}(z, z_0)$$

$${}_R A_{34}(z, z_0) = - {}_R A_{21}(z, z_0)$$

$${}_R A_{41}(z, z_0) = - {}_R A_{32}(z, z_0)$$

$${}_R A_{42}(z, z_0) = - \rho c^2 \gamma^2 \phi_\alpha \sin(\theta_\alpha) - \frac{\rho c^2 (\gamma - 1)^2}{\phi_\beta} \sin(\theta_\beta)$$

$${}_R A_{43}(z, z_0) = - {}_R A_{12}(z, z_0)$$

$${}_R A_{44}(z, z_0) = {}_R A_{22}(z, z_0) ,$$

where

$$\theta_\alpha = (z - z_0) \nu_\alpha = (z - z_0) k \phi_\alpha , \quad (2.4.45)$$

and

$$\theta_\beta = (z - z_0) \nu_\beta = (z - z_0) k \phi_\beta .$$

Once again, as with the SH case, we can see that although  $\phi_\alpha$ ,  $\nu_\alpha$ ,  $\phi_\beta$  and  $\nu_\beta$  are dual valued, the elements of the propagator matrix are all single valued.

In order to compute the propagator matrix for a liquid or acoustic layer let us renormalize the last two columns in  $[_R B]$  with  $1/(i\phi_\beta)$  and then let  $\beta \rightarrow 0$ . We can see from (2.4.41) that the last two columns and the last row of  $[_R B]$  will go to zero and the  $4 \times 4$   $[_R B]$  matrix will be singular and non-invertible. For an acoustic layer only the upward and downward P-wave solutions will exist and so we need to partition out a  $2 \times 2$  non-singular matrix from the  $4 \times 4$   $[_R B]$  matrix in order to determine a solution for the acoustic propagator matrix. We define the acoustic  $[B]$  matrix as follows.

$$\begin{Bmatrix} y_1(z) \\ y_3(z) \end{Bmatrix} = [{}_A B] \begin{Bmatrix} v_1(z) \\ v_2(z) \end{Bmatrix} \quad (2.4.46)$$

where

$$[{}_A B] = \begin{bmatrix} i\phi_a & -i\phi_a \\ -\rho c^2 & -\rho c^2 \end{bmatrix}. \quad (2.4.47)$$

We should note that the second and third rows of  $[{}_R B]$  are linearly dependent for  $\beta = 0$  and so for an acoustic layer,

$$y_3(z) = -\rho c^2 y_2(z). \quad (2.4.48)$$

We can invert  $[{}_A B]$  to get

$$[{}_A B]^{-1} = \frac{1}{2} \begin{bmatrix} \frac{1}{i\phi_a} & -1/\rho c^2 \\ -\frac{1}{i\phi_a} & -1/\rho c^2 \end{bmatrix}, \quad (2.4.49)$$

and obtain the  $2 \times 2$  acoustic propagator matrix.

$$\begin{Bmatrix} y_1(z) \\ y_3(z) \end{Bmatrix} = [{}_A A(z, z_0)] \begin{Bmatrix} y_1(z_0) \\ y_3(z_0) \end{Bmatrix} \quad (2.4.50)$$

$$[{}_A A(z, z_0)] = \begin{bmatrix} \cos(\theta_a) & -\phi_a \sin(\theta_a) \\ \frac{-\rho c^2 \sin(\theta_a)}{\phi_a} & -\rho c^2 \cos(\theta_a) \end{bmatrix}. \quad (2.4.51)$$

We can also rewrite (2.4.51) in terms of a  $4 \times 4$  matrix using equation (2.4.48).

$$[{}_A A(z, z_0)] = \begin{bmatrix} \cos(\theta_a) & -\phi_a \sin(\theta_a) & 0 & 0 \\ \frac{\sin(\theta_a)}{\phi_a} & \cos(\theta_a) & 0 & 0 \\ -\frac{\rho c^2}{\phi_a} \sin(\theta_a) & -\rho c^2 \cos(\theta_a) & 0 & 0 \\ 0 & 0 & 0 & 0 \end{bmatrix} \quad (2.4.52)$$

We have already dealt with the Love wave propagator matrix, but we will write down the solutions for  $[{}_L B]$ ,  $[{}_L B]^{-1}$ , and  $[{}_L A(z, z_0)]$  for the case of an isotropic homogeneous material.

$$[{}_L B] = \begin{bmatrix} 1 & 1 \\ \rho \beta^2 i \phi_\beta & -\rho \beta^2 i \phi_\beta \end{bmatrix}, \quad (2.4.53)$$

$$[{}_L B]^{-1} = \begin{bmatrix} 1 & \frac{1}{\rho \beta^2 i \phi_\beta} \\ 1 & -\frac{1}{\rho \beta^2 i \phi_\beta} \end{bmatrix}, \quad (2.4.54)$$

$$[{}_L A(z, z_0)] = \begin{bmatrix} \cos(\theta_\beta) & \frac{\sin(\theta_\beta)}{\rho \beta^2 \phi_\beta} \\ -\rho \beta^2 \phi_\beta \sin(\theta_\beta) & \cos(\theta_\beta) \end{bmatrix} \quad (2.4.55)$$

Equations (2.4.44), (2.4.55), and (2.4.52) give the stress-displacement propagator matrices for P-SV, SH, and acoustic materials which are completely homogeneous and isotropic. In order to compute propagator matrices for a homogeneous layered structure we need to apply the layer interface boundary conditions given by equations (2.2.16) and (2.2.17). First we start by defining the layer propagator matrix,  $[a^{(p)}]$ , which relates the stress-displacement vector at some point within the  $p^{\text{th}}$  homogeneous layer to the stress-displacement vector at the top of the layer.

$$\{y^{(p)}(\zeta^{(p)})\} = [a^{(p)}(\zeta^{(p)})] \{y^{(p)}(0)\}, \quad (2.4.56)$$

$$[a^{(p)}(\zeta^{(p)})] = [A(z, h^{(p-1)})], \quad (2.4.57)$$

where  $\zeta^{(p)} = z - h^{(p-1)}$ ,  $0 \leq \zeta^{(p)} < \xi^{(p)}$ ,

and  $\zeta^{(p)}$ ,  $\xi^{(p)}$  and  $h^{(p-1)}$  are shown in figure 1.

When  $\zeta^{(p)} = \xi^{(p)}$  then the layer propagator matrix will relate the stress-



displacement vector at the bottom of a layer to the vector at the top of the layer.

For a solid material we can now start at any layer interface,  $p$ , and propagate the stress-displacement vector to any other interface,  $q$ , (where  $p < q$ ) by applying the welded interface boundary conditions expressed by equations (2.2.16) and by repeating equation (2.4.56) and in doing so we define the interlayer propagator matrix,  $[A^{(q,p)}]$ ,

$$\{y(h^{(q)})\} = [A^{(q,p)}] \{y(h^{(p)})\}. \quad (2.4.58)$$

The interlayer propagator matrix is,

$$[A^{(q,p)}] = \prod_{l=p+1}^q \left[ a^{(q+p+1-l)}(\xi^{(q+p+1-l)}) \right] \quad (2.4.59)$$

For a solid-liquid, liquid-solid, or liquid-liquid interface, the situation is a little more complicated and I will cover these cases in the next section.

Equations (2.4.44), (2.4.52), (2.4.55), (2.4.57), and (2.4.59) give the *exact* solution for the stress-displacement propagator matrix in a vertically heterogeneous material made up of plane homogeneous layers. Thus the approximation made here is in the representation of the structural model and not in the solution itself. As I stated previously, candidate approximations for the propagator matrix in an arbitrarily heterogeneous material with depth must be compared on the basis of accuracy, efficiency and ease of implementation. The plane homogeneous layered approximation is exact for the structural model it represents and can be made arbitrarily accurate to represent any structural model in a straightforward and physically interpretable manner. Also this approximation is relatively efficient and easy to implement due to the simple algebraic-trigonometric form of the solution.

I was able to compare the homogeneous layered approximation directly with the full wave theory or Langer approximation which has been used extensively by Paul Richards and was modified by Vernon Cormier (1980) to compute the stress-displacement propagator matrix in a layered structure in which the layer elastic moduli vary linearly with depth. The Langer approximation ran about ten to twenty times slower than the homogeneous layered approximation on a per layer basis. Also the Langer approximation is an approximation of the solution and not in the representation of the structure and it breaks down when velocity gradients within a layer become large. When this happens the structure must be broken up into thin layers as with the homogeneous layered approximation.

## 2.5 Integral and Spectral Representations for the Solution of the Elastic Wave Equation

Equation (2.3.4) represents a solution of the elastic wave equation for all  $t$ ,  $r$ ,  $\theta$ , and  $z$  in terms of the constant parameters  $\omega$ ,  $k$  and  $m$ . The final solution will be some appropriate linear combination of solutions of form (2.3.4) spanning the range of the parameters  $\omega$ ,  $k$ , and  $m$ , and this appropriate combination will be determined by the source vector,  $\{w(\omega, k, m, z)\}$ , in equation (2.4.13). In order to determine the source vector we first define the following transforms:

$$F(f(t)) = \int_{-\infty}^{+\infty} f(t) e^{-i\omega t} dt, \quad -\infty \leq \omega \leq +\infty \quad (2.5.1)$$

$$F^{-1}(f(\omega)) = \frac{1}{2\pi} \int_{-\infty}^{+\infty} f(\omega) e^{+i\omega t} d\omega, \quad (2.5.2)$$

where  $F(\cdot)$  is the integral Fourier transform and  $F^{-1}(\cdot)$  is the inverse integral Fourier transform.

$$G(f(\theta)) = \int_0^{2\pi} f(\theta) e^{-im\theta} d\theta, \quad m = -\infty, \dots, -1, 0, 1, \dots, \infty \quad (2.5.4)$$

$$G^{-1}(f(m)) = \frac{1}{2\pi} \sum_{m=-\infty}^{+\infty} \left( f(m) e^{+im\theta} \right), \quad (2.5.5)$$

where  $G(\cdot)$  is the discrete Fourier transform  $G^{-1}(\cdot)$  is the inverse discrete Fourier transform,

$$H(f(r)) = \int_0^{\infty} f(r) J_m(kr) r dr, \quad (2.5.5)$$

$$0 \leq k \leq +\infty, \quad m = -\infty, \dots, -1, 0, 1, \dots, +\infty$$

$$H^{-1}(f(k, m)) = \int_0^{\infty} f(k, m) J_m(kr) k dk, \quad (2.5.6)$$

$H(\cdot)$  is the Hankel transform and  $H^{-1}(\cdot)$  is the inverse Hankel transform.

Note that these transforms are normalized so that,

$$F^{-1}\left(F(f(t))\right) = f(t),$$

$$G^{-1}\left(G(f(\theta))\right) = f(\theta),$$

$$H^{-1}\left(H(f(r))\right) = f(r), \text{ for all } m.$$

Ben-Menahem and Singh (1981) show how any vector,  $\chi(r, \theta)$ , can be expanded in terms of vector cylindrical harmonics

$$\chi(r, \theta) = \sum_{m=-\infty}^{+\infty} \frac{1}{2\pi} \int_0^{\infty} k dk \left[ \chi_P(k, m) P_k^m(r, \theta) + \chi_B(k, m) B_k^m(r, \theta) + \chi_C(k, m) C_k^m(r, \theta) \right], \quad (2.5.7)$$

where using the vector cylindrical harmonic orthogonality relations.

$$\chi_P(k,m) = \int_0^\infty r dr \int_0^{2\pi} d\theta \chi(r,\theta) \cdot \mathbf{P}_k^m(r,\theta), \quad (2.5.8)$$

$$\chi_B(k,m) = \int_0^\infty r dr \int_0^{2\pi} d\theta \chi(r,\theta) \cdot \mathbf{B}_k^m(r,\theta),$$

$$\chi_C(k,m) = \int_0^\infty r dr \int_0^{2\pi} d\theta \chi(r,\theta) \cdot \mathbf{C}_k^m(r,\theta),$$

and \* denotes complex conjugate. We can express the body force vector,  $\rho f(\omega, r, \theta, z)$ , as (2.5.7) and thus the displacement vector  $u(\omega, r, \theta, z)$ , as

$$u(\omega, r, \theta, z) = \frac{1}{2\pi} \sum_{m=-\infty}^{+\infty} \int_0^\infty k dk \left[ u_P(\omega, k, m, z) \mathbf{P}_k^m(r, \theta) + \right. \quad (2.5.9)$$

$$\left. + u_B(\omega, k, m, z) \mathbf{B}_k^m(r, \theta) + u_C(\omega, k, m, z) \mathbf{C}_k^m(r, \theta) \right].$$

In order to obtain the time domain solution, we apply the inverse integral Fourier transform to  $u(\omega)$ .

$$u(t, r, \theta, z) = \frac{1}{2\pi} \int_{-\infty}^{+\infty} d\omega e^{i\omega t} u(\omega, r, \theta, z) \quad (2.5.10)$$

The actual values of the stress-displacement vector,  $\{y\}$  and thus the values of  $u_P$ ,  $u_B$  and  $u_C$  will be functions of  $f_P$ ,  $f_B$  and  $f_C$  in equation (2.3.8) and using (2.5.8) these are,

$$f_P(\omega, k, m, z) = \int_0^\infty r dr \int_0^{2\pi} d\theta \rho f(\omega, r, \theta, z) \cdot \mathbf{P}_k^m(r, \theta), \quad (2.5.11)$$

$$f_B(\omega, k, m, z) = \int_0^\infty r dr \int_0^{2\pi} d\theta \rho f(\omega, r, \theta, z) \cdot \mathbf{B}_k^m(r, \theta),$$

$$f_C(\omega, k, m, z) = \int_0^\infty r dr \int_0^{2\pi} d\theta \rho f(\omega, r, \theta, z) \cdot \mathbf{C}_k^m(r, \theta),$$

where

$$\rho f(\omega, r, \theta, z) = \int_{-\infty}^{+\infty} d\omega e^{-i\omega t} \rho f(t, r, \theta, z) .$$

Equations (2.5.11) allow us to express any space and time distribution of body forces in terms of frequency and depth dependent vector cylindrical harmonics. Using equations (2.4.3) and (2.4.13) along with the expressions for the propagator matrix and the boundary conditions at the top and the bottom of the structure, we can compute the stress-displacement vector at any depth. Finally, with equations (2.4.2), (2.5.9) and (2.5.10) we can compute the displacement vector,  $u$ , for all space and time.

At this point I will make the following assumption regarding the source vector,  $\{w\}$ .

$$\{w(\omega, k, m, z)\} = \delta(z - z_s) \{\Sigma(\omega, k, m)\} \quad (2.5.12)$$

I am thus restricting the source to a horizontal plane at depth  $z_s$ . We can see from equation (2.4.13) that if  $z_s < z < z_0$ , or if  $z_s < z_0 < z$ , or if  $z_s > z > z_0$ , or if  $z_s > z_0 > z$  (i.e.  $z_s$  is not between  $z$  and  $z_0$ ), then the integral in (2.4.13) will be zero. On the other hand, if  $z < z_s < z_0$ , or  $z_0 < z_s < z$ , then

$$\{y(z)\} = [A(z, z_0)] \{y(z_0)\} - [A(z, z_s)] \{\Sigma\} , \quad (2.5.13)$$

$$z < z_s < z_0 \text{ or } z_0 < z_s < z .$$

The vector function  $\{\Sigma\}$  is called the source jump vector since it causes a discontinuous jump in the stress-displacement vector. Notice that this "jump" condition only exists when the source is restricted to a horizontal plane (or a point) and that for a spatially distributed source in depth, the

stress-displacement vector will remain continuous everywhere.

The problem of computing the stress-displacement vector for a given source at depth  $z_s$  has now been reduced to a linear algebra problem. For a completely solid material we can relate the stress-displacement vector at the top interface to the stress-displacement vector at the bottom interface as follows:

$$\{y(0)\} = [A(0, z_s)] \{y(z_s^-)\}, \quad (2.5.14)$$

$$\{y(H)\} = [A(H, z_s)] \{y(z_s^+)\},$$

$$\{y(z_s^-)\} = \{y(z_s^+)\} - \{\Sigma\},$$

where  $z_s^-$  is immediately above the source,

and  $z_s^+$  is immediately below the source,

and  $0 = z_T$  is the depth of the top boundary,

and  $H = z_B$  is the depth of the bottom boundary.

We now need to apply boundary conditions at the top and bottom of the structure. These boundary conditions can be expressed in terms of zeroing out some linear combinations of the stress-displacement vector and so we define the  $[E]$  matrices as,

$$[{}^T E] \{y(0)\} = \{0\}, \quad (2.5.15)$$

$$[{}^B E] \{y(H)\} = \{0\},$$

where the superscript T denotes the top interface and B denotes the bottom interface.

The two  $[E]$  matrices will, in general, not be square and may have different dimensions. For a solid structure both  $[^TE]$  and  $[^BE]$  will have six columns and the sum of the number of rows for both matrices will be six. The number of rows for each matrix will be equal to the number of boundary conditions at that interface and in practice there will be three boundary conditions at each of the top and bottom interfaces. The  $[E]$  matrices are given below for the various boundary conditions expressed by equations (2.2.11) through (2.2.15).

1. A traction free surface,

$$[E] = \begin{bmatrix} 0 & 0 & 1 & 0 & 0 & 0 \\ 0 & 0 & 0 & 1 & 0 & 0 \\ 0 & 0 & 0 & 0 & 0 & 1 \end{bmatrix} \quad (2.5.16)$$

2. A rigid surface.

$$[E] = \begin{bmatrix} 1 & 0 & 0 & 0 & 0 & 0 \\ 0 & 1 & 0 & 0 & 0 & 0 \\ 0 & 0 & 0 & 0 & 1 & 0 \end{bmatrix} \quad (2.5.17)$$

3. Zero shear tractions and zero vertical displacement.

$$[E] = \begin{bmatrix} 1 & 0 & 0 & 0 & 0 & 0 \\ 0 & 0 & 0 & 1 & 0 & 0 \\ 0 & 0 & 0 & 0 & 0 & 1 \end{bmatrix} \quad (2.5.18)$$

4. No upward propagating P or S wave radiation (Sommerfield radiation condition for a bottom half space). In order to do this we must first transform the stress-displacement vector to the wavefield vector using the transformation matrix,  $[B]^{-1}$ . We then pick out the first, third and fifth rows of  $[B]^{-1}$  to give for a solid half space.

$$[E] = \frac{1}{2} \begin{bmatrix} -\frac{(\gamma-1)}{i\phi_\alpha} & \gamma & -\frac{1}{\rho c^2} & \frac{1}{\rho c^2 i\phi_\alpha} & 0 & 0 \\ \gamma & -\frac{(\gamma-1)}{i\phi_\beta} & \frac{1}{\rho c^2 i\phi_\beta} & -\frac{1}{\rho c^2} & 0 & 0 \\ 0 & 0 & 0 & 0 & 1 & \frac{1}{\rho \beta^2 i\phi_\beta} \end{bmatrix}, \quad (2.5.19)$$

where the elastic moduli are those of the half space,

5. No downward propagating P or S wave radiation (Sommerfeld radiation condition for a top half space). In this case we pick out the second, fourth, and sixth rows of  $[B]^{-1}$ .

$$[E] = \frac{1}{2} \begin{bmatrix} \frac{(\gamma-1)}{i\phi_\alpha} & \gamma & -\frac{1}{\rho c^2} & -\frac{1}{\rho c^2 i\phi_\alpha} & 0 & 0 \\ \gamma & \frac{(\gamma-1)}{i\phi_\beta} & \frac{-1}{\rho c^2 i\phi_\beta} & -\frac{1}{\rho c^2} & 0 & 0 \\ 0 & 0 & 0 & 0 & 1 & -\frac{1}{\rho \beta^2 i\phi_\beta} \end{bmatrix}. \quad (2.5.20)$$

As with the propagator matrix, it is obvious that we can partition the  $[E]$  matrix into a  $2 \times 4$   $[{}_R E]$  matrix and a  $1 \times 2$   $[{}_L E]$  matrix.

From equations (2.5.14) and (2.5.15) we arrive at,

$$[{}^T E] [A(0, z_s)] \{y(z_s^-)\} = \{0\} \quad (2.5.21)$$

$$[{}^B E] [A(H, z_s)] \{y(z_s^+)\} = \{0\}.$$

$$[{}^B E] [A(H, z_s)] \{y(z_s^-)\} = [{}^B E] [A(H, z_s)] \{\Sigma\}. \quad (2.5.22)$$

we now define the  $[D]$  matrices as follows.

$$[{}^T D(z)] = [{}^T E] [A(0, z)], \quad (2.5.23)$$

$$[{}^B D(z)] = [{}^B E] [A(H, z)], \quad (2.5.24)$$



so that

$$[{}^TD(z)] \{y(z)\} = \{0\}, z < z_s, \quad (2.5.25)$$

and

$$[{}^BD(z)] \{y(z)\} = \{0\}, z > z_s, \quad (2.5.26)$$

Equations (2.5.25) and (2.5.26) are important relations and will constitute the basis for numerically stable computations of the stress-displacement vector. We can now specify the stress-displacement vector immediately above the source as,

$$[{}^TD(z_s)] \{y(z_s^-)\} = \{0\}. \quad (2.5.27)$$

$$[{}^BD(z_s)] \{y(z_s^-)\} = [{}^BD(z_s)] \{\Sigma\}.$$

This gives us six equations in the six unknowns,  $\{y(z_s^-)\}$ , so we can solve for  $\{y(z_s^-)\}$ . We can then compute the stress-displacement vector at any other depth by using the propagator matrix

$$[D(z_s)] \{y(z_s^-)\} = \begin{Bmatrix} \{0\} \\ [{}^BD(z_s)] \{\Sigma\} \end{Bmatrix}, \quad (2.5.28)$$

$$\{y(z)\} = [A(z, z_s)] \{y(z_s^-)\}, z < z_s, \quad (2.5.29)$$

$$\{y(z)\} = [A(z, z_s)] \left( \{y(z_s^-)\} - \{\Sigma\} \right), z > z_s, \quad (2.5.30)$$

where  $[D(z_s)]$  is a six by six matrix composed of  $[{}^TD(z_s)]$  and  $[{}^BD(z_s)]$  as,

$$[D(z_s)] = \begin{Bmatrix} [{}^TD(z_s)] \\ [{}^BD(z_s)] \end{Bmatrix}. \quad (2.5.31)$$

Once again  $[D(z_0)]$  can be partitioned into a four by four Rayleigh matrix and a two by two Love matrix.

So far, in order to compute the various  $[D]$  matrices, we have assumed solid-solid welded interfaces and this approach must be modified somewhat to handle acoustic layers. Of course, Love waves will be completely blocked at a solid-liquid interface and so we will only need to address the P-SV problem. Let us first consider the case of the P-SV stress-displacement vector being propagated upward through a solid to liquid interface. In this case we will denote the stress-displacement vector in the solid material immediately below the interface as  $\{Ry\}$  and the stress-displacement vector in the liquid material immediately above the interface as  $\{Ay\}$ . From equations (2.2.17), the boundary conditions at the interface require the following:

$$R^y_1 = A^y_1 \quad (2.5.32)$$

$$R^y_3 = A^y_3$$

$$R^y_4 = 0$$

$$A^y_4 = 0$$

In this case the shear displacement will generally be discontinuous. Within the solid layer there are generally four linearly independent components of the stress-displacement vector with a four column (and usually two rows)  ${}^B_R D$  matrix. Within the liquid layer there are two linearly independent components of the stress-displacement vector with a two column (and usually one row)  ${}^B_A D$  matrix. The problem then is to apply the boundary conditions given by equations (2.5.32) to determine the elements of  ${}^B_A D$  from

the elements of  ${}^B_RD$  at the interface. This is a straightforward problem and the results are as follows:

$${}^B_A D_1 = {}^B_R D_{11} {}^B_R D_{22} - {}^B_R D_{12} {}^B_R D_{21}, \quad (2.5.33)$$

$${}^B_A D_2 = {}^B_R D_{13} {}^B_R D_{22} - {}^B_R D_{12} {}^B_R D_{23},$$

where

$$0 = {}^B_A D \{ {}^B_A y \} = \begin{bmatrix} {}^B_A D_1 & {}^B_A D_2 \end{bmatrix} \begin{Bmatrix} y_1 \\ y_3 \end{Bmatrix} \quad (2.5.34)$$

For the case of the stress-displacement vector being propagated upward through a liquid to solid interface, the same boundary conditions apply and the resulting  ${}^B_RD$  matrix is as follows:

$${}^B_R D_{11} = {}^B_A D_1, \quad (2.5.35)$$

$${}^B_R D_{13} = {}^B_A D_2,$$

$${}^B_R D_{24} = 1$$

$${}^B_R D_{12} = {}^B_R D_{14} = {}^B_R D_{21} = {}^B_R D_{22} = {}^B_R D_{23} = 0.$$

The results for downward propagating  ${}^T_D$  matrices are identical.

Given the stress-displacement vector, we can write the integral equations for the displacement vector given by (2.5.9) as Rayleigh and Love wave components.

(2.5.36)

$$R^u_r(\omega, r, \theta, z) = \frac{1}{2\pi} \sum_{m=-\infty}^{+\infty} \int_0^\infty y_2(\omega, k, m, z; z_s) \left( \frac{z}{k_1} I_m(kr) - J_{m+1}(kr) \right) e^{im\theta} k dk$$

$$R^{u_\theta}(\omega, r, \theta, z) = \frac{1}{2\pi} \sum_{m=-\infty}^{+\infty} \int_0^\infty y_2(\omega, k, m, z, z_s) J_m(kr) \left( \frac{im}{kr} \right) e^{im\theta} k dk$$

$$R^{u_z}(\omega, r, \theta, z) = \frac{1}{2\pi} \sum_{m=-\infty}^{+\infty} \int_0^\infty y_1(\omega, k, m, z, z_s) J_m(kr) e^{im\theta} k dk$$

and

(2.5.37)

$$L^{u_r}(\omega, r, \theta, z) = \frac{1}{2\pi} \sum_{m=-\infty}^{+\infty} \int_0^\infty y_5(\omega, k, m, z, z_s) J_m(kr) \left( \frac{im}{kr} \right) e^{im\theta} k dk$$

$$L^{u_\theta}(\omega, r, \theta, z) = \frac{1}{2\pi} \sum_{m=-\infty}^{+\infty} \int_0^\infty y_5(\omega, k, m, z, z_s) \left( -\frac{m}{kr} J_m(kr) + J_{m-1}(kr) \right) e^{im\theta} k dk$$

$$L^{u_z}(\omega, r, \theta, z) = 0,$$

where  $y_1$ ,  $y_2$  and  $y_5$  come from equations (2.5.28), (2.5.29) and (2.5.30).

Equations (2.5.36) and (2.5.37) are the basis for the various numerical integration approaches which I refer to collectively as the reflectivity method. First popularized by Fuchs and Muller (1971) this direct integration method has been modified and expanded by Kind (1978), Kennett and Kerry (1979), who eliminated certain numerical instabilities, Cormier (1980), who applied the Langer approximation to model inhomogeneous layers and deformed the contour of integration to avoid singularities in the integrand function and Bonchou (1981), who established a spatial sampling theorem with respect to the Hankel transforms and applied this theorem in a discrete wavenumber method for evaluating the wavenumber integrals. All of the reflectivity methods have in common the direct numerical integration of the wavenumber or slowness integrals in equations (2.5.36) and (2.5.37).

Another approach for evaluating the wavenumber integrals is to deform the contour of integration in the complex wavenumber plane so as to encircle the singularities of the integrand function and then apply the residue theorem. The integrals given by equations (2.5.36) and (2.5.37) are not amenable to this since the Bessel functions blow up as  $|k| \rightarrow \infty$ , however, Lapwood (1949) and more recently Hudson (1969) have shown how the Bessel functions can be changed to Hankel functions of the second kind by extending the contour of integration to  $-\infty$ .

$$\int_0^{\infty} f(k,m) J_m(kr) k dk = \frac{1}{2} \int_{-\infty}^{+\infty} f(k,m) H_m^{(2)}(kr) k dk, \quad (2.5.38)$$

where  $f(k,n) = (-1)^{n+1} f(-k,n)$ ,

and  $H_m^{(2)}$  is the integer order Hankel function of the second kind.

The Hankel functions go to zero as  $|k| \rightarrow \infty$  and  $\text{Im}(k) < 0$ , so the contour of integration can be closed by including a semicircular arc at infinity in the lower half of the complex wavenumber plane. We now need to consider the locations and characteristics of the singularities of the integrand functions.

The singularities of the Hankel functions are well known and so we turn our attention to the singularities of the stress-displacement vector,  $\{y\}$ , as a function of complex wavenumber. First of all we will address the question of when  $\{y\}$  is a multivalued function of wavenumber with attendant branch points and branch cuts. The only multivalued functions to appear in the propagator matrices or boundary condition ( $[E]$ ) matrices are the dual valued vertical wavenumber functions,  $\nu_\alpha$  and  $\nu_\beta$  (as  $\phi_\alpha$  and  $\phi_\beta$ ). In the case of the propagator matrices, these functions always appear either as arguments of even functions (e.g.  $\cos((z - z_0)\nu_\alpha)$ ) or in products or quo-

tients (e.g.  $\nu_\alpha \sin((z - z_0) \nu_\alpha)$ ,  $\sin((z - z_0) \nu_\alpha)/\nu_\alpha$ ) such that the result is single valued, and thus the propagator matrices are single valued. The boundary condition matrices,  $[{}^T E]$  and  $[{}^B E]$ , however, may be either single valued or multivalued depending on the type of boundary condition.

For conditions where all incident seismic energy is reflected for all wavenumbers (equations (2.5.16), (2.5.17), and (2.5.18)), the  $[E]$  matrix is single valued and if both  $[{}^T E]$  and  $[{}^B E]$  are determined by one of these conditions then we will refer to this as the plate problem. For the plate problem the various  $[D]$  matrices will also be single valued, as can be seen from equations (2.5.23), (2.5.24) and (2.5.31) and since the source jump vector,  $\{\Sigma\}$ , is always single valued, the stress-displacement vector will also be single valued as can be seen from equations (2.5.28) to (2.5.30). Thus the contour of integration can encircle the lower half of the complex wavenumber plane without being required to detour around any branch cuts or branch points.

The case of most interest in seismology is what we will refer to as the half space problem, that is, a reflectivity boundary condition at the top and a radiation boundary condition at the bottom of the structure. The free surface boundary condition will be applied at the top of the structure and thus  $[{}^T E]$  will be single valued and given by equation (2.5.16). The radiation condition given by equation (2.5.19) will specify the boundary condition matrix at the bottom  $[{}^B E]$ , but in this case the matrix will be four valued for P-SV waves due to the  $\nu_\alpha$  and  $\nu_\beta$  functions (in the form of  $\phi_\alpha$  and  $\phi_\beta$ ), and two valued for SH waves due to  $\nu_\alpha$  ( $\phi_\beta$ ). We can see then that the P-SV stress-displacement vector will be four valued with two branch points at  $\nu_\alpha = 0$  and  $\nu_\beta = 0$  and two branch cuts emanating from

these branch points and the SH stress-displacement vector will be two valued with one branch point at  $\nu_\beta = 0$  and one associated branch cut. The contour of integration must be deformed around these branch cuts and branch points in order to stay on an analytic path and the resulting branch cut integral contributions are well known and physically attributable to the energy which "leaks" away into the bottom half space (Gilbert (1964)). We have been somewhat remiss in this analysis since  $\nu_\alpha$  and  $\nu_\beta$  are functions of  $k^2$  and so for every branch point at  $+k$  there is another at  $-k$ . Consequently, there are actually four branch points and branch cuts for the P-SV case and two branch points and branch cuts for the SH case, however since the integration contour circles only half of the complex wavenumber plane, only two branch cut integrals will occur for the P-SV case and one for the SH case. As we will see this symmetry will also be characteristic of the poles of  $\{y\}$  as well as the branch points and branch cuts.

The remaining singularities of the stress-displacement vector are the Rayleigh and Love poles which occur at values of  $\omega$  and  $k$  for which the  $[D]$  matrix in equation (2.5.28) is singular. For a fixed frequency these poles will occur at discrete wavenumbers, however in the  $(\omega, k)$  space these poles form continuous functions of  $\omega$  and  $k$  which are commonly called dispersion curves. Thus, in order to locate the poles, we can either fix frequency and look for discrete poles as a function of wavenumber (or phase velocity, slowness, etc.), or fix wavenumber and look for discrete poles as a function of frequency. Whenever the  $[D]$  matrix is singular, we can write equation (2.5.28) as follows:

$$[D(K(n, \omega), z_s)] \{E(n, \omega, z_s)\} = \{0\}, \quad (2.5.39)$$

where  $K(n, \omega)$  is the  $n^{\text{th}}$  value of wavenumber which at frequency  $\omega$  for

(2.5.39) is true given  $\{E(z_s)\} \neq \{0\}$ . Note that equations (2.5.39) and (2.5.28) are identical if  $\{y\} = \{E\}$  and if  $\{\Sigma\} = \{0\}$ . Thus the  $\{E\}$  vector is the stress-displacement vector for the unforced vibration problem, or in other words,  $\{E(n, \omega, z)\}$  is the depth dependence of the  $n^{\text{th}}$  flat earth normal mode at frequency  $\omega$ .

Kazi (1976) shows how (2.5.39) can be written as an eigenvalue problem for SH waves and defines a Love wave operator whose eigenvalues are  ${}_L K^2(n, \omega)$  and eigenfunctions are  $\{{}_L E(n, \omega, z)\}$ . The definition of a Rayleigh wave operator is not so straightforward because of the P-SV coupling, however, we can still compute Rayleigh wave eigenvalues and eigenfunctions by searching out the singular values of  $[_R D(\omega, k)]$ . In order to do this we will first propagate the eigenfunctions from the source depth to the surface so that,

$$[_D(K(n, \omega), 0)] \{E(n, \omega, 0)\} = \{0\}, \quad (2.5.40)$$

where

$$[_D(K(n, \omega), 0)] = \begin{bmatrix} [_T E(K(n, \omega))] \\ \hline [_B D(K(n, \omega), 0)] \end{bmatrix}. \quad (2.5.41)$$

Note that since the  $\{E\}$  vector is a particular type of stress-displacement vector, it has most of the properties of the stress-displacement vector and, in particular, it can be computed at different depths by applying the correct propagator matrix. One property of  $\{E\}$  which is not true of  $\{y\}$ , however, is that  $\{E\}$  is continuous everywhere with depth and does not suffer a discontinuity at the source depth. In fact, from equation (2.5.39) we can see that the eigenvalues and eigenfunctions are completely independent of any source characteristics since  $z_s$  in that equation can be replaced by any



other depth we chose (as in equation (2.5.40)) which of course is what we would expect for normal mode solutions. It is this decoupling of structural wave propagation characteristics, as manifested by its spectra or normal modes, from the source and receiver characteristics that makes the normal mode method an efficient solution of the elastic wave equation.

Returning to (2.5.40) we now need to compute the determinant of  $[D]$  which we will refer to as the characteristic function

$${}_R\Delta(\omega, k) = \det({}_R D(\omega, k, 0)) , \quad (2.5.42)$$

$${}_L\Delta(\omega, k) = \det({}_L D(\omega, k, 0)) .$$

Assuming a free surface boundary condition we can write the  $[D]$  matrices as follows:

$$[{}_R D(\omega, k, 0)] = \begin{bmatrix} 0 & 0 & 1 & 0 \\ 0 & 0 & 0 & 1 \\ {}_R D_{11}^{(0)} & {}_R D_{12}^{(0)} & {}_R D_{13}^{(0)} & {}_R D_{14}^{(0)} \\ {}_R D_{21}^{(0)} & {}_R D_{22}^{(0)} & {}_R D_{23}^{(0)} & {}_R D_{24}^{(0)} \end{bmatrix} , \quad (2.5.43)$$

and

$$[{}_L D(\omega, k, 0)] = \begin{bmatrix} 0 & 1 \\ {}_L B_{D_1}^{(0)} & {}_L B_{D_2}^{(0)} \end{bmatrix} \quad (2.5.44)$$

We can easily solve for the characteristic functions which are as follows:

$${}_R\Delta(\omega, k) = {}_R D_{11}(\omega, k, 0) {}_R D_{22}(\omega, k, 0) \quad (2.5.45)$$

$$- {}_R D_{12}(\omega, k, 0) {}_R D_{21}(\omega, k, 0) ,$$

$${}_L\Delta(\omega, k) = {}_L B_{D_1}(\omega, k, 0) \quad (2.5.46)$$

The characteristic functions are scalar functions of  $\omega$  and  $k$  and

define the eigenvalues by,

$${}_R\Delta(\omega, {}_RK(n, \omega)) = 0, \quad (2.5.47)$$

and

$${}_L\Delta(\omega, {}_LK(n, \omega)) = 0.$$

The normalization of the eigenfunctions is arbitrary and so we will assume a vertical displacement and SH shear displacement of unity at the free surface. We can solve for the remaining non-zero eigenfunction, the P-SV radial shear displacement in terms of the  $[D]$  matrix elements so that

$${}_RE_1(n, \omega, 0) = 1 \quad (2.5.48)$$

$$\begin{aligned} {}_RE_2(n, \omega, 0) = & - \left( {}_RD_{11}(\omega, {}_RK(n, \omega), 0) {}_RD_{24}(\omega, {}_RK(n, \omega), 0) \right. \\ & \left. - {}_RD_{14}(\omega, {}_RK(n, \omega), 0) {}_RD_{21}(\omega, {}_RK(n, \omega), 0) \right) \\ & / \left( {}_RD_{12}(\omega, {}_RK(n, \omega), 0) {}_RD_{24}(\omega, {}_RK(n, \omega), 0) \right. \\ & \left. - {}_RD_{14}(\omega, {}_RK(n, \omega), 0) {}_RD_{22}(\omega, {}_RK(n, \omega), 0) \right) \end{aligned}$$

$${}_RE_3(n, \omega, 0) = 0$$

$${}_RE_4(n, \omega, 0) = 0$$

$${}_LE_1(n, \omega, 0) = 1 \quad (2.5.49)$$

$${}_LE_2(n, \omega, 0) = 0$$

With the surface values of the eigenfunctions defined, we can compute the eigenfunctions at any other depth simply by using the appropriate propagator matrices

In order to use the normal modes we must say something about where the modes will be located. As with the branch points, for every eigenvalue at  $+k$  there will be one at  $-k$  due to the fact that the  $[D]$  matrix elements are functions of  $k^2$  (or equivalently  $c^2$ ). In general, for all of the Riemann sheets there will be both pure real and complex eigenwavenumbers (the exception to this are SH and acoustic plate problems for which the eigenwavenumbers are always either purely real or purely imaginary). The complex poles will be easy to deal with since we will include the residues of those complex poles which are within the contour of integration, however the poles on the real wavenumber axis cause a problem since the integration contour goes directly through those poles, and we cannot know off hand whether or not to include their residue contributions.

We could compute the principle values for these poles, but there is a simpler way to deal with this problem. Basically, we will apply a perturbation to the frequency,  $\omega$ , such that the poles move off of the real wavenumber axis and can be easily identified as being within or outside of the contour of integration. We can allow the frequency to have a small, constant imaginary component as long as  $\text{Im}(\omega) < 0$  in order to insure that the Fourier transform remains analytic. For each pole on the real wavenumber axis for real frequency, we can compute the group velocity,  $U$ , as the slope of the dispersion curve in the  $\omega, k$  space, or,

$$U(n, \omega) = \left. d\omega/dk \right|_{\omega, R} K(n, \omega) \quad (2.5.50)$$

A small change in  $\omega$ ,  $\delta\omega$ , will thus cause a small change in  ${}_R K(n, \omega)$ ,  $\delta K$ , such that,

$$\delta K = \delta\omega U \quad (2.5.51)$$

So for poles on the positive real wavenumber axis, if the group velocity is positive then a small negative imaginary perturbation of frequency will move the poles into the fourth quadrant where they would be within the integration contour, and if the group velocity is negative then the frequency perturbation will move the poles into the first quadrant where they will be outside of the integration contour. However, for every pole at  $+k$  there will be one at  $-k$  and it is easy to show that a pole at  $+k$  with group velocity  $U$  will have a companion pole at  $-k$  with group velocity  $-U$ . So the companion poles to those on the positive real wavenumber axis with positive group velocities will have negative group velocities and will move into the second quadrant where they will be outside of the contour of integration. The companion poles to those on the positive real wavenumber axis with negative group velocities will have positive group velocities and will move into the third quadrant where they will be within the contour of integration. The net result is that all poles with positive real wavenumbers and positive group velocity will contribute their residues to the wavenumber integral and those poles with positive real wavenumbers and negative group velocity will contribute with their companion poles at  $-k$ . The wavenumber integration contour in the complex wavenumber plane along with the branch points, branch cuts and poles are shown in figure 2-2 for the general P-SV half space problem. We can see from figure 2-2 that

$$\int_{-\infty}^{\infty} R_{\alpha}^I + R_{\beta}^I = -2\pi i \sum_D \text{residues}, \quad (2.5.52)$$

where the arcs at infinity do not contribute and the sum of residues are those within the integration contour,  $\Gamma$ .

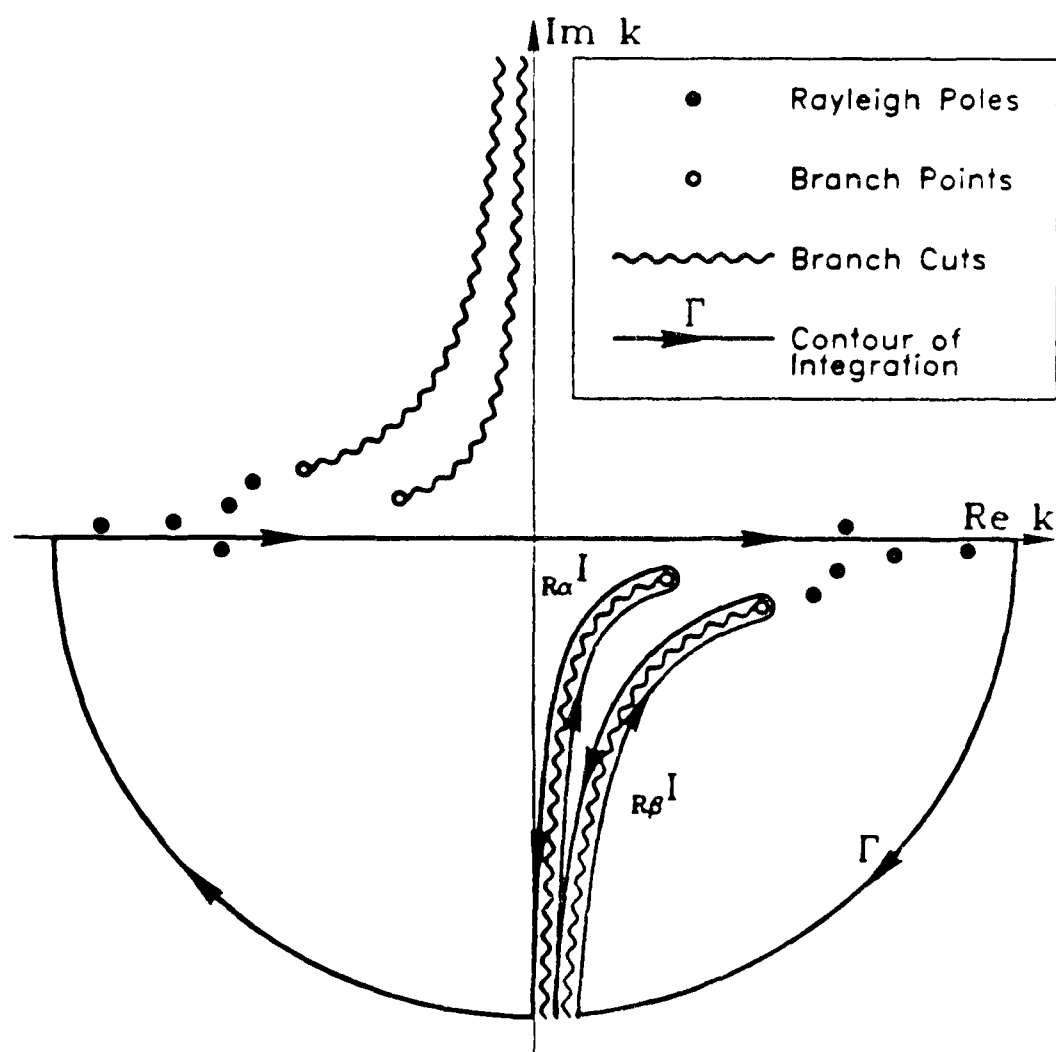


Figure 2-2. Wavenumber integration contour for a complex frequency with a small, negative imaginary component.

We now turn our attention to the evaluation of the residues. Returning to equation (2.5.28), we can write the solution for the stress-displacement vector at the top of the structure as we did with the eigenfunctions

$$[D(0)] \{y(0)\} = \left\{ \begin{array}{c} \{0\} \\ \hline [{}^B D(0)] [A(0, z_s)] \{\Sigma\} \end{array} \right\} \quad (2.5.53)$$

Once again we assume a free surface so that  $[D(0)]$  is given by equations (2.5.43) and (2.5.44). Substituting these relations in (2.5.53) it follows that

$$\left\{ \begin{array}{c} {}_R y_1(0) \\ {}_R y_2(0) \end{array} \right\} = \frac{1}{{}_R \Delta} \left[ \begin{array}{cc} {}_R D_{11}(0) & -{}_R D_{12}(0) \\ -{}_R D_{21}(0) & {}_R D_{11}(0) \end{array} \right] [{}^B D(0)] [{}_R A(0, z_s)] \{{}_R \Sigma\} \quad (2.5.54)$$

$${}_R y_3(0) = {}_R y_4(0) = 0,$$

and

$${}_L y_1(0) = -\frac{1}{{}_L \Delta} [{}_L D(0)] [{}_L A(0, z_s)] \{{}_L \Sigma\}, \quad (2.5.55)$$

$${}_L y_2(0) = 0.$$

We can see that the two by two minors of the two by four P-SV  $[{}_R {}^B D]$  matrix appear repeatedly throughout the analytical development of the eigenvalues, eigenfunctions and the stress-displacement vector. In order to save writing we will define the four by four anti-symmetric minor matrix  $[M]$ , as

$$\begin{aligned} M_{ij}(\omega, k, z) &= {}_R D_{1i}(\omega, k, z) {}_R D_{2j}(\omega, k, z) \\ &\quad - {}_R D_{1j}(\omega, k, z) {}_R D_{2i}(\omega, k, z). \end{aligned} \quad (2.5.56)$$

Obviously,

$$M_{ij}(\omega, k, z) = -M_{ji}(\omega, k, z),$$

$$M_{11} = M_{22} = M_{33} = M_{44} = 0.$$

We will also have two versions of the minor matrix,  $[^B M]$  and  $[^T M]$  corresponding to  $[^B D]$  and  $[^T D]$ . The minor matrix can now be used to simplify the solution to equation (2.5.54) as follows,

$$\begin{Bmatrix} R^y_1(0) \\ R^y_2(0) \end{Bmatrix} = \frac{1}{R\Delta} \begin{bmatrix} B_{M_{12}}(0) & 0 & -B_{M_{23}}(0) & -B_{M_{24}}(0) \\ 0 & B_{M_{12}}(0) & B_{M_{13}}(0) & B_{M_{14}}(0) \end{bmatrix} [^R A(0, z_s)] [^R \Sigma]. \quad (2.5.57)$$

We can also see from equation (2.5.45) that,

$$R\Delta = B_{M_{12}}(0). \quad (2.5.58)$$

The P-SV radial displacement eigenfunction at the surface, given by equation (2.5.48), can be written as follows

$$R^e(n, \omega) = \frac{{}_R E_2(n, \omega, 0)}{{}_R E_1(n, \omega, 0)} = {}_R E_2(n, \omega, 0) = \quad (2.5.59)$$

$$= - \frac{B_{M_{14}}(\omega, {}_R K(n, \omega), 0)}{B_{M_{24}}(\omega, {}_R K(n, \omega), 0)}$$

$$= - \frac{B_{M_{13}}(\omega, {}_R K(n, \omega), 0)}{B_{M_{23}}(\omega, {}_R K(n, \omega), 0)}.$$

where  $R^e(n, \omega)$  is the Rayleigh wave surface ellipticity for the  $n^{\text{th}}$  mode at frequency  $\omega$ .

Poles of equation (2.5.52) will occur whenever  $R\Delta = 0$  which implicitly defines the eigenwavenumbers. We can simplify equation (2.5.57) further when  $k$  is an eigenwavenumber and express it in terms of the

eigenfunctions, but first we must state two general properties.

$$M_{13}(\omega, k, z) = -M_{24}(\omega, k, z) \quad (2.5.60)$$

This is true for all  $\omega$ ,  $k$  and  $z$ . It is obviously true for the boundary conditions given by equations (2.5.16) through (2.5.20) at the top and bottom of the structure, and, with much tedious algebraic manipulation, it can be shown to be true at all depths. The second property allows one to relate the elements of a P-SV propagator matrix which propagates the stress-displacement vector upward between two depths to the elements of the downward propagator matrix.

$$R^A(z, z_0) = \begin{bmatrix} R^A_{35}(z_0, z) & R^A_{45}(z_0, z) & -R^A_{13}(z_0, z) & -R^A_{23}(z_0, z) \\ R^A_{34}(z_0, z) & R^A_{44}(z_0, z) & -R^A_{14}(z_0, z) & -R^A_{24}(z_0, z) \\ -R^A_{31}(z_0, z) & -R^A_{41}(z_0, z) & R^A_{11}(z_0, z) & R^A_{21}(z_0, z) \\ R^A_{32}(z_0, z) & R^A_{42}(z_0, z) & R^A_{12}(z_0, z) & R^A_{22}(z_0, z) \end{bmatrix} \quad (2.5.61)$$

This can be shown by using the relations that exist among the elements of the P-SV layer propagator matrix (equations (2.4.44)) and then reversing the order of layer multiplications. Equation (2.5.6) is a general property of the propagator matrix: it is true for all  $\omega$ ,  $k$ ,  $z$ , and  $z_0$  and it is true even for an arbitrarily inhomogeneous structure with depth. We now define the numerator vector in (2.5.57) as

$$\begin{bmatrix} R^N_1(z_0) \\ R^N_2(z_0) \end{bmatrix} = \frac{1}{R^A_{22}(z_0, z)} \begin{bmatrix} R^N_1(z) \\ R^N_2(z) \end{bmatrix} \quad (2.5.62)$$

Using equations (2.5.58), (2.5.59), and (2.5.60) we can solve for  $[N]$  evaluated at an eigenvalue  $\omega$  or  $k$  as



$$\begin{pmatrix} R N_1^{(0)} \\ R N_2^{(0)} \end{pmatrix} \bigg|_{k=R K(n, \omega)} = - B_{M_{23}}(0) \begin{pmatrix} 0 & 0 & 1 & R^\epsilon \\ 0 & 0 & R^\epsilon & R^{\epsilon^2} \end{pmatrix} R^A(0, z_s) \{R^\Sigma\} \bigg|_{k=R K(n, \omega)} \quad (2.5.63)$$

Using (2.5.61) this can be expressed as follows,

$$\begin{aligned} R N_1^{(0)} \bigg|_{k=R K(n, \omega)} &= \\ &= - B_{M_{23}}(0) \begin{pmatrix} 1 & R^\epsilon \end{pmatrix} \begin{bmatrix} -R A_{31}(z_s, 0) & -R A_{41}(z_s, 0) & R A_{11}(z_s, 0) & R A_{21}(z_s, 0) \\ -R A_{32}(z_s, 0) & -R A_{42}(z_s, 0) & R A_{12}(z_s, 0) & R A_{22}(z_s, 0) \end{bmatrix} \\ &\quad \cdot \{R^\Sigma\} \bigg|_{k=R K(n, \omega)} \end{aligned} \quad (2.5.64)$$

$$R N_2^{(0)} \bigg|_{k=R K(n, \omega)} = R^\epsilon R N_1^{(0)} \bigg|_{k=R K(n, \omega)}$$

We can write the Rayleigh wave eigenfunctions at the source depth as

$$\{R E(n, \omega, z_s)\} = \begin{bmatrix} R A_{11}(z_s, 0) & R A_{12}(z_s, 0) \\ R A_{21}(z_s, 0) & R A_{22}(z_s, 0) \\ R A_{31}(z_s, 0) & R A_{32}(z_s, 0) \\ R A_{41}(z_s, 0) & R A_{42}(z_s, 0) \end{bmatrix} \bigg|_{k=R K(n, \omega)} \begin{pmatrix} 1 \\ R^\epsilon(n, \omega) \end{pmatrix} \quad (2.5.65)$$

If we redefine a new vector for the source jump vector as,

$$[R^\Sigma(n, \omega)] = [R^\Sigma_3 \ R^\Sigma_4 \ -R^\Sigma_1 \ -R^\Sigma_2] \bigg|_{k=R K(n, \omega)} \quad (2.5.66)$$

and using (2.5.65) we can write (2.5.64) as



We may now evaluate the wavenumber integrals given by equations (2.5.36) and (2.5.37) in terms of branch cut integrals and residue contributions. Using equations (2.5.38), (2.5.52), (2.5.58), (2.5.68), (2.5.69) and (2.5.71) we can write the frequency dependent displacements at a receiver location  $(r_r, \theta_r, z_r)$  due to a source confined to a horizontal plane at depth  $z_s$  as follows.

$$R^u(\omega, r_r, \theta_r, z_r) = -R_\alpha^I - R_\beta^I \quad (2.5.72)$$

$$i \sum_n \sum_m \left( R^A(n, \omega) R^\Sigma(n, \omega, m) \{ R^E(n, \omega, z_s) \} R^\Psi(n, \omega, m, r_r, \theta_r, z_r) \right),$$

and

$$L^u(\omega, r_r, \theta_r, z_r) = -L_\beta^I \quad (2.5.73)$$

$$i \sum_n \sum_m \left( L^A(n, \omega) L^\Sigma(n, \omega, m) \{ L^E(n, \omega, z_s) \} L^\Psi(n, \omega, m, r_r, \theta_r, z_r) \right),$$

where the  $A$ 's are scalar amplitude factors and are,

$$R^A(n, \omega) = \frac{k B_{M_{23}}(0)}{\partial_{R\Delta} \partial k} \quad k = R^K(n, \omega) \quad (2.5.74)$$

and

$$L^A(n, \omega) = \frac{k B_{L D_2}(0)}{\partial_{L\Delta} \partial k} \quad k = L^K(n, \omega), \quad (2.5.75)$$

$R_\Delta$  and  $L_\Delta$  are defined by equations (2.5.45) and (2.5.46),  $R^\Sigma$  and  $L^\Sigma$  are defined by equations (2.5.66) and (2.5.70), and  $R^\Psi$  and  $L^\Psi$  are defined as follows.

$${}_R\hat{\Psi}(n, \omega, m, r_r, \theta_r, z_r) = {}_R E_1(n, \omega, z_r) \hat{P}(n, \omega, m, r_r, \theta_r) \quad (2.5.76)$$

$$+ {}_R E_2(n, \omega, z_r) \hat{B}(n, \omega, m, r_r, \theta_r),$$

$${}_L\hat{\Psi}(n, \omega, m, r_r, \theta_r, z_r) = {}_L E_1(n, \omega, z_r) \hat{C}(n, \omega, m, r_r, \theta_r), \quad (2.5.77)$$

where  $\hat{P}$ ,  $\hat{B}$  and  $\hat{C}$  are modified vector cylindrical harmonics and are,

$$\hat{P}(n, \omega, m, r_r, \theta_r) = \mathbf{e}_z \left( H_m^{(2)}(kr_r) e^{im\theta_r} \right) \Big|_{k={}_R K(n, \omega)} \quad (2.5.78)$$

$$\hat{B}(n, \omega, m, r_r, \theta_r) = \mathbf{e}_r \left( \frac{\partial H_m^{(2)}(kr)}{\partial(kr)} e^{im\theta_r} \right) \Big|_{k={}_R K(n, \omega), r=r_r} \quad (2.5.79)$$

$$+ \mathbf{e}_\theta \left( \frac{H_m^{(2)}(kr_r)}{(kr)} \frac{\partial e^{im\theta}}{\partial \theta} \right) \Big|_{k={}_R K(n, \omega), \theta=\theta_r}$$

and

$$\hat{C}(n, \omega, m, r_r, \theta_r) = \mathbf{e}_r \left( \frac{H_m^{(2)}(kr_r)}{(kr_r)} \frac{\partial e^{im\theta}}{\partial \theta} \right) \Big|_{k={}_R K(n, \omega), \theta=\theta_r} \quad (2.5.80)$$

$$+ \mathbf{e}_\theta \left( \frac{\partial H_m^{(2)}(kr)}{\partial(kr)} e^{im\theta_r} \right) \Big|_{k={}_L K(n, \omega), r=r_r}$$

## 2.6 The Branch Cut Integral Contributions

Finally we turn our attention to the branch cut integrals  ${}_R \alpha^l$ ,  ${}_R \beta^l$ , and  ${}_L \beta^l$ . Let us first consider the Rayleigh wave branch cut integrals as shown in figure 2-2. In order to facilitate the evaluation of the branch cut integrals we define the following complex valued functions of the real positive scalar variable  $\eta$

$${}_{R\alpha}\tilde{K}(\eta, \omega) = \text{P-wave branch cut,} \quad (2.6.1)$$

$${}_{R\beta}\tilde{K}(\eta, \omega) = \text{S-wave branch cut,}$$

where

$$\begin{aligned} {}_{R\alpha}\tilde{K}(0, \omega) &= \text{P-wave branch point,} \\ &= \omega_{\alpha}(N) \end{aligned}$$

$$\begin{aligned} {}_{R\beta}\tilde{K}(0, \omega) &= \text{S-wave branch point,} \\ &= \omega_{\beta}(N) \end{aligned}$$

and  $0 \leq \eta \leq \infty$ .

We will also denote wavenumber values immediately to the right and left of the branch cuts as viewed in figure 2-2 with + and - superscripts. We can now write the branch cut integrals as follows.

$$\begin{aligned} {}_{R\alpha}I &= \int_{\infty}^0 f({}_{R\alpha}\tilde{K}^-(\eta, \omega)) {}_{R\alpha}\tilde{K}^+ d\eta \\ &\quad + \int_0^{\infty} f({}_{R\alpha}\tilde{K}^-(\eta, \omega)) {}_{R\alpha}\tilde{K}^+ d\eta, \end{aligned} \quad (2.6.2)$$

and similarly for the  ${}_{R\beta}I$ , where

$${}_{R\alpha}\tilde{K}^+ = \frac{\partial}{\partial \eta} \left( {}_{R\alpha}\tilde{K}(\eta, \omega) \right)$$

and  $f(k)$  is the wavenumber integrand function. We can combine the two integrals in (2.6.2) to obtain the following

$$- {}_{R\alpha}I = \int_0^{\infty} \left( f({}_{R\alpha}\tilde{K}^-(\eta, \omega)) - f({}_{R\alpha}\tilde{K}^+(\eta, \omega)) \right) {}_{R\alpha}\tilde{K}^+ d\eta \quad (2.6.3)$$

The P and S-wave branch cuts define discontinuities in the bottom half space vertical wavenumbers,  $\nu_a^{(N)}$  and  $\nu_b^{(N)}$  so that as one crosses the P-wave branch cut,  $\nu_a^{(N)} \rightarrow \nu_a^{(N)}$ , and as one crosses the S-wave branch cut,  $\nu_b^{(N)} \rightarrow \nu_b^{(N)}$ . The only factors in the wavenumber integrand functions which will be discontinuous across the branch cuts will be the elements of the stress-displacement vector, and so in order to evaluate (2.5.29) we need to compute the stress-displacement difference function across the branch cut which we define as follows,

$$\{\delta y(\eta, z)\} = \{y^+(\eta, z)\} - \{y^-(\eta, z)\}, \quad (2.6.4)$$

where

$$\{y^+(\eta, z)\} = \{R^y(k, z)\}_{k = {}_R\tilde{K}^+(\eta)}$$

and

$$\{y^-(\eta, z)\} = \{R^y(k, z)\}_{k = {}_R\tilde{K}^-(\eta)}$$

For Rayleigh waves, we can use equation (2.5.57) to compute  $\{R^y^+\}$  and  $\{R^y^-\}$  at the surface. Remembering that the propagator matrix and source-jump vector are both single-valued functions, we can compute the stress-displacement branch cut jump at the surface as,

$$\begin{Bmatrix} \delta R^{y_1}(\eta, 0) \\ \delta R^{y_2}(\eta, 0) \end{Bmatrix} = \begin{bmatrix} 0 & 0 & \delta \left( \frac{B_{M_{23}}(0)}{B_{M_{12}}(0)} \right) & \delta \left( \frac{B_{M_{24}}(0)}{B_{M_{12}}(0)} \right) \\ 0 & 0 & \delta \left( \frac{B_{M_{13}}(0)}{B_{M_{12}}(0)} \right) & \delta \left( \frac{B_{M_{14}}(0)}{B_{M_{12}}(0)} \right) \end{bmatrix} [{}_R\mathbf{A}(0, z_s) \{P\Sigma\}]$$

where  $\delta(\cdot)$  defines the jump across the branch cut  $k$  with  $-2\pi < k < 0$ . So

$$\delta \left( \frac{B_{M_{13}}(0)}{B_{M_{12}}(0)} \right) = \frac{B_{M_{13}}(0) - B_{M_{13}}(0)}{B_{M_{12}}(0) - B_{M_{12}}(0)} = 0.$$

From equation (2.5.60) it is easy to see that

$$\delta \left( \frac{B_{M_{13}}(0)}{B_{M_{12}}(0)} \right) = \frac{B_{M_{13}}(0)}{B_{M_{12}}(0)} = 0. \quad (2.6.7)$$

We can see that equation (2.6.7) is a special case of (2.5.60) which expresses the solution of the stress and displacement vectors in terms of the discrete spectra of the Rayleigh wave operator. We can obtain a similar solution for the free surface problem by using the discrete improper eigenfunctions which will be obtained by solving the Rayleigh wave operator. We will obtain the displacement vector  $\{R\chi\}$  which is a function of  $x$  and  $z$  in the half space, but not necessarily the free surface boundary condition. In computing the  $\{R\chi\}$  vector we will also use the boundary condition (2.5.26) we can write the following,

$$\begin{bmatrix} B_{D_{11}} & B_{D_{12}} \\ B_{D_{21}} & B_{D_{22}} \end{bmatrix} \begin{bmatrix} R\chi_1 \\ R\chi_2 \end{bmatrix} = \begin{bmatrix} B_{D_{13}} & B_{D_{14}} \\ B_{D_{23}} & B_{D_{24}} \end{bmatrix} \begin{bmatrix} R\chi_3 \\ R\chi_4 \end{bmatrix} \quad (2.6.8)$$

Equation (2.6.7) will hold at all depths and so we will evaluate  $R\chi_2$  and  $R\chi_4$  at the surface where, using the  $D$  matrix minors we arrive at,

$$\begin{bmatrix} R\chi_1(0) \\ R\chi_2(0) \end{bmatrix} = \frac{1}{B_{M_{12}}(0)} \begin{bmatrix} B_{M_{23}}(0) & B_{M_{24}}(0) \\ B_{M_{13}}(0) & B_{M_{14}}(0) \end{bmatrix} \begin{bmatrix} R\chi_3(0) \\ R\chi_4(0) \end{bmatrix} \quad (2.6.8)$$

(Of course, equation (2.6.8) is only valid if  $B_{M_{12}}(0) \neq 0$ . We will now assume that  $R\chi_3(0) = 0$  so that we can solve for  $R\chi_1(0)$  and  $R\chi_2(0)$  in terms of  $R\chi_4(0)$ . We will also evaluate these at  $R\chi_1^+(0)$  and  $R\chi_1^-(0)$  so that,

$$R\chi_1(0) = \frac{B_{M_{24}}(0)}{B_{M_{12}}(0)} R\chi_4(0) \quad (2.6.9)$$

$$R\chi_2(0) = \frac{B_{M_{14}}(0)}{B_{M_{12}}(0)} R\chi_4(0)$$

and similarly for  $R\chi_1^+(0)$  and  $R\chi_2^+(0)$ . We will specify that,

$$R\chi_4^+(0) = R\chi_4(0) \quad (2.6.10)$$

so that

$$R\chi_1^+(0) = \frac{B_{M_{24}}^+(0)}{B_{M_{12}}^+(0)} \frac{B_{M_{12}}(0)}{B_{M_{24}}(0)} R\chi_1(0) \quad (2.6.11)$$

and

$$R\chi_2^+(0) = \frac{B_{M_{14}}^+(0)}{B_{M_{12}}^+(0)} \frac{B_{M_{12}}(0)}{B_{M_{14}}(0)} R\chi_2(0)$$

We can now define the stress-displacement vector  $\{R\tilde{E}\}$  as follows,

$$\{R\tilde{E}\} = \frac{\{\delta_R\chi\}}{\delta_R\chi_1(0)} = \frac{\{R\chi^+\} - \{R\chi^-\}}{\{R\chi_1^+(0)\} - \{R\chi_1^-(0)\}} \quad (2.6.12)$$

so that

$$\begin{pmatrix} R\tilde{E}_1(0) \\ R\tilde{E}_2(0) \\ R\tilde{E}_3(0) \\ R\tilde{E}_4(0) \end{pmatrix} = \begin{pmatrix} 1 \\ \frac{R\chi_2^+(0) - R\chi_2^-(0)}{R\chi_1^+(0) - R\chi_1^-(0)} \\ 0 \\ 0 \end{pmatrix}$$



$$= \begin{pmatrix} 1 \\ R^{\tilde{\epsilon}} \\ 0 \\ 0 \end{pmatrix}$$

where

$$R^{\tilde{\epsilon}} = - \frac{\delta \left( \frac{B_{M_{14}}(0)}{B_{M_{24}}(0)} \right)}{\delta \left( \frac{B_{M_{24}}(0)}{B_{M_{14}}(0)} \right)} \quad (2.6.13)$$

Following the same procedure except setting  $R\lambda_4^+(0) = R\lambda_4^-(0) = 0$  we can show that

$$R^{\tilde{\epsilon}} = - \frac{\delta \left( \frac{B_{M_{13}}(0)}{B_{M_{12}}(0)} \right)}{\delta \left( \frac{B_{M_{23}}(0)}{B_{M_{12}}(0)} \right)} \quad (2.6.14)$$

Equations (2.6.13) and (2.6.14) along with (2.6.6) allow us to express equation (2.5.5) in the following manner.

(2.6.15)

$$\begin{pmatrix} R^y_1(0) \\ R^y_2(0) \end{pmatrix} = \delta \left( - \frac{B_{M_{23}}(0)}{B_{M_{12}}(0)} \right) \begin{bmatrix} 0 & 0 & 1 & R^{\tilde{\epsilon}} \\ 0 & 0 & R^{\tilde{\epsilon}} & R^{\tilde{\epsilon}^2} \end{bmatrix} R^A(0, z_s) \{R\Sigma\}.$$

We can now repeat the derivation of equations (2.5.63) through (2.5.68) to show the following.

(2.6.16)

$$\{\delta R^y(\eta, z)\} = \delta \left( - \frac{B_{M_{23}}(0)}{B_{M_{12}}(0)} \right) \left( \left[ R^{\tilde{\Sigma}}(\eta, \omega) \right] \left\{ R^{\tilde{E}}(\eta, \omega, z_s) \right\} \right) \left\{ R^{\tilde{E}}(\eta, \omega, z) \right\}.$$

where

$$[{}_R\tilde{\Sigma}(\eta, \omega)] = [{}_R\Sigma_3 \quad {}_R\Sigma_4 - {}_R\Sigma_1 - {}_R\Sigma_3] \Big|_{k={}_R\hat{K}(\eta, \omega)}, \quad (2.6.17)$$

and

$$\{{}_R\hat{E}(\eta, \omega, z)\} = [{}_R\mathbf{A}(z, 0)] \Big|_{k={}_R\hat{K}(\eta, \omega)} \cdot \{{}_R\hat{E}(\eta, \omega, 0)\}. \quad (2.6.18)$$

In order to clean up the notation, we have dropped the  $\alpha$  and  $\beta$  subscripts denoting P and S-wave branch cuts throughout the developments but it is understood that there will be two versions of (2.6.15) corresponding to the two branch cut integrals,  ${}_R\alpha$  and  ${}_R\beta$ . Following a similar analysis for the Love waves we can express the stress-displacement vector jump across the Love wave branch cut as follows.

$$\{\delta_L y(\eta, z)\} = \delta \left( - \frac{{}_L B_{D_2}(0)}{{}_L B_{D_1}(0)} \right) \left( [{}_L\tilde{\Sigma}(\eta, \omega)] \left\{ {}_L\hat{E}(\eta, \omega, z_s) \right\} \right) \left\{ {}_L\hat{E}(\eta, \omega, z) \right\}. \quad (2.6.19)$$

where

$$[{}_L\tilde{\Sigma}(\eta, \omega)] = [{}_L\Sigma_2 - {}_L\Sigma_1] \Big|_{k={}_L\hat{K}(\eta, \omega)}, \quad (2.6.20)$$

$$\{{}_L\hat{E}(\eta, \omega, z)\} = [{}_L\mathbf{A}(z, 0)] \Big|_{k={}_L\hat{K}(\eta, \omega)} \cdot \{{}_L\hat{E}(\eta, \omega, 0)\}, \quad (2.6.21)$$

and

$$\{{}_L\hat{E}(\eta, \omega, 0)\} = \begin{Bmatrix} 1 \\ 0 \end{Bmatrix}.$$

### CHAPTER III

#### REFORMULATION OF THE NORMAL MODE PROBLEM TO AVOID NUMERICAL INSTABILITIES

One of the fundamental problems that has plagued previous efforts to compute synthetic seismograms by evaluation of the wavenumber integrals of equations (2.5.36) has been numerical instabilities that arise when computing the integrand functions,  $\{y(z)\}$ . In this chapter I will address these problems and I will describe several methods which can be used to overcome these problems and the limitations of these methods.

The basic source of the numerical problems is the exponential form of the propagator matrix elements, as given by equations (2.4.44), whenever P or S waves are evanescent. In these cases the arguments of the trigonometric functions are imaginary, causing both growing and decaying exponential solutions to exist. It is the growing exponential functions which are at the root of the numerical instability problem and this problem was first recognized when the matrix method of Thomson (1950) and Haskell (1953) was implemented on digital computers. However, the numerical instability is exacerbated as the frequency increases and since the earliest applications of the Thomson-Haskell matrix method were to compute low frequency fundamental mode Rayleigh and Love dispersion curves, the problem was not initially considered to be restrictive or important.

As the Thomson-Haskell matrix method was pushed to higher frequencies and mode numbers, the numerical problem became important. One of the earliest attempts to deal with the problem was by Press,

Harkrider and Seafeldt (1961) who introduced the layer reduction method. In this method layers which lie below the depth of penetration of the surface wave at a particular frequency are eliminated. A modification of this basic method was given by Rossenbaum (1964) for computing high order Rayleigh waves where P waves were evanescent but S waves were propagating. Although the layer reduction methods were very useful, they did not address the real cause of the numerical instability and they were not effective for certain types of complex structural models such as strong low velocity zones.

Knopoff (1964) developed a method for computing the Rayleigh and Love characteristic functions (equations 2.5.45 and 2.5.46) by using Laplace's development by minors. Dunkin (1965) elaborated on Knopoff's work and showed that this method did indeed eliminate the numerical instability of the characteristic functions for any arbitrary structural model and at any frequency. This then allowed for the accurate computation of Rayleigh and Love dispersion curves although the computational procedure was less efficient than the original Thomson-Haskell matrix method. Watson (1970) derived a more efficient algebraic solution which still embraced Knopoff's original method and Schwab and Knopoff (1970) combined this with the layer reduction method to come up with an accurate and efficient computer program for computing Rayleigh and Love eigenvalues.

Although Knopoff, *et. al.* had solved the numerical problems related to the computation of the dispersion curves, there were still numerical instabilities associated with the stress-displacement functions which prevented the computation of eigenfunctions or of forced solutions which were necessary for the direct integration seismogram synthesis methods. Once again the problem only existed when either P or S waves were

evanescent and so early synthetic seismograms had as the reflection coefficient (Fuchs (1968), Fuchs and Muller (1971)) assumed the problem of computing reflection coefficients for considering ranges of phase velocity for which total internal reflection was not propagating

The next major advance in the theory of reflection and transmission was made by Kennett and Kerry (1976) who showed how to compute reflection and transmission coefficients. This work was based on a series of papers written by Kennett and Kerry (1976) at the relationships between the representation of the wavefield in terms of representations of the wavenumber domain and the time domain. They were able to derive a complete solution of the system of equations for reflection and transmission as an algebraic function of generalized reflection and transmission coefficients. They also showed how these matrices could be computed in a numerically stable manner which avoided the problems with the previous methods. They applied their method to simple structural models with monotonic velocity gradients and to models with weak low velocity zones. They then found that their method could be applied both as a direct integration (Kennett et al. (1978), Kennett et al. (1980)) and as a mode sum (Kerry (1980)) and presented a comparison of the two methods.

The work by Kennett et al. and Kerry et al. was the starting point of my own research into the numerical methods for the computation of reflection and transmission coefficients. I chose to look for a numerically stable method for computing reflection and transmission coefficients in terms of stress-displacement eigenfunctions as opposed to the wavefield reflection and transmission functions which were computed by Kennett et al. I decided on this approach for two reasons. The first reason is that I considered the wavefield formulation of the solution to be overly complicated and not easy to relate to the space-time energy functions which naturally appear in the stress-displacement formulation. Although the Kennett method does allow for the decomposition of the solution by ray types, I feel

that is, a ray decomposition. These methods are really useful, ray decomposition is a very powerful tool to get into the behaviour of the seismic energy. These methods are most useful when you have situations where major changes in ray paths are the result of a change in velocity. These situations quite often occur in the presence of energy which can be most readily described as being trapped in the channel. When the seismic energy is trapped at energy surface as a waveguide, the ray decomposition which shows just where in the structure the seismic energy is distributed, is very useful in determining characteristics of the structure, low velocity channels and the resulting synthetic seismograms.

When I first began to work on solving the numerical problems associated with the numerical problems associated with the computation of normal modes, I was very much influenced by the reflection method when solving the numerical problems for structures with buried low velocity channels. It was necessary to reduce the structure into several zones, into several decoupled waveguide channels. One of the fundamental objectives of my research was to be able to handle very high frequency, near fault structures for shallow structural models which would involve multiple strong low velocity channels. With this in mind I decided to avoid the Kennett and Kerry approach and instead to expand along the lines of reasoning that were originally followed by Knopoff and Dunkin.

AD-R187 663

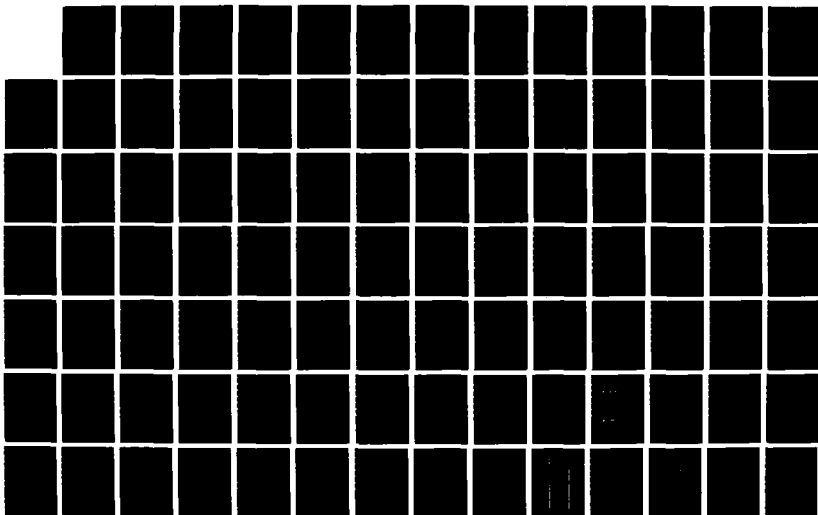
A SPECTRAL METHOD FOR COMPUTING COMPLETE SYNTHETIC  
SEISMOGRAMS(U) COLORADO UNIV AT BOULDER D J HARVEY  
MAR 87 AFGL-TR-87-0238 F19620-05-K-0016

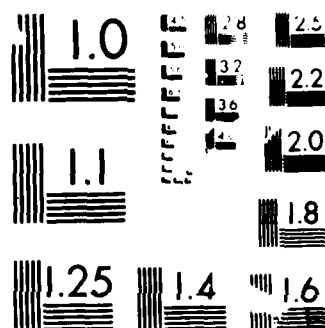
2/4

UNCLASSIFIED

F/G 8/11

NL





ANSI/ISO RESOLUTION TEST CHART

10101



In the following chapter I will first review the work of Knopoff, *et. al.* and show how and why the numerical problem can be overcome when computing Rayleigh eigenvalues. I will then derive a method for computing depth eigenfunctions in a numerically stable manner for relatively simple structural models. This method is comparable to the work done by Kerry although the method is derived in a completely different manner and I will discuss the relative merits of the two approaches. Next I will derive a more robust version of the eigenfunction computation method which will work for a wide variety of complex structural models. This goes beyond the method used by Kerry and I will show when my new method breaks down. Finally I will show a number of examples of numerically stable eigenfunctions as a function of depth and frequency for several structures.

### 3.1 Computation of the Rayleigh Eigenvalues

As with other eigenvalue problems the determination of Rayleigh wave eigenvalues is reduced to solving for the zeroes of a determinant. For this case the characteristic function is a sub-determinant of the  $[D]$  matrix (equation 2.5.45) which can be expressed as a linear combination of two by two sub-determinants of the propagator matrix. When the phase velocity is less than the P-wave and/or S-wave velocity in a given layer, both growing and decaying exponential terms will appear in every element of the layer propagator matrix. As the frequency increases, these growing exponential terms become quite large and any other additive decaying or propagating factors will be "swamped out" in the finite computer precision. The resulting layer propagator matrix will contain only the growing exponential factors.

In order to demonstrate the effect of this roundoff error, let us consider the problem of a layer over a half space. We can write the Rayleigh characteristic function as follows.

$$\Delta(\omega, k) = B_{D_{11}}(0) B_{D_{22}}(0) - B_{D_{12}}(0) B_{D_{21}}(0) \quad (\text{from 2.5.45})$$

where,

$$2 B_{D_{11}}(0) = - \frac{(\gamma-1)}{i\phi_\alpha} A_{11} + \gamma A_{21} - \frac{1}{\rho c^2} A_{31} - \frac{1}{\rho c^2 i\phi_\alpha} A_{41}, \quad (3.1.1)$$

$$2 B_{D_{12}}(0) = - \frac{(\gamma-1)}{i\phi_\alpha} A_{12} + \gamma A_{22} - \frac{1}{\rho c^2} A_{32} - \frac{1}{\rho c^2 i\phi_\alpha} A_{42},$$

$$2 B_{D_{21}}(0) = + \gamma A_{11} - \frac{(\gamma-1)}{i\phi_\beta} A_{21} + \frac{1}{\rho c^2 i\phi_\beta} A_{31} - \frac{1}{\rho c^2} A_{41},$$

$$2 B_{D_{22}}(0) = + \gamma A_{12} - \frac{(\gamma-1)}{i\phi_\beta} A_{22} + \frac{1}{\rho c^2 i\phi_\beta} A_{32} - \frac{1}{\rho c^2} A_{42}$$

The parameters  $\gamma, \phi_\alpha, \phi_\beta$  and  $\rho$  in equations (3.1.1) refer to the half space and the propagator matrix elements are those of the layer propagator matrix.

We can extend the applicability of equations (3.1.1) by letting the propagator matrix elements be those of the total propagator matrix from the surface to the half space for any arbitrary layered structure. Thus the most straightforward way to compute the characteristic function is to compute the total propagator matrix, compute the  $[D]$  matrix elements using equations (3.1.1) and then compute the characteristic function using equation (2.5.45) and this basically was the approach followed in early attempts to compute Rayleigh dispersion curves.

For the case of a single homogeneous layer over a half space we can use equations (2.4.44) directly for the propagator matrix elements where  $z-z_0=h$ , the layer thickness. When the phase velocity is greater than both the P and S wave velocities in the layer, then the terms  $\theta_\alpha$  and  $\theta_\beta$  are both real and the trigonometric functions in equations (2.4.44) have real arguments. For this case the straightforward method of computing the characteristic function is numerically stable. When the phase velocity is greater than the S wave velocity but less than the P wave velocity, then  $\theta_\beta$  is real with corresponding trigonometric (or propagating) solutions, but  $\theta_\alpha$  is imaginary which turn the trigonometric functions to exponential functions with real arguments. As the frequency increases so will the magnitude of  $\theta_\alpha$  and the growing exponential function of  $\theta_\alpha$  will overpower both the decaying exponential function of  $\theta_\alpha$  and the trigonometric functions of  $\theta_\beta$ . For high frequency then, we can approximate the propagator matrix elements as follows for cases where the phase velocity is less than the layer P wave velocity.

$$2 A_{11} \approx -(\gamma-1)e^{+\bar{\theta}_\alpha}, \quad (3.1.2)$$

$$2 A_{12} \approx \gamma \bar{\phi}_\alpha e^{+\bar{\theta}_\alpha},$$

$$2 A_{21} \approx -\frac{(\gamma-1)}{\bar{\phi}_\alpha} e^{+\bar{\theta}_\alpha},$$

$$2 A_{22} \approx \gamma e^{+\bar{\theta}_\alpha},$$

$$2 A_{31} \approx -\frac{\rho c^2 (\gamma-1)^2}{\bar{\phi}_\alpha} e^{+\bar{\theta}_\alpha},$$

$$2 A_{32} \approx \rho c^2 \gamma (\gamma - 1) e^{+\bar{\theta}_\alpha},$$

$$2 A_{41} \approx - \rho c^2 \gamma (\gamma - 1) e^{+\bar{\theta}_\alpha},$$

$$2 A_{42} \approx \rho c^2 \gamma^2 \bar{\phi}_\alpha e^{+\bar{\theta}_\alpha},$$

where,

$$\bar{\theta}_\alpha = i\theta_\alpha, \quad (3.1.3)$$

and,

$$\bar{\phi}_\alpha = i\phi_\alpha,$$

and  $\bar{\phi}_\alpha$ ,  $\bar{\theta}_\alpha$ ,  $\rho$  and  $\gamma$  refer to the layer. This approximation is also valid at high frequencies when the phase velocity is less than both the P and S wave velocities in the layer since  $e^{+\bar{\theta}_\alpha}$  will be much larger than  $e^{+\bar{\theta}_\beta}$ .

If we use the approximate values of the propagator matrix given by equations (3.1.2) and substitute these into equations (3.1.1) it is possible to show the following.

$$B_{D_{11}}(0) B_{D_{22}}(0) \approx B_{D_{12}}(0) B_{D_{21}}(0), \quad (3.1.4)$$

or

$$\Delta(\omega, k) \approx 0.$$

Thus the characteristic function becomes zero for all phase velocities and frequencies regardless of the elastic parameters in the layer over a half space structural model. This is clearly in error and points out that the straightforward method will not work at high frequencies when the P waves are evanescent. The culprits in this case are the propagator matrix element approximations, which although numerically valid for the elements themselves, introduce substantial numerical errors in the computation of the |D

matrix sub-determinant.

Another approach for computing the Rayleigh characteristic function is to compute the  $[D]$  matrix sub-determinants directly instead of computing the  $[D]$  matrix elements. We can compute the characteristic function as follows.

$$\Delta(\omega, k) = \delta D_{1122}(0) \quad (3.1.5)$$

$$\begin{aligned} &= \delta A_{1122} \delta E_{1122} + \delta A_{1132} \delta E_{1123} + \delta A_{1142} \delta E_{1124} + \\ &+ \delta A_{2132} \delta E_{1223} + \delta A_{2142} \delta E_{1224} + \delta A_{3142} \delta E_{1324} , \end{aligned}$$

where  $\delta(\cdot)_{ijkl}$  denotes a two by two sub-determinant of some matrix so that,

$$\delta A_{ijkl} = A_{ij} A_{kl} - A_{ik} A_{jl} \quad (3.1.6)$$

If we substitute into equation (3.1.5) the  $[E]$  matrix elements along with the  $[A]$  matrix element approximations we will end up with the same result as before. However, if we analytically compute the  $[A]$  matrix sub-determinants before applying the approximation then the characteristic function as given by equation (3.1.5) becomes numerically valid even for evanescent P waves. We can see this by considering the sub-determinant  $\delta A_{1122}$ . If we use the  $[A]$  matrix element approximations this becomes,

$$\delta A_{1122} \approx -4 \gamma (\gamma - 1) e^{+2\bar{\theta}} \alpha \quad (3.1.7)$$

$$+ 4 \gamma (\gamma - 1) e^{-2\bar{\theta}} \alpha$$

$$\text{or } \delta A_{1122} \approx 0 ,$$

which is the same as for the other  $[A]$  matrix sub-determinants. If we use the original  $[A]$  matrix element expressions as given by equations (2.4.44) however, and then apply the approximation of only including the growing P-wave exponential solution, then we obtain the following.

$$2 \delta A_{1122} \approx (\gamma^2 + (\gamma-1)^2) e^{+\bar{\theta}} a \cos \theta_\beta \quad (3.1.8)$$

$$+ (\gamma^2 \bar{\phi}_\alpha \bar{\phi}_\beta - \frac{(\gamma-1)^2}{\bar{\phi}_\alpha \bar{\phi}_\beta}) e^{+\bar{\theta}} a \sin \theta_\beta$$

By deriving similar expressions for the other  $[A]$  matrix sub-determinants and applying equation (3.1.5), we can compute a numerically accurate characteristic function for cases where the P waves are evanescent and this can be easily demonstrated by considering the case where the elastic parameters in the layer are the same as those in the half space.

It is possible to generalize the development of the characteristic function in terms of matrix sub-determinants for layered structures at all phase velocities and frequencies. This was first done by Knopoff (1964) and has been most recently reformulated by Abo-Zena (1979). We recall the definition of the anti-symmetric minor matrix,  $[M]$ , which from equation (2.5.56) can be expressed as follows.

$$M_{ij}(\omega, k, z) = \delta_R D_{112j}(\omega, k, z) \quad (3.1.9)$$

Using equations (2.5.16) through (2.5.20) we can compute the minor matrix starting values for various boundary conditions where,  $M_{ij} = \delta_R E_{112j}$ .

1. A traction free surface,

$$M_{12}(\omega, k, z_{T0}) = 0, \quad (3.1.10)$$

$$M_{13}(\omega, k, z_{T0}) = 0,$$

$$M_{14}(\omega, k, z_{T0}) = 0 ,$$

$$M_{23}(\omega, k, z_{T0}) = 0 ,$$

$$M_{24}(\omega, k, z_{T0}) = 0 ,$$

$$M_{34}(\omega, k, z_{T0}) = 1 ,$$

where  $z_{T0}$  = the depth of a traction free surface,

2. A rigid surface,

$$M_{12}(\omega, k, z_{D0}) = 1 , \quad (3.1.11)$$

$$M_{13}(\omega, k, z_{D0}) = 0 ,$$

$$M_{14}(\omega, k, z_{D0}) = 0 ,$$

$$M_{23}(\omega, k, z_{D0}) = 0 ,$$

$$M_{24}(\omega, k, z_{D0}) = 0 ,$$

$$M_{34}(\omega, k, z_{D0}) = 0 ,$$

where  $z_{D0}$  = the depth of a rigid surface,

3. Zero shear tractions and zero vertical displacement,

$$M_{12}(\omega, k, z_{M0}) = 0 , \quad (3.1.12)$$

$$M_{13}(\omega, k, z_{M0}) = 0 ,$$

$$M_{14}(\omega, k, z_{M0}) = 1 ,$$

$$M_{23}(\omega, k, z_{M0}) = 0 ,$$

$$M_{24}(\omega, k, z_{M0}) = 0 ,$$

$$M_{34}(\omega, k, z_{M0}) = 0 ,$$

where  $z_{M0}$  = the depth of a surface with zero shear traction and zero vertical displacement,

4. No upward propagating P or S wave radiation.

$$M_{12}(\omega, k, z_{SU}) = - \frac{1}{4} \left( \frac{(\gamma-1)^2}{\phi_\alpha \phi_\beta} + \gamma^2 \right) , \quad (3.1.13)$$

$$M_{13}(\omega, k, z_{SU}) = + \frac{1}{4} \left( \frac{(\gamma-1)}{\rho c^2 \phi_\alpha \phi_\beta} - \frac{\gamma}{\rho c^2} \right) ,$$

$$M_{14}(\omega, k, z_{SU}) = - \frac{1}{4} \left( \frac{1}{\rho c^2 \phi_\alpha} \right) ,$$

$$M_{23}(\omega, k, z_{SU}) = + \frac{1}{4} \left( \frac{1}{\rho c^2 \phi_\beta} \right) ,$$

$$M_{24}(\omega, k, z_{SU}) = -\frac{1}{4} \left( \frac{(\gamma-1)}{\rho c^2 \phi_\alpha \phi_\beta} + \frac{\gamma}{\rho c^2} \right),$$

$$M_{34}(\omega, k, z_{SU}) = +\frac{1}{4} \left( \frac{1}{\rho^2 c^4 \phi_\alpha \phi_\beta} + \frac{1}{\rho^2 c^4} \right),$$

where  $z_{SU}$  = the depth at which there is no upward propagating P or S wave radiation,

5. No downward propagating P or S wave radiation,

$$M_{12}(\omega, k, z_{SD}) = -\frac{1}{4} \left( \frac{(\gamma-1)^2}{\phi_\alpha \phi_\beta} + \gamma^2 \right), \quad (3.1.14)$$

$$M_{13}(\omega, k, z_{SD}) = +\frac{1}{4} \left( \frac{(\gamma-1)}{\rho c^2 \phi_\alpha \phi_\beta} + \frac{\gamma}{\rho c^2} \right),$$

$$M_{14}(\omega, k, z_{SD}) = +\frac{1}{4} \left( \frac{1}{\rho c^2 \phi_\alpha} \right),$$

$$M_{23}(\omega, k, z_{SD}) = -\frac{1}{4} \left( \frac{1}{\rho c^2 \phi_\beta} \right),$$

$$M_{24}(\omega, k, z_{SD}) = -\frac{1}{4} \left( \frac{(\gamma-1)}{\rho c^2 \phi_\alpha \phi_\beta} + \frac{\gamma}{\rho c^2} \right),$$

$$M_{34}(\omega, k, z_{SD}) = +\frac{1}{4} \left( \frac{1}{\rho^2 c^4 \phi_\alpha \phi_\beta} + \frac{1}{\rho^2 c^4} \right),$$

where  $z_{SD}$  = the depth at which there is no downward propagating P or S wave radiation.

Using equations (2.5.56) and (2.4.15) we can relate the  $[D]$  matrix at one depth to the  $[D]$  matrix at another depth as follows.

$$[D(z_2)] = [D(z_1)] [A(z_1, z_2)] \quad (3.1.15)$$

From this equation we can derive a similar propagator relation for the minor matrix.

$$[M(z_2)] = [A(z_1, z_2)]^T [M(z_1)] [A(z_1, z_2)] \quad (3.1.16)$$

This equation is given by Abo-Zena (1979).



Because of the anti-symmetric properties of  $[M]$ , it is easy to show that equation (3.1.16) can be rewritten as follows.

$$\begin{aligned} M_{ij}(z_2) = & M_{12}(z_1) \delta(A(z_1, z_2))_{ij12} + M_{13}(z_1) \delta(A(z_1, z_2))_{ij13} + \\ & M_{14}(z_1) \delta(A(z_1, z_2))_{ij14} + M_{23}(z_1) \delta(A(z_1, z_2))_{ij23} + \\ & M_{24}(z_1) \delta(A(z_1, z_2))_{ij24} + M_{34}(z_1) \delta(A(z_1, z_2))_{ij34} \end{aligned} \quad (3.1.17)$$

Watson (1970) first derived the relation (3.1.17) and he also pointed out that two of the six elements of the minor matrix are linearly dependent for all depths, frequencies and wavenumbers. Recalling equation (2.5.60),  $M_{13} = -M_{24}$ , we can rewrite (3.1.17) as follows.

$$\{\bar{M}(z_2)\} = [R(z_1, z_2)] \{\bar{M}(z_1)\}, \quad (3.1.18)$$

where  $\{\bar{M}(z)\}$  is a five element vector and is related to the minor matrix as follows.

$$\begin{aligned} \bar{M}_1(z) &= M_{12}(z), \\ \bar{M}_2(z) &= M_{13}(z), \\ \bar{M}_3(z) &= M_{14}(z), \\ \bar{M}_4(z) &= M_{23}(z), \\ \bar{M}_5(z) &= M_{34}(z), \end{aligned} \quad (3.1.19)$$

and  $[R(z_1, z_2)]$  is the five by five minor propagator matrix whose elements will be equal to linear combinations of the propagator matrix two by two sub-determinants (from equation 3.1.17).

The P-SV  $[R]$  matrix elements can be computed for a solid homogeneous layer from equations (2.4.44), (3.1.17) and (2.5.60) and are given below.

$$\begin{aligned} R R_{11}(z, z_0) = & -2\gamma(\gamma-1) + (\gamma^2 + (\gamma-1)^2) \cos(\theta_\alpha) \cos(\theta_\beta) \\ & + (\gamma^2 \phi_\alpha \phi_\beta - \frac{(\gamma-1)^2}{\phi_\alpha \phi_\beta}) \sin(\theta_\alpha) \sin(\theta_\beta) \end{aligned} \quad (3.1.20)$$

$$\begin{aligned} R R_{12}(z, z_0) = & 2\rho c^2 [-\gamma(\gamma-1)(2\gamma-1)(1 - \cos(\theta_\alpha) \cos(\theta_\beta)) \\ & + (\gamma^3 \phi_\alpha \phi_\beta - \frac{(\gamma-1)^3}{\phi_\alpha \phi_\beta}) \sin(\theta_\alpha) \sin(\theta_\beta)] \end{aligned}$$

$$R R_{13}(z, z_0) = \rho c^2 [-\gamma^2 \phi_\alpha \sin(\theta_\alpha) \cos(\theta_\beta) - \frac{(\gamma-1)^2}{\phi_\beta} \sin(\theta_\beta) \cos(\theta_\alpha)]$$

$$R R_{14}(z, z_0) = \rho c^2 [+ \frac{(\gamma-1)^2}{\phi_\alpha} \sin(\theta_\alpha) \cos(\theta_\beta) + \gamma^2 \phi_\beta \sin(\theta_\beta) \cos(\theta_\alpha)]$$

$$\begin{aligned} R R_{15}(z, z_0) = & \rho^2 c^4 [2\gamma^2(\gamma-1)^2(1 - \cos(\theta_\alpha) \cos(\theta_\beta)) \\ & - (\gamma^4 \phi_\alpha \phi_\beta - \frac{(\gamma-1)^4}{\phi_\alpha \phi_\beta}) \sin(\theta_\alpha) \sin(\theta_\beta)] \end{aligned}$$

$$\begin{aligned} R R_{21}(z, z_0) = & \frac{1}{\rho c^2} [(2\gamma-1)(1 - \cos(\theta_\alpha) \cos(\theta_\beta)) \\ & - (\gamma \phi_\alpha \phi_\beta - \frac{(\gamma-1)}{\phi_\alpha \phi_\beta}) \sin(\theta_\alpha) \sin(\theta_\beta)] \end{aligned}$$

$$\begin{aligned} R R_{22}(z, z_0) = & 1 + 2 [2\gamma(\gamma-1)(1 - \cos(\theta_\alpha) \cos(\theta_\beta)) \\ & - (\gamma^2 \phi_\alpha \phi_\beta - \frac{(\gamma-1)^2}{\phi_\alpha \phi_\beta}) \sin(\theta_\alpha) \sin(\theta_\beta)] \end{aligned}$$

$$R R_{23}(z, z_0) = + \gamma \phi_\alpha \sin(\theta_\alpha) \cos(\theta_\beta) + \frac{(\gamma-1)}{\phi_\beta} \sin(\theta_\beta) \cos(\theta_\alpha)$$

$$R R_{24}(z, z_0) = - \frac{(\gamma-1)}{\phi_\alpha} \sin(\theta_\alpha) \cos(\theta_\beta) - \gamma \phi_\beta \sin(\theta_\beta) \cos(\theta_\alpha)$$

$$R R_{25}(z, z_0) = \frac{1}{2} R R_{12}(z, z_0)$$

$$R R_{31}(z, z_0) = \frac{1}{\rho c^2} \left[ + \frac{1}{\phi_\alpha} \sin(\theta_\alpha) \cos(\theta_\beta) + \phi_\beta \sin(\theta_\beta) \cos(\theta_\alpha) \right]$$

$$R R_{32}(z, z_0) = - 2 R R_{24}(z, z_0)$$

$$R R_{33}(z, z_0) = \cos(\theta_\alpha) \cos(\theta_\beta)$$

$$R R_{34}(z, z_0) = \frac{\phi_\beta}{\phi_\alpha} \sin(\theta_\alpha) \sin(\theta_\beta)$$

$$R R_{35}(z, z_0) = - R R_{14}(z, z_0)$$

$$R R_{41}(z, z_0) = \frac{1}{\rho c^2} \left[ - \phi_\alpha \sin(\theta_\alpha) \cos(\theta_\beta) - \frac{1}{\phi_\beta} \sin(\theta_\beta) \cos(\theta_\alpha) \right]$$

$$R R_{42}(z, z_0) = - 2 R R_{23}(z, z_0)$$

$$R R_{43}(z, z_0) = \frac{\phi_\alpha}{\phi_\beta} \sin(\theta_\alpha) \sin(\theta_\beta)$$

$$R R_{44}(z, z_0) = \cos(\theta_\alpha) \cos(\theta_\beta)$$

$$R R_{45}(z, z_0) = - R R_{13}(z, z_0)$$

$$R R_{51}(z, z_0) = \frac{1}{\rho^2 c^4} \left[ 2(1 - \cos(\theta_\alpha) \cos(\theta_\beta)) \right. \\ \left. - \left( \phi_\alpha \phi_\beta - \frac{1}{\phi_\alpha \phi_\beta} \right) \sin(\theta_\alpha) \sin(\theta_\beta) \right]$$

$$R R_{52}(z, z_0) = + 2 R R_{21}(z, z_0)$$

$$R R_{53}(z, z_0) = - R R_{41}(z, z_0)$$

$$R R_{54}(z, z_0) = - R R_{31}(z, z_0)$$

$${}_R R_{55}(z, z_0) = - {}_R R_{11}(z, z_0)$$

where  $c$ ,  $\gamma$ ,  $\phi_\alpha$  and  $\phi_\beta$  are given by (2.4.42) and  $\theta_\alpha$  and  $\theta_\beta$  are given by (2.4.45).

The recursive application of equation (3.1.18) will allow the minor matrix elements to be computed at any depth by starting with the bottom boundary condition and working up or by starting with the top boundary condition and working down. The elements of the minor propagator matrix,  $[R]$ , bear some of the same relations as those of the propagator matrix,  $[A]$ . However the most important characteristic of the  $[R]$  matrix elements is that terms involving  $\cos^2(\theta_\alpha)$ ,  $\sin^2(\theta_\alpha)$ ,  $\cos^2(\theta_\beta)$  and  $\sin^2(\theta_\beta)$  are absent. One might expect such terms to be present from a first inspection of the  $[A]$  matrix elements and certainly if the  $[A]$  matrix sub-determinants were computed numerically such terms would appear in the course of the arithmetic operations.

When we compute the  $[A]$  matrix sub-determinants algebraically, however, we find that the  $\cos^2(\cdot)$ ,  $\sin^2(\cdot)$  terms explicitly and exactly cancel out and this cancellation is what provides for the numerical stability of the  $[R]$  matrix. Dunkin (1965) first proved that these terms could not appear in the  $[A]$  matrix sub-determinants and he pointed out that the P-wave terms,  $\cos^2(\theta_\alpha)$  and  $\sin^2(\theta_\alpha)$ , would be much larger than any of the other trigonometric terms whenever P-waves are evanescent and as frequency increases. Numerical computation of  $[D]$  matrix sub-determinants involve arithmetic cancellation of the  $\cos^2(\theta_\alpha)$ ,  $\sin^2(\theta_\alpha)$  terms and the resulting roundoff error will be scaled by the magnitude of the squared terms. At some point the scaled roundoff error will be equal to the other terms in the sub-determinant and when this happens the resulting sub-determinant

computation is in error.

The  $[R]$  matrix elements given by equations (3.1.20) and the minor matrix elements given by equation (3.1.18) along with their numerical properties are the foundation of my own work. Assuming that the minor matrix elements are numerically stable using the  $[R]$  matrix, then the problem of computing numerically valid synthetic seismograms reduces to that of computing numerically stable eigenfunctions. Although Dunkin was able to prove that certain destabilizing terms were absent in the minor matrix elements using the approach described here, he, nor anyone else to my knowledge, has been able to prove theoretically that the minor matrix elements will be numerically valid for arbitrary structural models. Computer algorithms using this method to compute the Rayleigh characteristic function and the Rayleigh eigenvalues have been written by a number of researches including myself. My experience with this method when used to compute the Rayleigh characteristic function is that it does produce a numerically accurate result for a wide range of structural models and frequency bandwidths. In fact I have never seen this method fail to produce accurate eigenvalues even for complex structures involving liquid layers and multiple strong low velocity zones.

Based on this experience, I started out with the tentative hypothesis that all minor matrix elements were numerically stable, when using the computational method given in this section, for all depths, structural models, frequencies and wavenumbers. In the next section I will show how depth eigenfunctions can be computed in a simple manner using the minor matrix elements and I will show when this simple method starts to break down.

### 3.2 Computation of the Rayleigh Eigenfunctions: I - A Simple but Stable Numerical Algorithm

Although Knopoff and Dunkin were able to solve the numerical problem of computing accurate  $D$  matrix sub-determinants and thus Rayleigh eigenvalues, no one had solved the problem of computing numerically accurate eigenfunctions at depth. The surface values of the eigenfunctions can be directly related to the minor matrix elements and so it has been possible to compute numerically stable synthetic seismograms for surface sources and receivers, but this has been a severe restriction especially for earthquake research. One of the major contributions of my research has been to provide an algorithm for computing eigenfunctions at any depth and frequency for a large variety of structural models that would be interesting to geophysical researchers.

The standard method for computing eigenfunctions at depth has been to compute the surface values of the eigenfunctions using equations (2.5.48) and then multiply the propagator matrix to the desired depth by the surface eigenfunction vector. In many cases the eigenfunctions become numerically unstable with increasing depth and the problem is more pronounced as the frequency is increased. Basically, what is happening is that small roundoff errors in the four eigenfunctions are effectively amplified by subsequent propagator matrix multiplications until the errors get bigger than the correct values of the eigenfunctions. Thus the computed eigenfunctions at half space depths generally no longer meet the Sommerfeld radiation condition.

In order to demonstrate this problem I use as an example the only structure for which I could readily obtain an exact analytic expression for the eigenfunctions namely an infinite homogeneous half space. Using

propagator matrix elements from equations (2.4.44) the first displacement eigenfunction can be written as follows.

$$\begin{aligned}
 E_1(z) = & \frac{1}{2}(-(\gamma-1)+R^{\epsilon}_1\bar{\phi}_\alpha\gamma)\exp(+\frac{\omega z}{R^{c}_1}\bar{\phi}_\alpha) \\
 & + \frac{1}{2}(-(\gamma-1)-R^{\epsilon}_1\bar{\phi}_\alpha\gamma)\exp(-\frac{\omega z}{R^{c}_1}\bar{\phi}_\alpha) \\
 & + \frac{1}{2}(\gamma-R^{\epsilon}_1\frac{(\gamma-1)}{\bar{\phi}_\beta})\exp(+\frac{\omega z}{R^{c}_1}\bar{\phi}_\beta) \\
 & + \frac{1}{2}(\gamma+R^{\epsilon}_1\frac{(\gamma-1)}{\bar{\phi}_\beta})\exp(-\frac{\omega z}{R^{c}_1}\bar{\phi}_\beta)
 \end{aligned} \tag{3.2.1}$$

where we have dropped the layer index and  $R^{\epsilon}_1$  is the ellipticity for the fundamental mode and  $R^{c}_1$  is the eigenphase velocity which of course is frequency independent. Also,

$$\bar{\phi}_\alpha = -i\phi_\alpha$$

and,

$$\bar{\phi}_\beta = -i\phi_\beta$$

Since the value of  $R^{c}_1$  is less than the S-wave velocity, the functions  $\phi_\alpha$  and  $\phi_\beta$  are positive imaginary (see equations 2.4.42) and so functions  $\bar{\phi}_\alpha$  and  $\bar{\phi}_\beta$  are real and positive. Thus the arguments of the exponential functions in equation (3.2.1) are real and there are both growing and decaying solutions with depth. If we replace the ellipticity with an analytic expression in  $\bar{\phi}_\alpha$ ,  $\bar{\phi}_\beta$  and  $\gamma$ , which we can derive for this simple case, we find that equation (3.2.1) can be reduced to the following.

$$E_1(z) = -(\gamma-1)\exp(-\frac{\omega z}{R^{c}_1}\bar{\phi}_\alpha) + \gamma\exp(-\frac{\omega z}{R^{c}_1}\bar{\phi}_\beta) \tag{3.2.2}$$

The cause of the eigenfunction numerical instability can be seen when one compares equation (3.2.1) with (3.2.2). The Sommerfeld radiation condition requires that the growing exponential solutions vanish which is the case with equation (3.2.2). This comes about because the terms which multiply the growing exponential functions in equation (3.2.1) are identically zero. In order to show this one must substitute an explicit analytic expression for the ellipticity which in general is impossible to derive but for this simple case is easy to derive. If, however, one were to code equation (3.2.1) in a computer program to compute the eigenfunction, then the terms which multiply the growing exponential functions would be computed numerically and instead of being identically zero, they would be of the order of the computer word roundoff error. These small but finite terms would then be multiplied by growing exponential functions and at some depth the eigenfunction error terms would overcome the correct decaying solutions. Since the growing exponential arguments are directly proportional to frequency, this numerical problem becomes more pronounced for a given depth as frequency increases. Also, this problem exists at some depth for all frequencies.

One can see from equation (3.2.1) that the type of algebraic cancellation which was present in the characteristic function computations can only be realized with the eigenfunction computations if an explicit analytic solution for the ellipticity can be derived. In general such an expression cannot be derived and so in general we are stuck with using equation (3.2.1) or a more complicated version for multi-layered models.

The errors in the eigenfunction computations can be thought of as unstable drifting errors with respect to depth since there is no inherent mechanism in the computations to stabilize them and so my initial attempt



to solve this problem was based on finding a constraining relation among the four eigenfunctions which would provide a "feedback" mechanism to control and minimize the errors. The most obvious constraining relation can be easily derived from equation (2.5.40).

$$[B_D(z)] \{E(z)\} = \{0\} \quad (3.2.3)$$

From this equation we can relate the stress eigenfunctions to the displacement eigenfunctions and the minor matrix elements.

$$\begin{pmatrix} E_3(z) \\ E_4(z) \end{pmatrix} = - \frac{1}{B_{M_{34}}(z)} \begin{bmatrix} +B_{M_{14}}(z) & +B_{M_{24}}(z) \\ -B_{M_{13}}(z) & -B_{M_{23}}(z) \end{bmatrix} \begin{pmatrix} E_1(z) \\ E_2(z) \end{pmatrix} \quad (3.2.4)$$

We can see from equation (3.2.4) that this is a relation which must exist at all frequencies and throughout the structure. The other important characteristic of equation (3.2.4) is that it is an expression of the Sommerfeld radiation condition at the bottom of the structure and so it is a constraining relation which inherently forces the bottom boundary condition to be met regardless of errors which may be present in the eigenfunctions. Since the constraining relation contains only minor matrix elements which I had hypothesized to be numerically stable under all circumstances, equation (3.2.4) became the basis for computing numerically stable eigenfunctions.

In order to use the constraining relation (3.2.4) to stabilize eigenfunction computations I follow the procedure outlined below.

1. The minor matrix elements are computed using equations (3.1.18) and (3.1.20) at each layer interface in the course of finding the Rayleigh eigenvalues.

2. The surface eigenfunctions are computed using equations (2.5.48).
3. The two displacement eigenfunctions are computed at the next deepest layer interface using the first two rows of the propagator matrix.
4. The constraining relation (3.2.4) is used to compute the two stress eigenfunctions at that interface instead of using the propagator matrix.
5. Steps 3 and 4 are repeated recursively until the desired depth is reached.

This procedure will keep the eigenfunction errors small only if the layers are suitably thin. Since the propagator matrix is used to compute the two displacement eigenfunctions, roundoff errors in these eigenfunctions are amplified by growing exponential functions in the propagator matrix elements for cases of P or S wave evanescence. The constraining relation introduces compensating terms in the stress eigenfunctions which force the bottom boundary condition to be met. These compensating terms will tend to control and minimize the errors in the displacement eigenfunctions at the next layer interface as long as the layer is not so thick that the propagator matrix exponential functions amplify the errors to too high a value.

For structures which involve thick layers and for cases where the frequency is very high, it is necessary to introduce pseudo-layers into the structural model. These are simply some number of thinner layers with identical elastic parameters which replace a single thicker layer. This allows the constraining relation to be applied within the original thick layer at pseudo-layer interfaces to control the eigenfunction errors before they become too large. This pseudo-layering in no way effects the resulting synthetic seismograms and is only used to stabilize the eigenfunction computations.

Results using this method are graphically displayed in figures 3-1 through 3-6. The half space problem used earlier is displayed in figure 3-1 to 3-3 which shows plots of the vertical displacement and normal stress eigenfunctions as a function of depth at a frequency of five Hertz. The S-wave velocity for this half space is four km/sec and Poisson's ratio is 0.25. For each of the eigenfunctions there are two traces, the left trace consists of both the numerically computed eigenfunction shown with a thin line along with the exact solution shown with a thick line and the right trace is the difference between the computed solution and the exact solution. Both traces are plotted on a logarithmic (base 10) scale so as to show the fine details of the errors. In figure 3-1 there was no pseudo-layering and the eigenfunctions were computed using the propagator matrix only without using the constraining relation. The numerical instability due to the growing exponential functions is quite apparent and this instability causes the eigenfunctions to "blow up" at about five km depth. As can be seen from the error plots this instability is due to amplification of the initial small errors in the surface values of the eigenfunctions. In figure 3-2 a pseudo-layer interface was placed at five km depth and the constraining relation was applied at this interface. Although the eigenfunctions do not "blow up" they are clearly in error around five km depth and they are showing signs of instability at about ten km depth. In this case the error was allowed to become large before the constraining relation was applied at five km depth, but even in the case where the eigenfunction computations are clearly in error the use of equation (3.2.4) forces a certain stability. From this figure we can see that the pseudo-layer thickness must be less than five km and in figure 3-3 a pseudo-layer thickness of 2.5 km has been used. In this case the error never gets large and the use of equation (3.2.4) keeps the

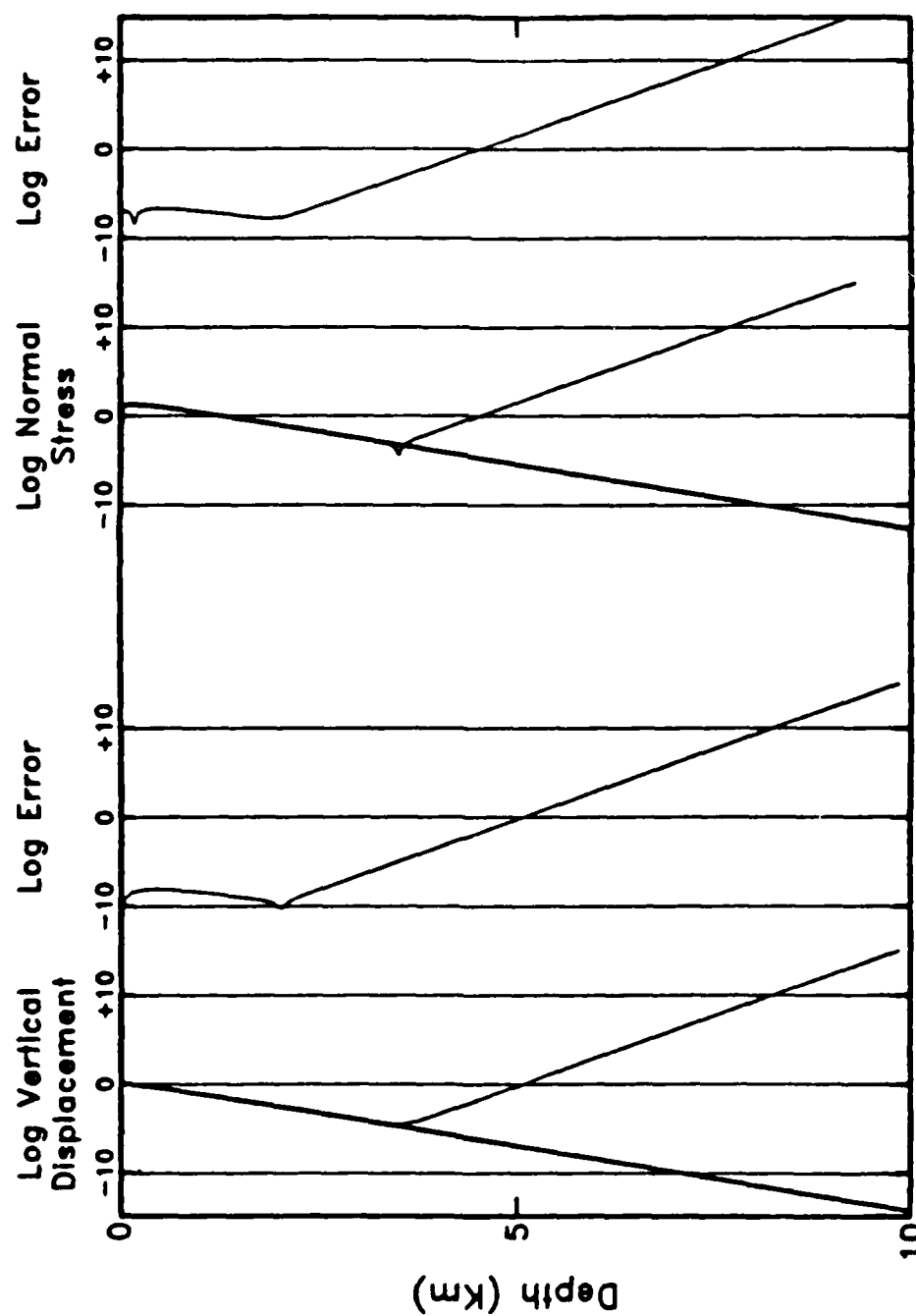


Figure 3-1. Vertical displacement and normal stress eigenfunctions for an infinite homogeneous half space. The thick lines represent the exact solution and the thin lines were generated using the traditional Thomson-Haskell matrix method.

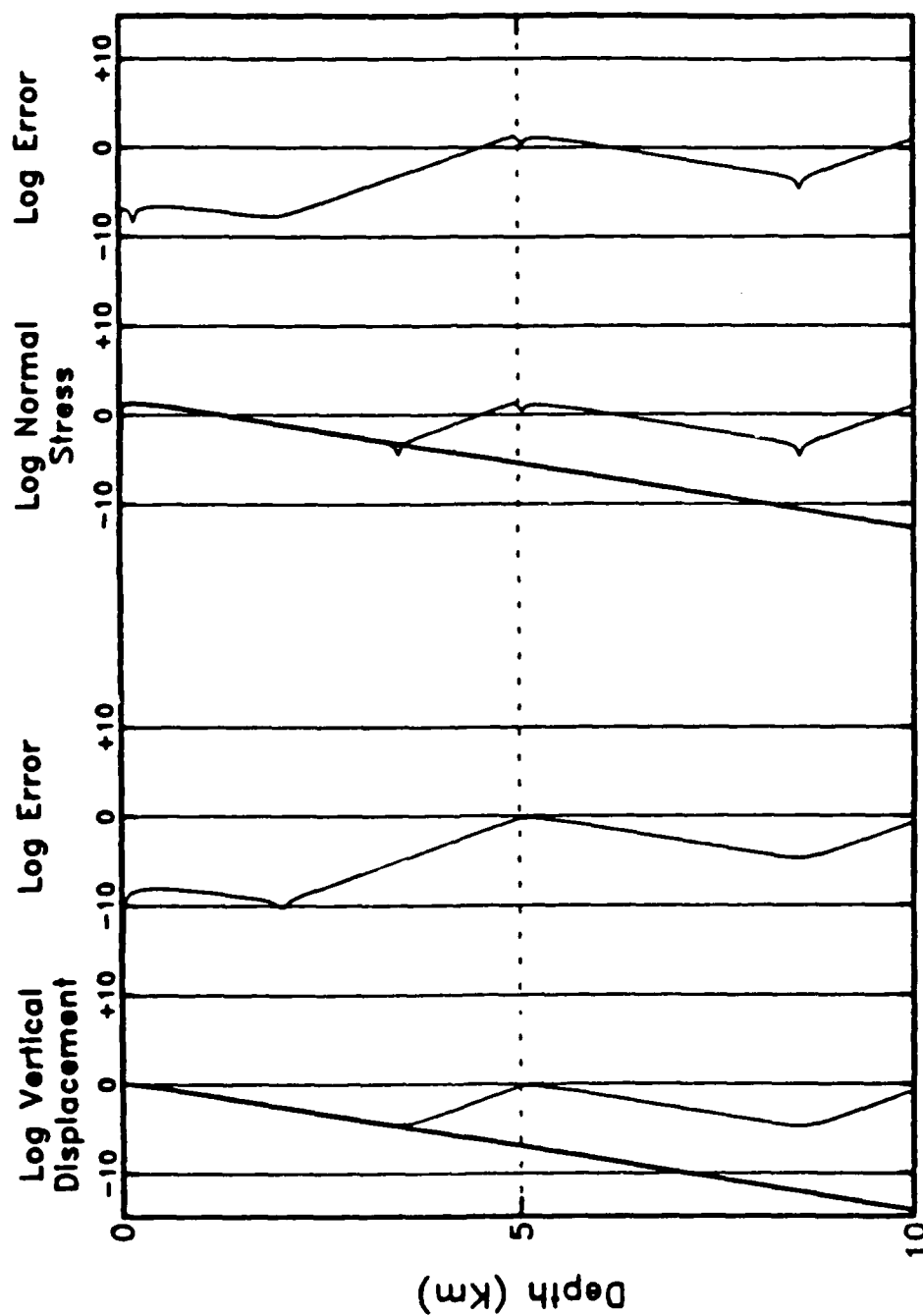


Figure 3-2. Vertical displacement and normal stress eigenfunctions for an infinite homogeneous half space. The thick lines represent the exact solution and the thin lines were generated using a stabilized version of the Thomson-Haskell matrix method. The constraint equations were applied at five km depth.

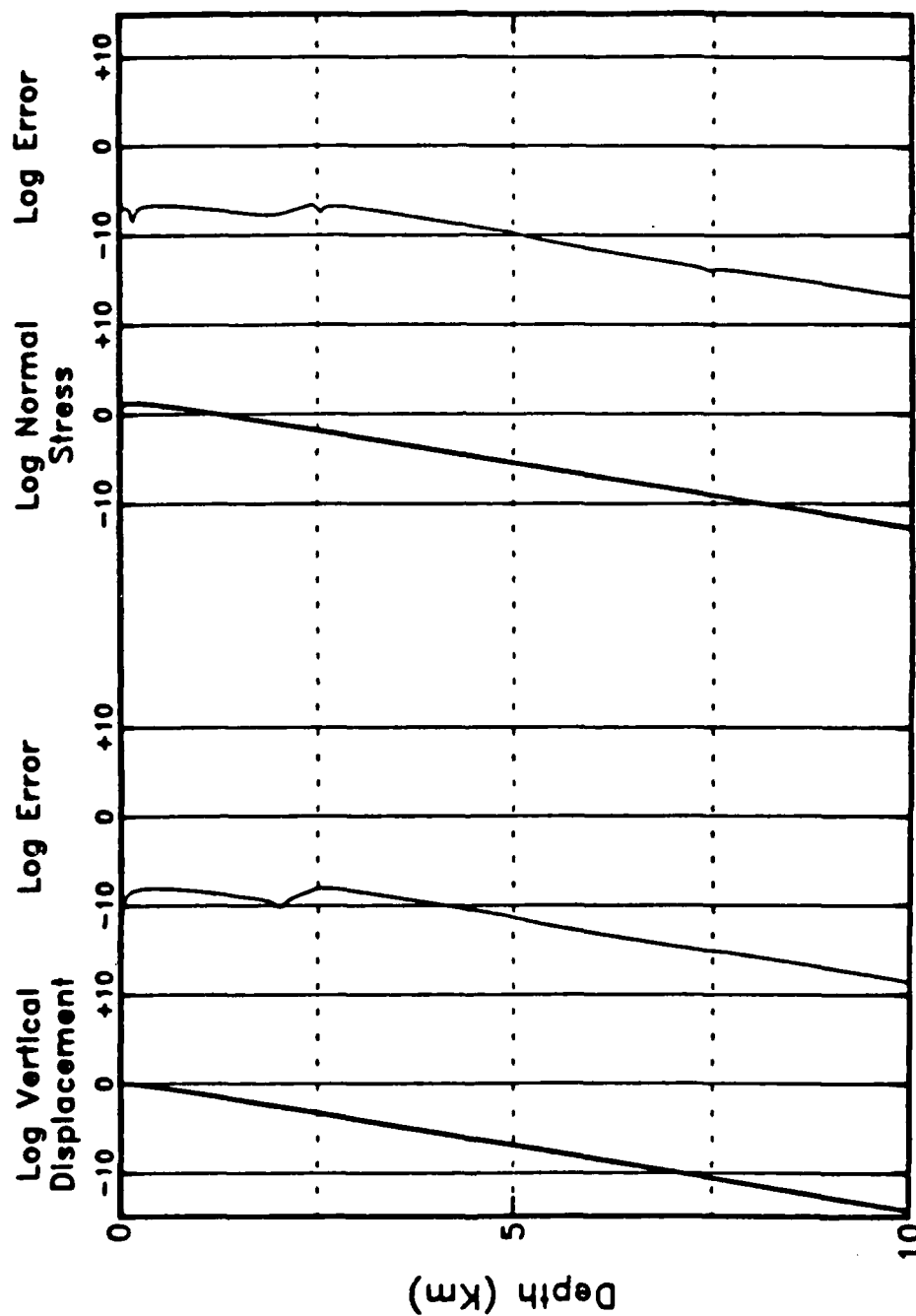


Figure 3-3. Vertical displacement and normal stress eigenfunctions for an infinite homogeneous half space. The thick lines represent the exact solution and the thin lines were generated using a stabilized version of the Thomson-Haskell matrix method. The constraint equations were applied at 2.5, 5.0, and 7.5 km depth.

error small. Figures 3-1 to 3-3 show that this stabilization method is only accurate if the error is not allowed to become large, *i.e.* the pseudo-layer thickness is below some critical value which will be inversely proportional to the frequency.

From a practical standpoint we will not be very interested in computing eigenfunctions for a half space and so the computed eigenfunctions are shown for a more complex structure in figures 3-4 to 3-6. This particular structure is two five km thick layers over a half space and the eigenfunctions correspond to a high order mode at five Hertz frequency. The eigenphase velocity for this mode is such that the S-waves are propagating in the top two layers and the P-waves are evanescent throughout the structure. The error plots are missing in these figures since there is no exact solution to compare against. Once again the computed eigenfunctions using the standard method are shown in figure 3-4 and as with the half space case they "blow up" at about five km depth. The constraining relation (3.2.4) has been applied at the layer interfaces at five and ten km depth in figure 3-5, but as before we might suspect that the errors have become too large for accurate computations at and below five km depth. Two pseudo-layer interfaces are added at 2.5 and 7.5 km depth and the results can be seen in figure 3-6. If we continue to add pseudo-layers to the structure and make the pseudo-layer thicknesses smaller the resulting eigenfunctions do not change from those shown in figure 3-6 and thus it can be concluded that these computed eigenfunctions are good approximations to the exact solution.

A simple criterion for determining pseudo-layer thicknesses can be derived from the exponential arguments in equation (3.2.1).

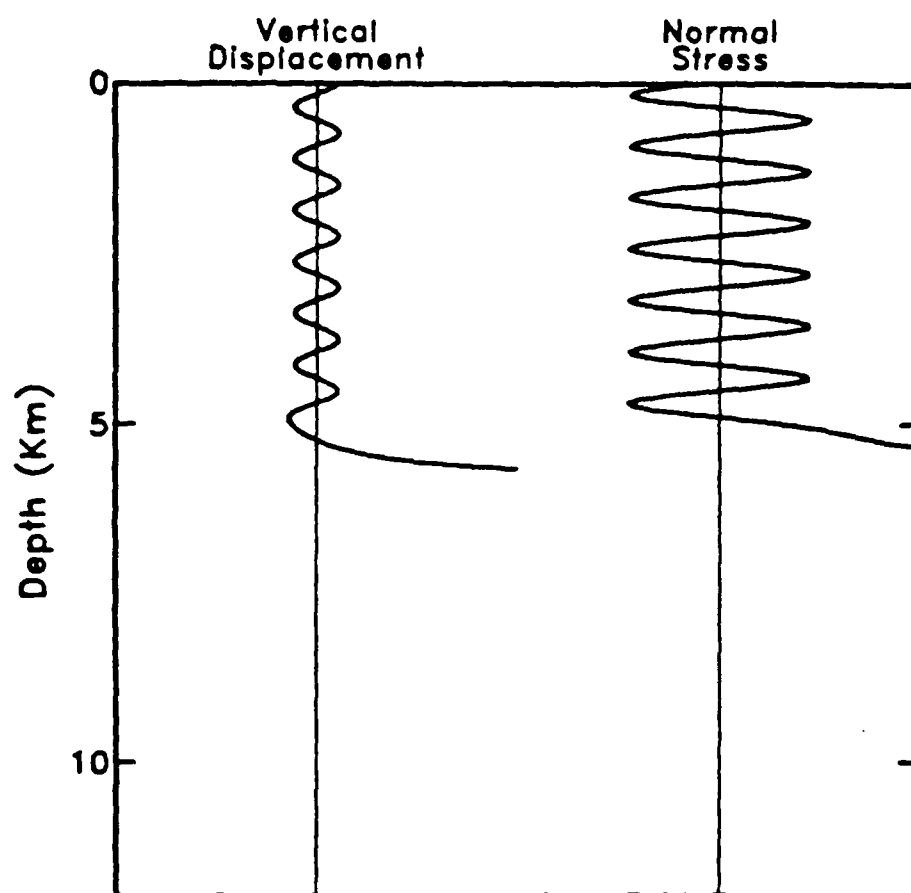


Figure 3-4. Vertical displacement and normal stress eigenfunctions for a two layer over a half space structural model. Layer interfaces are at depths of five and ten km. These eigenfunctions were generated using the traditional Thomson-Haskell matrix method.



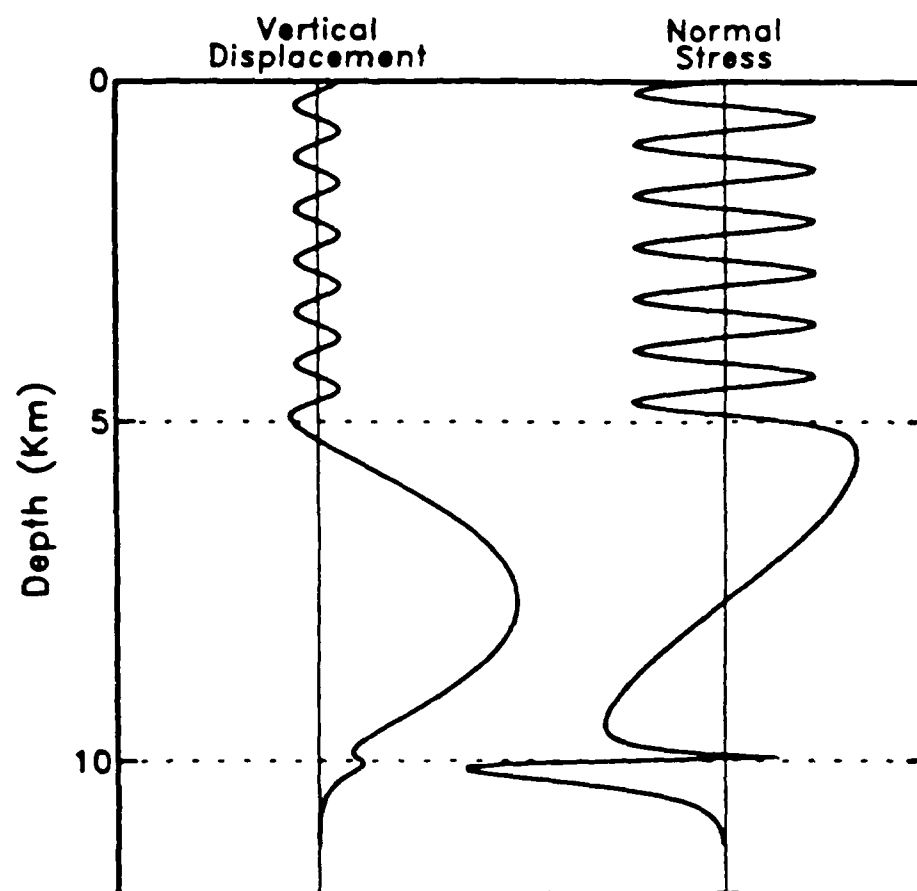


Figure 3-5. Vertical displacement and normal stress eigenfunctions for a two layer over a half space structural model. Layer interfaces are at depths of five and ten km. These eigenfunctions were generated using a stabilized version of the Thomson-Haskell matrix method. The constraint equations were applied at five and ten km depths.

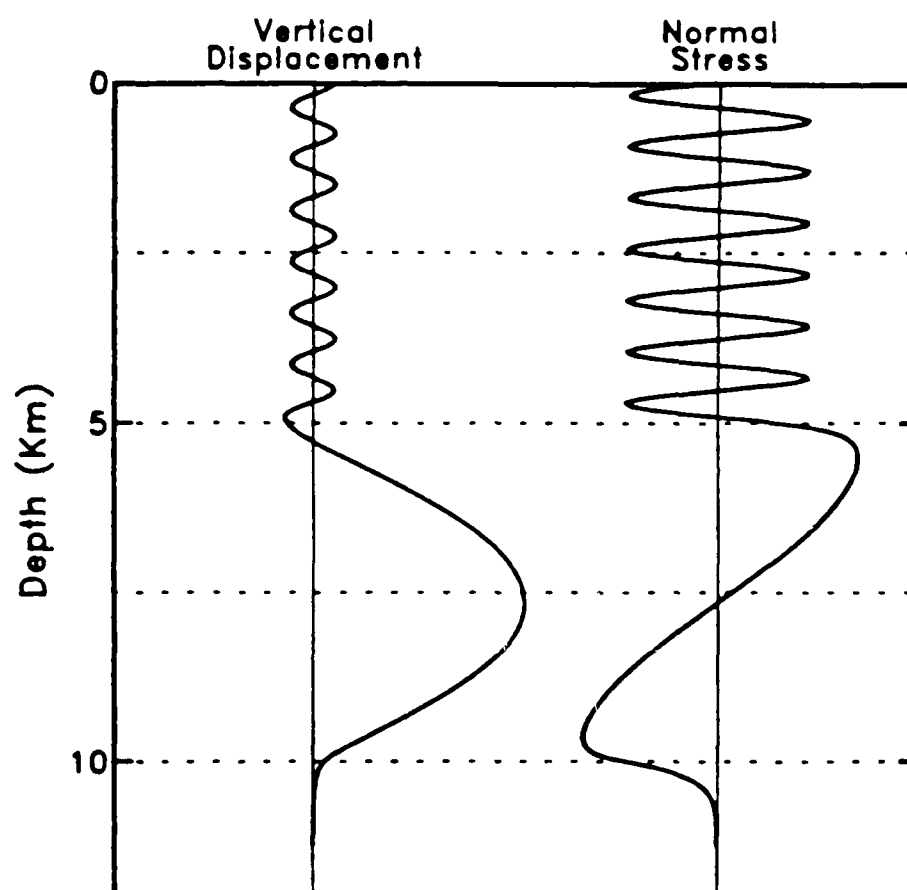


Figure 3-6. Vertical displacement and normal stress eigenfunctions for a two layer over a half space structural model. Layer interfaces are at depths of five and ten km. These eigenfunctions were generated using a stabilized version of the Thomson-Haskell matrix method. The constraint equations were applied at 2.5, 5.0, 7.5, and 10.0 km depths.

$$h_{\max} = \frac{R_n^c}{\omega \sqrt{1 - (R_n^c/\alpha)^2}} \ln(G_{\max}) \quad (3.2.5)$$

where  $h_{\max}$  is the maximum pseudo-layer thickness for a layer with P-wave velocity  $\alpha$  at frequency  $\omega$  and for a normal mode with eigenphase velocity  $R_n^c$ .  $G_{\max}$  in this equation refers to the maximum amplification factor permitted which for double precision computations should be set to about  $10^7$ . I first find the eigenvalues without pseudo-layering since this is not necessary for computing the minor matrix elements. I then relayer the structure using equation (3.2.5) to determine the pseudo-layer thicknesses. For layers which are thinner than  $h_{\max}$  this is not necessary and for layers which require additional pseudo-layers, I split the layer into pseudo-layers with identical thicknesses which are less than or equal to  $h_{\max}$  so that I can use the same propagator matrix for each pseudo-layer. Obviously for layers where the eigenphase velocity is greater than the P-wave velocity pseudo-layering is not necessary. Also it is obvious that the pseudo-layering need only be done down to the depth of the deepest source or receiver. After the pseudo-layering is completed I recompute the minor matrix elements at each layer and pseudo-layer interface. Finally I apply the method described earlier to compute the eigenfunctions at the desired depths.

I have used the method described in this section to compute eigenfunctions and synthetic seismograms for a wide variety of structural models, source depths, receiver ranges and frequency bandwidths. As long as the structural model does not contain liquid layers or strong low velocity zones this method works very well regardless of the complexity of the structural model or the frequency bandwidth. However, I was never able to know for sure whether the eigenfunctions which I computed were numerically

accurate and ultimately it was the appearance and characteristics of the resulting synthetic seismograms which verified these computations. The one exception to this was for the surface values of the eigenfunctions. By using equation (3.2.4) I was able to compute the two stress eigenfunctions at the surface which had to be zero in order to meet the free surface boundary condition. If this was not the case then either the eigenvalue was in error or one or more of the minor matrix elements were in error.

I first encountered non-zero surface stress eigenfunctions when computing the normal modes for crust and upper mantle structural models which had lithospheric low velocity zones. This occurred at high frequencies and for normal modes which corresponded to trapped energy within the low velocity zone and evanescence above and below the low velocity zone. In every case where this occurred the mode amplitude factor (equation 2.5.74) was of the order of the computer word roundoff and so for typical source and receiver depths the modal contributions to the synthetic seismograms were negligible. What appeared to be happening is that whenever a mode became effectively decoupled from the free surface, its surface eigenfunctions were in error. Thus the only time this presented a problem was when both sources or receivers were in or close to the low velocity zone which normally did not occur with earthquake and nuclear explosion seismology.

There is one other researcher who has produced a method for computing model synthetic seismograms which is functionally similar to my own method as described in this section and that is Kerry (1981). Kerry's method is based upon the work done by Kennett and Kerry (1979) which avoids the computation of stress-displacement eigenfunctions and instead uses a complicated formulation involving generalized reflection and

transmission coefficients. Although he has formulated the problem along different lines which he claims eliminates all possibility of numerical problems due to growing exponential solutions, Kerry's method suffers from exactly the same problem as my own. He is not able to accurately compute the modal contributions due to trapped channel modes within lithospheric low velocity zones. He states several times in his paper that it is necessary to effectively ignore the contributions due to trapped channel waves at high frequencies and that this is not a problem as long as either source or receiver is at or near the free surface.

My original objective was to develop a method for computing modal synthetic seismograms which were numerically accurate for a wide variety of structural models and frequency bandwidths. Although I had developed a method which was adequate for standard problems involving continental earthquake seismology, my method suffered restrictions when applied to exploration seismology in which shallow low velocity zones were of interest and my method failed when applied to oceanic structures which had liquid layers at the surface. These failures always occurred whenever the surface energy of a given mode was vanishingly small. In these cases the starting values of the eigenfunctions were in error and so the eigenfunctions at depth were also in error since they were obtained through recursive computations which were initialized by the surface values. Another problem with the method given in this section was that even in cases where the surface eigenfunctions appeared to be alright, I could never be sure that the eigenfunctions at depth were accurate since I had no independent check of their accuracy and since the computational method tended to produce stable looking eigenfunctions even when they were wrong.

With these shortcomings in mind I embarked on an undertaking which had as its objective the development of an algorithm for computing the depth eigenfunctions which was numerically accurate under all circumstances and which had independent checks of numerical accuracy. In order to accomplish this I felt that the recursive algorithm used in this section had to be abandoned and replaced by a method which would directly compute the eigenfunctions at a given depth and in the next section I describe the results of my research in this regard.

### 3.3 Computation of the Rayleigh Eigenfunctions: II - A More Robust Method

In both the standard method and my own simple method given in the previous section the fundamental procedure for computing modal solutions is the same. Eigenfunctions at the surface are first computed. We can think of these eigenfunctions as including both the unnormalized eigenfunctions (those resulting from setting  $E_1 = 1$ ) and the amplitude factor  $A$ , given by equation (2.5.74), which as I will show later normalizes the surface eigenfunctions. The values of the eigenfunctions at the source and receiver depths are then computed using a recursive algorithm which is initialized with the surface eigenfunctions. Finally equation (2.5.72) is used to compute the contribution for each mode. The only difference between my own method and the standard method is in the recursive algorithm which is used to compute the eigenfunctions at depth.

Because of the nature of the recursive algorithms, multiplicative error factors in the surface solutions will be carried along at all depths throughout the structure. In most cases where modes are trapped within low velocity channels or along liquid-solid interfaces as Stoneley waves, the

surface excitation is very small and it is possible for the surface starting values to have large multiplicative errors as the exact solutions for the eigenfunctions go to zero. One obvious solution to this problem is to compute the starting solution at some depth other than the free surface and in particular at a depth where the mode is energetic.

Let us consider the stress-displacement vector,  $\{y\}$ , at some depth  $z$  which is above the source at depth  $z_s$ . From equations (2.5.28), (2.5.29) and (2.5.31) we can write the following.

$$[^TD(z)] \{y(z)\} = \{0\} \quad (3.3.1)$$

and,

$$[^BD(z)] \{y(z)\} = [^BD(z)] [A(z, z_s)] \{\Sigma\} \quad (3.3.2)$$

We will drop the  $z$  and  $z_s$  in the rest of this development and note that the  $[D]$  matrix elements and the  $\{y\}$  vector elements are evaluated at depth  $z$  and the  $[A]$  matrix is evaluated from  $z$  to  $z_s$ . From equation (3.3.1) and the definitions of the minor matrix elements we can relate the  $y_3$  and  $y_4$  elements to the  $y_1$  and  $y_2$  elements as follows.

$$\begin{Bmatrix} y_3 \\ y_4 \end{Bmatrix} = \frac{1}{T\bar{M}_5} \begin{bmatrix} -T\bar{M}_3 & +T\bar{M}_2 \\ +T\bar{M}_2 & +T\bar{M}_4 \end{bmatrix} \begin{Bmatrix} y_1 \\ y_2 \end{Bmatrix}, \quad (3.3.3)$$

where the  $\{\bar{M}\}$  elements are related to the minor matrix elements by equations (3.1.19). Equation (3.3.3) is the same as the constraining relation (3.2.4) except that it is being applied to the stress-displacement vector and it is an expression of the boundary condition at the top of the structure. In the rest of this development we will also be dropping the  $-$  over the  $M$  and

let the single subscript be a shorthand notation for the two subscripts of the  $[M]$  matrix.

Equation (3.3.3) can be substituted into (3.3.2) to give the following.

$$[C] \begin{Bmatrix} y_1 \\ y_2 \end{Bmatrix} = [B_D] [A] \{\Sigma\} \quad (3.3.4)$$

where  $[C]$  is a two by two matrix whose elements are as follows.

$$C_{11} = B_{D11} - \frac{T_{M3}}{T_{M5}} B_{D13} + \frac{T_{M2}}{T_{M5}} B_{D14} \quad (3.3.5)$$

$$C_{12} = B_{D12} + \frac{T_{M2}}{T_{M5}} B_{D13} + \frac{T_{M4}}{T_{M5}} B_{D14}$$

$$C_{21} = B_{D21} - \frac{T_{M3}}{T_{M5}} B_{D23} + \frac{T_{M2}}{T_{M5}} B_{D24}$$

$$C_{22} = B_{D22} + \frac{T_{M2}}{T_{M5}} B_{D23} + \frac{T_{M4}}{T_{M5}} B_{D24}$$

The  $[C]$  matrix can be inverted to obtain a solution for the  $y_1$  and  $y_2$  elements at any depth.

$$\begin{Bmatrix} y_1 \\ y_2 \end{Bmatrix} = \frac{1}{\Delta} \begin{bmatrix} -C_{22} & -C_{12} \\ -C_{21} & -C_{11} \end{bmatrix} [B_D] [A] \{\Sigma\} \quad (3.3.6)$$

where

$$\Delta = C_{11}C_{22} - C_{12}C_{21} \quad (3.3.7)$$



Equation (3.3.6) is a more general form of equation (2.5.54) and allows us to compute the integrand solutions for the two displacement elements of the stress-displacement vector at any depth. In this case  $\bar{\Delta}$  replaces the Rayleigh characteristic function,  ${}_R\Delta$ , which is evaluated at the surface and the  $[C]$  matrix replaces the first two columns of the  $[B_D]$  matrix evaluated at the surface. We can express (3.3.6) as follows.

$$\begin{Bmatrix} y_1 \\ y_2 \end{Bmatrix} = \frac{1}{\bar{\Delta}} [\bar{W}] [A] \{\Sigma\} \quad (3.3.8)$$

where

$$[\bar{W}] = \begin{bmatrix} +C_{22} & -C_{12} \\ -C_{21} & +C_{11} \end{bmatrix} [B_D] \quad (3.3.9)$$

Equation (3.3.8) is a general form of equation (2.5.57) and the  $[\bar{W}]$  matrix is a two by four which replaces the two by four matrix in equation (2.5.57).

From equations (3.3.5) and (3.3.7) along with the definitions of the minor matrix elements (2.5.56) and (3.1.19),  $\bar{\Delta}$  can be derived and is given below.

$$\begin{aligned} \bar{\Delta} = & B_{M_1} + \frac{1}{T_{M_5}} (T_{M_3} B_{M_4} - B_{M_3} T_{M_4} - 2 T_{M_2} B_{M_2}) \\ & - \frac{B_{M_5}}{(T_{M_5})^2} \left( (T_{M_2})^2 + T_{M_3} T_{M_4} \right) \end{aligned} \quad (3.3.10)$$

From equations (3.3.5) and (3.3.9) we can similarly derive the elements of  $[\bar{W}]$  which are as follows.

$$\begin{aligned} \bar{W}_{11} = \bar{\Delta} + \frac{B_{M_5}}{(T_{M_5})^2} \left( (T_{M_2})^2 + T_{M_3} T_{M_4} \right) \\ - \frac{1}{T_{M_5}} (T_{M_3} B_{M_4} + T_{M_2} B_{M_2}) \end{aligned} \quad (3.3.11)$$

$$\bar{W}_{12} = \frac{1}{T_{M_5}} (T_{M_2} B_{M_4} - B_{M_2} T_{M_4})$$

$$\bar{W}_{13} = \frac{1}{T_{M_5}} (T_{M_4} B_{M_5} - B_{M_4} T_{M_5})$$

$$\bar{W}_{14} = \frac{1}{T_{M_5}} (T_{M_5} B_{M_2} - B_{M_5} T_{M_2})$$

$$\bar{W}_{21} = \frac{1}{T_{M_5}} (T_{M_3} B_{M_2} - B_{M_3} T_{M_2})$$

$$\begin{aligned} \bar{W}_{22} = \bar{\Delta} + \frac{B_{M_5}}{(T_{M_5})^2} \left( (T_{M_2})^2 + T_{M_3} T_{M_4} \right) \\ - \frac{1}{T_{M_5}} (T_{M_4} B_{M_3} + T_{M_2} B_{M_2}) \end{aligned}$$

$$\bar{W}_{23} = \frac{1}{T_{M_5}} (T_{M_5} B_{M_2} - B_{M_5} T_{M_2})$$

$$\bar{W}_{24} = \frac{1}{T_{M_5}} (T_{M_5} B_{M_3} - B_{M_5} T_{M_3})$$

We have succeeded in eliminating the  $[D]$  matrix elements from equation (3.3.8) and replaced them with minor matrix elements corresponding to the top and bottom boundary conditions. We now need to eliminate the propagator matrix,  $[A]$ , and replace it with the eigenfunctions.

We can relate the two stress eigenfunctions to the two displacement eigenfunctions as follows.

$$\begin{Bmatrix} E_3 \\ E_4 \end{Bmatrix} = -\frac{1}{T_{M_5}} \begin{bmatrix} +T_{M_3} & -T_{M_2} \\ -T_{M_2} & -T_{M_4} \end{bmatrix} \begin{Bmatrix} E_1 \\ E_2 \end{Bmatrix} \quad (3.3.12)$$

Equation (3.3.12) is the same as the constraining relation (3.2.4) except that it is an expression of the top boundary condition. We can subtract equation (3.2.4) from (3.3.12) to obtain the following.

$$\begin{bmatrix} \left( \frac{B_{M_3}}{B_{M_5}} - \frac{T_{M_3}}{T_{M_5}} \right) & \left( \frac{T_{M_2}}{T_{M_5}} - \frac{B_{M_2}}{B_{M_5}} \right) \\ \left( \frac{T_{M_2}}{T_{M_5}} - \frac{B_{M_2}}{B_{M_5}} \right) & \left( \frac{T_{M_4}}{T_{M_5}} - \frac{B_{M_4}}{B_{M_5}} \right) \end{bmatrix} \begin{Bmatrix} E_1 \\ E_2 \end{Bmatrix} = \begin{Bmatrix} 0 \\ 0 \end{Bmatrix} \quad (3.3.13)$$

Equation (3.3.13) is true at all depths but only at eigenphase velocities and from this equation we can derive expressions for the depth dependent ellipticity,  $\tilde{\epsilon}$ , as follows.

$$\begin{aligned} \tilde{\epsilon}(z) = \frac{E_2(z)}{E_1(z)} = & + \frac{(T_{M_3} B_{M_5} - B_{M_3} T_{M_5})}{(T_{M_2} B_{M_5} - B_{M_2} T_{M_5})} \\ & - \frac{(T_{M_2} B_{M_5} - B_{M_2} T_{M_5})}{(T_{M_4} B_{M_5} - B_{M_4} T_{M_5})} \end{aligned} \quad (3.3.14)$$

From equations (3.2.4) and (3.3.12) we can also write the following.

$$\frac{E_3}{E_1} = -\frac{T_{M_3}}{T_{M_5}} + \tilde{\epsilon} \frac{T_{M_2}}{T_{M_5}} = -\frac{B_{M_3}}{B_{M_5}} + \tilde{\epsilon} \frac{B_{M_2}}{B_{M_5}} \quad (3.3.15)$$

$$\frac{E_4}{E_1} = + \frac{T_{M_2}}{T_{M_5}} + i \frac{T_{M_4}}{T_{M_5}} = + \frac{B_{M_2}}{B_{M_5}} + i \frac{B_{M_4}}{B_{M_5}} \quad (3.3.16)$$

We can now relate the elements of the  $[\tilde{W}]$  matrix to the eigenfunctions at that depth. Once again it should be pointed out that these relations are only true at phase velocities corresponding to normal modes for which  $\tilde{\Delta} = 0$ . So from equations (3.3.11), (3.3.14), (3.3.15) and (3.3.16) we can write the following.

$$\left. \frac{\tilde{W}_{11}}{\tilde{W}_{13}} \right|_{k=RK(n,\omega)} = - \frac{E_3(z)}{E_1(z)} \quad (3.3.17)$$

$$\left. \frac{\tilde{W}_{12}}{\tilde{W}_{13}} \right|_{k=RK(n,\omega)} = - \frac{E_4(z)}{E_1(z)}$$

$$\left. \frac{\tilde{W}_{14}}{\tilde{W}_{13}} \right|_{k=RK(n,\omega)} = + \frac{E_2(z)}{E_1(z)}$$

$$\left. \frac{\tilde{W}_{21}}{\tilde{W}_{23}} \right|_{k=RK(n,\omega)} = - \frac{E_3(z)}{E_1(z)}$$

$$\left. \frac{\tilde{W}_{22}}{\tilde{W}_{23}} \right|_{k=RK(n,\omega)} = - \frac{E_4(z)}{E_1(z)}$$

$$\left. \frac{\tilde{W}_{24}}{\tilde{W}_{23}} \right|_{k=RK(n,\omega)} = + \frac{E_2(z)}{E_1(z)}$$

$$\left. \frac{\tilde{W}_{23}}{\tilde{W}_{13}} \right|_{k=RK(n,\omega)} = - \frac{E_2(z)}{E_1(z)}$$

These equations allow us to express the  $[\tilde{W}]$  matrix as follows.

$$[\tilde{W}] \Big|_{\mathbf{k}=\mathbf{R}K(n,\omega)} = \frac{1}{T_{M_5}} (T_{M_4} B_{M_5} - B_{M_4} T_{M_5}) \cdot \quad (3.3.18)$$

$$\begin{bmatrix} -\frac{E_3}{E_1} & -\frac{E_4}{E_1} & +1 & +\frac{E_2}{E_1} \\ -\frac{E_3 E_2}{E_1^2} & -\frac{E_4 E_2}{E_1^2} & +\frac{E_2}{E_1} & +\frac{E_2^2}{E_1^2} \end{bmatrix}$$

The numerator vector elements defined in equation (2.5.62) can be defined at depth as follows.

$$\begin{Bmatrix} y_1(z) \\ y_2(z) \end{Bmatrix} = \frac{1}{\tilde{\Delta}(z)} \begin{Bmatrix} \tilde{N}_1(z) \\ \tilde{N}_2(z) \end{Bmatrix} \quad (3.3.19)$$

Finally we can write the numerator vector elements evaluated at eigenphase velocities as follows.

$$\begin{Bmatrix} \tilde{N}_1(z) \\ \tilde{N}_2(z) \end{Bmatrix} \Big|_{\mathbf{k}=\mathbf{R}K(n,\omega)} = \frac{1}{T_{M_5}} (T_{M_4} B_{M_5} - B_{M_4} T_{M_5}) \cdot \quad (3.3.20)$$

$$\begin{bmatrix} -\frac{E_3}{E_1} & -\frac{E_4}{E_1} & +1 & +\frac{E_2}{E_1} \\ -\frac{E_3 E_2}{E_1^2} & -\frac{E_4 E_2}{E_1^2} & +\frac{E_2}{E_1} & +\frac{E_2^2}{E_1^2} \end{bmatrix} \cdot \begin{Bmatrix} A(z, z_s) \\ \Sigma \end{Bmatrix} \Big|_{\mathbf{k}=\mathbf{R}K(n,\omega)}$$

Equation (3.3.20) is a general form of equation (2.5.63) and if we let  $z = 0$

these two equations are identical.

We can follow the development given by equations (2.5.64) through (2.5.67) to eliminate the propagator matrix. The two elements of  $\{\tilde{N}\}$  in equation (3.3.20) can be expressed as follows using equation (2.5.61).

$$\begin{aligned} \tilde{N}_1(z) \Big|_{k=R K(n,\omega)} &= \frac{1}{T_{M_5}} (T_{M_4} B_{M_5} - B_{M_4} T_{M_5}) \cdot \\ &\cdot \frac{1}{E_1(z)} [-E_3(z) - E_4(z) E_1(z) E_2(z)] \cdot \\ &\cdot \begin{bmatrix} +A_{33}(z_s, z) & +A_{43}(z_s, z) & -A_{13}(z_s, z) & -A_{23}(z_s, z) \\ +A_{34}(z_s, z) & +A_{44}(z_s, z) & -A_{14}(z_s, z) & -A_{24}(z_s, z) \\ -A_{31}(z_s, z) & -A_{41}(z_s, z) & +A_{11}(z_s, z) & -A_{21}(z_s, z) \\ -A_{32}(z_s, z) & -A_{42}(z_s, z) & +A_{12}(z_s, z) & +A_{22}(z_s, z) \end{bmatrix} \{\Sigma\} \Big|_{k=R K(n,\omega)} \end{aligned} \quad (3.3.21)$$

$$\tilde{N}_2(z) \Big|_{k=R K(n,\omega)} = \frac{E_2(z)}{E_1(z)} \tilde{N}_1(z) \Big|_{k=R K(n,\omega)} \quad (3.3.22)$$

Using the rearranged  $\{\bar{\Sigma}\}$  vector given by equation (2.5.66) we can now write the numerator vector as follows.

$$\begin{aligned} \begin{bmatrix} {}_R \tilde{N}_1(z) \\ {}_R \tilde{N}_2(z) \\ {}_R \tilde{N}_3(z) \\ {}_R \tilde{N}_4(z) \end{bmatrix} \Big|_{k=R K(n,\omega)} &= \frac{(T_{M_4}(z) B_{M_5}(z) - B_{M_4}(z) T_{M_5}(z))}{T_{M_5}(z)} \Big|_{k=R K(n,\omega)} \cdot \\ &\cdot \left( {}_R \bar{\Sigma}(n,\omega) \{ {}_R \hat{E}(n,\omega, z_s; z) \} \right) \{ {}_R \hat{E}(n,\omega, z; z) \} \end{aligned} \quad (3.3.23)$$

where  $\{ {}_R \hat{E} \}$  is a version of the Rayleigh eigenfunctions which is "normal-

ized" at some arbitrary depth,  $z_N$ , and is as follows.

$$\{ {}_R \tilde{E}(n, \omega, z; z_N) \} = \frac{1}{{}_R E_1(n, \omega, z_N)} \{ {}_R E(n, \omega, z) \} \quad (3.3.24)$$

Obvious corollaries are given below.

$$\{ \tilde{E}(z_N; z_N) \} = \begin{Bmatrix} 1 \\ E_2(z_N)/E_1(z_N) \\ E_3(z_N)/E_1(z_N) \\ E_4(z_N)/E_1(z_N) \end{Bmatrix} \quad (3.3.25)$$

$$\{ \tilde{E}(z; 0) \} = \{ E(z) \}$$

$$\{ \tilde{E}(z_2; z_N) \} = [A(z_2, z_1)] \{ \tilde{E}(z_1; z_N) \} \quad (3.3.26)$$

Equation (3.3.26) allows us to express the numerator vector given by (3.3.23) at receiver depth,  $z_r$ , but still allow us to normalize the eigenfunctions at some arbitrary depth,  $z_N$ , and this is given as follows.

$$\{ {}_R \hat{N}(z_r) \} \Big|_{k=R K(n, \omega)} = \frac{(T_{M_4}(z_N) B_{M_5}(z_N) - B_{M_4}(z_N) T_{M_5}(z_N))}{T_{M_5}(z_N)} \Big|_{k=R K(n, \omega)} \cdot \left( [{}_R \Sigma(n, \omega)] \{ {}_R \tilde{E}(n, \omega, z_s; z_N) \} \right) \{ {}_R \tilde{E}(n, \omega, z_r; z_N) \} \quad (3.3.27)$$

Finally we can write down the frequency dependent displacements at some receiver location  $(r_r, \theta_r, z_r)$  in a manner similar to equation (2.5.72) as follows.

$$\begin{aligned} {}_R u(\omega, r_r, \theta_r, z_r) = & -R_\alpha I - R_\beta I \\ & - i \sum_n \sum_m \left( k {}_R \tilde{A}(n, \omega, z_N) [{}_R \Sigma(n, \omega, m)] \{ {}_R \tilde{E}(n, \omega, z_s; z_N) \} \right) \end{aligned} \quad (3.3.28)$$

$$\cdot {}_R \tilde{\Psi}(n, \omega, m, r_r, \theta_r, z_r; z_N)$$

where  ${}_R \tilde{A}$  is a depth dependent amplitude factor similar to  ${}_R A$  in equation (2.5.74) and is given below.

$${}_R \tilde{A}(n, \omega, z_N) = \frac{(T M_4(z_N) B M_5(z_N) - B M_4(z_N) T M_5(z_N))}{T M_5(z_N) \partial \hat{\Delta}(z_N) / \partial k} \Big|_{k = {}_R K(n, \omega)} \quad (3.3.29)$$

and  ${}_R \tilde{\Psi}$  is defined as follows.

$$\begin{aligned} {}_R \tilde{\Psi}(n, \omega, m, z_r, \theta_r, z_r; z_N) = & {}_R \tilde{E}_1(n, \omega, z_r; z_N) \hat{P}(n, \omega, m, r_r, \theta_r) + \\ & + {}_R \tilde{E}_2(n, \omega, z_r; z_N) \hat{B}(n, \omega, m, r_r, \theta_r) \end{aligned} \quad (3.3.30)$$

We have succeeded in deriving modal solutions which depend only on the minor matrix elements and eigenfunctions which can be normalized at any depth. The values of the eigenfunction vector  $\{\tilde{E}\}$  can always be computed at the normalization depth,  $z_N$ , using equations (3.3.25), and (3.3.14) to (3.3.16). Using this as a starting solution the recursive method I described in the previous section can be used to compute the eigenfunctions at the source and receiver depths. Whenever the source and receiver are at the same depth we can directly compute the modal solutions by setting the normalization depth to the source and receiver depth. We can use this method for computing modal synthetic seismograms for oceanic structural models for which receivers are on the ocean bottom and the sources are within the oceanic crust. For this example the normalization depth is chosen to be equal to the ocean bottom depth at which energy levels, corresponding to trapped modes on or close to the solid-liquid interface, will be suitably high.



Although I have referred to the eigenfunctions as being normalized, I have used this word rather loosely in that the normalization is completely arbitrary and is accomplished by setting the first element of the eigenfunction vector to unity at some specified depth. The specification of the normalization depth must be made prior to computing the eigenfunctions and sometimes it is not obvious how this depth should be chosen. It would be desirable to normalize the eigenfunctions in some integral norm sense with respect to depth which would eliminate the necessity for choosing a normalizing depth while at the same time allowing accurate computations of the eigenfunctions. In order to do this let us consider a solution for one mode from equations (3.3.28), (3.3.29) and (3.3.30). We could express the normalization depth dependent part of this solution as follows.

$$S(z_r; z_s) = \tilde{A}(z_N) \tilde{E}_1(z_r; z_N) \tilde{E}_1(z_s; z_N) \quad (3.3.31)$$

Although I have referred to this as the part of the solution which is dependent on the normalization depth, clearly the final modal solution itself is independent of the normalization depth and only the individual factors on the right hand side of the equation show any dependence on  $z_N$ . Since the solution is independent of the normalization depth it would be desirable to rewrite the right hand side of the equation as follows.

$$S(z_r; z_s) = \bar{E}_1(z_r) \bar{E}_2(z_s) \quad (3.3.32)$$

In this equation  $\bar{E}$  refers to eigenfunctions which have been normalized in some different manner than  $\tilde{E}$ . Since we can choose the normalizing depth arbitrarily, we can write equation (3.3.31) as follows using equation (3.3.25).

$$S(z_r; z_s) = \tilde{A}(z_r) \tilde{E}_1(z_s; z_r) \quad (3.3.33)$$

and

$$S(z_r; z_s) = \hat{\Lambda}(z_s) \hat{E}_1(z_r; z_s) \quad (3.3.34)$$

We can also show the following from equation (3.3.24).

$$\hat{E}_1(z_s; z_r) = 1/\hat{E}_1(z_r; z_s) \quad (3.3.35)$$

Combining equations (3.3.33), (3.3.34) and (3.3.35) we arrive at the following.

$$S^2(z_r; z_s) = \hat{\Lambda}(z_r) \hat{\Lambda}(z_s) \quad (3.3.36)$$

Comparing this to equation (3.3.32) produces the following result.

$$\bar{E}_1^2(z_r) \bar{E}_1^2(z_s) = \hat{\Lambda}(z_r) \hat{\Lambda}(z_s) \quad (3.3.37)$$

Since (3.3.37) must be true for all source and receiver depths we can write the following.

$$\bar{E}_1^2(z) = \hat{\Lambda}(z) \quad (3.3.38)$$

$$|\bar{E}_1(z)| = \sqrt{\hat{\Lambda}(z)} \quad (3.3.39)$$

We have finally succeeded in deriving normalized eigenfunctions which do not depend on a normalization depth. It should be once again pointed out that all of the eigenfunctions given here are similar and conform to the following rules.

$$\frac{E_i(z)}{E_j(z)} = \frac{\hat{E}_i(z)}{\hat{E}_j(z)} = \frac{\bar{E}_i(z)}{\bar{E}_j(z)} \quad (3.3.40)$$

where

$$i, j = 1, 2, 3, 4$$

We can compute the magnitude of the first element of  $\{\bar{E}\}$  at any depth using equations (3.3.39) and (3.3.29). We can then compute the other elements of  $\{\bar{E}\}$  using equations (3.3.14), (3.3.15) and (3.3.16). This then gives us a method for computing normalized eigenfunctions to within a factor of plus or minus one at any depth as a functions of minor matrix elements only.

The frequency dependent displacement solutions from equation (3.3.28) can be expressed in terms of  $\{\bar{E}\}$  as follows.

$$\begin{aligned} {}_R u(\omega, r_r, \theta_r, z_r) = & -R\alpha^I - R\beta^I \\ & - i \sum_n \sum_m \left( k [{}_R \Sigma(n, \omega, m)] \{ {}_R \bar{E}(n, \omega, z_s) \} {}_R \Psi(n, \omega, m, r_r, \theta_r, z_r) \right) \end{aligned} \quad (3.3.41)$$

where,

$$\begin{aligned} {}_R \bar{\Psi}(n, \omega, m, z_r, \theta_r, z_r) = & {}_R \bar{E}_1(n, \omega, z_r) \dot{P}(n, \omega, m, r_r, \theta_r) + \\ & {}_R \bar{E}_2(n, \omega, z_r) \dot{B}(n, \omega, m, r_r, \theta_r) \end{aligned} \quad (3.3.42)$$

The problem is completely reduced to evaluating the eigenfunction vector,  $\{\bar{E}\}$ . From equation (3.3.38) we can see that this evaluation amounts to computing  $\bar{\Lambda}$  at the source and receiver depths. In order to simplify the expression for  $\bar{\Lambda}$  given by equation (3.3.29) we first need to derive a general relation which exists among the elements of the minor matrix. Consider equations (2.5.27) which constrain the elements of the stress-displacement vector and which are valid at all frequencies and phase velocities. We can extend these equations to any depth to give the following constraining relations.

$$[{}^T D(z)] \{ {}^T v(z) \} = \{ 0 \} \quad (3.3.43)$$

$$[B_D(z)] \{B_v(z)\} = \{0\}$$

In these equations the vectors  $\{T_v\}$  and  $\{B_v\}$  simply refer to some depth dependent vectors which can be equal to the stress-displacement vector or the stress-displacement vector minus the source jump vector propagated to depth  $z$  depending on whether  $z$  is above or below the source depth. Equations (3.3.43) are the same as the constraining relations for the eigenfunctions which are expressed by equation (3.2.3) except that equations (3.3.43) are valid at all phase velocities and obviously  $\{T_v\} = \{B_v\} = \{E\}$  at eigenphase velocities.

As we did with the eigenfunctions, we can relate the three and four elements of  $\{v\}$  to the one and two elements as follows.

$$\begin{pmatrix} v_3 \\ v_4 \end{pmatrix} = \begin{bmatrix} -\frac{M_3}{M_5} & +\frac{M_2}{M_5} \\ +\frac{M_2}{M_5} & +\frac{M_4}{M_5} \end{bmatrix} \begin{pmatrix} v_1 \\ v_2 \end{pmatrix} \quad (3.3.43)$$

We have dropped the T and B superscripts to indicate that equation (3.3.43) is valid in both cases. We can just as easily relate the one and two elements to the three and four elements directly from equations (3.3.43) as follows.

$$\begin{aligned} \begin{pmatrix} v_1 \\ v_2 \end{pmatrix} &= - \begin{bmatrix} D_{11} & D_{12} \\ D_{21} & D_{22} \end{bmatrix}^{-1} \begin{bmatrix} D_{13} & D_{14} \\ D_{23} & D_{24} \end{bmatrix} \begin{pmatrix} v_3 \\ v_4 \end{pmatrix} \\ &= + \begin{bmatrix} -\frac{M_4}{M_1} & -\frac{M_2}{M_1} \\ -\frac{M_2}{M_1} & -\frac{M_3}{M_1} \end{bmatrix} \begin{pmatrix} v_3 \\ v_4 \end{pmatrix} \end{aligned} \quad (3.3.44)$$

Comparing equations (3.3.43) and (3.3.44), the following must be true.

$$\begin{bmatrix} +\frac{M_4}{M_1} & -\frac{M_2}{M_1} \\ -\frac{M_2}{M_1} & -\frac{M_3}{M_1} \end{bmatrix}^{-1} = \begin{bmatrix} -\frac{M_3}{M_5} & +\frac{M_2}{M_5} \\ +\frac{M_2}{M_5} & +\frac{M_4}{M_5} \end{bmatrix} \quad (3.3.45)$$

This equations leads to the final result which is given below for both top and bottom minor matrix elements.

$$\begin{aligned} T_{M_1}(z)T_{M_5}(z) + T_{M_2}^2(z) - T_{M_3}(z)T_{M_4}(z) &= 0 \\ B_{M_1}(z)B_{M_5}(z) + B_{M_2}^2(z) - B_{M_3}(z)B_{M_4}(z) &= 0 \end{aligned} \quad (3.3.46)$$

Equations (3.3.46) are true at all frequencies, phase velocities and depths and effectively eliminate one of the five linearly independent minor matrix elements. Unfortunately since these equations are non-linear, we cannot reduce the  $[R]$  matrix down to a four by four, however we can use the equations as an independent check on the numerical accuracy of the minor matrix elements at any frequency, phase velocity or depth.

We can use equations (3.3.46) directly to simplify the expression for the Rayleigh characteristic function given by equation (3.3.10) as follows.

$$\begin{aligned} {}_R\bar{\Delta} = T_{M_5} \hat{\Delta} = T_{M_1}B_{M_5} + B_{M_1}T_{M_5} + 2T_{M_2}B_{M_2} + \\ + T_{M_3}B_{M_4} + B_{M_3}T_{M_4} \end{aligned} \quad (3.3.47)$$

This equation can also be written as follows using equations (3.3.46).

$$\begin{aligned} {}_R\bar{\Delta} = T_{M_5} \hat{\Delta} = - (T_{M_1} - B_{M_1})(T_{M_5} - B_{M_5}) - (T_{M_2} - B_{M_2})^2 \\ - (T_{M_3} - B_{M_3})(T_{M_4} - B_{M_4}) \end{aligned} \quad (3.3.48)$$

We can readily verify equations (3.3.46) at the top and bottom of the structure for boundary conditions given by equations (3.1.10) through (3.1.14). We can also derive certain relations among the elements of the  $[R]$  matrix which must be true in order for equations (3.3.46) to hold at all depths. Using equation (3.1.18) we can write the following.

$$\begin{aligned}
 M_1(z_2)M_5(z_2) + M_2^2(z_2) + M_3(z_3)M_4(z_2) &= \quad (3.3.49) \\
 &= \sum_{i=1}^5 \left( R_{1i}R_{5i} + R_{2i}^2 + R_{3i}R_{4i} \right) M_1^2(z_1) + \\
 &+ \sum_{i=1}^4 \left( \sum_{j=i+1}^5 \left( R_{1i}R_{5j} + R_{1j}R_{5i} + 2R_{2i}R_{2j} + R_{3i}R_{4j} + R_{3j}R_{4i} \right) M_1(z_1)M_j(z_1) \right)
 \end{aligned}$$

where all of the  $[R]$  matrix elements go from  $z_1$  to  $z_2$ . We know that equation (3.3.49) must be equal to zero which gives us a starting point for deriving the following relations among the elements of the  $[R]$  matrix.

$$R_{12}R_{52} + R_{22}^2 - R_{32}R_{42} = 1 \quad (3.3.50)$$

$$R_{11}R_{55} + R_{15}R_{51} + 2R_{21}R_{25} + R_{31}R_{45} + R_{35}R_{41} = 1$$

$$R_{13}R_{54} + R_{14}R_{53} + 2R_{23}R_{24} + R_{33}R_{44} + R_{34}R_{43} = 1$$

$$R_{1i}R_{5i} + R_{2i}^2 + R_{3i}R_{4i} = 0, \quad i = 1, 3, 4, 5$$

$$\begin{aligned}
 R_{11}R_{5i} + R_{1i}R_{51} + 2R_{21}R_{2i} + R_{31}R_{4i} + R_{3i}R_{41} &= 0, \\
 i &= 2, 3, 4
 \end{aligned}$$

$$\begin{aligned}
 R_{12}R_{5i} + R_{1i}R_{52} + 2R_{22}R_{2i} + R_{32}R_{4i} + R_{3i}R_{42} &= 0, \\
 i &= 3, 4, 5
 \end{aligned}$$

$$R_{1i}R_{55} + R_{15}R_{5i} + 2R_{25}R_{2i} + R_{3i}R_{45} + R_{35}R_{4i} = 0, \\ i = 4, 5$$

Equations (3.3.50) give us fifteen non-linear relations among the fifteen linearly independent elements of the  $[R]$  matrix and they allow us to make an important statement regarding the Rayleigh characteristic functions given by equation (3.3.48). Using these relations we can show that  $\bar{\Delta}$  is independent of depth.

$$\bar{\Delta}(z_1) = \bar{\Delta}(z_2) \quad (3.3.51)$$

We can now go back and rewrite  $\bar{\Delta}$  from equation (3.3.29) as follows.

$${}_R\bar{\Delta}(n, \omega, z) = \frac{(T_{M_4}(z)B_{M_5}(z) - B_{M_4}(z)T_{M_5}(z))}{\partial_R \bar{\Delta}(\omega, k) \partial k} \Big|_{k = {}_R K(n, \omega)} \quad (3.3.29)$$

Finally using equation (3.3.38) along with (3.3.14), (3.3.15) and (3.3.16) we can derive the following expressions for the normalized eigenfunctions.

$$(3.3.53)$$

$${}_R\bar{E}_1^2(n, \omega, z) = {}_R\bar{\Delta}(n, \omega) (T_{M_4}(\omega, k, z)B_{M_5}(\omega, k, z) - B_{M_4}(\omega, k, z)T_{M_5}(\omega, k, z)) \Big|_{k = {}_R K(n, \omega)}$$

$${}_R\bar{E}_2^2(n, \omega, z) = {}_R\bar{\Delta}(n, \omega) (T_{M_5}(\omega, k, z)B_{M_3}(\omega, k, z) - B_{M_5}(\omega, k, z)T_{M_3}(\omega, k, z)) \Big|_{k = {}_R K(n, \omega)}$$

$${}_R\bar{E}_3^2(n, \omega, z) = {}_R\bar{\Delta}(n, \omega) (T_{M_3}(\omega, k, z)B_{M_1}(\omega, k, z) - B_{M_3}(\omega, k, z)T_{M_1}(\omega, k, z)) \Big|_{k = {}_R K(n, \omega)}$$

$${}_R\bar{E}_4^2(n, \omega, z) = {}_R\bar{\Delta}(n, \omega) (T_{M_1}(\omega, k, z)B_{M_4}(\omega, k, z) - B_{M_1}(\omega, k, z)T_{M_4}(\omega, k, z)) \Big|_{k = {}_R K(n, \omega)}$$

where,

$${}_R\bar{A}(n, \omega) = \frac{1}{\partial_R \Delta(\omega, k) / \partial k} \Big|_{k={}_RK(n, \omega)} \quad (3.3.54)$$

We can also derive the following relations which involve products of the eigenfunction vector elements.

$$\begin{aligned} &{}_R E_1(n, \omega, z) {}_R E_2(n, \omega, z) \\ &= {}_R\bar{A}(n, \omega) ({}^T M_5(\omega, k, z) B M_2(\omega, k, z) - B M_5(\omega, k, z) {}^T M_2(\omega, k, z)) \Big|_{k={}_RK(n, \omega)} \end{aligned} \quad (3.3.55)$$

$$\begin{aligned} &{}_R \bar{E}_2(n, \omega, z) {}_R E_3(n, \omega, z) \\ &= {}_R\bar{A}(n, \omega) ({}^T M_2(\omega, k, z) B M_3(\omega, k, z) - B M_2(\omega, k, z) {}^T M_3(\omega, k, z)) \Big|_{k={}_RK(n, \omega)} \end{aligned}$$

$$\begin{aligned} &{}_R E_1(n, \omega, z) {}_R E_4(n, \omega, z) \\ &= {}_R\bar{A}(n, \omega) ({}^T M_4(\omega, k, z) B M_2(\omega, k, z) - B M_4(\omega, k, z) {}^T M_2(\omega, k, z)) \Big|_{k={}_RK(n, \omega)} \end{aligned}$$

$$\begin{aligned} &{}_R \bar{E}_3(n, \omega, z) {}_R E_4(n, \omega, z) \\ &= {}_R\bar{A}(n, \omega) ({}^T M_1(\omega, k, z) B M_2(\omega, k, z) - B M_1(\omega, k, z) {}^T M_2(\omega, k, z)) \Big|_{k={}_RK(n, \omega)} \end{aligned}$$

Equations (3.3.53) allow us to compute the four P-SV eigenfunctions to within factors of plus or minus one at any depth within the structure directly as a function of minor matrix elements without the direct use of the propagator matrix. Equations (3.3.55) will allow us to compute the signs of the eigenfunction vector elements relative to one of the elements. These equations also allow us to make independent checks of numerical



accuracy at any depth since they must be consistent with equation (3.3.53). However we are still left with a one hundred and eighty degree phase ambiguity for the eigenfunction vector as a whole and this ambiguity must be resolved whenever the source and receiver are at different depths.

My purpose for the development in this section was to provide a way for computing eigenfunctions at depth directly as a function of minor matrix elements which had independent checks for verifying numerical accuracy. Although I have come very close to this objective, I am frustrated by the phase ambiguity in my derived solutions. This ambiguity is resolved by using the propagator matrix and the details of the numerical algorithm, which uses as its basis the results of this section, will be given in the last section of this chapter. Before giving this however, I will make the derivations complete by showing eigenvalue and eigenfunction relations for SH and acoustic waves in a manner and notation which is consistent with those used for P-SV waves.

### 3.4 Computation of the Love and Acoustic Eigenvalues and Eigenfunctions

Love wave model synthesis has never suffered from numerical stability problems to the extent that Rayleigh waves have and so SH modal synthetics are rather common in the literature. For this reason I have not emphasized the SH case and have given SH derivations only in the interest of presenting a complete solution for the case of elastic wave propagation. With this in mind I will simply write down the SH modal solutions in terms of eigenfunctions which are normalized in a manner similar to the Rayleigh eigenfunctions.

Love wave eigenvalues are defined whenever the Love characteristic function is zero which is repeated below from equation (2.5.46).

$${}_L\Delta(\omega, k) = - {}_L^B D_1(\omega, k, 0)$$

Since the  ${}_L D$  matrix for Love waves is in fact a two element row vector, we can consider the two elements of  ${}_L D$  to be functionally equivalent to the Rayleigh minor matrix elements. The values of  ${}_L D$  at different depths are computed directly by using the two by two Love propagator matrix. In this case there is no need to derive an equivalent  ${}_L R$  matrix. The Love eigenfunction vector has only two elements, however we can relate the stress eigenfunction to the displacement eigenfunction in a manner similar to the Rayleigh eigenfunction relation. We can thus write a final solution for SH waves as follows.

$$\begin{aligned} {}_L u(\omega, r_r, \theta_r, z_r) = & - {}_L \beta I \\ & - i \sum_n \sum_m \left( k {}_L \Sigma(n, \omega, m) \{ {}_L \bar{E}(n, \omega, z_s) \} {}_L \Psi(n, \omega, m, r_r, \theta_r, z_r) \right) \end{aligned} \quad (3.4.1)$$

where  ${}_L \Sigma$  is given by equation (2.5.70) and

$${}_L \Psi(n, \omega, m, r_r, \theta_r, z_r) = {}_L \bar{E}_1(n, \omega, z_r) \hat{C}(n, \omega, m, r_r, \theta_r) \quad (3.4.2)$$

and  $\{ {}_L \bar{E} \}$  is a two component eigenfunction vector which has been normalized in a manner similar to the Rayleigh eigenfunction vector and is given below.

$${}_L \bar{\Delta}(\omega, k) = {}_L^T D_2(\omega, k, z) {}_L^B D_1(\omega, k, z) - {}_L^B D_2(\omega, k, z) {}_L^T D_1(\omega, k, z) \quad (3.4.3)$$

$${}_L\bar{A}(n,\omega) = \frac{1}{\partial {}_L\bar{\Delta}(\omega,k)/\partial k} \bigg|_{k={}_LK(n,\omega)} \quad (3.4.4)$$

$${}_L\bar{E}_1^2(n,\omega,z) = {}_L\bar{A}(n,\omega) {}_L^TD_2(\omega,k,z) {}_L^BD_2(\omega,k,z) \bigg|_{k={}_LK(n,\omega)} \quad (3.4.5)$$

$${}_L\bar{E}_2^2(n,\omega,z) = {}_L\bar{A}(n,\omega) {}_L^TD_1(\omega,k,z) {}_L^BD_1(\omega,k,z) \bigg|_{k={}_LK(n,\omega)} \quad (3.4.6)$$

$${}_L\bar{E}_1(n,\omega,z) {}_L\bar{E}_2(n,\omega,z) = \quad (3.4.7)$$

$$- {}_L\bar{A}(n,\omega) {}_L^TD_1(\omega,k,z) {}_L^BD_2(\omega,k,z) \bigg|_{k={}_LK(n,\omega)}$$

$$- {}_L\bar{A}(n,\omega) {}_L^TD_2(\omega,k,z) {}_L^BD_1(\omega,k,z) \bigg|_{k={}_LK(n,\omega)}$$

Modal synthesis for purely acoustic structures is very similar to SH modal synthesis. Once again the  $[{}_AD]$  matrix is in fact a two element row vector with the elements being functionally equivalent to the P-SV minor matrix elements. Also, as with Love waves, the two by two acoustic propagator matrix is used directly to compute  $[{}_AD]$  at different depths. The fundamental difference between acoustic and Love waves is that the modal solution for acoustic waves contains the same vector cylindrical harmonic components as for P-SV waves and in fact we can consider acoustic waves to be a special case of P-SV waves. Thus, whereas Love eigenfunctions are

completely decoupled from Rayleigh eigenfunctions and can exist simultaneously with Ray eigenfunctions at the same eigenphase velocity, acoustic eigenfunctions are completely coupled with Rayleigh eigenfunctions and the acoustic modal solution is identical in form to the solution for Rayleigh waves given by equations (3.3.41) and (3.3.42). Whenever a layer within a structure is acoustic the Rayleigh eigenfunction vector becomes an acoustic eigenfunction vector which still has four components corresponding to vertical and horizontal displacement and normal and shear stress. However in acoustic layers the fourth eigenfunction vector component (shear stress) is identically zero at all depths within that layer and the horizontal displacement and normal stress components (elements two and three) are linearly related (equation 2.4.48) as shown below.

$$\{ {}_A \bar{E}(n, \omega, z) \} = \begin{Bmatrix} {}_R \bar{E}_1(n, \omega, z) \\ {}_R \bar{E}_3(n, \omega, z) \end{Bmatrix} \quad (3.4.8)$$

$${}_R \bar{E}_4(n, \omega, z) = 0, \text{ for acoustic layers}$$

$${}_R \bar{E}_2(n, \omega, z) = - \frac{1}{\rho c^2} {}_R \bar{E}_3(n, \omega, z), \text{ for acoustic layers}$$

The equations for the normalized acoustic eigenfunctions are identical to those for Love waves. Thus for an acoustic layer the P-SV eigenfunctions are as follows.

$${}_R \bar{\Delta}(\omega, k) = {}_A^T D_2(\omega, k, z) {}_A^B D_1(\omega, k, z) - {}_A^B D_2(\omega, k, z) {}_A^T D_1(\omega, k, z) \quad (3.4.9)$$

$${}_R \bar{\Lambda}(n, \omega) = \frac{1}{\partial {}_R \bar{\Delta}(\omega, k) / \partial k} \bigg|_{k = {}_R K(n, \omega)}$$

$${}_R \bar{E}_1^2(n, \omega, z) = {}_R \bar{A}(n, \omega) \left. {}_A D_2(\omega, k, z) {}_A^B D_2(\omega, k, z) \right|_{k = {}_R K(n, \omega)} \quad (3.4.10)$$

$${}_R \bar{E}_2^2(n, \omega, z) = {}_R \bar{A}(n, \omega) \left. {}_A D_1(\omega, k, z) {}_A^B D_1(\omega, k, z) \right|_{k = {}_R K(n, \omega)} \quad (3.4.11)$$

$${}_R \bar{E}_1(n, \omega, z) {}_R \bar{E}_2(n, \omega, z) = \quad (3.4.12)$$

$$- {}_R \bar{A}(n, \omega) \left. {}_A D_1(\omega, k, z) {}_A^B D_2(\omega, k, z) \right|_{k = {}_R K(n, \omega)}$$

$$- {}_R \bar{A}(n, \omega) \left. {}_A D_2(\omega, k, z) {}_A^B D_1(\omega, k, z) \right|_{k = {}_R K(n, \omega)}$$

The case of most interest to seismologists which involves acoustic layers is whenever acoustic layers coexist with elastic layers in the same structural model. Oceanic models are a good example of this and I will be using oceanic structures as examples of numerically stable eigenfunction computations as well as complete modal synthetic seismograms. When computing the P-SV eigenfunctions as well as the modal solutions within a structure with both acoustic and elastic layers, one simply uses the appropriate relations which I have given previously depending on the depth. In chapter two I gave the interface boundary conditions at solid-liquid interfaces and these are repeated below in terms of the minor matrix elements.

1. For a solid to liquid interface:

$$\begin{aligned} {}_A D_1 &= + {}_R \bar{M}_1 \\ {}_A D_2 &= - {}_R \bar{M}_4 \end{aligned} \quad (3.4.13)$$

2. For a liquid to solid interface:

$$\begin{aligned} {}_R \bar{M}_1 &= 0 \\ {}_R \bar{M}_2 &= 0 \\ {}_R \bar{M}_3 &= {}_A D_1 \\ {}_R \bar{M}_4 &= 0 \\ {}_R \bar{M}_5 &= {}_A D_2 \end{aligned} \quad (3.4.14)$$

At this point I have developed all of the elastic wave theory necessary for computing modal synthetic seismograms for SH elastic, P-SV elastic, acoustic and mixed acoustic-elastic problems. In the final section of this chapter I will give the details of the numerical algorithm used to compute the eigenfunctions.

### 3.5 Rayleigh Eigenfunctions: The Final Numerical Algorithm

The first check of the accuracy of equations (3.3.53) for computing the normalized eigenfunctions is the infinite homogeneous half space structure which we used previously. Once again an exact analytic solution is available which allows us to compute an error function of depth. Figure 3-7 shows the vertical displacement and normal stress eigenfunctions plotted on a logarithmic (base 10) scale along with their associated error functions also plotted on a logarithmic (base 10) scale. In this case we renormalized the eigenfunctions such that the vertical displacement at the surface was unity so as to allow ready comparison with figures 3-1 to 3-3, otherwise equations (3.3.53) were used directly to compute the eigenfunctions. The heavy lines in figure 3-7 refer to the exact solution and the lighter lines are the direct results of equations (3.3.53).

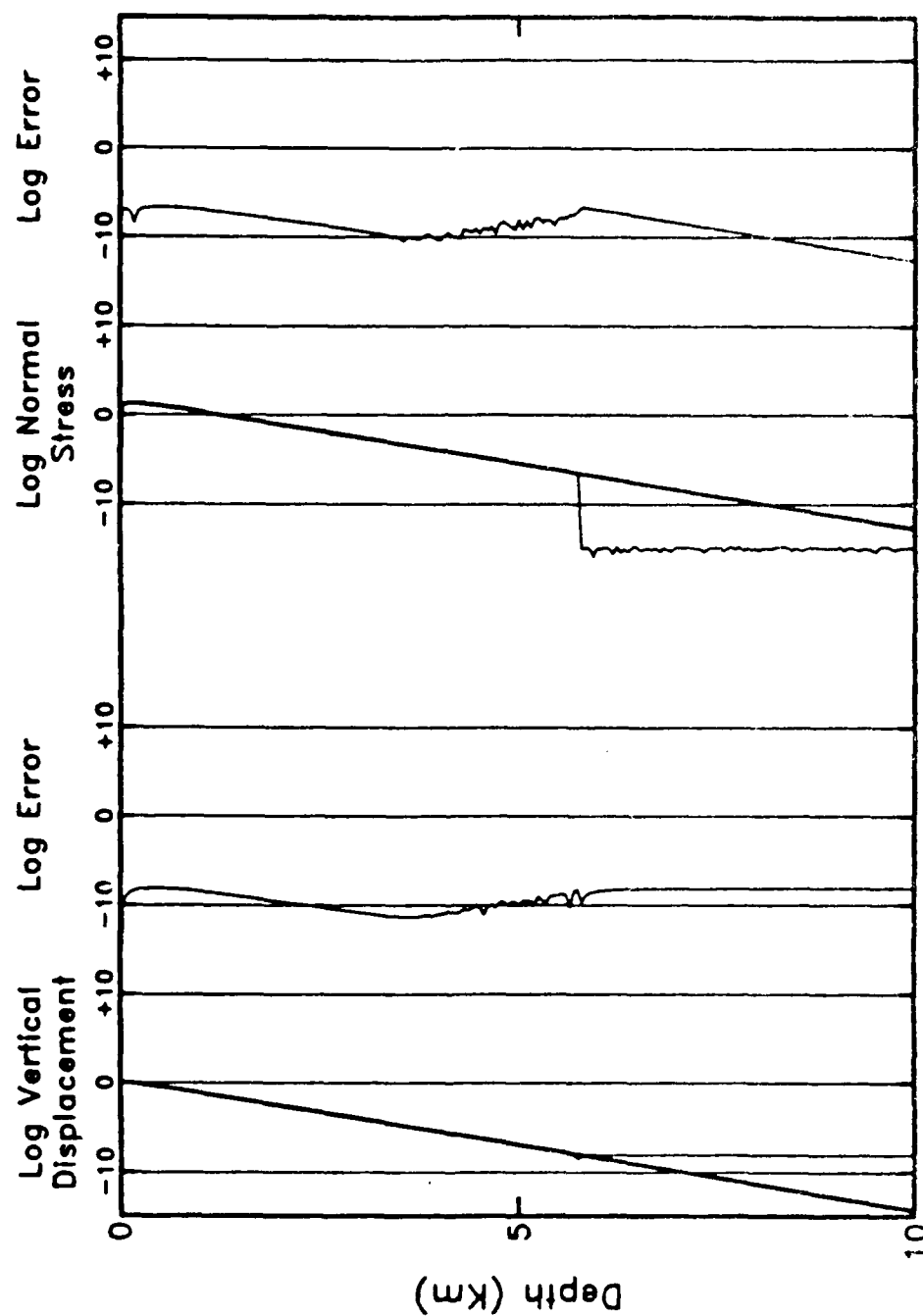


Figure 3-7. Vertical displacement and normal stress eigenfunctions for an infinite homogeneous half space. The thick lines represent the exact solution and the thin lines were generated using equations (3.3.53)

It is apparent that the log error never gets larger than  $10^{-8}$  of the maximum value of the vertical displacement or shear stress. However, when compared to figure 3-3, the errors shown in figure 3-7 are larger at depths below five km. It appears from figure 3-7 that the error at all depths is scaled by the maximum value of the eigenfunctions at a single depth and the scale factor is about  $10^{-8}$ . Since all of the computations given by equation (3.3.53) involve square roots to determine the eigenfunctions themselves, this error translates into roundoff errors of  $10^{-16}$  for the squared eigenfunctions which is the double precision word roundoff error. It is very likely that if we had done the computations in single precision the error factor for the eigenfunctions would have been about  $10^{-4}$ .

The next check of the accuracy of the new method is the two layer model which was used in figures 3-4 to 3-6 and the results of this are shown in figure 3-8. This figure shows the vertical displacement and normal stress eigenfunctions versus depth plotted on a linear scale and error functions of depth plotted on a logarithmic (base 10) scale. In this case the heavy lines refer to the previous solutions shown in figure 3-6 which for this comparison is considered to be a close approximation to the exact solution. The eigenfunctions given by equations (3.3.53) overlay the heavy lines and thus do not appear separately. The error functions are computed by differencing the eigenfunctions from equations (3.3.53) with those obtained by the simple method of section 3.2 and they are given as a ratio of the vertical displacement eigenfunction at the surface which has been set to unity to preserve the comparison. As with the infinite homogeneous half space, the errors for this two layer model tend to be constant with depth and are scaled by the maximum value of the eigenfunctions with the scale factor



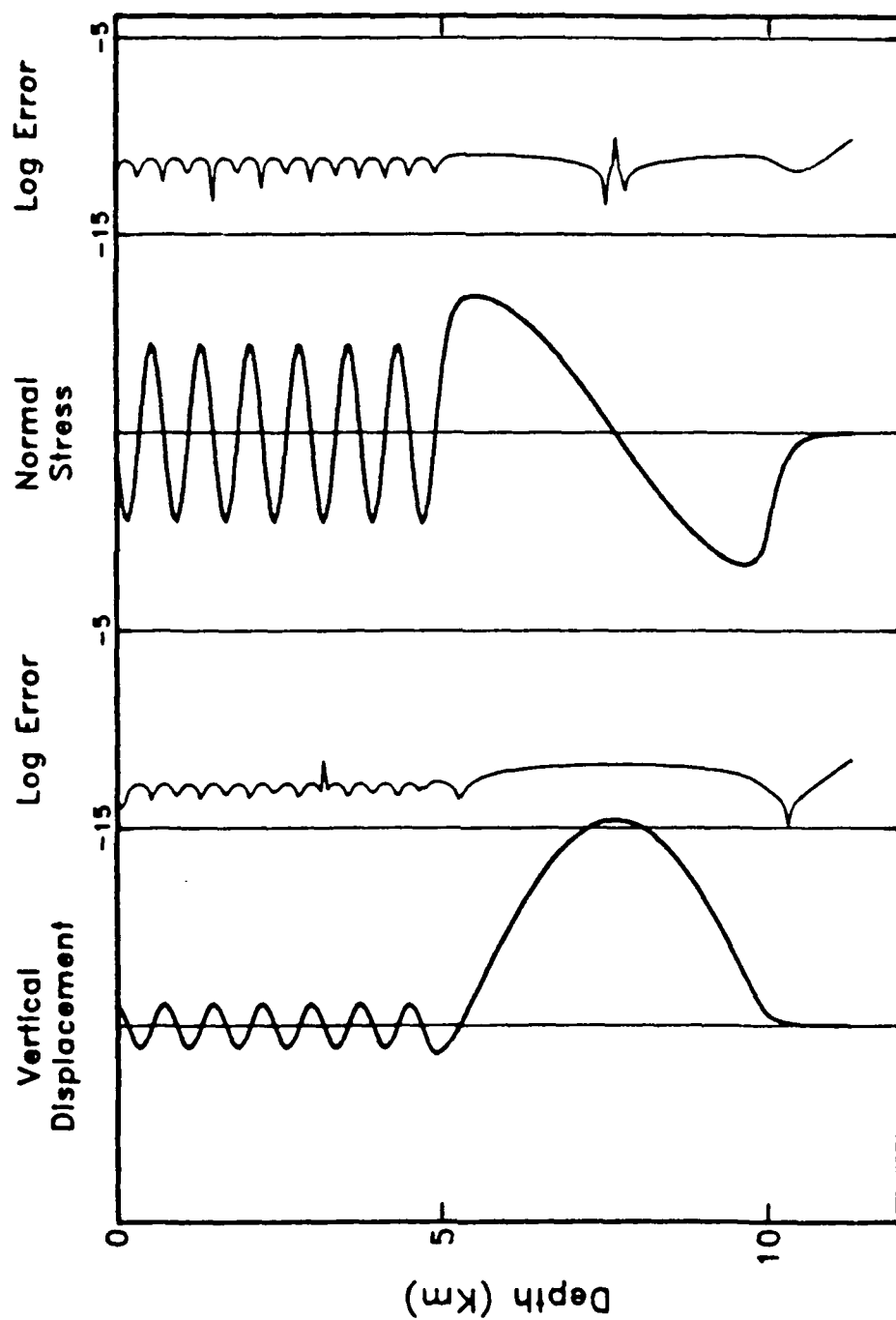


Figure 3-8. Vertical displacement and normal stress eigenfunctions for a two layer over a half space structural model. Layer interfaces are at depths of five and ten km. These eigenfunctions were generated using equations (3.3.53).

being about  $10^{-8}$ .

The eigenfunctions shown in figure 3-8 were computed fundamentally in the same manner as those shown in figure 3-7 using equations (3.3.53). However due to the oscillatory nature of the eigenfunctions it was necessary to resolve the one hundred and eighty degree phase ambiguity which is inherent in the solutions. This was done by first using the propagator matrix to compute estimates of the two displacement eigenfunctions at each depth value. The largest of these two values was then used to determine the sign of that eigenfunction at each depth. Equations (3.3.55) were then used to compute the relative signs of the other three eigenfunctions and the signs of these eigenfunctions were set appropriately. In no instances were the actual numeric values of the eigenfunctions which were estimated from the propagator matrix actually used as the final output eigenfunctions and the use of the propagator matrix was solely to determine the eigenfunction sign with depth relationship. Unfortunately, because of the use of the propagator matrix, it was necessary, as with the simple method, to employ pseudo-layering so that the estimated eigenfunctions were not in error.

If one compares figures 3-1 to 3-3 and figure 3-7 it would seem that the new method for computing eigenfunctions is less accurate than the simpler recursive method described in section 3.2. Although this is true for an infinite homogeneous half space, in general this will not be the case and for certain types of structural models the recursive method will fail completely. It is simple to explain why the recursive method works so well for the infinite homogeneous half space if we examine the constraining relation used in the recursive method. This relation insures that the Sommerfeld radiation condition is met at the bottom of the structure and for an infinite

homogeneous half space this forces the growing exponential solutions with depth to be identically zero at all depths where the constraining relation is applied. Thus the errors for the recursive method in this case tend to be scaled at each depth by the correct value of the eigenfunction which exponentially decays with depth. The errors for the new method, however, appear to be relatively constant with depth and are scaled by the maximum value of the eigenfunctions over the entire depth of the structural model. Thus when the correct eigenfunction solutions decay to less than about  $10^{-8}$  of the maximum value, then the computed eigenfunctions are in error.

The recursive method works at least as well as the new method for structural models which involve no liquid layers and which have monotonically increasing P and S wave velocities with depth. Since the new method is computationally more expensive than the recursive method, it is desirable to use the recursive method whenever possible and I have used this method to compute eigenfunctions for a wide variety of structural models which basically conform to the restrictions given previously. Even in cases where weak low velocity zones exist, such as lithospheric low velocity zones, the recursive method works quite well as long as neither source nor receiver is within the low velocity zone. By computing the surface stress values from the constraining relation it is possible to check the numerical accuracy for each mode computation and whenever the surface stress values become too large the modal contribution for that mode is ignored. The recursive method when used in this manner becomes functionally identical to the method developed by Kerry (1981) both in terms of the manner by which the channel modes are identified (by checking the surface stress values) and by the way channel modes are taken into account (by ignoring them).

For more exotic structural models, such as structures with multiple strong low velocity zones or structures with both acoustic and elastic layers, the recursive method breaks down and the new method is the only way that I know of to compute numerically stable eigenfunctions. In order to demonstrate this I will first show results for a structural model which is an infinite homogeneous elastic half space which has embedded within it two low velocity layers. The half space has a P-wave velocity of 6 km/sec and a S-wave velocity of 3.5 km/sec. The two low velocity layers are each five km thick and have P-wave velocities of approximately 3 km/sec and S-wave velocities of approximately 1.75 km/sec. One of the low velocity layers is embedded with its top interface 5 km below the free surface and the second low velocity layer is embedded with its top interface 15 km below the free surface so that the final structural model consists of four 5 km thick layers over a half space with layers one and three having the same elastic parameters as the bottom half space and layers two and four being the low velocity channels.

In order to force the eigenvalues to be distinctly different for channel modes the P and S wave velocities for the lower channel were set to be slightly higher (by one part in  $10^5$ ) than those of the upper channel. Figure 3-9 shows computed eigenfunctions for the first two modes as a function of depth for this structural model at a frequency of seven Hertz. The thin lines on this plot represent the computed eigenfunctions using the recursive method and the thicker lines are the computed eigenfunctions using the new method. Once again these eigenfunctions are plotted on a logarithmic (base 10) scale in order to show the fine detail. In this case the true normalized ( $\{\bar{E}\}$ ) eigenfunctions are shown and for the recursive method the surface eigenfunctions were set equal to the normalized  $\{\bar{E}\}$  eigenfunctions at the

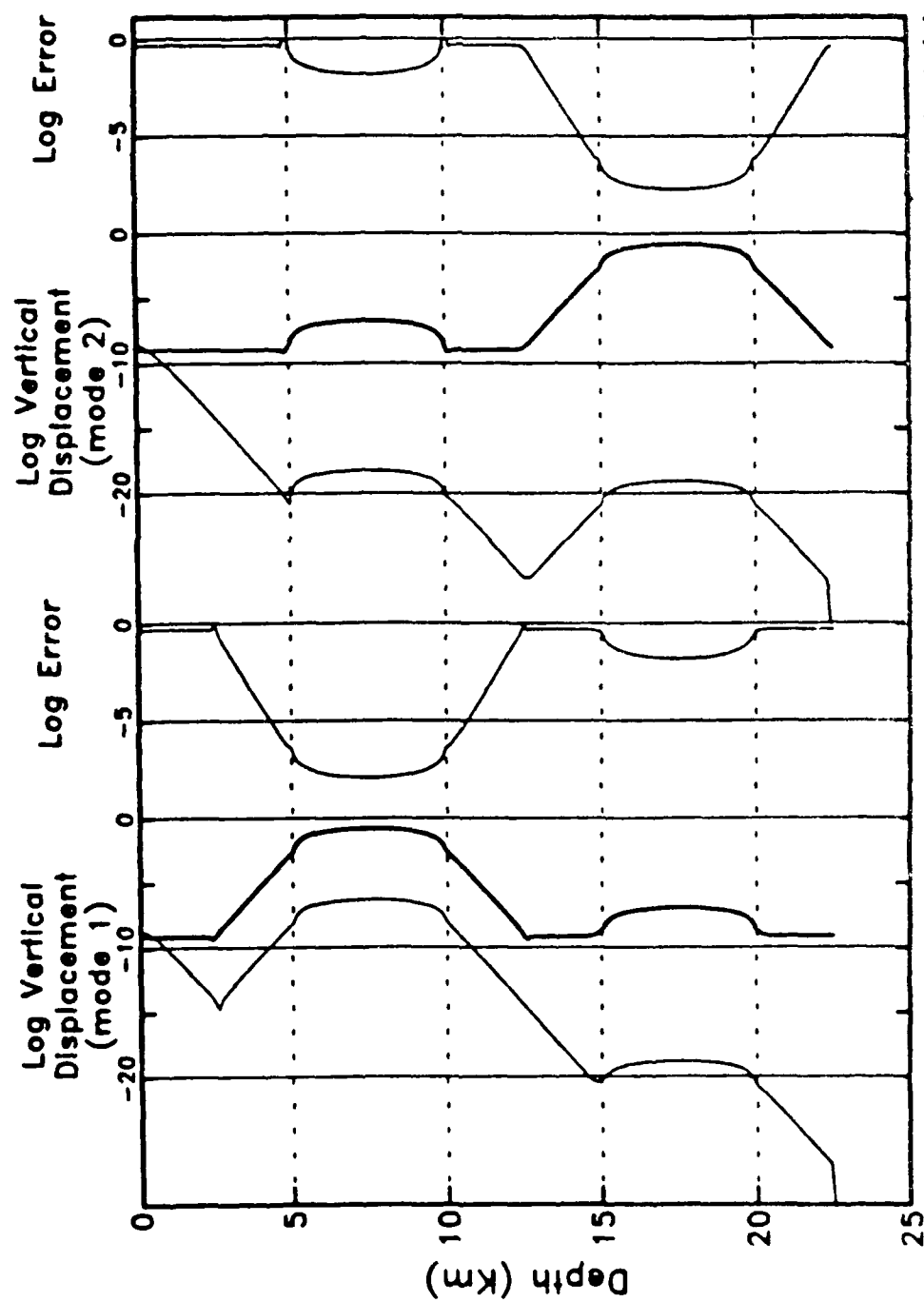


Figure 3-9. Vertical displacement eigenfunctions for a structural model with two buried low velocity layers. Layer interfaces are shown with the dashed lines. Eigenfunctions generated using the recursive method are shown with the thin lines and eigenfunctions generated from equations (3.3.53) are shown with the thick lines.

surface. Also shown in figure 3-9 are error plots on a logarithmic (base 10) scale for each mode. Since there was no exact or approximate correct solution to compare against these errors were computed by differencing the square of  $\bar{E}_1 \bar{E}_2$  as computed in equations (3.3.55) with the product of  $\bar{E}_1^2$  and  $\bar{E}_2^2$  as computed in equations (3.3.53). The square root of this difference is computed and the error is expressed as a ratio of that square root with  $\bar{E}_1^2 + \bar{E}_2^2$ . These error plots then show an independent check of the numerical accuracy of the computed eigenfunctions at each depth.

At high frequencies the first two modes correspond to SV channel modes which are trapped in the low velocity layers. The eigen phase velocities for both modes are slightly higher than the S wave velocities within the low velocity layers and thus the P waves are evanescent throughout the structure and S waves are propagating in the low velocity layers and evanescent in the surrounding high velocity layers. Since the P and S wave velocities in the upper low velocity layer are slightly less than those in the lower low velocity layer, the eigen phase velocities for the first two modes are distinctly separated, in the infinite frequency limit, and the two modes are "tuned" to each low velocity layer in turn.

In figure 3-9 we can see that the recursive method produced rather erratic looking eigenfunctions whereas the new method produced a pair of eigenfunctions which look like mirror images of each other. At a frequency of seven Hertz the two low velocity layers are effectively decoupled from the free surface and we would expect the eigenfunctions to be the same as those that would be obtained if the top boundary were replaced by an infinite half space. We would also expect the first two normal modes of such a structure to display a strong symmetry and so it seems likely that the

eigenfunctions produced by the new method are correct. The small values of the error functions in the regions where the peak values of the eigenfunctions occur would tend to verify this conclusion. As with the previous two examples, the eigenfunctions appear to be in error when they fall to about  $10^{-8}$  of the peak value and this also can be ascertained from the error functions. Even with this very ill conditioned example it would seem that the new method produces numerically stable eigenfunctions at depths where the normal mode is energetic.

The final algorithm which I developed uses equations (3.3.53) to compute the eigenfunctions and equations (3.3.55) to compute an error function with depth. I also pseudo-layer the structure and use the propagator matrix to determine the relative depth to depth eigenfunction signs. The error function is then checked at each interface and pseudo-interface and, if it is above some threshold value ( $10^{-2}$ ), then the four eigenfunctions at that depth are set to zero. We can see in figure 3-9 that applying this algorithm results in zero eigenfunction values for the first mode from the surface to about three km depth and from about twelve km depth on down. We would thus be eliminating the small amount of mode coupling that exists between the two low velocity layers at this frequency however mode coupling between these two layers will be much more pronounced at the lower frequencies where the proper coupling will be computed using my new method.

## CHAPTER IV

### NORMAL MODE SEISMOGRAM SYNTHESIS: THE NUMERICAL ALGORITHMS

Three component synthetic spectra due to Rayleigh and Love normal modes can be computed using equations (3.3.41) and (3.4.1) along with the equations for the normalized eigenfunctions. The fundamental mode Rayleigh and Love surface waves can be computed using these relations and low frequency synthetic Rayleigh and Love surface waves have been computed routinely since the early sixties. The synthesis of higher order normal modes has not been very common and the first direct comparison between mode sums and complete synthetic seismograms by direct wavenumber integration was by Swanger and Boore (1978). In this case only a few modes were included in the sum and most all of the comparisons were done with SH waves, however there was a remarkably good comparison. Even with just a few modes included, the modal summed synthetics showed features which would normally be attributed to geometric ray arrivals. However, as Swanger and Boore pointed out, it is impossible to obtain exact and complete solutions of the elastic wave equation using only normal modes for flat earth structural models which have an infinite half space on the bottom.

It is possible to represent the exact and complete solution of the elastic wave equation as an infinite sum of normal modes for spherical earth models. As the number of modes in the sum are increased the frequency bandwidth of the resulting synthetic seismograms is also increased and so a



mode sum involving a finite number of modes effectively places a frequency band limit on the resulting synthetic seismograms. As I showed in chapter two, the exact solution of the elastic wave equation for flat earth models which have a free top boundary and a bottom boundary which is an infinite homogeneous half space involves both a normal mode sum and branch cut integral contributions. Normally the branch cut integral contributions account for energy which cannot be represented as normal modes which have real eigenwavenumbers. This energy is typically associated with nearly vertically propagating P and S waves and part of this energy tends to "leak" away into the bottom half space. If we eliminate the bottom half space in a flat layered model and replace it with a free or fixed boundary, then the branch cuts are eliminated and, as in the spherical earth case, the complete and exact solution can be represented as an infinite mode sum. In this case the totally reflective bottom boundary eliminates the possibility of energy leaking out to infinite depth which turns this into a layered plate problem. The difficulty with plate problems is that the eigenwavenumbers of many plate modes are complex and they are quite difficult to locate in the complex wavenumber plane.

Modes which have real eigenwavenumbers correspond to trapped or locked modes and their energy stays within the layers above the half space and does not leak away into the half space. For flat layered half space structures the modes with real eigenwavenumbers can only occur to the right of the S-wave branch point on the real wavenumber axis. Thus the eigenphase velocities of such modes must be less than the S-wave velocity of the bottom half space. If we were to compute synthetic seismograms using only the locked modes then we might expect the resulting synthetics to be good approximations to the complete solution at the tail end of the seismic

coda where the slower arrivals would account for most of the energy. Certainly we would not expect the P-waves for such synthetics to be represented in the solution since for typical structural models the P-waves would travel at phase velocities higher than the S-wave velocity of the bottom half space. However if we allow our structural model to be very deep where the seismic velocities become high, we might be able to synthesize the P-waves in the layers near the surface where the P-wave velocity could be less than the S-wave velocity at the bottom of the structure. This is exactly what Kerry (1981) did when he computed synthetic seismograms using only the locked modes for a structural model which went to 1000 km depth where the S-wave velocity was close to eight km/sec. His synthetics included P-wave arrivals which traveled through the crust at velocities of between six and seven km/sec as well as most of the important S-wave arrivals which traveled throughout the structural model. He showed that nearly complete solutions could be obtained using only the locked modes as long as the structural model was very deep with resulting high S-wave velocities at the bottom.

Very thick structural models are relatively expensive to compute since the number of locked modes at a given frequency tends to be linearly related to the thickness of the model and since the number of layers needed to represent a structural model tends to increase with the model thickness. For those who are interested in wave propagation through the crust and upper mantle, it is not very attractive to use a structural model which goes down to depths of 1000 km, however this is necessary in order to trap energy associated with crustal P-waves. Even if we use very thick structural models there is an upper limit to S-wave velocities for realistic earth models which will place an upper limit on the phase velocities which we can

represent in a mode sum. Thus situations in which strong arrivals correspond to high phase velocities, such as strong motion synthetics where the receiver epicentral range is small compared to the source depth, cannot be adequately modeled using mode sums as long as real earth structures are used, regardless of the thickness of the structure.

In this chapter I will show how a simple modification to the structural model will allow complete synthetic seismograms to be computed from only the locked modes and without using thick structures. This method, which I call the locked mode approximation, produces synthetic seismograms to high frequencies and phase velocities and is especially useful for crust and upper mantle problems in the ten to five hundred km distance range. This method also runs significantly faster than comparable wavenumber integration computer programs and it allows timely and accurate results to be produced on a relatively small and slow computer.

In the following chapter I first describe the numerical algorithms which I developed to compute flat earth locked mode eigenvalues. This includes the development of a dynamic scaling method which gets around the problem of the large dynamic range of the elements of the minor matrix. Also included in this is the development of a searching algorithm which will find all locked modes at a given frequency in an efficient manner regardless of the complexity of the dispersion curves. Next I show how frequency dependent anelastic attenuation can be accounted for by deriving a first order perturbation of the eigen phase velocities. Then I will go into the details of the computer programs which produce locked mode synthetic seismograms from a starting structural model to the final three component synthetics at user specified receivers and for user specified sources. Next I will discuss in detail the locked mode approximation and show when the

approximation breaks down and how spurious arrivals caused by the approximation can be controlled. Finally I will show examples of locked mode synthetics and compare these against synthetics for the same structural models generated by other synthesis methods.

#### 4.1 Eigenvalue Computation: The Mode Searching Algorithm

Computing the Rayleigh and Love eigenvalues is the most time consuming part of the total task of computing locked mode synthetic seismograms. This is due to the implicit relationship between the phase velocity and the Rayleigh and Love characteristic functions which forces the use of a zero searching algorithm to find the eigenvalues. In general it is not possible to derive inverse characteristic functions analytically and so the phase velocity (or frequency) is changed in an iterative manner to cause the characteristic function to go to zero. A consequence of this implicit relationship between phase velocity and the characteristic functions is that generally one cannot be sure that all of the locked modes at a given frequency have been located. Modes which have been missed in the searching algorithm will produce incoherent errors in the final synthetic seismograms, assuming the missed modes are distributed randomly in the frequency-phase velocity domain, and even a small percentage of missed modes can render useless the final results. This should not be surprising if one considers the effect in the time domain of applying a small number of very narrow, uniformly distributed notch filters in the frequency domain spectrum of a time domain signal.

The first and foremost criterion for the mode searching algorithm is that it be reliable and by that I mean that the searching algorithm find all of the locked modes within a given frequency-phase velocity window. We

can usually devise reliable and simple searching algorithms by stepping the phase velocity at nearly infinitesimal increments and looking at the resulting characteristic functions. Such algorithms however are so inefficient from a computer time standpoint that they are practically useless. On the other end of the spectrum we can usually devise simple searching algorithms which are very efficient but which tend to miss modes especially when the dispersion curves form complicated and irregular patterns in the frequency-phase velocity domain. The speed of such algorithms is usually based on assumptions of simplicity and regularity of the dispersion curves and when this assumption is not true the algorithms become unreliable. There is an inherent inverse proportionality between reliability and efficiency of zero searching algorithms in general and finding the correct trade off between the two is an important part of solving the locked mode synthesis problem.

Unfortunately not much detailed information can be found in the literature regarding flat earth normal mode searching algorithms. It is a simple task to find the fundamental Rayleigh and Love normal mode eigenvalues as well as the first few higher order modes. The searching algorithms can be designed rather sloppily for these cases and still yield useful and inexpensive results. When hundreds of modes must be located over a wide frequency range however, accurate and inexpensive searching algorithms can be quite difficult to obtain and this can constitute the major effort of a modal synthesis program as it did in my own case.

The first and potentially the most important decision which must be made regarding the mode searching algorithm is which of the independent variables frequency and wavenumber (or phase velocity) is to be held constant and which is to be iterated to find the zeroes of the Rayleigh and Love characteristic functions. Traditionally the frequency is held constant

while the phase velocity is changed to find the eigenphase velocities. This is the method that I use and I will explain why I chose this method over other methods which have been used in the past.

The major effort in computing synthetic seismograms for flat layered earth models is the computation of the Fourier and Hankel inverse integral transforms for all times and distances of interest. The inverse Fourier transform of frequency can be evaluated in an efficient manner for all time values using the fast Fourier transform (FFT) algorithm. No such numerical technique exists, to my knowledge, for evaluating the inverse Hankel wavenumber transform and so it would seem reasonable to use the mode residues to approximate this integral. In order to use the FFT to evaluate the frequency integral one must sample in the frequency domain at equally spaced frequency increments starting at zero frequency and going out to the highest frequency of interest. The frequency increment used is inversely related to the time window of the resulting synthetic seismograms. One distinct advantage of using a FFT to compute the frequency integral is that the errors due to this particular numerical integration scheme are well understood and easily quantifiable. Sampling a continuous, analytic function in the frequency domain will produce aliasing in the time domain which will manifest itself as time wrap-around about the time window which is determined by the frequency sampling increment. The time window must be made large enough to include the entire seismic coda and when the coda becomes longer than the time window, wrap-around will superimpose the end of the coda on the beginning of the coda rendering that part of the synthetic seismogram useless. Thus a particular frequency sampling increment places an effective limit on the maximum source-receiver range which can be synthesized without significant aliasing in the time domain.

An alternative approach is to reverse the order of integration, use the mode residues to approximate the frequency integral and evaluate the inverse Hankel transform using some standard numerical integration method and this was done by Rosenbaum (1960). In this case the normal modes are found by fixing wavenumber and searching for eigenfrequencies. This technique avoids the problem of time aliasing however it introduces a number of problems associated with the wavenumber integral. If there are very many source-receiver distances of interest then the inverse Hankel transform can be expensive to compute and errors in the numerical integration are not well understood or quantifiable as in the case of the FFT. Although this approach can be used to handle certain problems involving very long seismic codas without aliasing in the time domain, this approach is much less efficient than the traditional method due to the necessity of computing the inverse Hankel transform numerically.

A third approach was used by Kerry (1981) and combines features of both the traditional method and the method used by Rosenbaum. The original order of integration is used so that the FFT is used to evaluate the frequency residue and the mode residues are used to approximate the wavenumber integral however, instead of searching for eigen phase velocities at fixed frequency values, a set of fixed phase velocity values are used and the mode searching is accomplished by searching in the frequency domain as Rosenbaum did. Kerry does this to increase the efficiency of the mode searching algorithm and he gives two reasons for this increase in efficiency. If one looks at the elements of the  $[R]$  matrix in equations (3.1.20) the only place the frequency appears is through the arguments of the trigonometric functions,  $\theta_\alpha$  and  $\theta_\beta$ . Thus a substantial portion of the algebra in these equations is only dependent on the layer elastic parameters and the

phase velocity. If one looks for normal modes by fixing phase velocity and searching in the frequency domain, all of the arithmetic which is independent of frequency can be done once and intermediate computations can be stored and used repeatedly at different frequency values. This results in a substantial decrease in the number of arithmetic operations required at different frequency values assuming the phase velocity remains fixed. The second reason Kerry gives for searching in the frequency domain is that for simple structural models with monotonically increasing velocities with depth, the dispersion curves are spaced in a regular manner in the frequency direction. This makes it easier to design a simple and efficient but reliable searching algorithm.

I rejected Rosenbaum's approach because in most cases that method is both inefficient and inaccurate due to the numerical wavenumber integration. I then decided to follow the traditional method and use the FFT to evaluate the frequency integral and the mode residues to evaluate the wavenumber integral however, instead of using Kerry's method to find the normal modes, I decided to search for normal modes in the phase velocity domain at fixed frequency values that would be used in the FFT. The approach used by Kerry necessitates the use of modal interpolation to resample the dispersion curves at the frequency values required by the FFT. A number of problems come about due to this interpolation and Kerry spends considerable effort in his paper discussing these problems and how he deals with them. The choice of the fixed phase velocities used in the mode search is arbitrary and to a certain extent the problem of choosing these phase velocities is similar to choosing the wavenumber values in a numerical integration of the inverse Hankel transform. If the phase velocity samples are too far apart then the interpolated modes will have large errors



and so, in order to insure accurate results, it is necessary for Kerry to take a conservative approach and use finely sampled phase velocity values. The net result of this is that he must locate and save more modes than would be necessary if one used the approach that I took (the example that Kerry gives in his paper represents three times the number of modes that I would have needed for the same structure and frequency bandwidth). The problem of accurate interpolation of normal modes is also very dependent on the particular structural model and frequency bandwidth used. The presence of a weak low velocity zone in the model that Kerry used caused a number of problems for him and had he used a complex structural model with stronger low velocity zones and to higher frequencies it is not at all clear that he would have been able to use his method successfully without using exceedingly fine phase velocity samples which would have reduced the efficiency even more than for the simpler structure.

As I have stated previously one of my major objectives in this research was to obtain an accurate means of computing synthetic seismograms for the widest possible range of structural models and frequency bandwidths. In the case of the mode searching algorithm I chose the most reliable and accurate course which had satisfactory efficiency. In view of the comments I made previously I am not sure that Kerry's mode searching algorithm is in fact more efficient than my own but I can guarantee that Kerry's algorithm is less accurate than mine because of his use of modal interpolation. The only sources of error with my method are the integration errors due to the FFT and the exclusion of the branch cut integral factors and I will show the manifestations of these errors later in this chapter.

Once the order of integration and order of mode searching has been established one must decide upon an overall strategy for the mode searching algorithm. There seem to be two basic strategies that have been used in the past and in the end I made use of both of these strategies. The first strategy, which I refer to as the zero searching strategy, is one where one variable (frequency in my case) is held fixed and the other variable (phase velocity in my case) is changed so as to find the zero crossings of the characteristic function. This strategy, if used alone, treats the searching of zeroes at each frequency in an entirely independent manner and it does not depend upon any sort of mode association from frequency to frequency. In order for this strategy to work, if used by itself, the zero searching algorithm must be very robust, reliable and be satisfactorily efficient. The second strategy which is commonly used is what I refer to as the pole tracking strategy. In this strategy a set of poles is found at some limiting value of frequency which is usually the highest frequency of interest. (Actually a zero searching strategy is necessary to initialize the pole tracking but the zero searching algorithm can be simple and relatively inefficient since it will only be used once at one frequency.) The dispersion curves are then followed along the frequency direction by using the slopes of the dispersion curves at each frequency to predict the eigen phase velocities at the next adjacent frequency. This strategy depends entirely upon mode association from frequency to frequency and this strategy breaks down whenever dispersion curves are misconnected between adjacent frequencies.

Wang and Herrmann (1980) have used the pole tracking strategy successfully in a hybrid seismogram synthesis method in which the mode residues are computed along with numerical approximations of the branch cut integrals and they claimed that the pole tracking strategy was much

more efficient than the zero searching strategy which seems to be the common wisdom on this subject. However, as with the examples given by Kerry, the structural models used by Wang and Herrmann were simple and the frequency bandwidths were not high (about one Hertz) so it was not obvious that a pole tracking strategy would give the most reliable and efficient for more complicated problems. I was especially cautious about adopting a pole tracking strategy after reviewing published dispersion curves (Abo-Zena (1979) and Kerry (1981) are good examples). There is a tendency for high order dispersion curves to form a lattice like pattern in the frequency-phase velocity plane and at the corners of the lattice pattern the dispersion curves have large and sudden changes in slope. This irregularity in the dispersion curve slope becomes more pronounced as the frequency increases and is particularly pronounced whenever low velocity zones exist in the structural model. Pole tracking algorithms are easily confused whenever apparent slope discontinuities exist in the dispersion curves. The normal solution to this is to smoothly track through the sudden slope change by reducing the frequency tracking increment which can significantly reduce the efficiency of the pole tracking algorithm.

In view of my skepticism about the effectiveness of the pole tracking strategy for handling certain complicated problems and since the pole tracking strategy required the development of a very reliable (although not necessarily efficient) zero searching algorithm for initialization, I decided to attempt to develop a reliable and efficient zero searching algorithm. My initial goal was to use the zero searching strategy by itself and I was able to make this work for elastic structures with no more than one low velocity zone. Ultimately I was forced to use mode association to check for poles dropped by the zero searching algorithm, but I have only had to do this for

the most complex structural models at high frequencies involving more than one low velocity zone or with liquid layers.

The mode searching problem then reduces to a problem of finding the zeroes of a real scalar function of a real, scalar and positive variable which on the surface would seem to be a very straightforward problem. Certainly there is a large volume of published articles and books relating to zero searching algorithms, however there is no standard procedure for finding the zeroes of an arbitrary function which will provide both reliable and efficient results. The only similar feature that seems to exist for the majority of published zero searching algorithms is that they tend to work in a two stage manner. The first stage involves a coarse searching algorithm where the independent variable is changed with relatively coarse increments until a zero crossing is detected. The second stage then comes into action and this stage uses a fine searching algorithm which "homes in" on the zero crossing. The details of the coarse and fine searching algorithms are very much dependent on the behavior of the function whose zeroes are being sought.

Our first look at the numerical behavior of the Rayleigh characteristic function will immediately reveal that for high frequencies the function has a dynamic range which is well beyond that available on most digital computers. For this I am assuming that a typical dynamic range for most computers is seventy orders of magnitude ( $10^{-35}$  to  $10^{+35}$ ). This is due to growing exponential terms which are associated with evanescent P or S waves and the arguments of these evanescent terms are directly scaled by frequency. These exponential terms do not cause the types of numerical problems which I discussed in chapter three and in fact they are eventually canceled out by division, however in order to avoid overflow or underflow

problems with the computer programs it is necessary to address the problem of dynamic range before the mode searching program can be developed.

I was able to solve the dynamic range problem by introducing a phase velocity dependent scaler to the elements of the  $[R]$  matrix. The scaler function is always positive and so it does not effect the pole positions and the scaler function is also applied to the numerator function so that it does not effect the final mode residue. The scaler function along with the modified  $[R]$  matrix elements are defined in Appendix A and basically this function transforms the hyperbolic sines, present whenever  $\theta_\alpha$  or  $\theta_\beta$  are imaginary, to hyperbolic tangents and the hyperbolic cosines to unity. This eliminates growing exponential solutions from the  $[R]$  matrix elements and allows for the computation of a scaled Rayleigh characteristic function which has a well behaved dynamic range.

After properly scaling the Rayleigh characteristic function, I turned my attention to the details of the zero searching algorithm. The scaled characteristic function resembles an amplitude and phase modulated periodic function and it seemed to me that it would be an easy task to find its zeroes. My initial attempt at designing a searching algorithm was not very successful. My first searching algorithm had a regular tendency to drop pairs of poles which were very close to each other unless I set the coarse searching increment to a very small number which made the algorithm too inefficient for practical use. The basic objective of the coarse searching algorithm is to find the general locations of all of the poles. The simplest sort of coarse searching algorithm uses a constant searching increment and in order for this type of algorithm to be reliable, the searching increment must be less than the minimum spacing between any two adjacent poles. In situations where two sets of modes are approximately decoupled from each other

the pole spacing is very erratic and it is not unusual for two poles to be very close to each other.

Erratic pole spacing is demonstrated in figure 4-1 where I show the Rayleigh characteristic function plotted versus phase velocity for a simple three layer crust and upper mantle structural model which is given in table 4-1. The frequency is fixed at 9.15 Hertz and the structural model contains a lithospheric low velocity zone with a S-wave velocity of 4.2 km/sec under a layer with a S-wave velocity of 4.5 km/sec and the top of this layer is the Moho discontinuity. I will refer to the top layer in the structural model as the crustal layer, the second layer as the lid layer and the third low velocity layer as the channel layer. The scaled Rayleigh characteristic function resembles a phase and amplitude modulated sinusoid whose oscillation frequency along the phase velocity axis slowly increases to maximum values at phase velocities corresponding to P or S wave layer velocities in the structural model. Also shown in figure 4-1 are two sets of vertical bars along the top of the plot which simply mark important positions along the phase velocity axis. The bottom set of vertical bars mark the actual pole positions or zero crossings of the characteristic function.

Since the lowest layer P-wave velocity is higher than the half space S-wave velocity, P waves are evanescent throughout the structure for all of the locked modes and at all frequencies. In the phase velocity range of 4.6 to 4.5 km/sec the SV waves are propagating through all three layers and all of the normal modes in this range have energy distributed throughout the three layers. When this situation arises the normal modes will sometimes space themselves out in a smooth manner which can be seen in figure 4-1 by the relatively uniform spacing of the zero crossings. In the phase velocity range of 4.5 to 4.2 km/sec SV waves are propagating in

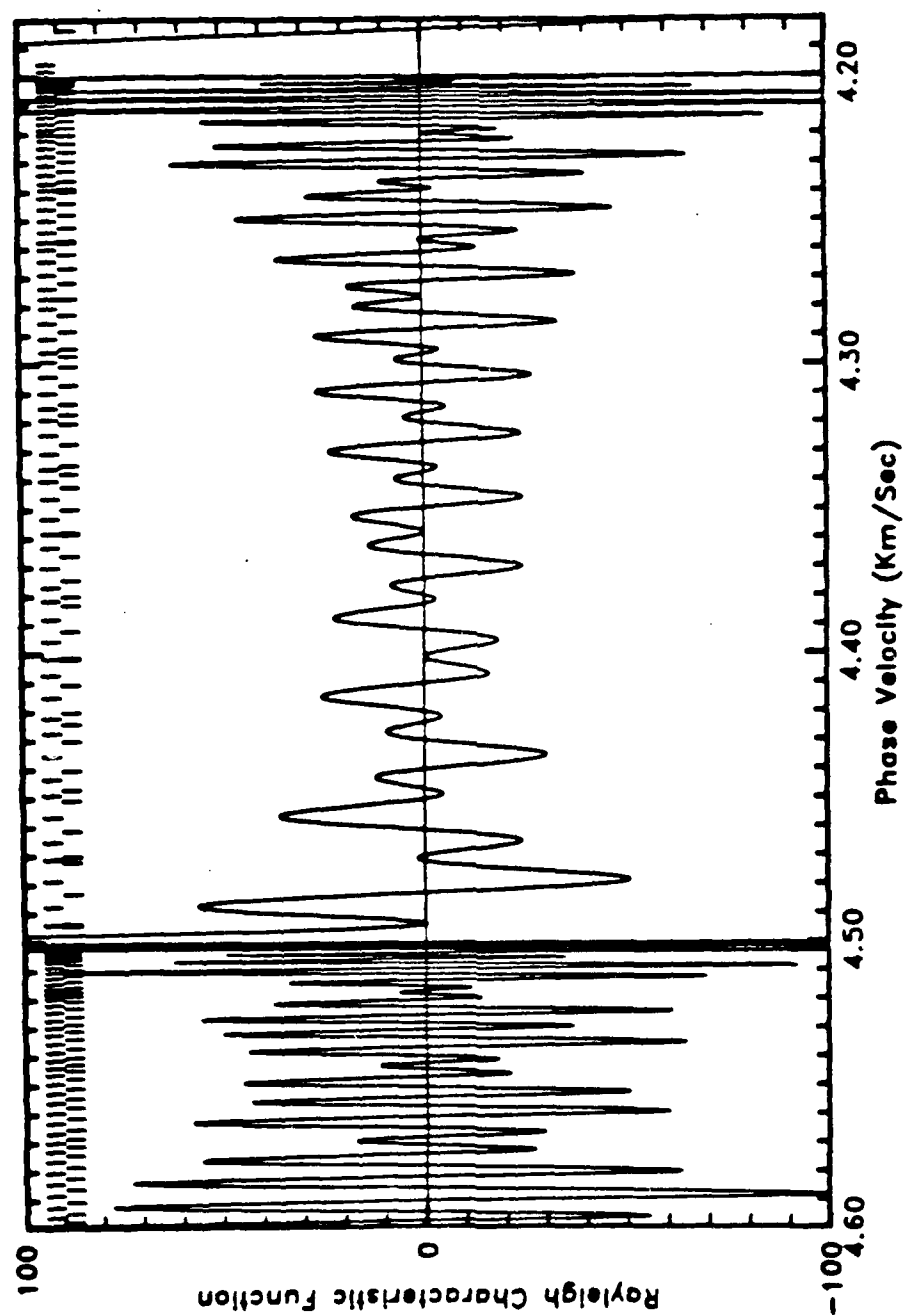


Figure 4-1. The Rayleigh characteristic function at a frequency of 9.15 Hertz for the structure given in table 4-1. The vertical bars at the top of the figure mark the zero crossings and local maxima of the Rayleigh characteristic function.

Table 4-1

Three Layer Crust and Upper  
Mantle Structure

Layer no.	Thickness (km)	$\alpha$ (km/sec)	$\beta$ (km/sec)	$\rho$ (gm/cc)
1	35	6.1	3.5	2.8
2	35	8.1	4.5	3.1
3	35	7.9	4.2	3.1
Half Space	-	8.2	4.6	3.2



the crustal and channel layers but they are evanescent in the lid layer. Because the frequency is high and the lid layer is relatively thick the normal modes in this phase velocity range fall into two families, one representing modes trapped within the crustal layer and the other representing modes trapped within the channel layer. These two families of modes are approximately decoupled from each other with the lid layer acting as a barrier to separate the crustal and channel modes and whenever this situation arises the normal mode spacing is very erratic which can also be seen in figure 4-1.

One of the most obvious improvements that can be made to the coarse searching algorithm is to adaptively change the coarse searching increment instead of using a constant increment. Normally the searching increment is set to some fraction of the previous pole spacing so that the function is tracked in a smooth manner from zero crossing to zero crossing. As long as the pole spacing is constant or varies slowly with the independent variable, this type of adaptive coarse search works well and the number of coarse searches between adjacent poles can be made small without effecting the reliability and thus improving the efficiency. In the phase velocity range of 4.6 to 4.5 km/sec such an algorithm will work quite well as long as the initial increment is made adequately small. If we start the search at the upper phase velocity value of 4.6 km/sec and proceed by decreasing the phase velocity, the searching increment will be slowly decreased as the average pole spacing decreases until a minimum value will be reached at 4.5 km/sec. When the search proceeds below 4.5 km/sec the searching algorithm will be too small for the sake of efficiency and in such circumstances it is advisable to accelerate the search by adaptively increasing the searching increment. This can be easily accomplished by keeping track of the number of times the characteristic function has been sampled

without the detection of a zero crossing. If this number exceeds some chosen value then the searching increment is increased by a specified multiplicative factor.

The type of coarse searching algorithm which I just described has four parameters which must be specified and which control the reliability and efficiency of the algorithm. The first parameter is the initial searching increment in phase velocity and this needs to be set small enough to reliably find the first mode (which is actually the highest order mode if we start at the highest phase velocity and go down). The second parameter is the number of times we wish to sample the characteristic function between zero crossings and I will refer to this as the interpolate sampling frequency. The sampling increment will be set to the previous interpolate spacing divided by the interpolate sampling frequency. The third and fourth parameters are the search acceleration parameters and they are the number of times we will allow the characteristic function to be sampled without a zero crossing before we increase the searching increment and the multiplicative factor we use to increase the searching increment once this number has been exceeded.

The parameter which has the largest effect on both the efficiency and the reliability of the searching algorithm is the interpolate sampling frequency. The lower this number the fewer times the characteristic function is computed between poles and the higher the efficiency. As the interpolate sampling frequency is increased the efficiency becomes inversely proportional. There is a less direct relationship between the interpolate sampling frequency and the reliability of the searching algorithm and this relationship is very dependent on the particular structural model, phase velocity and frequency which is being used. When the pole spacing is uniform or changes slowly the

reliability can be kept high with a low value of the interpolate spacing frequency which will maximize the efficiency of the searching algorithm. When the pole spacing is irregular the interpolate sampling frequency must be set to a higher value to insure that all of the zero crossings will be detected and this will decrease the efficiency. We can quantify the minimum interpolate sampling frequency necessary for reliable pole detection in terms of the ratio of the pole spacings in phase velocity of two adjacent poles. Modes are typically skipped when the interpolate spacing suddenly decreases and, in order for the zero crossing to be detected in a situation like this, the interpolate sampling frequency must be set to at least one divided by the ratio of the suddenly decreased interpolate spacing to the previous interpolate spacing.

Figure 4-2 shows the interpolate spacing ratios for adjacent poles for the case where the phase velocity search is proceeding in the direction of decreasing phase velocity and for the characteristic function shown in figure 4-1. The ratio is expressed as a base ten logarithm and each ratio is plotted with a "P" symbol at the phase velocity corresponding to the pole position. Positive values indicated that the pole spacing has increased and these situations do not jeopardize the searching algorithm reliability assuming that the previous poles have been properly located. The only problem with large values of the interpolate spacing ratio is that the characteristic function will be oversampled at the corresponding poles thus decreasing the efficiency. Very small values of the interpolate spacing ratio indicate that the pole spacing has suddenly decreased and this can result in a pair of dropped poles. From figure 4-2 we can see that in order to detect the pair of poles at about 4.275 km/sec phase velocity it would be necessary to set the interpolate sampling frequency to about one hundred which is the inverse of the minimum interpolate spacing ratio of about 0.01. Normally a priori information

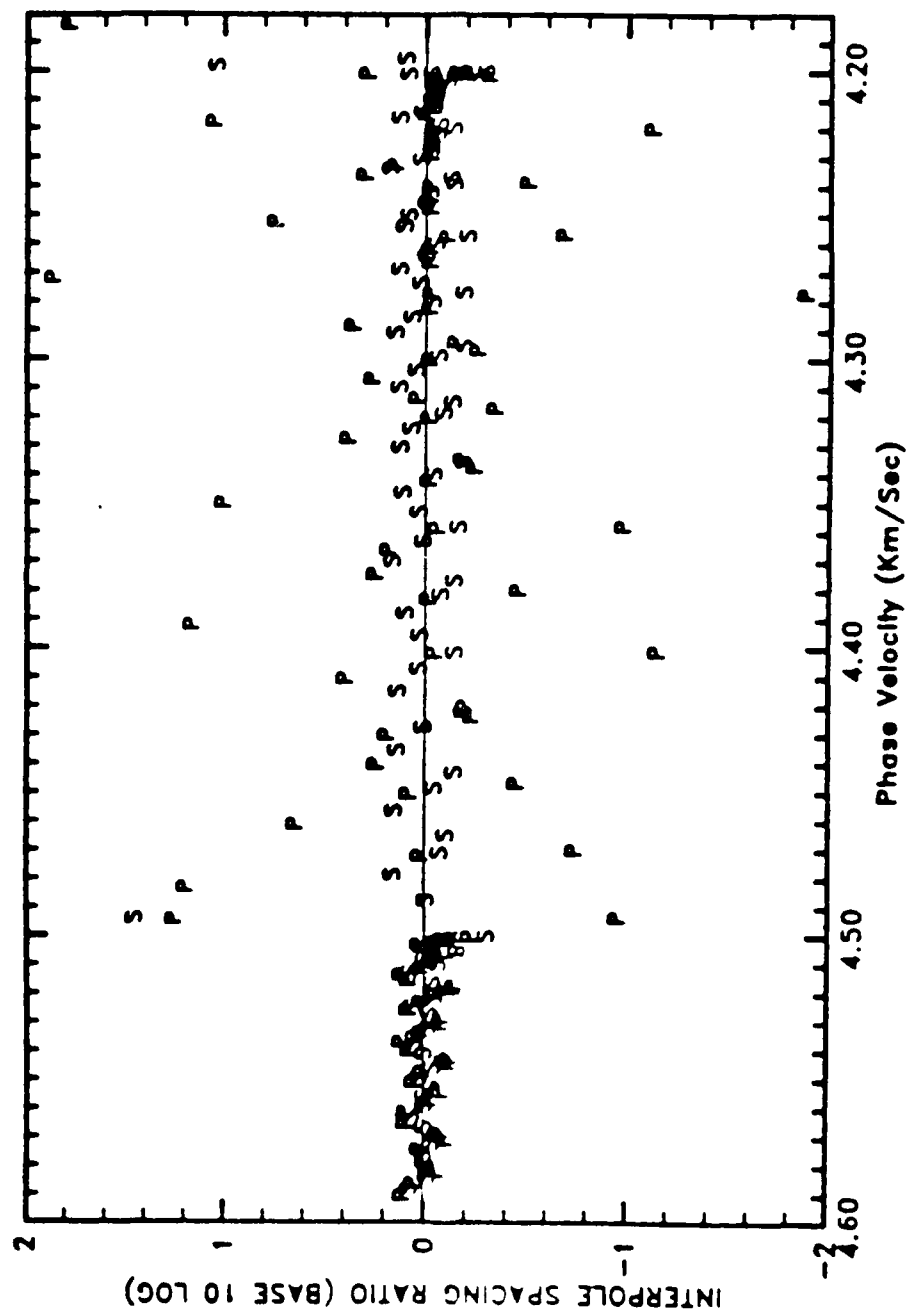


Figure 4-2. Interpole spacing ratios for the Rayleigh characteristic function shown in figure 4-1. The "p" symbols refer to the spacing between zero crossings and the "s" symbols refer to the spacing between local maxima.

about the minimum interpole spacing ratio will not be available and so some choice of the interpole sampling frequency will define how close two poles can come to each other before the poles will be dropped. It is not unusual for interpole spacing ratios to be as low as 0.001 or 0.0001 at high frequencies and for situations where different families of normal modes which are approximately decoupled coexist in the same phase velocity range. In order for the coarse searching algorithm to be reliable in such cases it is necessary to sample the characteristic function many thousands of times between zero crossings and this is unsatisfactory from an efficiency standpoint.

If we look back at figure 4-1 we can see a second upper set of vertical bars which mark the zero crossings of the slope of the characteristic function. The spacing between these bars is much more uniform in the 4.2 to 4.5 km/sec phase velocity range than the interpole spacing in the same range. These vertical bars mark local extrema of the characteristic function and extrema spacing ratios computed in the same manner as the interpole spacing ratios are shown in figure 4-2 as the points labelled "S". The minimum value of the extremum spacing ratio is about 0.5 as compared to the minimum interpole spacing ratio of 0.01. If we were to design the coarse searching algorithm to reliably find all of the zero crossings of the slope of the characteristic function we could set the interextremum sampling frequency to a low number and be confident of detecting all of the local extrema in a very efficient manner.

The final version of the zero searching algorithm which I designed has as its basis a coarse searching algorithm which looks for local extrema of the characteristic function. We can think of this as a "wiggle" detector since it tracks the oscillations of the characteristic function as opposed to its

actual zero crossings. For elastic structural models which have no more than one low velocity zone I have found that the minimum value of the extremum spacing ratio is about 0.2 at all frequency bandwidths. I have used this coarse searching algorithm for a large number of structural models and frequency bandwidths with the interextremum sampling frequency set to the value of six and, as long as the structural model is elastic and contains no more than one low velocity zone, the algorithm has never skipped over a local extremum of the characteristic function.

The particular coarse searching algorithm which I developed had a strong influence on the details of the final fine searching algorithm. Coarse searching algorithms which are based upon tracking the actual characteristic function zero crossings call up the fine searching algorithm whenever a zero crossing has been detected. The fine searching algorithm is initialized with the two values of phase velocity, determined by the coarse searching algorithm, which bracket the zero crossing. The objective of the fine searching algorithm is to refine the phase velocity zero estimate to within some specified accuracy and this is normally accomplished in one of two ways. The most straightforward and probably least efficient method is the iterative rebracketing approach in which the characteristic function is computed at the center of the bracket, the zero crossing is rebracketed using the original bracket values plus the new value just computed, and this sequence is carried out iteratively until the bracket width in phase velocity is below the desired accuracy. A more sophisticated method is what I refer to as the iterative interpolation approach in which a local fit of the characteristic function is made using a liner or polynomial function in phase velocity, the zero crossing of the fit function is computed, the characteristic function is computed at the zero crossing of the fit function, a new local fit is made

using the new value of the characteristic function just computed, and the whole sequence is repeated iteratively until the desired accuracy is achieved. When the fit function is linear this method is normally referred as the Newton root finding method although there actually a number of variations to the Newton method as I will discuss.

The convergence of the iterative rebracketing method is easy to determine and is entirely independent of the characteristic function. The zero crossing is refined by a factor of two for each iteration so to refine the zero crossing by fifteen orders of magnitude it will take about fifty iterations. The convergence of the iterative interpolation method is very much dependent on the degree to which the fit function actually represents the characteristic function in the neighborhood of the zero crossing. When the fit function is a good approximation of the characteristic function the zero crossing estimate can be refined by many orders of magnitude in each iteration, however when the fit function is a poor approximation the convergence can be as slow as the iterative rebracketing method and in the worst cases the determination of the zero crossing will not converge at all.

I used a version of the Newton root finding method as the final fine search algorithm. The Newton root finding method normally depends upon having an analytic evaluation of both the function whose zero is being found along with the first derivative of the function. A straight line tangent to the function is then projected to the zero axis and a new estimate of the zero is obtained. As I will show later in this chapter, an analytic expression for the partial derivative of the characteristic function with respect to phase velocity can be obtained, however the analytic derivative computation is just as expensive to compute as the characteristic function itself so it would be desirable to avoid an analytic computation of the derivative if possible.

A standard modification of the Newton root finding method is to use a first difference approximation for the analytic derivative. I avoid computing the derivative analytically and my final version of the Newton root finding algorithm is as follows.

1. A straight line is connected between the initial points which bracket the zero crossing and its intersection in phase velocity with the zero axis is computed. This phase velocity value becomes the first iteration value.
2. The characteristic function is computed at the first iteration phase velocity and a straight line is fit between this point and one of the original bracket points. The intersection in phase velocity with the zero axis of this straight line is computed and this phase velocity value becomes the second iteration.
3. The characteristic function is computed at the most recent iteration phase velocity and a straight line is fit between this point and the previous iteration point. The intersection in phase velocity with the zero axis of this straight line is computed and this phase velocity value becomes the next iteration.
4. Step 3 is repeated until the desired accuracy is achieved.

I use two tests to determine adequate convergence of the Newton root finding algorithm. The absolute difference between two successive iterations in phase velocity must be below some threshold value which is normally set to  $10^{-12}$  km/sec and when this is true I will sample the characteristic function one more time at a phase velocity value which is some very small increment from the the final iteration but which should bracket the zero crossing with the final iteration value acting as the other bracket. If there as a change of sign of the characteristic function between these two



final bracket values then I use the final phase velocity value as the estimate of the eigen phase velocity.

I have found that this version of the Newton root finding method can refine the estimate of the characteristic function zero crossing by a factor of fifteen orders of magnitude in about six iterations on average which represents a factor of eight increase in efficiency over the iterative rebracketing algorithm. There are some situations however for which the Newton root finding method will converge very slowly or not at all and I make several tests to check for this. The first test is that the number of iterations be less than some maximum number which I have set to twenty. The second test is that new iterations of the phase velocity must lie within the original zero crossing bracket values. If either test is not met then it is assumed that the Newton method is not convergent and the iterative rebracketing algorithm is used until the bracket width has been decreased by a factor of eight. These new brackets are then used to reinitialize the Newton root finder.

The relationship between the fine searching algorithm and the coarse searching algorithm which I developed was complicated by my choice of tracking the characteristic function extrema as opposed to the zero crossings. The coarse searching algorithm, as it is sampling the characteristic function and looking for the next extremum, checks at each phase velocity sample to see if a zero crossing has occurred since the previous phase velocity sample. If a zero crossing has occurred then a flag is set and the bracketing values of the phase velocity and the characteristic function are saved. Once an extremum has been located the coarse searching algorithm checks the zero crossing flag and if this flag is set then the fine searching algorithm is called with the saved bracket values and the zero crossing flag is cleared

for the next coarse searching leg. Normally the zero crossing flag will be set for each extremum which is detected however there will be situations corresponding to irregularly and closely spaced poles in which the actual zero crossing will not be detected.

In cases where an extremum is detected but the zero crossing flag is not set the coarse searching algorithm checks to see if the local extremum appears to be close to the characteristic function zero axis and this is done in the following manner. The extremum must a local minimum whenever the characteristic function values for the previous coarse searching leg were all positive or the extremum must be a local maximum whenever the previous characteristic function values were all negative. If this is true then a second difference is computed using the three samples which define the local extremum and another second difference is computed by replacing the actual extremum sample characteristic function value by zero. If the local extremum is in fact not close to the zero axis then a second difference computed by replacing the local extremum sample by zero should be much larger than the actual second difference and so the ratio of these two second differences is computed and if it is less than a specified threshold then the local extremum is considered to be close to the zero axis.

If the local extremum appears to be close to the zero axis then a version of the iterative rebracketing algorithm is used to resample the characteristic function in the near vicinity of the local extremum in hopes of detecting two closely spaced zero crossings. This special rebracketing algorithm uses as its initial brackets the two phase velocity values which flank the actual local extremum and on the initial iteration two more points are sampled midway between the two brackets points and the middle extremum point which produces a total of five sample points counting the original

three samples which initialized the rebracketing algorithm. These five points are checked for zero crossings of the characteristic function (there should never be just one zero crossing) and if detected then the bracketing values of the two zero crossings are used to initialize two calls of the fine searching algorithm. If no zero crossings are detected then a new local extremum is determined among the five points along with its flanking points, the new extremum is checked for closeness to the zero axis and if it is determined to be close another iteration of the rebracketing algorithm is executed. Once a pair of poles is located or the extremum is no longer determined to be close to the zero axis the coarse searching algorithm proceeds to the next extremum. Notice that the coarse searching phase velocity increment is not effected in any way by the very fine phase velocity resampling in the near vicinity of the local extremum which accounts for the high reliability and efficiency of this method. For the example shown in figure 4-1 zero crossings were not initially detected for the closely spaced poles associated with the local extrema at phase velocities of 4.22, 4.275 and 4.4 km/sec. Rebracketing in the vicinity of these local extrema did locate the poles without the necessity of increasing the interextremum sampling frequency.

Examples of Rayleigh dispersion curves using the zero searching algorithm which I have just described are shown in figures 4-3 and 4-4. Figure 4-3 shows dispersion curves for the same structural model as that used to generate the Rayleigh characteristic function shown in figure 4-1. The phase velocity range is also the same as that of figure 4-1 and the frequency ranges from nine to ten Hertz. In order to show the lattice like detail of the dispersion curves with high resolution, a total of two hundred frequency values were searched for modes in the range of nine to ten Hertz and there are over 20,000 poles plotted in figure 4-3. The frequency to frequency mode

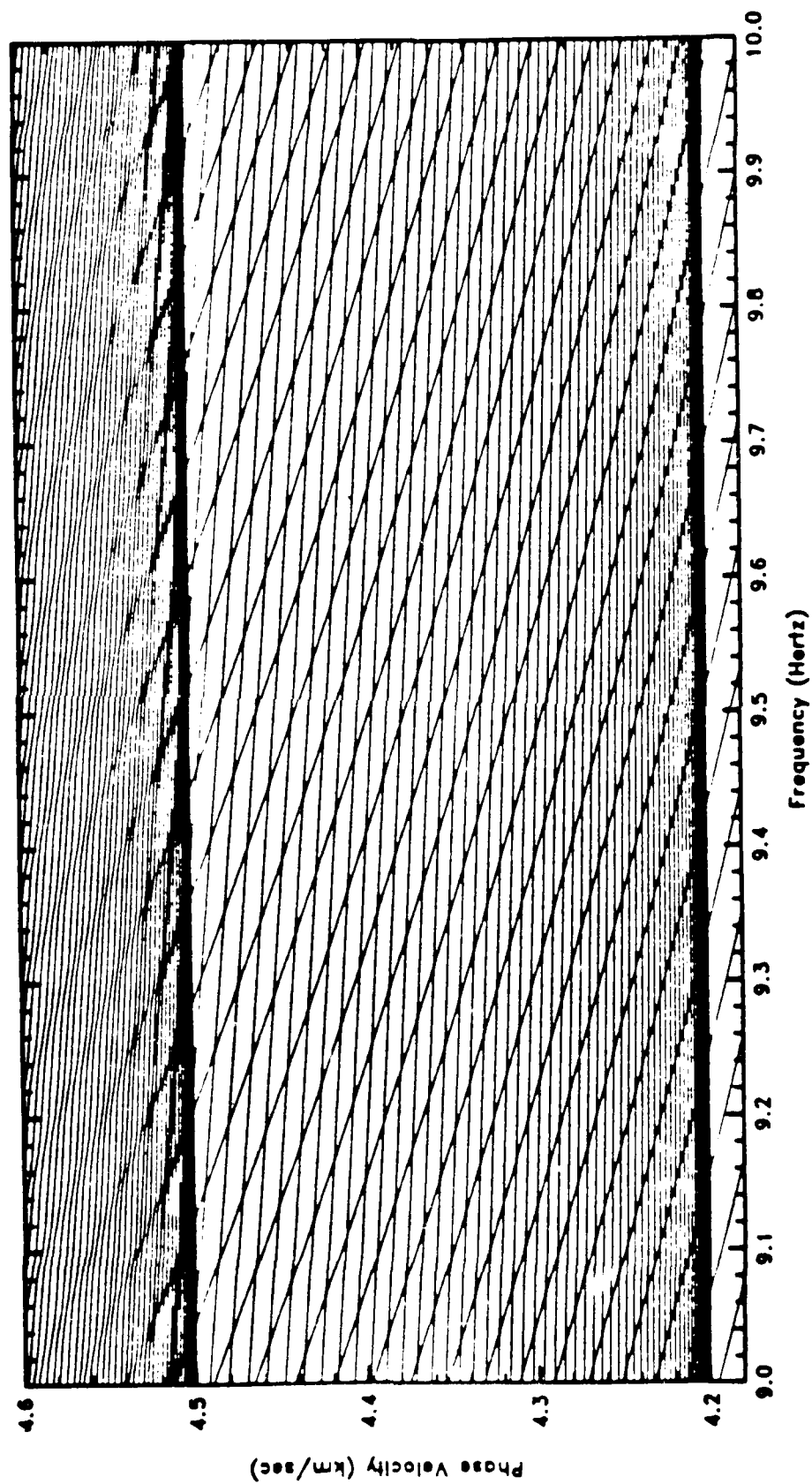


Figure 4-3. Rayleigh dispersion curves for the three layer crust and upper mantle structure.

association which was necessary to produce dispersion curve plots was done by assigning an integer mode number to each pole at each frequency and then all of the poles at different frequencies but with the same mode number were plotted as one dispersion curve. Mode numbers were assigned by simply ordering the poles at each frequency by increasing phase velocity starting with the fundamental Rayleigh mode and assigning the numbers sequentially according to the order. Figure 4-4 shows a more typical set of dispersion curves in the zero to one Hertz frequency range for a slightly more complex structural model which was obtained from Kanamori and Hadley (1975) and which is supposed to be representative of the southern California crust and upper mantle east of the San Andreas fault. This structural model is defined in table 4-2 and it will be used to generate synthetic seismograms which will be shown later in this chapter. An interesting feature of the structural model shown in table 4-2 is the anomalously high P and S wave velocities of the bottom half space. This allows locked modes to be computed in the zero to fifteen km/sec phase velocity range and flattening of the dispersion curves in figure 4-4 can be seen at all of the P and S wave layer velocities for the thicker layers in the structural model. I will discuss the consequences of this high velocity "cap" layer later in this chapter.

A zero searching strategy based upon the zero searching algorithm that I have described in this chapter was used by itself to generate the dispersion curves shown in figures 4-3 and 4-4. By this I mean that no attempt was made to check for dropped poles or to make any sort of frequency to frequency mode association other than that required to make the plots. If poles had been dropped they would have shown up as A shaped features in the dispersion curves and would be quite distinctive. I have

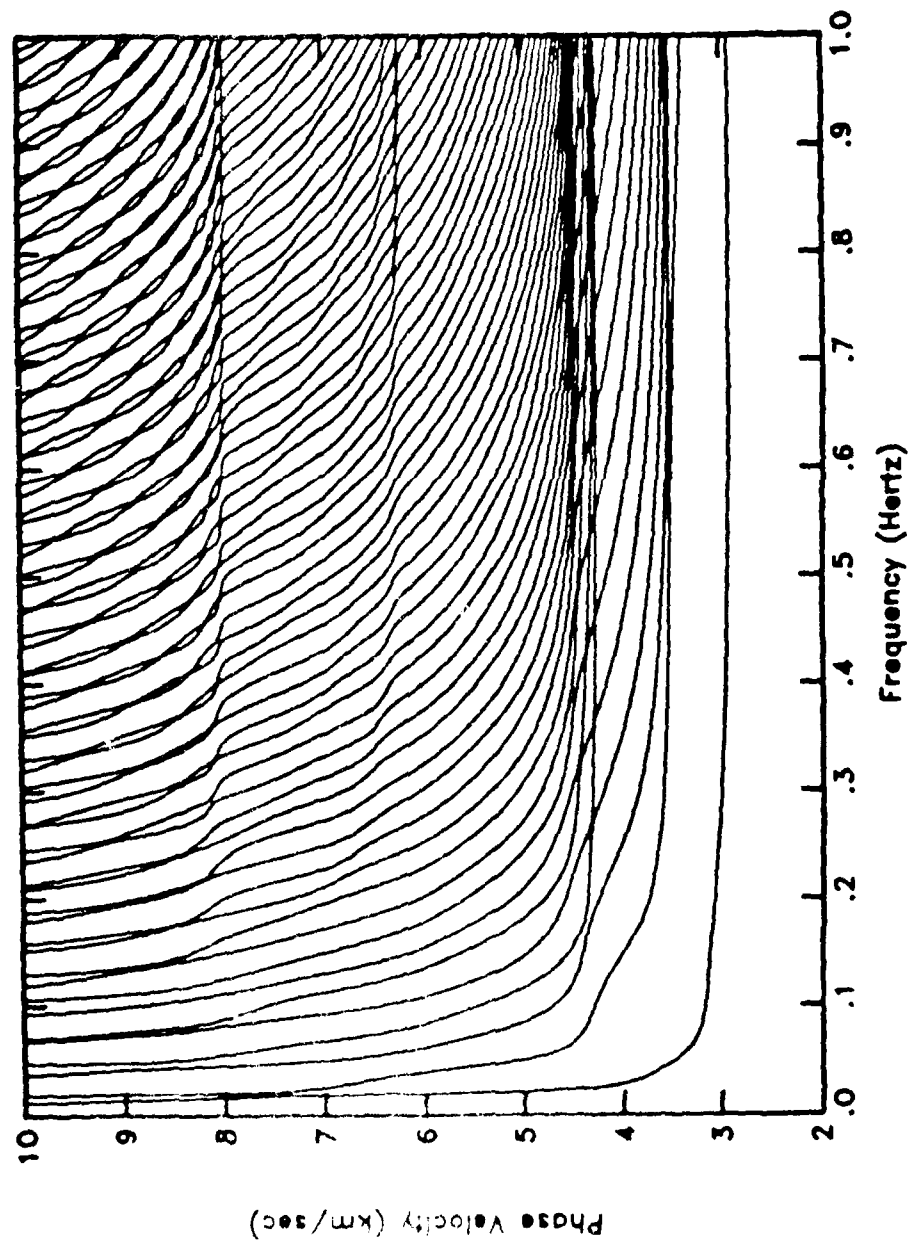


Figure 4-4. Rayleigh dispersion curves for a southern California structural model.

Table 4-2

Southern California Crust and Upper Mantle  
Structure East of the San Andreas Fault

Layer no.	Thickness (km)	$\alpha$ (km/sec)	$\beta$ (km/sec)	$\rho$ (gm/cc)
1	5	5.50	3.175	2.73
2	24	6.20	3.500	2.73
3	5	6.70	3.770	2.88
4	6	7.80	4.400	3.25
5	30	8.02	4.460	3.25
6	40	7.95	4.250	3.29
Half Space	-	20.0	15.0	5.0

found the zero searching algorithm that I developed to be completely reliable for elastic structural models with no more than one low velocity zone and I have also found that for a wide variety of structural models and frequency bandwidths I can reliably locate all of the normal mode eigen phase velocities to an accurate of  $10^{-12}$  km/sec using a total of fifteen evaluations of the characteristic function on average per pole. This includes all evaluations of the characteristic function in both the coarse and fine searching algorithms. It seems unlikely to me that the efficiency of this zero searching algorithm could be increased by any more than a factor of three and so I have deemed this zero searching algorithm to be satisfactorily efficient. One distinct advantage of using a zero searching strategy is that the poles need to be located only at the frequencies which are necessary for the FFT and it is not necessary to locate additional poles in order to smoothly track the dispersion curves as is necessary with pole tracking strategies or with the mode searching method developed by Kerry. In figures 4-3 and 4-4 the frequency was sampled at a very fine interval however this was only done in order to generate high resolution dispersion curves for display purposes and this fine frequency sampling was not necessary to generate synthetic seismograms.

Early attempts to use this zero searching algorithm to compute Rayleigh dispersion curves for structural models with more than one low velocity zone indicated that poles were being dropped. This was verified primarily by visual inspection of the dispersion curve plots but it also could be seen by the total number of poles located at each frequency as the frequency was changed. There is a very strong tendency for the total number of locked modes at each frequency to either remain the same or increase with increasing frequency and when this number decreases with increasing



AD-A187 663

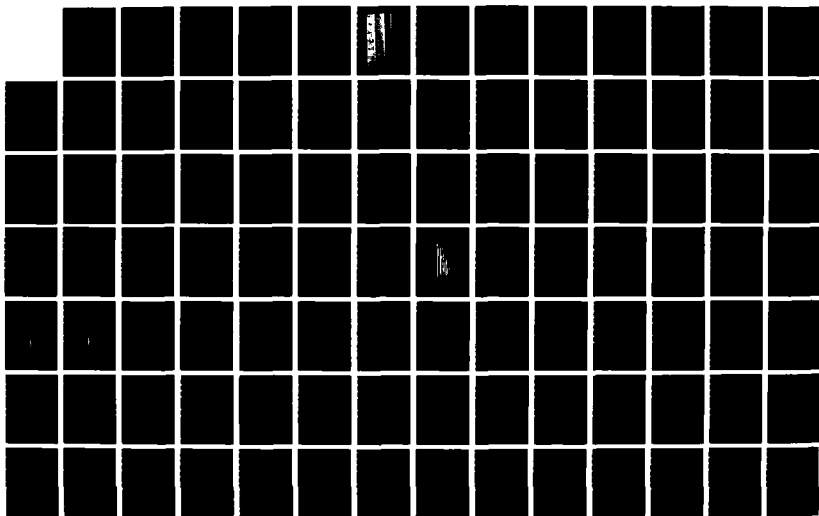
A SPECTRAL METHOD FOR COMPUTING COMPLETE SYNTHETIC  
SEISMOGRAMS(U) COLORADO UNIV AT BOULDER D J HARVEY  
MAR 87 AFGL-TR-87-8238 F19628-85-K-8816

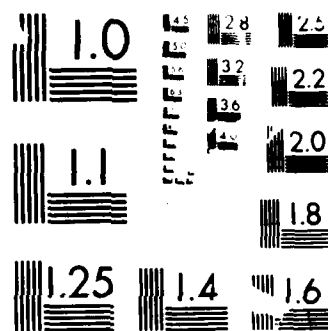
3/4

UNCLASSIFIED

F/G 8/11

NL





MICROCOPY RESOLUTION TEST CHART

1010-A

frequency it is very likely that poles have been dropped at the frequency where the decrease is observed. There is also a strong tendency for dispersion curves to be monotonically decreasing in phase velocity with increasing frequency, as can be seen in figures 4-3 and 4-4, especially at the high phase velocity ends of the dispersion curves and whenever the phase velocity of the dispersion curve with the highest mode number appears to increase with frequency it is very likely that poles have been dropped.

The coarse searching algorithm which I developed is based upon tracking the zero crossings of the slope of the characteristic function and this algorithm works well as long as the slope zero crossings are regularly spaced in phase velocity. I found that the characteristic function extremum spacing was regular for structural models in which no more than two decoupled waveguides existed and when more than two decoupled waveguides exist this is no longer true. Structural models with more than one low velocity zone can have a number of waveguides which is equal to one plus the number of low velocity zones and the number of waveguides is the same as the number of tightly clustered poles which can occur in phase velocity ranges in which the waveguides are approximately decoupled. For simple structural models with no more than two waveguides there will be no more than two poles which will cluster closely together and for these situations the characteristic function extremum spacing will remain regular. In situations where more than two poles can cluster closely together the characteristic function extremum spacing must obviously be irregular and these situations occur when more than two approximately decoupled waveguides exist in the structural model.

I have a strong suspicion that the zero crossings of higher order derivatives of the characteristic function are more uniformly spaced in phase velocity and I suspect that the coarse searching algorithm would work as long as it is tracking the zero crossings of the  $n^{\text{th}}$  order derivative of the characteristic function where  $n$  is equal to the number of low velocity zones in the structural model. I chose however not to pursue this potential method for increasing the zero searching algorithm reliability for several reasons. First of all it becomes quite expensive to compute high order derivatives of the characteristic function either numerically or analytically and secondly the relationship between the coarse and fine searching algorithms becomes complicated and somewhat muddled when the coarse searching algorithm is based on tracking the zeroes of high order derivatives of the characteristic function.

I chose instead a method which has been used successfully in the past to recover zeroes which were skipped over by a zero searching algorithm and this method is described by Acton (1970). The method involves searching a modified version of the characteristic function for the missing zeroes and this modified function is equal to the original function with the zeroes that were found in the first search analytically removed. Removing a zero analytically from any function is quite straightforward and simply involves dividing the original function by some known function which is analytic and which has a zero equal to the zero of the original function. The resulting modified function will no longer have a zero crossing corresponding to the one which was removed and this procedure can be repeated for as many zeroes as desired. The analytic function that I chose to use to remove the zeroes was the hyperbolic tangent function since it is linear in the vicinity of the zero crossing but well behaved as one proceeds away from the

zero crossing.

The final version of my mode searching algorithm involved both zero searching strategy and some elements of a pole tracking strategy. The zero searching algorithm was the primary means of finding the normal mode eigen phase velocities and pole tracking was only used to check for dropped poles at each frequency. This was accomplished by checking to see if the number of modes at each frequency either remained the same or increased with increasing frequency and by checking to see if the phase velocity of the highest order mode was monotonically decreasing with increasing frequency. If either of these two checks failed at a particular frequency then the zeroes found on the first pass through the zero searching algorithm were analytically removed from the characteristic function and a second pass was made through the zero searching algorithm using the modified characteristic function to find the dropped poles. The poles found in the second pass were then merged with the poles found in the original pass and the check for dropped modes was made again and if there still appeared to be dropped modes the whole process was repeated. Dropped poles normally occur very infrequently even in very ill conditioned structural models and so the modified characteristic functions normally have only a small number of zero crossings which are quite easy to locate.

I have found only one class of structural models for which my mode searching algorithm is not completely reliable and that is structures which contain multiple low velocity zones which have identical elastic parameters. In such cases, as the frequency goes to infinity, families of dispersion curves will asymptotically approach each other and the pole spacings between these families of dispersion curves will become infinitesimally small over wide frequency ranges. At some frequency the pole spacing will

fall below the numerical resolution of the computer and when that happens it will be numerically impossible to distinguish or find the poles. We could consider these to be second or higher order poles at one phase velocity however I have found that this problem can be avoided completely by seeing to it that structural models do not have low velocity zones with identical elastic parameters. I have found that by simply changing the P and S wave velocities by one part in  $10^6$  in one of two identical low velocity layers the mode searching algorithm will work quite fine as long as the arithmetic is done in double precision on the computer.

A final example of dispersion curves found by my mode searching algorithm for a very ill conditioned structural model is given in figure 4-5. The structural model parameters are given in table 4-3 and this model contains three low velocity layers with similar elastic parameters. The dispersion curves are shown over a frequency range of zero to five Hertz and the mode spacing can be seen to be quite irregular both in the frequency direction as well as the phase velocity direction and at virtually all frequencies and phase velocities. Because of the similarity of the three low velocity layers there are three sets of dispersion curves, which can be seen in the 0 to 3.5 km/sec phase velocity range, which correspond to three families of approximately decoupled normal modes in the three waveguides with almost identical eigen phase velocities. These appear as thick looking dispersion curves which are in fact sets of three dispersion curves which are very close to each other. The thin and flat looking dispersion curve at about 3.2 km/sec phase velocity which appears to cut across the waveguide dispersion curves at frequencies over one Hertz is what we would typically refer to as the high frequency surface Rayleigh wave. It is quite apparent that the fundamental P-SV normal mode is not in fact a "surface" wave at high

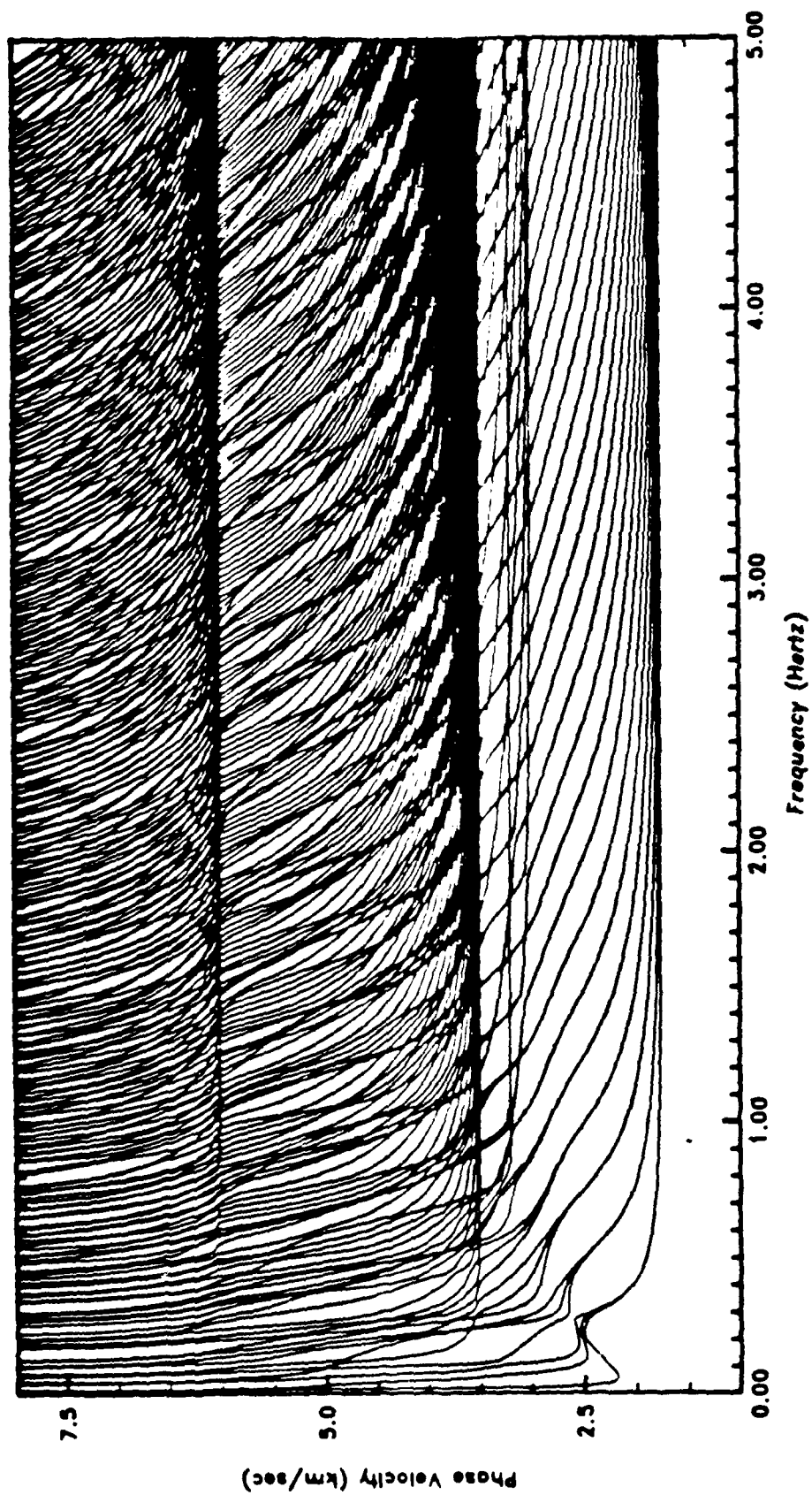


Figure 4-5. Rayleigh dispersion curves for a structural model with three similar low velocity zones.

Table 4-3

A Structural Model with Three  
Similar Low Velocity Zones

Layer no.	Thickness (km)	$\alpha$ (km/sec)	$\beta$ (km/sec)	$\rho$ (gm/cc)
1	5	6.000	3.500	3.0
2	5	3.000	1.750	2.5
3	5	6.000	3.500	3.0
4	5	3.001	1.751	2.5
5	5	6.000	3.500	3.0
6	5	3.002	1.752	2.5
7	5	6.000	3.500	3.0
Half Space	-	20.0	15.0	5.0



frequencies (by that I mean a wave whose energy is trapped on or near the free surface) and instead the fundamental mode becomes a trapped channel wave in the second layer as the frequency goes to infinity.

In this section I have gone into considerable detail to describe the mode searching algorithm which I developed. I felt justified in doing this since the development of this algorithm in its final form constituted the single most time consuming part of my research. The problem of locating the flat earth normal mode eigenvalues in a reliable and efficient manner was not easy to solve and I suspect that this problem, as much as the numerical stability problem, has stopped other researchers from using the normal mode method to compute complete synthetic seismograms. In the next section I will describe how the various partial derivatives, which are necessary for computing group velocities and for normalizing the eigenfunctions, are computed and how these derivatives can also be used to make a first order correction of the eigen phase velocities to account for frequency dependent anelastic attenuation in the structural model.

#### **4.2 Eigenvalue Computation: Computing the Group Velocity, Normalizing the Eigenfunctions, and Accounting for Frequency Dependent Anelastic Attenuation**

From equations (3.3.53) and (3.3.54) we can see that it is necessary to compute the partial derivative of the characteristic function with respect to wavenumber in order to compute the normalized eigenfunctions. Since we have expressed the  $[R]$  matrix elements as functions of frequency and horizontal phase velocity, it is desirable to rewrite equation (3.3.54) as follows.

$$c = \frac{\omega}{k}, \quad \frac{\partial c}{\partial k} = -\frac{c^2}{\omega} \quad (4.2.1)$$

$$\partial_R \bar{\Delta}(\omega, k) / \partial k = -\frac{c^2}{\omega} \partial_R \bar{\Delta}(\omega, c) / \partial c \quad (4.2.2)$$

$$\left. \partial_R \bar{\Delta}(\omega, c) / \partial c = -\frac{\omega}{c^2 \partial_R \bar{\Delta}(\omega, c) / \partial c} \right|_{c = {}_R C(n, \omega)} \quad (4.2.3)$$

$$\text{where } {}_R C(n, \omega) = \frac{\omega}{{}_R K(n, \omega)}$$

A useful although unnecessary quantity to compute is the group velocity as a function of frequency for each dispersion curve and from Achenbach (1984) this is given as follows.

$$\left. {}_R c_g(n, \omega) = \frac{d\omega}{dk} \right|_{k = {}_R K(n, \omega)} = \frac{1}{\frac{d{}_R K(n, \omega)}{d\omega}} \quad (4.2.4)$$

Using the relationship of phase velocity and wavenumber to frequency it is easy to rewrite equation (4.2.4) as follows.

$$\left. {}_R c_g(n, \omega) = \frac{c}{1 - \frac{\omega}{c} \frac{dc}{d\omega}} \right|_{c = {}_R C(n, \omega)} \quad (4.2.5)$$

The total differential of the characteristic function is always equal to zero along a dispersion curve which leads to the following.

$$d_R \bar{\Delta}(\omega, c) = \frac{\partial_R \bar{\Delta}(\omega, c)}{\partial \omega} d\omega + \frac{\partial_R \bar{\Delta}(\omega, c)}{\partial c} dc \quad (4.2.6)$$

$$\left. \frac{d_R \bar{\Delta}(\omega, c)}{dc} \right|_{c = {}_R C(n, \omega)} = 0 \quad (4.2.7)$$

$$\left. \frac{dc}{d\omega} \right|_{c = {}_R C(n, \omega)} = - \left. \frac{\partial_R \bar{\Delta}(\omega, c) / \partial \omega}{\partial_R \bar{\Delta}(\omega, c) / \partial c} \right|_{c = {}_R C(n, \omega)} \quad (4.2.8)$$

$${}_R c_g(n, \omega) = \left. \frac{c}{1 + \frac{\omega \partial_R \bar{\Delta}(\omega, c) / \partial \omega}{c \partial_R \bar{\Delta}(\omega, c) / \partial c}} \right|_{c = {}_R C(n, \omega)} \quad (4.2.9)$$

From equation (4.2.3) we can see that it is only necessary to compute the partial derivative of the characteristic function with respect to horizontal phase velocity in order to compute the normalized eigenfunctions and thus to compute synthetic seismograms. If we also compute the partial derivative of the characteristic function with respect to frequency, then equation (4.2.9) can be used to compute the frequency dependent group velocity for each normal mode. Because of the nature of the fine searching algorithm which I use, a numerical approximation of the partial derivative with respect to phase velocity is available for free and initially I used this numerical estimate to compute the normalized eigenfunctions. I became apprehensive about using this numerical approximation however, since it was a potential source of errors which I could not easily quantify, and so I started computing the partial derivative analytically for the purpose of checking the accuracy of the numerical estimate. I found that the numerical derivative was usually accurate to about four decimal places which was adequate for computing synthetic seismograms in most situations but I decided to start using the analytic derivative routinely in order to avoid unforeseen

numerical problems associated with the use of the numerical derivative. Although it is rather expensive to compute the various partial derivatives analytically, the derivatives are never computed inside the mode searching algorithm except for one time per located pole and so the incremental cost of computing the derivatives analytically is not high.

Partial derivatives of the characteristic function are also necessary to model the effects of frequency dependent anelastic attenuation using first order perturbation theory. Aki and Richards (1980) discuss physical phenomena which account for anelastic attenuation and just how such attenuation enters into the theory relating to elastic wave propagation. One particular physical model which they give was popularized by Liu et. al. (1976) and is based upon a superposition of relaxation phenomena each one of which is represented by a stress-strain relation which involves linear terms of stress and strain time derivatives. This is the stress-strain law for a standard linear solid and Aki and Richards show that such a physical attenuation mechanism can be accounted for in the theory by making complex, frequency dependent changes in the layer P and S wave velocities. The resulting equivalent elastic P and S wave velocities are given as follows.

$$\alpha(\omega) = \frac{\alpha_P(\omega)}{1 - \frac{1}{4Q_\alpha^2(\omega)}} \left( 1 - \frac{i}{2Q_\alpha(\omega)} \right) \quad (4.2.10)$$

$$\beta(\omega) = \frac{\beta_P(\omega)}{1 - \frac{1}{4Q_\beta^2(\omega)}} \left( 1 - \frac{i}{2Q_\beta(\omega)} \right)$$

where  $Q_\alpha(\omega)$  and  $Q_\beta(\omega)$  are the frequency dependent dimensionless quantities which relate the incremental losses of P and S wave energy in a wave

cycle to the peak energy in that cycle and  $\alpha_p(\omega)$  and  $\beta_p(\omega)$  are the actual dispersed and frequency dependent P and S wave phase velocities which would be observed in an attenuating medium.

Computing flat earth normal modes for structures which have arbitrary, complex, frequency dependent layer P and S wave velocities is a very difficult problem. Aside from the fact that complex layer P and S wave velocities will make all of the layer [R] and minor matrix element arithmetic complex as well, the most significant problem with complex layer velocities is that it moves all of the normal mode poles off of the real wavenumber axis and into the complex k-plane. This behavior of the normal mode eigenfunctions is exploited by those researchers, such as Kind (1978), who use the reflectivity method and integrate along the real wavenumber axis. Moving the poles off of the real wavenumber axis allows a numerical integration to be done along the real axis without encountering the errors associated with numerically integrating through the poles. For those of us who are looking for normal mode poles, moving the poles off of the real wavenumber axis can significantly complicate the task of locating these poles and in the worst cases it can make the problem of reliable and efficient pole location virtually impossible to solve.

In order to make maximum the utilization of the efficient and reliable mode searching algorithm which I developed for structural models with real layer P and S wave velocities, I decided to adopt a two stage approach to account for anelastic attenuation. We can expand the equivalent elastic layer P and S wave velocities from equations (4.2.10) in terms of their real and imaginary components as follows.

$$\alpha(\omega) = \alpha_R(\omega) + i \alpha_I(\omega) \quad (4.2.11)$$

$$\beta(\omega) = \beta_R(\omega) + i \beta_I(\omega)$$

where  $\alpha_R$ ,  $\alpha_I$ ,  $\beta_R$ , and  $\beta_I$  are real numbers.

$$\alpha_R(\omega) = \frac{\alpha_P(\omega)}{1 - \frac{1}{4Q_\alpha^2(\omega)}} \quad (4.2.12)$$

$$\beta_R(\omega) = \frac{\beta_P(\omega)}{1 - \frac{1}{4Q_\beta^2(\omega)}}$$

$$\alpha_I(\omega) = - \frac{\alpha_R(\omega)}{2Q_\alpha(\omega)} \quad (4.2.13)$$

$$\beta_I(\omega) = - \frac{\beta_R(\omega)}{2Q_\beta(\omega)}$$

In the first stage we set the equivalent elastic velocities to  $\alpha_R$  and  $\beta_R$  given by equations (4.2.12) and set the imaginary components to zero. This results in elastic layer velocities which are frequency dependent but real which keeps the normal mode poles on the real wavenumber axis and allows for the use of real arithmetic in the characteristic function computations. The mode searching algorithm which I described in section 4.1 can then be used without modification to find the poles at each frequency. The second stage involves computing an imaginary incremental shift of the normal mode eigen phase velocities due to a purely imaginary change in the layer P and S wave velocities (this imaginary shift is set to  $\alpha_I$  and  $\beta_I$ ) using first order perturbation theory.

The anelastic attenuation must be low (i.e. the  $Q$  values must be high) in order for a first order perturbation approximation of the eigen phase velocities to yield accurate results. Probably a more straightforward approach would have been to compute a complex first order shift in the eigen phase velocities due to complex incremental changes in the layer  $P$  and  $S$  wave velocities relative to an unattenuating medium with constant  $P$  and  $S$  wave velocities however it is easy and cheap to include the velocity dispersion effects directly at the beginning of the mode searching and this also eliminates complex arithmetic from the perturbation computations. We can apply first order perturbation theory to expand the Rayleigh characteristic function as follows.

$$d_R \bar{\Delta}(\omega, c) = \frac{\partial_R \bar{\Delta}(\omega, c)}{\partial c} dc + \sum_{i=1}^n \left( \frac{\partial_R \bar{\Delta}(\omega, c)}{\partial \alpha^{(i)}} d\alpha^{(i)} + \frac{\partial_R \bar{\Delta}(\omega, c)}{\partial \beta^{(i)}} d\beta^{(i)} \right) \quad (4.2.14)$$

where  $i$  is the layer index and  $n$  is the total number of layers including the bottom half space (if any). As with the computation of the group velocity, small changes in layer  $P$  and  $S$  wave velocities will shift an eigen phase velocity such that  $d_R \bar{\Delta}(\omega, c) = 0$ . We can thus write down the shift in the eigen phase velocity,  $dc$ , due to shifts in the  $P$  and  $S$  wave velocities  $d\alpha^{(i)}$  and  $d\beta^{(i)}$  as follows.

$$dc = - \frac{\sum_{i=1}^n \left( \frac{\partial_R \bar{\Delta}(\omega, c)}{\partial \alpha^{(i)}} d\alpha^{(i)} + \frac{\partial_R \bar{\Delta}(\omega, c)}{\partial \beta^{(i)}} d\beta^{(i)} \right)}{\partial_R \bar{\Delta}(\omega, c) / \partial c} \quad (4.2.15)$$

$c = {}_R C(n, \omega)$

We can see from equation (4.2.15) that if the complex values of  $d\alpha^{(i)}$  and  $d\beta^{(i)}$  all have the same phase angle, then  $dc$  will also have the same phase angle (to within 180 degrees) and this is because all of the partial derivatives in (4.2.15) are real for real frequency, horizontal phase velocity, and layer velocities. Thus purely imaginary  $d\alpha^{(i)}$  and  $d\beta^{(i)}$  values will produce a purely imaginary  $dc$ .

Once the complex eigen phase velocities have been obtained for a structural model with frequency dependent anelastic attenuation the remaining computations appear to be straightforward. One would typically use the complex eigen phase velocities to compute complex eigenfunctions and then compute the mode residue contributions using a Hankel function algorithm which can properly handle complex arguments. There is a hidden problem in all of this and this problem is not obvious unless one carefully considers the dispersion curves which I showed in section 4.1. When normal mode poles cluster very closely together, even very small errors in the eigen phase velocities can cause substantial errors in the vertical eigenfunctions. This extreme sensitivity of the eigenfunctions to the eigen phase velocities is one of the reasons that I compute the characteristic function using double precision arithmetic and is the primary reason why I locate the eigen phase velocities to within  $10^{-12}$  km/sec accuracy in the mode searching algorithm. The small errors, which are bound to occur when using a first order perturbation approximation for the eigen phase velocities, can produce large erroneous values for the eigenfunctions in situations where normal mode poles are very close to each other. The situations in which this is a real problem, as with many of the other problems which I have discussed, are very much dependent on the particular structural model and frequency



bandwidths which are used. For simple structural models for which the pole spacing is uniformly regular one can simply substitute the first order complex eigen phase velocities into the eigenfunction computations and expect reasonable results however, for more complex structural models with irregular pole spacing this approach will not work at all.

One potential way of solving the eigenfunction sensitivity problem is to use a complex version of the fine searching algorithm to refine the complex eigen phase velocities, initializing the algorithm with the first order estimates of the eigen phase velocities. In order for such a method to be reliable it is necessary for the first order estimates of the complex pole locations to be close to the actual pole locations. Normally "close" means that the distance between the first order pole and the actual pole must be small when compared to the actual pole magnitude in the complex plane however in our case "close" also means that the distance between the first order pole and the actual pole must be small when compared to the distances between the first order pole and any other poles. It is this second restriction which causes the complex fine searching algorithm to be not completely reliable, once again, in situations of tightly clustered poles. I did develop a computer program which uses a complex fine searching algorithm to refine the eigen phase velocity estimates and I also developed full complex versions of the eigenfunction and mode residue computation programs. Predictably these programs run much slower than their real arithmetic counterparts and also the complex fine searching algorithm is not completely reliable.

I felt that it was necessary to develop completely reliable and faster versions of the computer programs which account for attenuation and I finally settled on a method which is numerically stable over a wide range of  $Q$  values but which introduces an additional unwanted approximation

relating to the attenuation of elastic energy propagating through the medium. In this method I use purely real eigen phase velocities to compute the eigenfunctions and these real poles are equal to the original real eigen phase velocities which were located by the mode searching algorithm. Because of this the eigenfunctions are obviously numerically stable and the dispersive effects of the attenuation are properly accounted for however, since the imaginary component of the eigen phase velocities are not used, the vertical eigenfunctions do not properly account for the amplitude attenuation. The imaginary components of the eigen phase velocities determined from the first order perturbation are passed on to the mode residue computation program and the full complex eigenwavenumbers are used in the radial Hankel eigenfunctions. The net result of this is that energy propagating in the vertical direction is not attenuated but energy propagating in the horizontal direction is attenuated. Certainly this is a less than ideal solution to the problem however the incremental cost of accounting for attenuation using this method is very small and as I will show later in this chapter the main applicability of the locked mode method for computing synthetic seismograms is for situations where the seismic energy is propagating fundamentally in the horizontal direction.

All of the necessary equations to compute the partial derivatives of the characteristic function with respect to frequency and phase velocity are given in appendix B. The partial derivatives of the characteristic function suffer from the same dynamic range problem as the characteristic function itself and so I show how the partial derivative computations can be dynamically scaled in the same manner as the characteristic function computations. Finally in appendix B I derive a method for computing the first order change in the eigen phase velocities due to a small change of the layer

P and S wave velocities. This method gives the same identical results as equation (4.2.15) but it avoids the separate computations of the partial derivatives of the characteristic function with respect to each layer P and S wave velocity.

In the next section I will describe the actual computer programs which I wrote that use the methods and equations given in this dissertation to compute locked mode synthetic seismograms. These programs allow the user to find P-SV and SH dispersion curves starting from a specified plane layered structural model and at specified frequency samples, compute the P-SV and SH depth dependent eigenfunctions for each mode-frequency and at specified depths, sum the mode residues at each component-frequency for specified source-receiver geometries and source types, and transform each receiver-component into the time domain after applying various user specified filters.

#### **4.3 Locked Mode Seismogram Synthesis: The Computer Programs**

I implemented the theoretical and numerical methods which I developed in a set of computer programs which allows one to compute locked mode synthetic seismograms in a straightforward manner for a large range of frequency bandwidths, structural models, source-receiver configurations and source types. These programs have undergone an historical development which paralleled the development of the theory and numerical methods and the results of early versions of these programs dictated the course of action which I took in the theoretical development. The final versions of these programs provide a very simple user interface and can be run on most computers, big or small, as long as sufficient disk space and cpu cycles are available.

The bulk of the program development was done on a digital equipment corporation (DEC) PDP 11/70 mini-computer with the UNIX operating system and using the FORTRAN 77 programming language (some low level subroutines were written in the C programming language). The PDP 11/70 computer has a sixteen bit direct address length which places a rather severe restriction on the maximum program size and, using the UNIX operating system, this maximum size is 64K bytes (1K = 1024, 1 byte = 8 bits) of program text and 64K bytes of data in core memory. The most restrictive of this was the limit on the program text which limited the actual number of lines of code in any one executable program and this limit had a strong effect on the way in which I modularized the computational procedure. Another aspect of the PDP 11/70 computer which effected the program development was that it was a relatively slow machine especially when compared to large mainframe machines such as the IBM 370 or the CDC 7600. Because of these restrictions I was forced to be clever in the development of the programs to reduce both the size and the run times of each program so that I could use the 11/70 to generate locked mode synthetic seismograms at high frequencies and for realistic structural models. In the end this all proved to be an advantage since the programs which I developed run relatively fast and can be put on almost any computer (I have a working version of the mode searching program running on an IBM PC-AT microcomputer). The final versions of the programs, which run on much larger virtual memory computers, are organized in the same manner as the original 11/70 versions.

The overall arrangement of the programs is diagrammed in figure 4-6 along with the intermediate data files which communicate between the programs. The first program to be run for a new structural model or

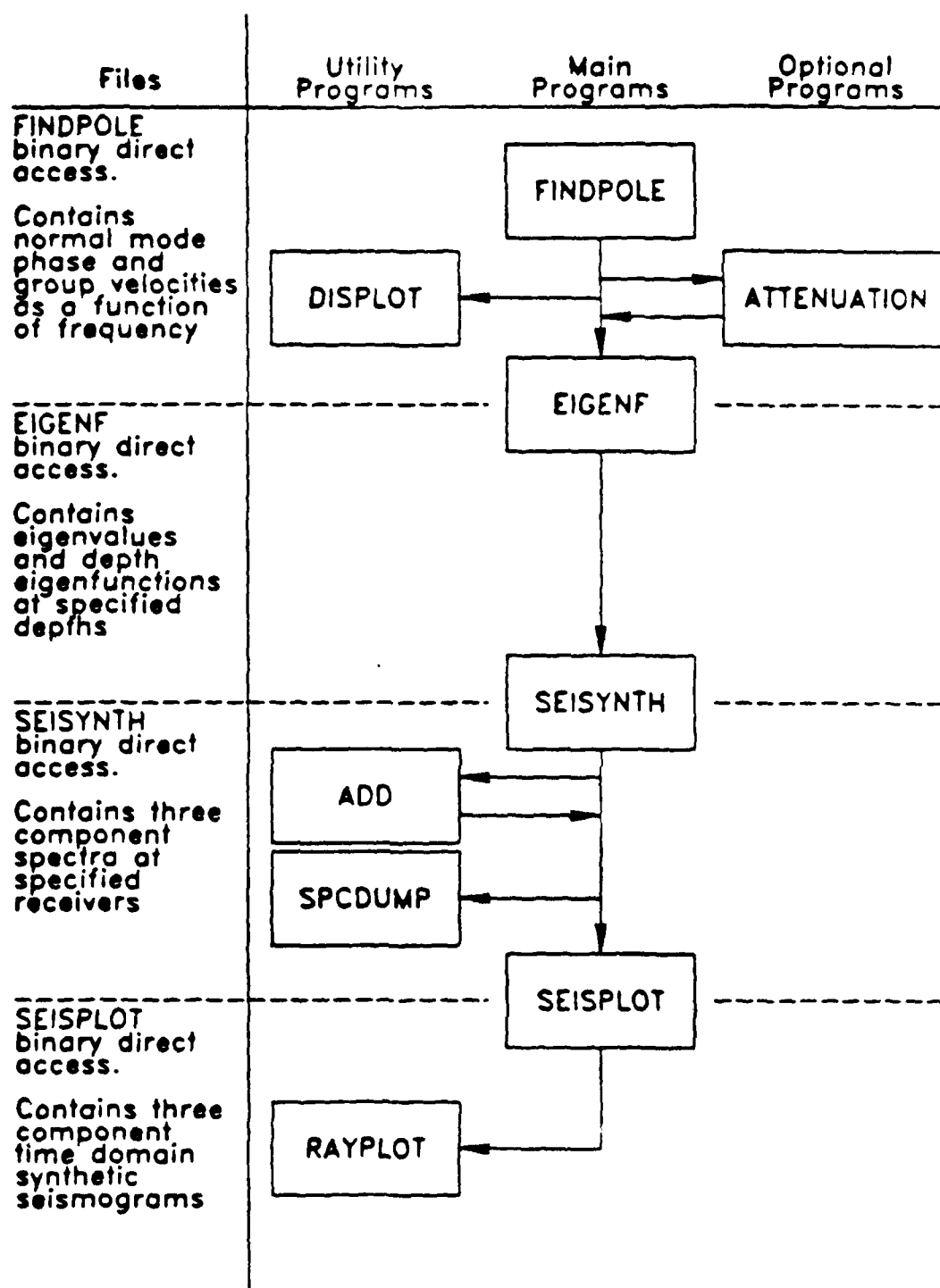


Figure 4-6. Computer programs used to compute locked mode synthetic seismograms.

frequency bandwidth is always program FINDPOLE which uses the mode searching algorithm, which I described in section 4.1, to locate the Rayleigh and Love eigen phase velocities for a set of specified frequencies. The only required inputs into the program are the elastic parameters (P wave velocity, S wave velocity, density) and the thicknesses of all the layers in the structural model and the set of equally spaced frequency values at which the normal modes will be evaluated. The frequency sampling is carried through the remainder of the programs and is used to compute the inverse Fourier transforms in the final step which produces time domain synthetic seismograms. The program will automatically choose a phase velocity range for the mode search which will pick up all locked modes (the user can override this and specify a phase velocity range). The program will also automatically choose a starting value for the phase velocity searching increment which will insure reliable yet efficient results. The group velocity for each mode is computed and the phase velocities, group velocities and all other pertinent information are written out to a binary data file.

Running program FINDPOLE usually takes more time than any of the other programs which follow. For a typical situation where ten or twenty synthetic seismograms are computed at one source depth, FINDPOLE runs about ten times slower than any of the other programs. This can be expected since, on average, the characteristic function is evaluated fifteen times for each pole that is located whereas the other programs, which compute the eigenfunctions and the residue contributions, will be making their respective computations only once per mode and it is this feature of the locked mode method that is primarily responsible for its efficiency. Because of the long run times which can be expected in certain cases, this particular program has a restart capability which allows the user to recover

the results of a previous run which may have been prematurely terminated either purposely or accidentally. Also because of the long potential run times, program FINDPOLE is usually run in a batch mode at off hours using low priority. The actual run time for program FINDPOLE is about 30 milliseconds per layer per mode per frequency on a DEC VAX 11/780 computer.

As I outlined in section 4.2, attenuation would normally be modeled in a two step process. The first step would be to run program FINDPOLE with the real parts of the frequency dependent layer P and S wave velocities in order to account for the dispersive effects of attenuation. I must confess however that I have not implemented the interpolation routines in program FINDPOLE which would be necessary to change the P and S wave velocities as the frequency is changed. Program FINDPOLE, as it exists now, assumes constant P and S wave velocities, but it would be a trivial exercise to modify the program to make the elastic velocities frequency dependent. I can also say with confidence that such a modification would not require any changes in the mode searching algorithm and it would not effect either the performance or the reliability of the program. For most frequency bandwidths and distance ranges for which I have used the locked mode methods, I have found the effects of attenuation to be small and the dispersive effects would be unnoticeable.

After program FINDPOLE has been executed the next step would typically be to run program ATTENUATION. Actually this step is optional and the user can go on to program EIGENF if it is not necessary to account for attenuation. If the user does run program ATTENUATION, then the user will be required to input a tabulated set of  $Q_\alpha$  and  $Q_\beta$  values for each layer and for any number of frequencies. The program will linearly

interpolate the  $Q$  values between the specified frequencies and then use equations (4.2.13) to compute the imaginary components of the layer  $P$  and  $S$  wave velocities with the real parts of these velocities set to the velocities used by program FINDPCLE. The imaginary value of each eigen phase velocity is then computed using the equations in appendix B.

Program ATTENUATION reads the binary data file which is written by program FINDPOLE and the imaginary values of the eigen phase velocities are deposited into the FINDPOLE output file. Thus program ATTENUATION modifies the FINDPOLE output file instead of writing a new one and an output file from FINDPOLE can be rerun through program ATTENUATION if it is necessary to change the attenuation. This is another reason why I chose to keep the elastic velocities constant in program FINDPOLE since, if dispersion were properly modeled, a change in the  $Q$  values would require a complete rerun of program FINDPOLE. program ATTENUATION runs much faster than program FINDPOLE and the run time is about 2.5 milliseconds per layer per mode per frequency on a DEC VAX 11/780 computer.

Program EIGENF computes the four components of the Rayleigh eigenfunctions and the two components of the Love eigenfunctions. This program reads an output file from program FINDPOLE, which may or may not have been modified by program ATTENUATION, and computes the eigenfunctions using the algorithm described in section 3.5. The only required user inputs are a set of depths at which the eigenfunctions are computed and where potential sources or receivers will be located. A binary data file is written by program EIGENF which contains all of the eigenvalues and eigenfunctions at each mode-frequency and for each specified depth and this output file is usually the largest of the intermediate data



files. The size of the EIGENF output file is about 36 bytes per depth per mode per frequency and the run time is about 4 milliseconds per layer per mode per frequency on a DEC VAX 11/780 computer.

In order to compute the eigenvalues and eigenfunctions for the widest range of frequency bandwidths and structural models I have found it necessary to use double precision (64 bit) arithmetic for all of the internal computations in programs FINDPOLE, ATTENUATION and EIGENF. Abo-Zena (1979) claims that the Rayleigh characteristic function can be computed in a numerically stable manner using only single precision (32 bit) arithmetic and I concur with his statement however I think that seven or eight decimal places of resolution is not enough to reliably locate the dispersion curves and especially to compute the eigenfunctions of tightly clustered poles. I have also found that for most modern computers 64 bit arithmetic is not excessively slow, in fact for many computers and operating systems the actual hardware arithmetic operations are done in extended precision regardless of the programming. Obviously the numbers in the FINDPOLE output file are written in double precision to preserve the resolution in program EIGENF. I have found that the computations which take place after program EIGENF can be done in single precision without adverse effects and so, primarily to reduce the sizes of the intermediate data files and the required core memory data storage sizes, all of the arithmetic done after program EIGENF is done in single precision. With this in mind the numbers in the EIGENF output file are written in single precision even though they are computed in double precision. Another distinct change in the nature of the computations after program EIGENF is that the structural model is no longer needed or used directly so that the speed of subsequent computations is not dependent on the number of layers in the elastic

model.

The three component synthetic spectra are computed in program SEISYNTH which reads the eigenvalues and eigenfunctions from an EIGENF output file and computes the spectra from the locked mode contributions in equations (3.3.41) and (3.4.2). At this point the user must specify the source and receiver spatial configurations along with the source parameters. The program allows for both multiple sources and multiple receivers and the only constraint on the locations is that no receiver can have the same exact map coordinates as a source (zero distance is not allowed due to the singularity of the Hankel function at zero). The contributions at each receiver due to multiple sources can either be summed together, with appropriate individual source gains and origin time shifts, or the three component spectra for each source can be kept separate for parametric source studies. The user must also specify the depths of each source and receiver and these must correspond to the depths for which the eigenfunctions have been computed. The source jump vectors are uniquely determined by the source types (e.g. explosion, shear dislocation point source, etc.) and appendix C gives a number of different jump vectors for various source types. Another set of important parameters which the user must input are phase velocity, group velocity and frequency filters. Normally the only filter which would be applied at this point would be a phase velocity filter which applies a scalar gain factor to each mode residue contribution as a function of the eigen phase velocity and the use of these filters will be discussed later in this chapter.

Program SEISYNTH computes the three component normal mode residues at each receiver and for each source, applies the filtering gains to each residue, sums all of the weighted residues together at each

frequency and writes the locked mode spectra to a binary data file. This program requires the use of Bessel function subroutines and the program run time is primarily effected by the efficiency of these subroutines. The run time for program SEISYNTH is about 1.5 milliseconds per receiver per mode per frequency for all three components on a DEC VAX 11/780 computer.

The final step involves running program SEISPLOT which transforms the three component spectra into the time domain. This program reads the SEISYNTH output data file and has to demultiplex each receiver-component spectrum out of the data file. A number of different filters can be applied in the frequency domain which account for simple models of the source spectra and the receiver instrument responses. Finally the spectra for each receiver-component are transformed into the time domain through the use of a fast Fourier transform subroutine and the synthetic seismograms are written to a binary data file.

In addition to the main programs which I have just described a number of utility programs were developed which are primarily aimed at displaying the results of the main programs. Program DISPLOT will make dispersion curve plots of phase velocity, group velocity, or the imaginary component of phase velocity versus frequency for all of the normal modes and this program reads a FINDPOLE output data file which may or may not have been modified by program ATTENUATION. Program SPCDUMP will read a SEISYNTH output data file and produce a neatly formatted printer listing of the locked mode synthetic spectra. Program ADD allows the spectra from two different runs of program SEISYNTH to be summed together for each receiver-component. Program RAYPLOT will read the output data file from program SEISPLOT and plot a suite of synthetic

seismograms and optionally compute and display a set of theoretical ray travel time curves over the locked mode synthetics. In addition to the graphics produced by programs DISPLOT and RAYPLOT, the main program SEISPLOT also will display the synthetic seismograms on a graphics terminal as they are being transformed into the time domain.

#### 4.4 Locked Mode Seismogram Synthesis: The Locked Mode Approximation

The locked mode method provides an efficient way of computing a portion of the complete synthetic seismogram. The particular portion of the complete solution which this method gives is entirely dependent on the S wave velocity of the bottom half space which effectively applies a low pass phase velocity filter to the complete solution. One way of increasing the locked mode synthetic phase velocity bandpass is to move the bottom of the structural model down which, for realistic earth models, will result in increasing the S wave velocity of the bottom half space. The resulting locked mode synthetics will contain earlier arrivals and the representation of near surface wave propagation will become more complete. In the limiting case we could take a spherical earth structural model and apply a flattening transformation which, for a whole earth model, would result in a flat earth structure with elastic velocities approaching infinity as the depth approaches the earth's radius.

Flattened whole earth models are in fact plate structures and for plate structures the locked mode method provides almost complete synthetic seismograms (complete seismograms would require the inclusion of modes with complex eigenwavenumbers). Unfortunately there is an almost direct proportionality between the number of locked modes at a particular

frequency and the total thickness of the structural model and, for models with thicknesses of planetary dimensions, an excessive number of locked modes will exist for frequencies over 0.1 Hertz. This problem is the reason why spherical earth normal modes cannot be used to generate complete high frequency synthetic seismograms without expending an exorbitant computational effort. This also has a lot to do with why flat earth models are so popular with theoretical seismologists who are trying to compute high frequency synthetic seismograms. Flat earth models allow the seismologist to arbitrarily limit the total thickness of the structural model which has the effect of ignoring the wave propagation outside of that thickness while reducing the computational effort required to synthesize waves propagating within the thickness.

In order to realize the maximum efficiency of the locked mode method it is necessary to make the total structure thickness as small as possible. Thin structural models however tend to produce incomplete locked mode synthetics due to the low S wave velocities of the bottom half space. The essence of the locked mode approximation is to place an unrealistically high velocity half space at the bottom of the structural model and I refer to this high velocity half space as the cap layer. I then require that this cap layer be placed at a depth such that the earliest P wave reflection from the top of the cap layer arrives after the seismic coda of interest. As the S wave velocity of the cap layer is increased, the entire seismic coda, including the earliest P wave arrivals, can be synthesized using only the locked mode residue contributions. The choice of a cap layer depth will place a limit on the maximum source-receiver distance, for which locked mode synthetic seismograms can be computed, without significant contamination from cap layer reflections. This maximum distance will be roughly proportional to the cap

layer depth and so the locked mode approximation will be most efficient in the near field (I am using this to mean 0 to 500 km) distance range and the efficiency will decrease as the source-receiver distance increases.

There are a number of problems with the locked mode approximation which I will discuss in detail in this section where I will show, with numerical results, how and under what circumstances these problems can be overcome. The problems fall into three categories which I give below.

1. Spurious reflections off of the cap layer.
2. Time wrap around of the synthetic seismogram in the time domain due to sampling in the frequency domain.
3. The truncation effects due to cutting off the mode sum to some finite number of modes (phase velocity filtering).

In order to check the validity of the locked mode approximation I decided to try to match a wave propagation problem which had been solved exactly. I chose the problem of a vertical vector point source with a step function time history applied at the free surface of an infinite homogeneous half space, Lamb's problem. A solution of Lamb's problem for the case of a material with a Poisson's ratio of 0.25 was derived by Pekeris (1955) and is given in terms of elliptic integrals.

I placed the cap layer at a depth of 100 km and gave it a shear wave velocity of 12 km/sec. The 100 km thick layer above had a shear wave velocity of 4 km/sec and a Poisson's ratio of 0.25 (a P wave velocity of about 7 km/sec). The useful source-receiver distance was restricted to less than about 100 km since for distances greater than that the cap layer reflections would interfere with the desired solution. Figure 4-7 shows the synthetic surface displacements from the locked mode method at a distance of 75 km and with a bandwidth of 8 Hertz along with the exact solution from

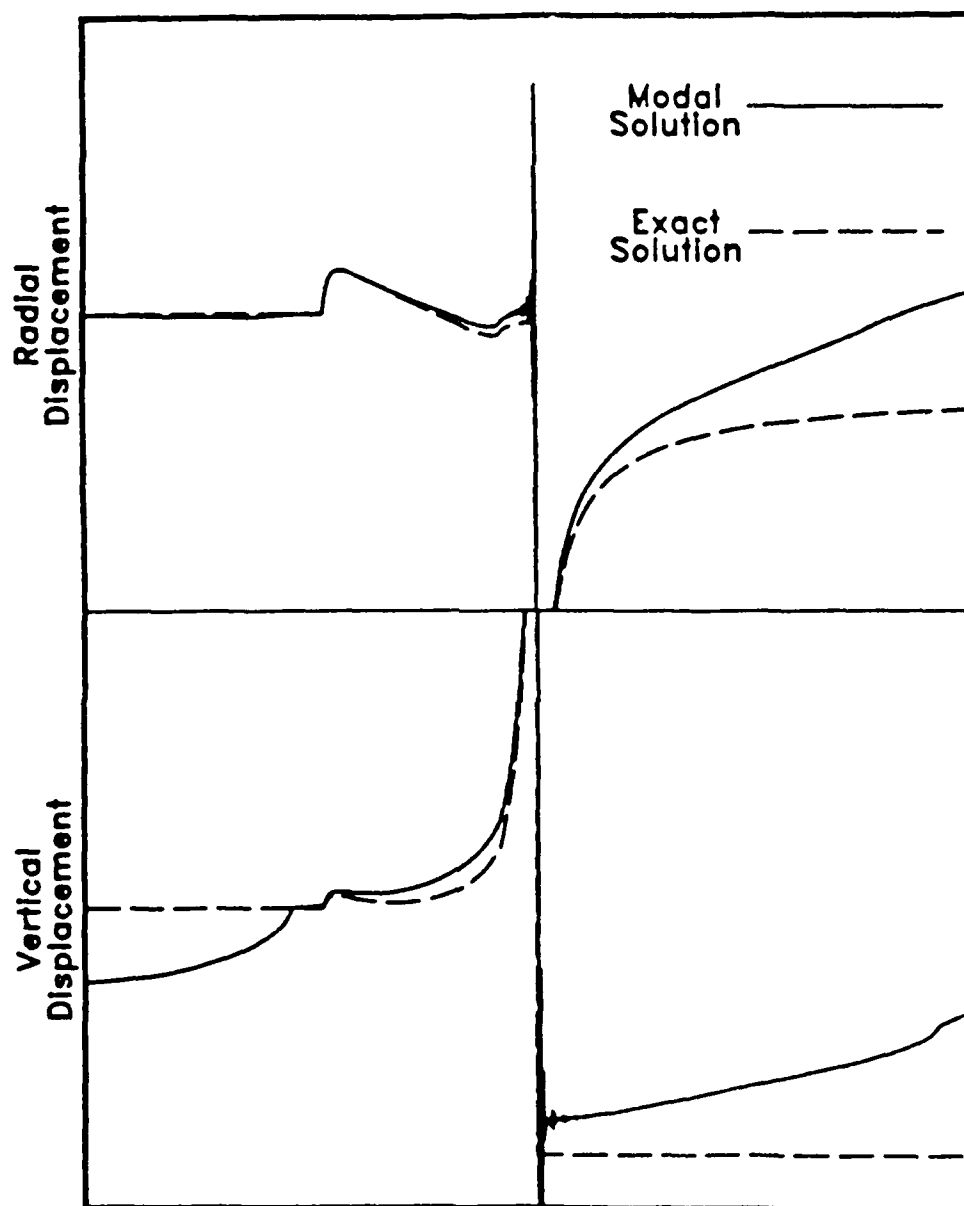


Figure 4-7. A comparison of the locked mode approximation solution of Lamb's problem with the exact solution (from Pekeris (1955)).

Pekeris.

The match between the two solutions for the radial displacement is quite good up until the arrival of the fundamental Rayleigh surface wave. After the arrival of the Rayleigh wave, which for Lamb's problem is a logarithmic singularity, the modal solution drifts away from the correct solution which asymptotically approaches the static offset due to the step function source. At first this may seem to be unusual, since one might expect a modal solution of Lamb's problem to work quite well in synthesizing the surface wave and not so well in synthesizing the P and S body waves, but the opposite conclusion must be drawn here. The reason for this is twofold; first, the strong step function static offset in the solution of Lamb's problem causes a singularity in the spectrum at zero frequency, and secondly, adding a cap layer to the structure will obviously effect the fundamental Rayleigh dispersion curve at low frequencies.

The spectrum of a simple step function at zero time is  $1/(i\omega)$  and this gives an obvious singularity at zero frequency. Whenever a static offset appears in the solution of the elastic wave equation, whether it be at some arbitrary time and in the presence of other dynamic solutions, the analytic expression of the spectrum must be singular at zero frequency. If one computes the spectrum of a step function analytically, samples that analytic spectrum in the frequency domain, and then uses a fast Fourier transform to transform the sampled spectrum into the time domain, the resulting time domain trace will look like a saw-tooth wave instead of a step function. This comes about due to undersampling of the spectral singularity at zero frequency and the resulting aliasing which is manifested as wrap around in the time domain. This is a basic problem which is shared by all frequency domain synthesis methods and so even if we were to synthesize only the



Rayleigh surface wave using an infinite half space as the structure, we would see a similar drifting error as we see it in figure 4-7.

The vertical displacement match between the two solutions is not so good although the major features of the P, S and Rayleigh waves do agree between the two solutions. Once again we can see the low frequency drifting error in the locked mode approximation when we compare the Rayleigh wave with the exact solution, which is a step function. WE also see more low frequency error in the P and S waves than we did for the radial displacement. The most obvious error in the locked mode approximation solution is the large acausal reverse step that immediately precedes the P wave arrival. This is due to an upper phase velocity cutoff of 8 km/sec which I imposed when summing the modes. The phase velocity filtering causes a spurious arrival to precede the P wave and I refer to this arrival as the truncation phase, since it is due to truncating the mode sum. I will discuss the effects of phase velocity filtering in more detail, but for now note that the P wave arrival and the rest of the seismic coda does not seem to be effected by the truncation phase even when the phase velocity cutoff is set close to the P wave velocity. The last feature that I would like to point out is the small bump near the end of the trace. This is the cap layer reflection and as can be seen it does not interfere with the earlier seismic coda. As I stated, the addition of a cap layer to the structural model will obviously effect the Rayleigh wave dispersion curve in the low frequency limit, however this effect must be causal and this bump represents the first place in the seismogram where the effect of the cap layer can be seen.

There is an apparent flaw in the locked mode approximation which is a consequence of both the wrap around problem and the presence of the cap layer. We can insure that the first cap layer reflection arrives

after some given time in the seismic coda at a given distance by placing the cap layer at sufficient depth. After the first cap layer reflection arrival, the coda will be contaminated by a host of multiple reverberations associated with the cap layer, and so one might think that this part of the coda would be rendered useless. For the case of a rigid cap layer these multiple reflections would continue for infinite time and slowly decrease in amplitude due to geometric spreading. Since I sample in the frequency domain one would expect multiple reflections due to the cap layer to wrap around into the earlier part of the coda and thus contaminate the entire seismogram.

This does happen with the locked mode approximation when using a rigid cap layer and when including a large number of modes with very high phase velocities. If, however, a low pass phase velocity filter is applied in the form of a mode truncation based on the eigen phase velocity the wrap around cap layer reflection problem is greatly diminished. This is the reason for the phase velocity filter which was used for Lamb's problem; originally a prominent cap layer reflection appeared half way between the P and S wave arrivals due to wrap around, but the phase velocity filter removed the reflection at the expense of producing a rather large truncation phase. This effect can be easily explained when we consider the horizontal phase velocity of a cap layer reflection body wave. Normally cap layer reflections will arrive at the surface with steep angles of incidence and thus they will have high horizontal phase velocities, and the later cap layer reflections which correspond to multiple reflections will have even higher phase velocities. Thus a low pass phase velocity filter with a cutoff set slightly above the highest P wave velocity will tend to pass most of the seismic coda and remove the cap layer reflections. I will demonstrate this in a more quantitative manner in the next example.

After checking the locked mode approximation with the exact solution of Lamb's problem I proceeded to compute synthetic seismograms for a more realistic earth structure. I chose a six layer southern California crust and upper mantle structure which I obtained from Kanamori and Hadley (1975). I computed the eigenvalues and eigenfunctions for two versions of the structural model. The first version is given in table 4-2 and has a cap layer with a shear wave velocity of 15 km/sec at a depth of 110 km and the eigenvalues and eigenfunctions were computed over a frequency range of 8 Hertz with a sampling interval corresponding to a 64 second time window. The second version was the same as the first except that the cap layer was put at a depth of 190 km and the eigenvalues and eigenfunctions were computed over a frequency range of 4 Hertz with a sampling interval corresponding to a 128 second time window. I refer to the first version as the "thin" structure and the second version as the "thick" structure and I computed a number of synthetic seismograms using these two similar structural models so that I could see the effects of cap layer depth and frequency sampling on the locked mode synthetics.

In order to test the effects of phase velocity filtering and to verify that I could use this filtering to decontaminate the seismograms of cap layer reflections, I computed a number of seismograms at a fixed source-receiver distance and for a fixed source, for the thin structure varying only the phase velocity filter cutoff, and compared these against a seismogram at the same distance for the thick structure. The results of these computations can be seen in Figure 4-8 where I plot vertical displacements at the surface for the P waves and the first part of the S wave coda. These seismograms were computed at a distance of 200 km and the source was placed at a depth of 7 km. The source model I used was a relaxation source (Stevens (1980)) with

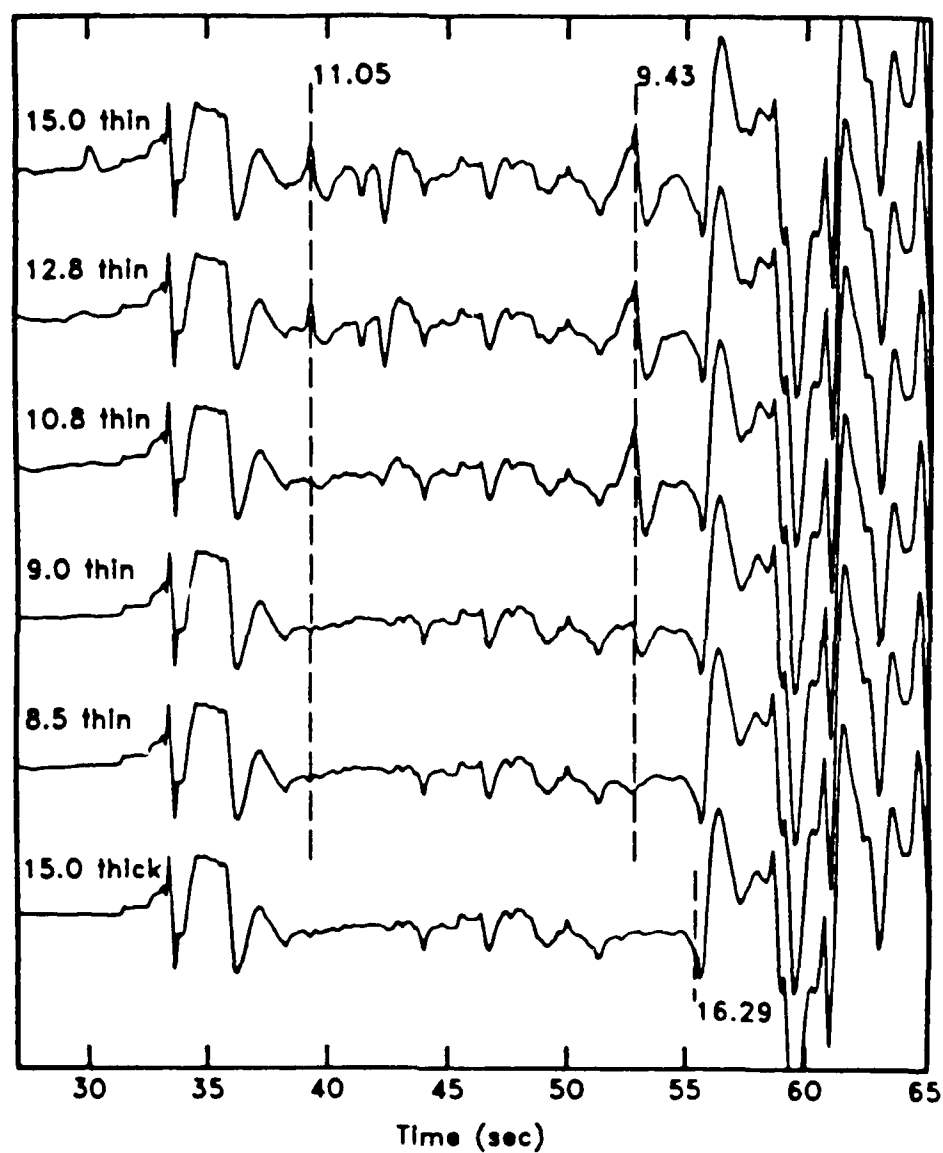


Figure 4-8. A comparison of synthetic surface displacements using the locked mode approximation for various phase velocity cutoffs and as the cap layer depth is changed. Dashed lines indicate cap layer reflection arrivals.

a relaxation radius of 1 km and a prestress corresponding to a thrust event. The individual traces are labelled with a number which is the phase velocity filter cutoff and either thin or thick which specifies the structural model used.

We would expect the seismograms for the thin structure to be heavily contaminated with cap layer reflections since the source-receiver distance is almost twice the cap layer depth and this is the case for the top trace of figure 4-8. The vertical dashed lines show the ray arrival times of two prominent cap layer reflections, the earlier arrival being the first P wave reflection, and the numbers beside each line are the horizontal phase velocities of the two reflection body waves. In addition to these two reflections there are a number of other spurious arrivals including one prior to the first legitimate P wave arrival which is a wrapped around cap layer reflection. As we decrease the phase velocity filter cutoff these spurious arrivals appear to vanish, as can be seen in the successive seismograms below the top trace. The individual cap layer reflections are filtered out when the phase velocity cutoff drops below the horizontal phase velocity associated with that reflection. At the lowest phase velocity cutoff of 8.5 km/sec the resulting seismogram appears to be devoid of cap layer reflections, with the exception of a small bump at the second indicated reflection arrival. In order to check this I computed a seismogram using the thick structure and this is shown as the bottom trace of figure 4-8. The first P wave cap layer reflection is indicated by the vertical dashed line but because of the high phase velocity of this arrival it does not appear in the seismogram. I overlaid the bottom two traces and found that with the exception of a small bump at about 53 seconds for the thin structure, the two seismograms matched perfectly.

If cap layer reflections were present in either of the two bottom traces of figure 4-8 these traces could not possibly match. Not only is the cap layer depth different for these two seismograms but the frequency sampling interval is different as well so that wrapped around reflections would appear at different times. Also the phase velocity filter cutoff is different between the two seismograms and so we cannot attribute the matching to some filtering effect. Phase velocity filtering appears to be a very powerful tool for the locked mode approximation and it allows us to extend the usable distance limit as we can see with this example.

In the last section of this chapter I will show comparisons of synthetic seismograms produced by the locked mode approximation with those produced by other complete solution methods. I will also discuss the errors which are introduced by the locked mode approximation and how these errors limit the situations in which this method can be successfully used.

#### 4.5 The Locked Mode Approximation: Comparisons with Other Complete Solution Methods and a Discussion of Its Limitations

Probably one of the more difficult tasks which faces the theoretical seismologist who has just developed a new seismogram synthesis method is to prove that the new method actually works. Virtually all methods have assumptions or approximations which turn this task into one of finding the ranges of parameters for which the method works. One obvious way is to compare against exact solutions, as I did in the previous section, however such solutions are rare and only exist for very simple structural models. Another approach would be to compare against real observed data, as I will do in the next chapter, however such an exercise is usually too poorly con-

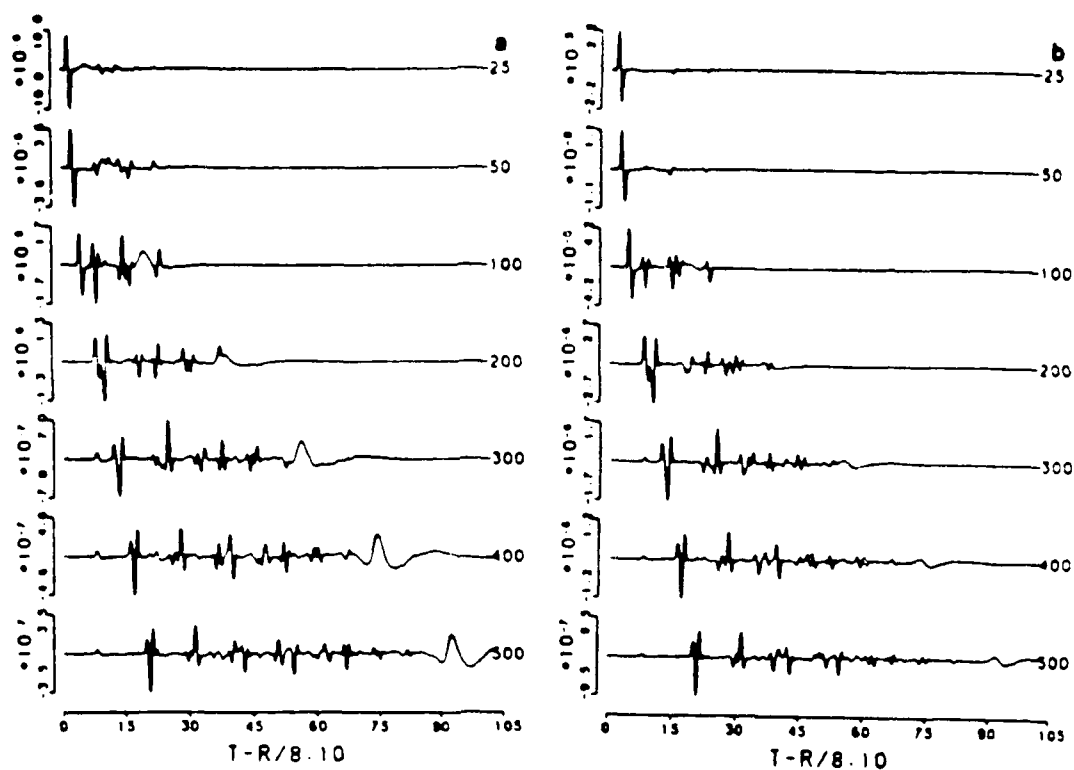
strained to provide conclusive verification. In this section I take the third approach which is to compare the locked mode approximation against other complete synthesis methods and in particular against the complete spectral solution method by Wang and Herrmann (1980).

Generating synthetic seismograms for the purpose of comparing with other synthetic seismograms can be a very tedious task. In order for the comparison to have any chance of success, every parameter which can effect the result must be specified exactly, which includes the structural model (layer thicknesses, P wave velocities, S wave velocities and densities), the attenuation model (layer  $Q_\alpha$  and  $Q_\beta$  as a function of frequency), the source type, the source-receiver configuration and all filtering parameters. In the past several years I have been able to obtain very good comparisons between the locked mode approximation and the reflectivity method by Kind (1978), the reflectivity method by Kennett (1980) and the WKBJ ray theoretical method developed by Chapman (1978) however I will be showing a comparison here which is based on published and well documented results which were generated by Wang and Herrmann (1980) using a complete spectral method. Their method is based upon using the locked mode contribution without a cap layer as well as a numerical integral of the branch cuts and I consider their method to be one of the most complete and error free methods which I could compare against.

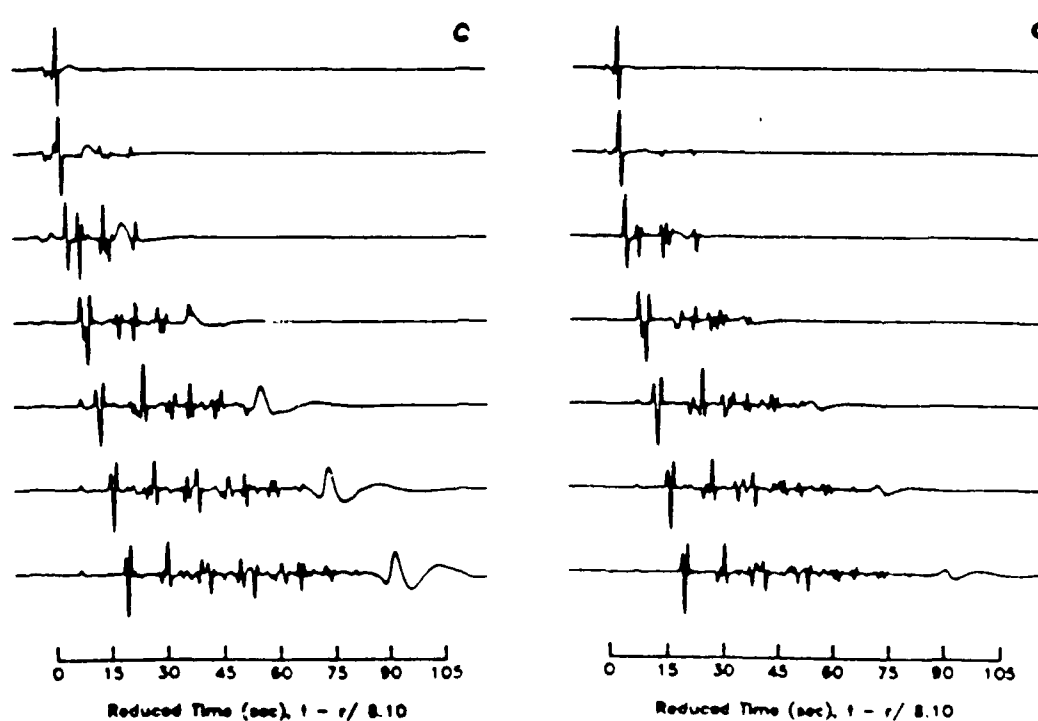
Figure 4-9 shows a comparison of synthetic seismograms using the locked mode approximation with seismograms produced by the complete spectral method of Wang and Herrmann. Figures 4-9(a) and 4-9(b) came directly from Wang and Herrmann's paper and show the vertical and radial component ground velocities due to a center of compression source at a depth of 10 km in a simple layer over a half space structural. The frequency

Figure 4-9. A comparison of synthetic seismograms produced by the locked mode approximation and the complete spectral method of Wang and Herrmann (1980). A direct copy of Fig. 7 from page 1030 of Wang and Herrmann is shown as (a) and (b) which are the vertical and radial component ground velocities due to a center of compression source at a depth of 10 km. The comparison ground velocity traces using the locked mode approximation are shown in (c) and (d).





Source: Wang, C., and Herrmann, R., 1980, A numerical study of P-, SV-, and SH-wave generation in a plane layered medium: Bulletin of the Seismological Society of America, v. 70, p. 1015-1036.



bandwidth was 0 to 1.25 Hertz and the seismograms were computed at seven receiver locations with source-receiver distances of 25, 50, 100, 200, 300, 400 and 500 km which are labelled beside the traces in figures 4-9(a) and 4-9(b). The times for each trace were reduced by 8.1 km/sec which is close to the half space P wave velocity. Figures 4-9(c) and 4-9(d) are the corresponding vertical and radial component ground velocities using the locked mode approximation. I placed the cap layer at a depth of 500 km and the structural model used to compute these seismograms is given in table 4-4. I used a phase velocity filter with a ramping cutoff from 9 to 10 km/sec.

The agreement between these two methods is very good except for the vertical component at distances of 25 and 50 km and the radial component at a distance of 25 km. In these case there are small arrivals which can be seen in the latter part of the seismic coda for the complete spectral method which are absent with the locked mode approximation. These correspond to multiple reflections in the top layer which arrive at the free surface with steep incidence angles and which have high horizontal phase velocities. Since I applied a phase velocity filter to remove potential cap layer reflections these legitimate arrivals were also filtered out and this illustrates one of the major sources of error with the locked mode approximation. The other major difference between the two methods is the presence of a truncation phase which can be seen moving away from the first P wave arrival in the negative time direction at distances of 25, 50 and 100 km for the locked mode approximation synthetics.

A completely independent comparison of the locked mode approximation with the complete spectral method of Wang and Herrmann and also with the generalized ray theory method was made by Herrmann and Wang

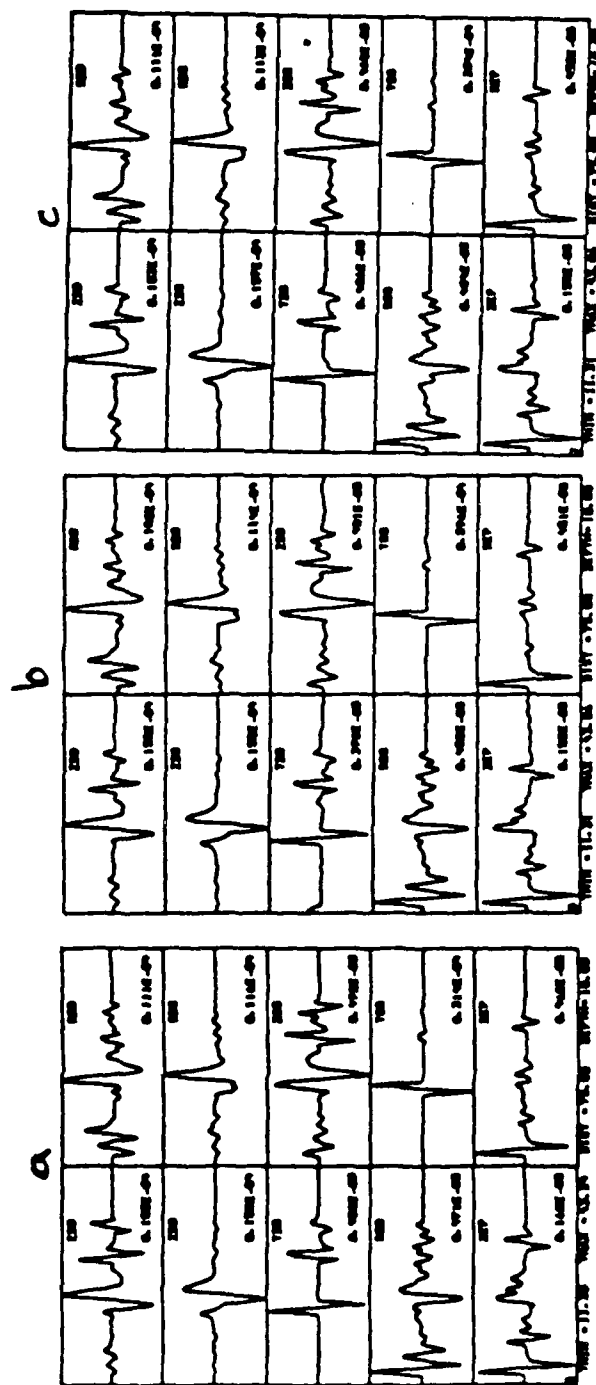
Table 4-4

## A Simple Two Layer Structural Model

Layer no.	Thickness (km)	$\alpha$ (km/sec)	$\beta$ (km/sec)	$\rho$ (gm/cc)
1	40	6.15	3.55	2.8
2	460	8.09	4.67	3.3
Half Space	-	20.0	15.0	5.0

(1985) using the same basic structural model as in table 4-4. Figure 4-10 shows the results of this comparison and these traces are copied directly from Herrmann and Wang's paper. There are three sets of synthetic time traces and each set corresponds to one of the three methods which was used. Each set consists of ten time traces and Herrmann and Wang show how all three components of a synthetic seismogram due to an arbitrarily oriented double couple point source can be composed of a linear combination of these ten traces. All of these traces were produced with a source at 10 km depth and a source-receiver distance of 75 km and the frequency bandwidth was 0 to 2 Hertz. Figure 4-10(a) shows the results using the generalized ray theory method (Cagniard-de Hoop), figure 4-10(b) shows the results using the locked mode approximation and figure 4-10(c) shows the results using the complete spectral method of Wang and Herrmann (1980). The structural model used for the ray theoretical and the complete spectral methods was the same as the structure in table 4-4 without the cap layer. The structural model used by the locked mode approximation was the same as in table 4-4 except that the cap layer was put at a depth of 240 km and the cap layer S wave velocity was 10 km/sec.

Herrmann and Wang used their own implementation of the locked mode approximation and I present their results only to confirm the validity of the approximation. Once again the comparison between the locked mode approximation and the complete spectral method is very good. Also for this simple structural model we can see that the comparison between the two complete solution methods and the generalized ray theory method is good.



Source: Herrmann, R., and Wang, C., 1985, A comparison of synthetic seismograms: Bulletin of the Seismological Society of America, v. 75, p. 41-56.

Figure 4-10. A comparison of synthetic seismograms produced by three different methods. This is a direct copy of figures 6, 8 and 7 in that order on pages 52 and 53 of Herrmann and Wang (1985). Synthetic time traces produced by the generalized ray theory method are shown in (a), the locked mode approximation are shown in (b) and the complete spectral method of Wang and Herrmann (1980) are shown in (c).

The errors which are introduced by the locked mode approximation fall into two categories; spurious cap layer reflections and the effects of truncating the mode sum. As we have seen it is possible to minimize the cap layer contamination of the synthetic seismograms by applying phase velocity filters. The problem with this is that the narrower the phase velocity filter, the larger will be the mode truncation error, so it would seem that we end up trading off one source of error against the other. If we look at the truncation error by itself we can see that it becomes smaller for a fixed phase velocity bandpass as the source-receiver distance is increased. The reason for this is that as the receiver is moved away from the source, the elastic energy which propagates between the two travels in a more horizontal direction and thus has a lower horizontal phase velocity associated with it. By choosing the phase velocity cutoff to be slightly higher than the highest P wave velocity, we insure that all horizontally propagating seismic energy will be included in the truncated mode sum and this is verified by the extremely good comparison of the synthetic seismograms in figure 4-9 as the distance increases.

As the receiver is moved towards the source, the elastic energy which propagates between the two travels in a more vertical direction and clearly, at some point, important arrivals will no longer be contained in the truncated mode sum. We can first notice this in figure 4-9 at a distance of 50 km and this source of error becomes more pronounced as the distance decreases. In these situations it is advisable to increase the bandpass of the phase velocity filter which will cause the truncated mode sum to contain energy which propagates at steeper incidence angles. Unfortunately this remedy will only work to a limited extent since, at some small value of the source-receiver distance, the cap layer reflections will come in at nearly the

same horizontal phase velocities as the desired elastic energy. I have found that for typical earthquake depths the minimum source-receiver distance at which the locked mode approximation can be used is about 10 km.

The only limiting factor on the maximum source-receiver distance is the computer run time. As I have shown the locked mode approximation becomes more accurate as the distance increases until we reach the distance where a cap layer reflection phase velocity falls below the cutoff phase velocity. I refer to this maximum distance as the cutoff distance and we can arbitrarily increase the cutoff distance by moving the cap layer down. The number of modes in the 0 to 10 km/sec phase velocity range at a fixed frequency is roughly proportional to the depth of the cap layer so we can increase the cutoff distance by increasing the cap layer depth which will increase the total number of modes which will increase the computer time needed to compute those modes.

Similarly the maximum frequency is only limited by the computer run time. The number of modes for a fixed cap layer depth and a fixed phase velocity range are directly proportional to the frequency. I have found that for typical continental crust and upper mantle structural models there are about 0.6 modes per Hertz per km of depth to the cap layer in the phase velocity range of 0 to 10 km/sec.

$$N_{\text{freq}} = 0.6 f H$$

where

- $N_{\text{freq}}$  = no. of modes per frequency in the 0-10 km/sec phase velocity range
- $f$  = frequency in Hertz
- $H$  = depth to the cap layer in km

In the next chapter I will be showing a number of examples showing synthetic seismograms which were computed with the locked mode approximation and I will be making comparisons between synthetic seismograms and observed data.



## CHAPTER V

### NUMERICAL EXAMPLES OF THE LOCKED MODE APPROXIMATION

I have used the locked mode approximation to compute many thousands of synthetic seismograms and in this chapter I will show some of these seismograms. I will start by showing a number of synthetic seismograms which demonstrate the properties of elastic wave propagation in layered structural models which can be seen when using a complete solution method. I will then show a comparison of synthetic and real seismograms for a nuclear explosion which took place in northern New Mexico.

The first example I will show is a more complete version of the vertical component seismograms which I computed to use in the comparison of section 4.5 and these are shown in figure 5-1. There are 100 synthetic seismograms in this figure and I have reduced the times for each trace by the P wave velocity of the top layer. The trace to trace amplitudes are correct however I applied a gain factor to each trace which was equal to the source-receiver distance in order to remove the geometric spreading effect. As we can see, even for a simple layer over a half space structural model, the seismograms can get complicated as the distance increases. This figure allows us to get a good look at the truncation phase which is moving away from the first P wave arrival, at zero reduced time, towards the negative time direction. The truncation phase does not become completely separate from the first P wave arrival until a distance of about 75 km but its amplitude decreases rapidly at distances above 100 km. We can also notice the

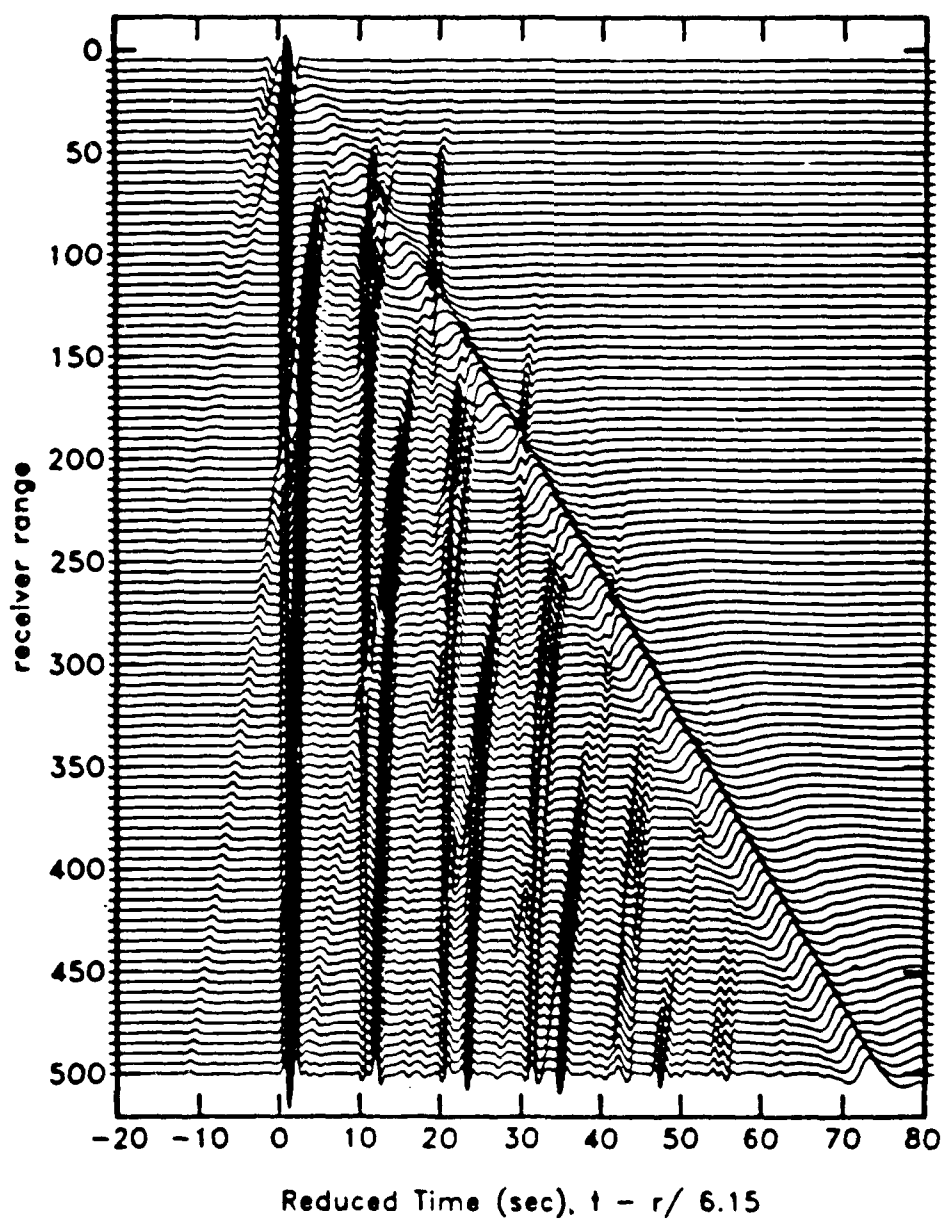
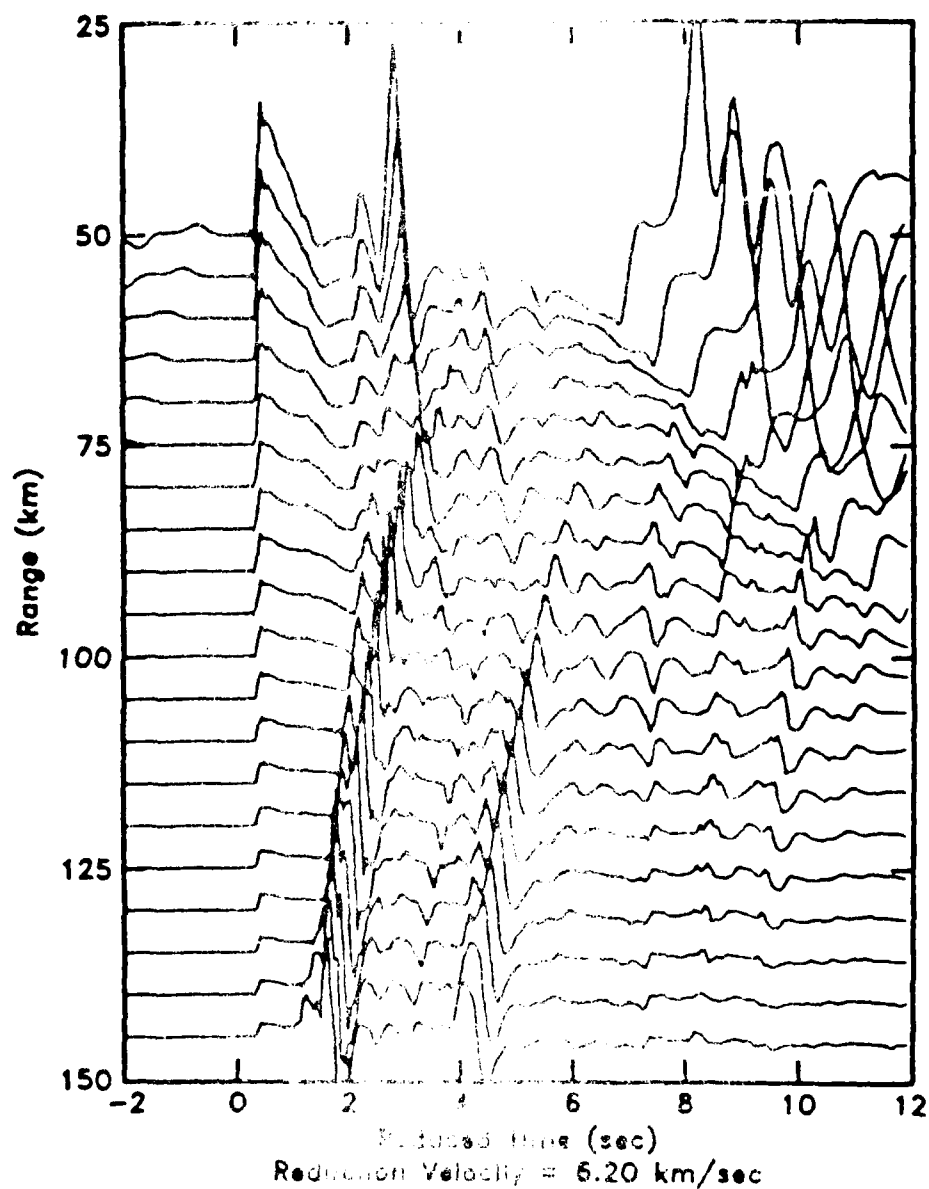


Figure 5-1. Vertical velocity ground motion produced by the locked mode approximation for the structural model given in table 4-4. These seismograms directly compare to those shown in figure 4-9.

rapid decrease in amplitudes of the multiple reflections as the distance goes to zero which is part of the mode truncation effect. All of these seismograms were computed over a frequency bandwidth of 0 to 1.25 Hertz.

Figure 5-2 shows vertical displacement seismograms which were computed over a much higher frequency bandwidth of 0 to 8 Hertz. These seismograms were generated using the southern California structural model given in table 4-2 for a strike slip relaxation source at a depth of 7 km. The source relaxation radius was 0.5 km and the phase velocity cutoff was set to 9 km/sec. Once again the first several traces show the truncation phase prior to the first P wave arrival but this spurious phase moves away from the P wave arrival and decreases in amplitude as the distance increases. The head wave nature of the direct P arrival is obvious and we can see a large number of ray arrivals which we would expect for a complex structural model and at high frequency.

Locked mode synthetic  $P_g$  codas are shown in figure 5-3 for distances of 300 to 450 km and for an explosion source with an elastic radius of 0.6 km and at a depth of 1 km. These synthetics were generated using the thick version of the southern California structure and they have a bandwidth of 4 Hertz. The vertical displacements were filtered with the response of a Benioff 1 second short period seismograph to produce the resulting seismograms. The most obvious feature is the strong  $P_g$  phase and trailing coda which is observed throughout the western United States. Unlike the previous example there are no clearly discernible ray arrivals contained in the coda and it is quite likely that a very large number of rays would be necessary to reproduce this coda. This is a good example of seismic coda synthesis without using lateral scattering.



**Figure 5-2.** Vertical ground motion predicted by the locked mode approximation for the southern California structure model. These seismograms were generated with a strike slip relative source at a depth of 7 km and the frequency bandwidth is 8 hertz.

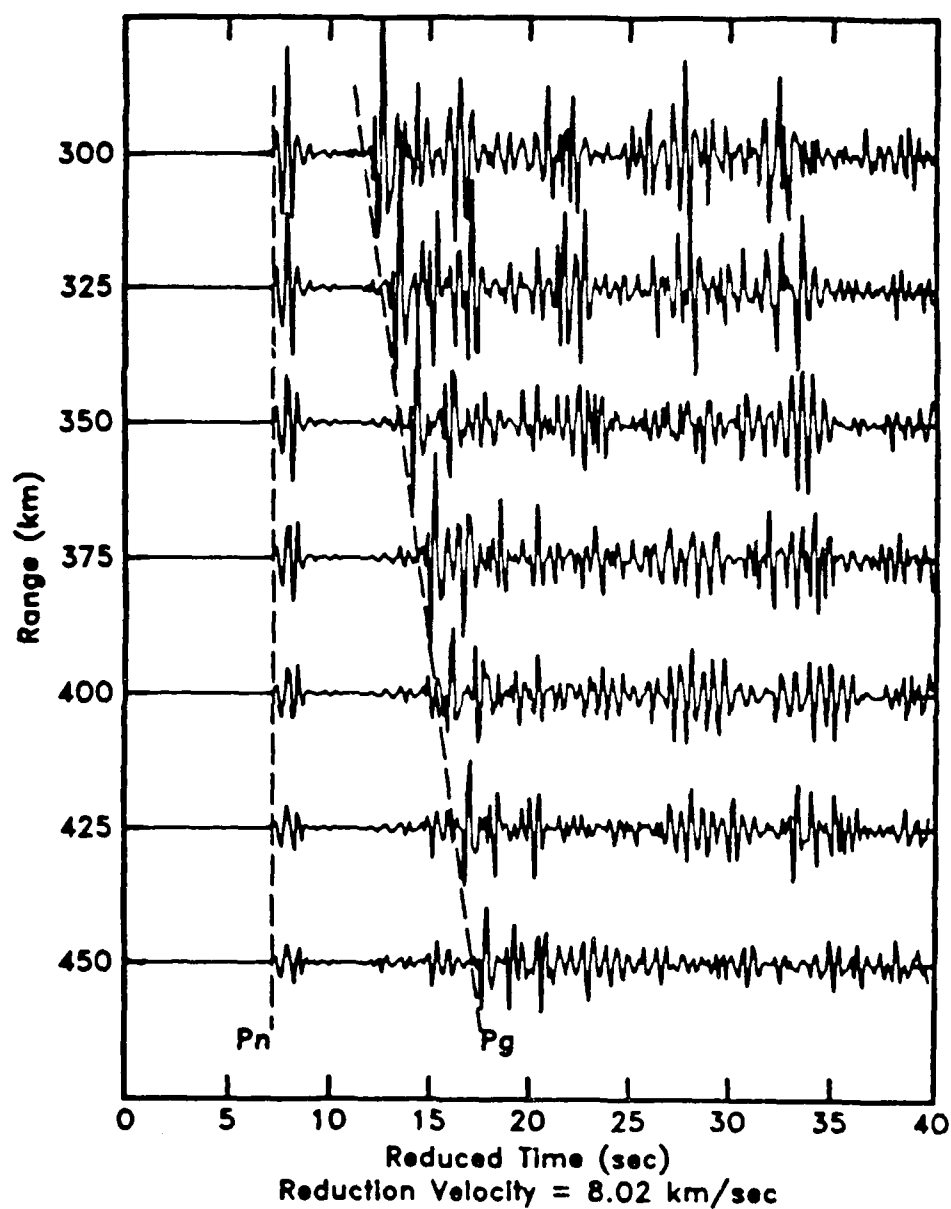


Figure 5-3. Vertical component synthetic seismograms produced by the locked mode approximation for the southern California structure model.  $P_g$  codas for an explosion source at 1 km depth.

There are similarities between the examples shown in figures 5-2 and 5-3 and the synthetic traces shown in figure 5-1. The southern California structural model has a high velocity crust which matches the velocity of the top layer in the layer over a half space model used by Wang and Herrmann. All of the synthetic seismograms show an energetic  $P_g$  and a rather weak  $P_n$  and the major effect of making the model more complex is to introduce more noticeable scattering in the synthetic seismograms. The next example is for a crustal model which has had a very thin and low velocity alluvial layer added to the top and a thicker but slightly higher velocity layer inserted which represents a sandstone stratigraphic sequence and which would be characteristic of the Colorado plateau. This particular model is intended to represent the border between Colorado and Utah and has been used to model underground nuclear explosions which took place in western Colorado. The structural model, which I refer to as the Rulison model, is given in table 5-1 and the Q model which was used is given in table 5-2.

A set of fifty synthetic seismograms were generated using the locked mode approximation and these are shown in figures 5-4 and 5-5 which give the vertical and radial components of the ground velocity due to an explosion source at a depth of 2.5 km. There is a marked difference between these synthetic seismograms and the examples which preceded them. The  $P_g$  phase which would normally be traveling at about 6 km/sec is almost entirely missing in figures 5-4 and 5-5 and instead there is a rather strong  $P_n$  phase and a low velocity arrival with an attached coda. Because of the thick low velocity sedimentary layers at the top of the structure, the seismic energy is being trapped within these layers and the low velocity

Table 5-1

## The Rulison Structural Model

Layer no.	Thickness (km)	$\alpha$ (km/sec)	$\beta$ (km/sec)	$\rho$ (gm/cc)
1	0.2	2.50	1.50	2.25
2	1.7	3.80	2.10	2.30
3	3.6	4.60	2.46	2.35
4	19.5	6.00	3.50	2.80
5	15.0	6.60	3.85	2.84
6	10.0	8.00	4.60	3.30
7	10.0	8.10	4.65	3.35
8	20.0	7.95	4.45	3.25
9	30.0	7.80	4.20	3.24
10	20.0	7.95	4.45	3.25
11	20.0	8.35	4.80	3.40
Half Space	-	20.0	10.0	3.60

Table 5-2

## The Rulison Q Model

Layer no.	$Q_\alpha$	$Q_\beta$
1	300	180
2	400	230
3	800	380
4	2000	880
5	3000	1100
6	4000	1800
7	6000	2700
8	800	380
9	400	230
10	800	380
11	9000	4000
Half Space	9000	4000



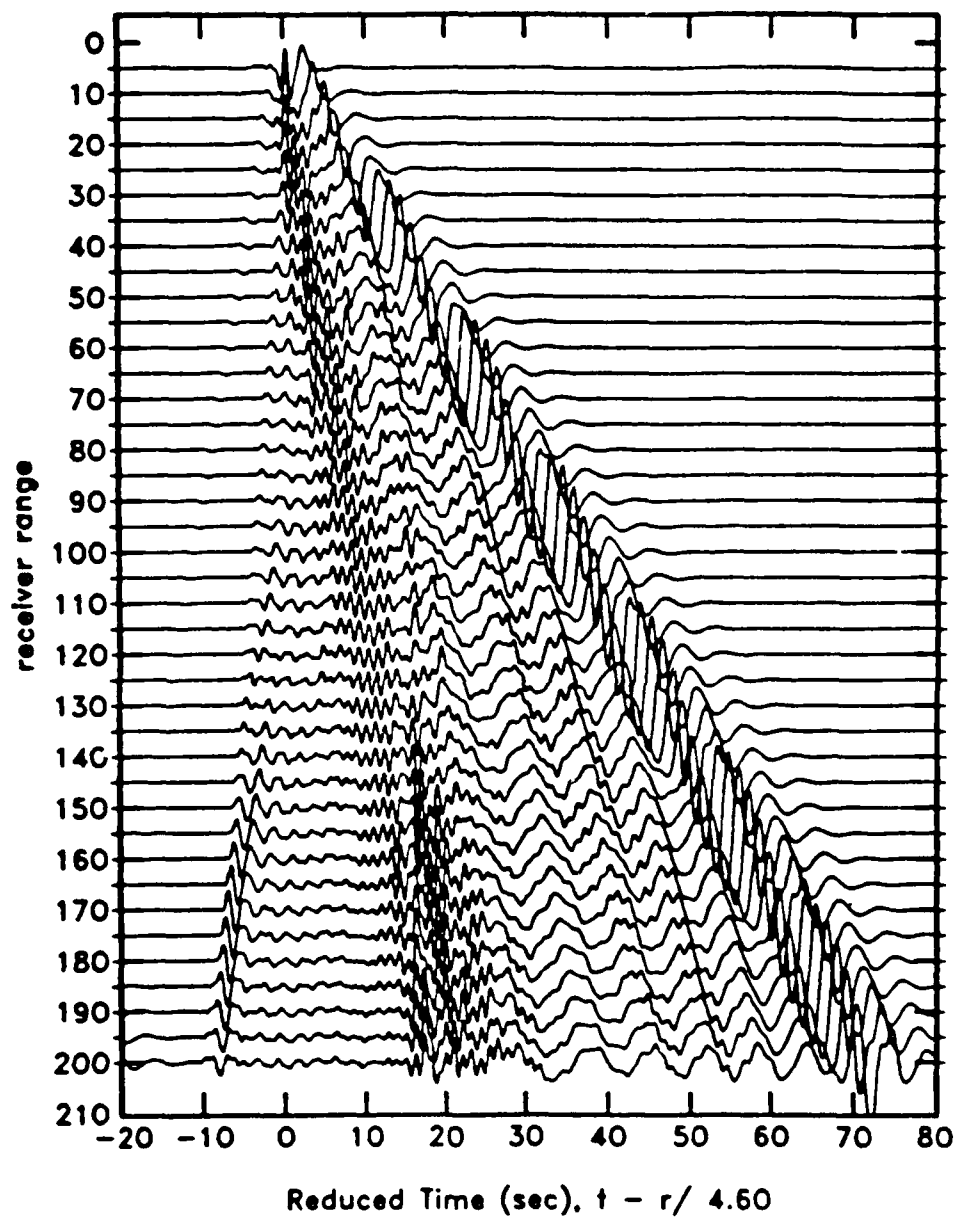


Figure 5-4. Vertical velocity ground motion produced by the locked mode approximation for the Rulison structure model. These seismograms were generated with an explosion source at 2.5 km depth and for a bandwidth of 1.25 Hertz.

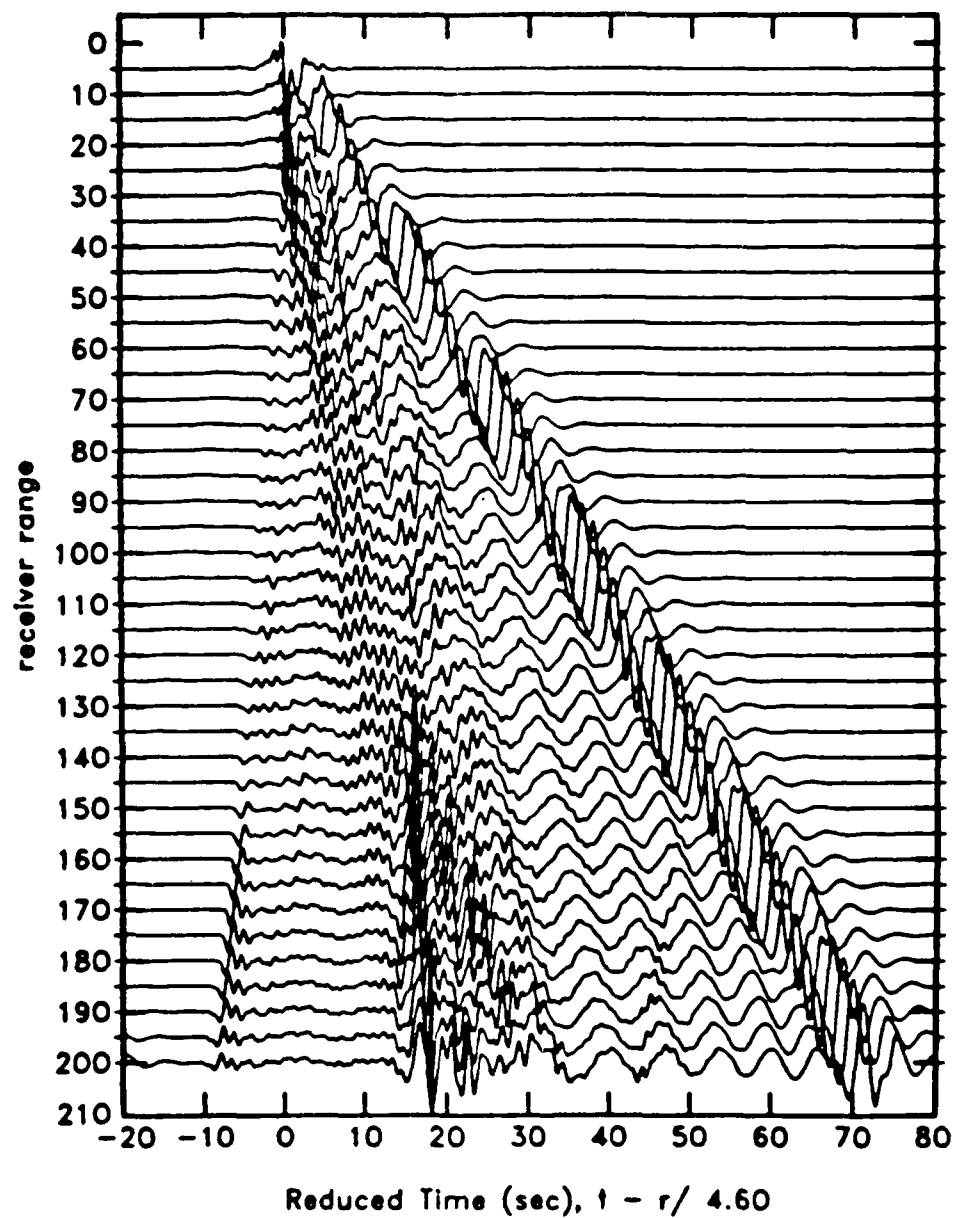


Figure 5-5. Radial velocity ground motion produced by the locked mode approximation for the Rulison structure model. These seismograms were generated with an explosion source at 2.5 km depth and for a bandwidth of 1.25 Hertz.

arrival represents channeled seismic energy within the sediments. This channeled energy would normally be propagating through the lower granitic part of the crust, if the sediments weren't there, which would show up as  $P_g$  energy, but in this case the upper sedimentary layers trap the energy in an efficient manner. The apparent acausal arrivals at 200 km distances are actually the tail end of the seismic coda which has been wrapped around.

In the final example I will be comparing synthetic seismograms produced by the locked mode approximation with real observed data for the Gasbuggy underground nuclear explosion which took place in northern New Mexico. This work was done by myself and Jack R. Murphy of S-Cubed in Reston, Virginia and was presented at the annual meeting of the Seismological Society of America in April of 1982. I provided Mr. Murphy with my programs and assisted him in generating the synthetic seismograms which he required for the comparison. The structural model used for this study is similar to the Rulison model and is given in table 5-3. Synthetic seismograms were generated for a bandwidth of 10 Hertz and for a Mueller-Murphy explosion source at a depth of 1.293 km.

The comparisons of the radial ground velocity at two stations is shown in figure 5-6. Considerable effort was expended to arrive at the correct source parameters and to come up with a  $Q$  model which would match the synthetic spectra to the spectra of the data. Although there certainly is not a wiggle for wiggle match, the overall strength and duration of the coda matches rather well and the major conclusions of this study were that the locked mode approximation could be used to invert for source parameters and local attenuation.

Table 5-3

## The Gasbuggy Structural Model

Layer no.	Thickness (km)	$\alpha$ (km/sec)	$\beta$ (km/sec)	$\rho$ (gm/cc)
1	1.2	3.90	1.90	2.43
2	3.1	4.10	2.46	2.58
3	20.7	6.20	3.62	2.80
4	15.0	6.60	3.85	2.84
5	30.0	8.00	4.60	3.30
Half Space	-	20.0	15.0	5.00

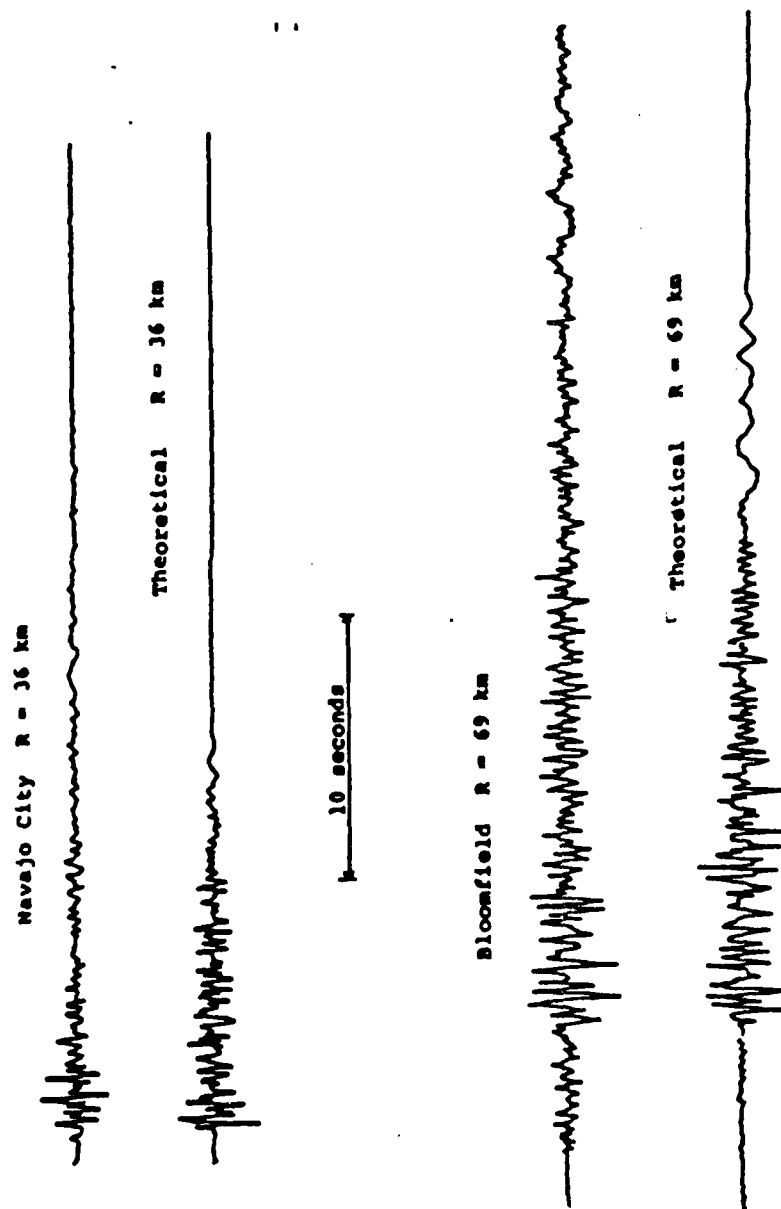


Figure 5-6. A comparison of synthetic and observed Gasbuggy partial velocity seismograms.

This last example points out a major problem which exists when trying to model high frequency elastic wave propagation through the real earth. Even in a case such is this one in which the source parameters were well constrained and the structural model was well known and was reasonably close to being flat and plane layered, it was impossible to obtain wiggle for wiggle matches of the synthetic and real seismograms in the 10 Hertz frequency bandwidth without undertaking a lengthy study which would have involved such things as parametric changes in the structural model, more complicated source modelling to account for tectonic release, etc. The problem of matching complete solution synthetic seismograms with real data for complex sources and structural models and at high frequencies is formidable and can easily be more difficult than the theoretical problems which have to be solved to produce the synthetic seismograms. There is no tractable and systematic method which can use forward seismogram synthesis to invert for the source and structural parameters when these parameters are not well constrained.

In the last chapter I will conclude this dissertation by making a qualitative comparison of the locked mode approximation with other synthesis methods and I will discuss the possibilities of future research in this area.

## CHAPTER VI

### CONCLUDING REMARKS

In order for any new seismogram synthesis method to be generally useful to the seismological community, the advantages and disadvantages of the method must be identified, and the parameter space within which the method will produce accurate results must be determined. I have shown that the spectral method which I developed and refer to as the locked mode approximation works best, for problems in earthquake and nuclear explosion seismology, in the 50 to 500 km distance range and the method can be pushed into the 10 to 50 km and 500 to 1000 km distances ranges. I have also developed numerical algorithms which can handle virtually any structural model and frequency bandwidth. In this final chapter I will make a qualitative comparison of the locked mode approximation with the other seismogram synthesis methods and I will discuss issues, such as efficiency and ease of use, which I have not addressed previously. I will finally remark on the logical extensions of my research.

I feel that the only way a definitive and quantitative comparison could be made among a set of seismogram synthesis methods would be to obtain the computer programs for each method and execute these programs on the same computer and for a set of representative wave propagation problems. One would then evaluate the relative merits of the methods based on the accuracy of the results, the amount of computer time and space needed to produce the results and the amount of human interaction needed

to specify the input parameters and to run the programs. From time to time someone will make a comparison study and publish the results (e.g. Herrmann and Wang (1985)) however the issues of human interaction and computer time are rarely discussed and usually these studies focus on accuracy comparisons as I did in section 4.5.

There has only been one occasion on which I was able to make a direct comparison of the locked mode approximation with two other seismogram synthesis methods on the same computer and for the same wave propagation problem. The structure was a 17 layer very near surface model and this was a geophysical exploration problem which involved very high frequencies (to 130 Hertz) and very small source-receiver distances (0.1 to 1 km). I computed complete synthetic seismograms using the locked mode approximation for 100 different receivers. I also computed synthetic seismograms using the reflectivity method developed by Kennett (1980) at the 100 receiver locations. For this particular problem all of the early arriving energy was propagating at very steep incidence angles and Kennett's program was run with a narrow slowness window which was adequate to synthesize the first part of the seismic coda. The two methods gave good agreement for the first part of the coda except at the smallest distances where the locked mode approximation broke down due to the very high phase velocities of the propagating seismic energy. The middle and end parts of the seismic coda were completely missing however from the synthetic seismograms produced by the reflectivity program and this was due to the narrow range of integration in the slowness domain which was used. The reason I kept the range of integration so small was that the computer run time would have been prohibitive had I integrated over the entire slowness axis. I estimated that the reflectivity method would have taken about 20



times longer to run than the locked mode approximation had the slowness integral been extended to include the same phase velocity range as that used by the locked mode approximation.

After obtaining complete solutions I displayed them and discovered that the early part of the coda could be explained by a relatively small number of ray arrivals (about fifteen). I computed ray travel time curves and overlaid these on the synthetic seismograms and by trial and error I was able to determine just which ray paths were important. I then took this information and used the WKBJ ray theoretical method of Chapman (1978) to synthesize ray theoretical seismograms. As with Kennett's method, the comparison was quite good for the first part of the coda and Chapman's method ran many orders of magnitude times faster than the locked mode approximation. It took much more of my own time however to set up and run the ray theoretical programs than it did to run my own program.

Clearly, from a human interaction standpoint, complete solution methods are rather straightforward in terms of the required inputs to run the programs whereas ray theoretical programs require ray path specifications and it can take a lot of human time to determine which ray paths are important for complicated structural models. For the comparison that I just mentioned, the seismic energy was propagating in a nearly vertical direction so it was relatively easy to determine the important ray paths. Had I moved the receiver out to 5 km distance, it would have been virtually impossible to determine the important ray paths and I suspect that an enormous number of rays would be necessary to match the complete solution. Even assuming that the important ray paths could be automatically determined and specified, as the distance increases, the number of important rays increase and,

at some point, the number of important rays will exceed the number of modes required by the locked mode approximation. When the number of necessary rays becomes excessive, the ray theoretical methods will no longer offer an advantage in computer run time.

I felt that the primary reason for developing a new complete seismogram synthesis method, based upon a spectral solution of the elastic wave equation, was to increase the efficiency of seismogram synthesis over that of complete solution methods which were available when I started my research. The method which is most often used to compute complete solutions is the reflectivity method and based upon the comparison with Kennett's program it would seem that I succeeded. The basic reason that the reflectivity method runs so much slower is the use of numerical integration to evaluate the wavenumber integral of the inverse Hankel transform. The wavenumber integrand function is very much influenced by its singularities which are the normal mode poles and the integrand function goes through one oscillation as it goes by a pole. The wavelengths of these oscillations will be equal to the average pole spacing in a particular region of the complex wavenumber plane. In order for a numerical integration of this function to produce accurate results, the function must be sampled a sufficient number of times over the wavelength of the oscillations. It would be very unlikely that a numerical integration could achieve sufficient accuracy if the integrand function were sampled less than ten times per oscillation. Also with the reflectivity method, the wavenumber sampling, which is necessary to accurately approximate the wavenumber integrals, must be carried through all the way to the evaluation of the Bessel functions at each source-receiver.

The mode searching algorithm which I developed is able to locate each pole with about fifteen evaluations of the characteristic function. This is about the same as the number of times one would have to evaluate the integrand function between two poles in order to apply the reflectivity method however it is much less expensive to compute the characteristic function than it is to compute the complete integrand function and this is why the locked mode method is faster. Also it allows us to concentrate the effort to increase the efficiency even more in one place, namely in the mode searching algorithm. I have stated repeatedly in this dissertation that the development of an efficient, accurate and reliable mode searching algorithm was absolutely necessary in order for the locked mode method to be a viable alternative to other complete solution methods. I also have a strong suspicion that this has been a stumbling block for other researchers who have used the spectral method and I have an even stronger suspicion that my flat earth normal mode searching algorithm is the most efficient, reliable and accurate algorithm of its type in the world today.

I will conclude this dissertation by briefly discussing the logical extensions of my research. Probably the most obvious and effective way to improve the efficiency of the method would be to try to increase the efficiency of the mode searching algorithm. It would appear that the most I could ever hope to achieve would be about a factor of five improvement in efficiency and I am sure such an increase would be well worth the effort. I think the most likely way to achieve this would be to use a first or second order extrapolation of the dispersion curves to the next adjacent frequency and then use these estimates of the eigen phase velocities to directly initialize the fine searching algorithm. Hopefully most of the poles would be located with just a few iterations and then a pass through the normal mode

searching algorithm would be made with all of the found poles removed to pick up those poles that were not found from the extrapolated estimates.

Another area of research which I have been looking at recently is to obtain a truly complete spectral solution for the plate problem. There are no branch cut integrals for layered plate structural models and so the complete solution can be represented as an infinite sum of discrete normal modes. The difficulty with plate problems is that the dispersion curves leave the real wavenumber axis and take off into the complex wavenumber plane and thus the locked mode method cannot provide a complete solution. I have recently been able to develop a different mode searching algorithm which can track the dispersion curves all the way back to zero frequency and follow them through the complex wavenumber plane. Once all of the complex eigenwavenumbers have been found the procedure for computing synthetic seismograms is identical to the methods I have given here except that all of the arithmetic is complex. The plate method offers some advantages over the locked mode method. First, it allows for the proper modelling of vertically propagating elastic energy. Second, it allows for exact modelling of frequency dependent anelastic attenuation. Third, it allows complex frequencies to be used which removes the time wrap around problem.

A final exotic area of research which I have done some work in is to develop a spectral method which uses the so called "leaking" modes. This method is based upon deforming the branch cut integrals to expose parts of the other Riemann sheets which contain poles with complex eigenwavenumbers. These are leaking modes and finding them is similar to finding complex plate modes. The obvious advantage of this method is that it maximizes the completeness of a spectral solution which does not include any numerical integrals without the necessity of introducing an artificial

reflecting boundary.

(

## REFERENCES

- Abo-Zena, A., 1979, Dispersion function computations for unlimited frequency values: *Geophysical Journal of the Royal Astronomical Society*, v. 58, p. 91-105.
- Achenbach, J., 1984, in, *Wave Propagation in Elastic Solids*, North-Holland, Amsterdam, 209 pp.
- Acton, F., 1970, in, *Numerical Methods that Usually Work*, Harper and Row, New York.
- Aki, K. and Richards, P., 1980, in, *Quantitative Seismology Theory and Methods*, v. 1, W. H. Freeman, San Francisco
- Bache, T. and Harkrider, D., 1976, The body waves due to a general seismic source in a layered earth model: 1. formulation of the theory: *Bulletin of the Seismological Society of America*, v. 66, p. 1805-1819.
- Ben-Menahem, A. and Singh, S., 1972, Computations of models of elastic dislocations in the earth: in, *Methods in Computational Physics*, v. 12, Academic Press, New York, p. 300-372.
- Ben-Menahem, A. and Singh, S., 1981, in, *Seismic Waves and Sources*, Springer-Verlag, New York.
- Bouchon, M., 1981, A simple method to calculate Green's functions for elastic layered media: *Bulletin of the Seismological Society of America*, v. 71, p. 959-971.
- Cormier, V., 1980, The synthesis of complete seismograms in an earth model specified by radially inhomogeneous layers: *Bulletin of the Seismological Society of America*, v. 70, p. 691-716.
- Dorman, J., Ewing, M. and Oliver, J., 1960, Study of the shear-velocity distribution in the upper mantle by mantle Rayleigh waves: *Bulletin of the Seismological Society of America*, v. 50, p. 87-115.
- Dunkin, J., 1965, Computation of modal solutions in layered elastic media at high frequencies: *Bulletin of the Seismological Society of America*, v. 55, p. 335-358.
- Fuchs, K. and Muller, G., 1971, Computation of synthetic seismograms with the reflectivity method and comparison with observations: *Geophysical*

- Journal of the Royal Astronomical Society, v. 23, p. 417-433.
- Gilbert, F., 1964, Propagation of transient leaking modes in a stratified elastic wave-guide: Reviews of Geophysics, v. 2, p. 123-154.
- Gilbert, F. and Backus, G., 1966, Propagator matrices in elastic wave and vibration problems: Geophysics, v. 31, p. 326-332.
- Harkrider, D., 1964, Surface waves in multi-layered elastic media I. Rayleigh and Love waves from buried sources in a multi-layered elastic half space: Bulletin of the Seismological Society of America, v. 54, p. 627-679.
- Hartzell, S. and Helmberger, D., 1982, Strong-motion modelling of the Imperial valley earthquake of 1979: Bulletin of the Seismological Society of America, v. 72, p. 571-596.
- Harvey, D., 1981, Seismogram synthesis using normal mode superposition: the locked mode approximation: Geophysical Journal of the Royal Astronomical Society, v. 66, p. 37-61.
- Haskell, N., 1953, The dispersion of surface waves on multilayered media: Bulletin of the Seismological Society of America, v. 43, p. 17-34.
- Herrmann, R. and Wang, C., 1985, A comparison of synthetic seismograms: Bulletin of the Seismological Society of America, v. 75, p. 41-56.
- Hudson, J., 1969, A quantitative evaluation of seismic signals at teleseismic distances - II. body waves and surface waves from an extended source: Geophysical Journal of the Royal Astronomical Society, v. 18, p. 353-370.
- Kanamori, H. and Hadley, D., 1975, Crustal structure and temporal velocity change in southern California: Pure and Applied Geophysics, v. 113, p. 258-280.
- Kazi, M., 1976, Spectral representation of the Love wave operator: Geophysical Journal of the Royal Astronomical Society, v. 47, p. 225-249.
- Kennett, B., Kerry, N. and Woodhouse, J., 1978, Symmetries in the reflection and transmission of elastic waves: Geophysical Journal of the Royal Astronomical Society, v. 52, p. 215-230.
- Kennett, B. and Kerry, N., 1979, Seismic waves in a stratified half space: Geophysical Journal of the Royal Astronomical Society, v. 57, p. 557-583.
- Kennett, B., 1980, Seismic waves in a stratified half space - II. theoretical seismograms: Geophysical Journal of the Royal Astronomical Society, v. 61, p. 1-10.
- Kerry, N., 1981, Synthesis of seismic surface waves: Geophysical Journal of the Royal Astronomical Society, v. 64, p. 425-446.

- Kind, R., 1978, The reflectivity method for a buried source: *Journal of Geophysics*, v. 44, p. 603-612.
- Knopoff, L., 1964, A matrix method for elastic wave problems: *Bulletin of the Seismological Society of America*, v. 54, p. 431-438.
- Knopoff, L., Schwab, F. and Kansel, E., 1973, Interpretation of  $L_g$ : *Geophysical Journal of the Royal Astronomical Society*, v. 33, p. 389-404.
- Lapwood, E., 1949, The disturbance due to a line source in a semi-infinite elastic medium: *Philosophical Transactions of the Royal Society of London*, v. A242, p. 63-100.
- Liu, H., Anderson, D. and Kanamori, H., 1976, Velocity dispersion due to anelasticity: implications for seismology and mantle composition: *Geophysical Journal of the Royal Astronomical Society*, v. 47, p. 41-58.
- Mantovani, E., Schwab, F., Liuo, H. and Knopoff, L., 1977, Generation of complete theoretical seismograms for SH - II: *Geophysical Journal of the Royal Astronomical Society*, v. 48, p. 531-536.
- Nakanishi, K., Schwab, F. and Knopoff, L., 1977, Generation of complete theoretical seismograms for SH - I: *Geophysical Journal of the Royal Astronomical Society*, v. 48, p. 525-530.
- Press, F., Harkrider, D. and Seafeldt, C., 1961, A fast, convenient program for computation of surface-wave dispersion curves in multilayered media: *Bulletin of the Seismological Society of America*, v. 51, p. 495-502.
- Rosenbaum, J., 1960, The long-time response of a layered elastic medium to explosion sound: *Journal of Geophysical Research*, v. 65, p. 1577-1613.
- Rosenbaum, J., 1964, A note on the computation of Rayleigh wave dispersion curves for layered elastic media: *Bulletin of the Seismological Society of America*, v. 54, p. 1013-1019.
- Schwab, F. and Knopoff, L., 1970, Surface-wave dispersion computations: *Bulletin of the Seismological Society of America*, v. 60, p. 321-344.
- Sezawa, K., 1931, On the transmission of seismic waves on the bottom surface of an ocean: *Bulletin of the Earthquake Research Institute Tokyo Imperial University*, v. 9, p. 115-142.
- Stevens, J., 1980, Seismic radiation from the sudden creation of a spherical cavity in an arbitrarily prestressed elastic medium: *Geophysical Journal of the Royal Astronomical Society*, v. 61, p. 303-328.
- Swanger, H. and Boore, D., 1978, Simulation of strong-motion displacements using surface-wave modal superposition: *Bulletin of the Seismological Society of America*, v. 68, p. 907-922.



- Takeuchi, H. and Saito, M., 1972, Seismic surface waves: in, *Methods in Computational Physics*, v. 11, Academic Press, New York, p. 217-295.
- Thomson, W., 1950, Transmission of elastic waves through a stratified solid medium: *Journal of Applied Physics*, v. 21, 89 pp.
- Wang, C. and Herrmann, R., 1980, A numerical study of P-, SV-, and SH-wave generation in a plane layered medium: *Bulletin of the Seismological Society of America*, v. 70, p. 1015-1036.
- Watson, T., 1970, A note on fast computation of Rayleigh wave dispersion in the multi-layered elastic half space: *Bulletin of the Seismological Society of America*, v. 60, p. 161-166.

## APPENDIX A

### A METHOD OF REDUCING THE DYNAMIC RANGE OF THE [R] MATRIX ELEMENTS

The [R] matrix elements given by equations (3.1.20) involve trigonometric sine and cosine functions of the vertical wavecycle functions  $\theta_\alpha$  and  $\theta_\beta$  which are given by equations (2.4.45). These wavecycle functions are equal to the product of the vertical wavenumber and the layer thickness to give the number of wave cycles in the vertical direction expressed in radians over the layer thickness. Whenever the horizontal phase velocity is less than a particular layer P or S wave velocity, then the corresponding wave in that layer will be evanescent in the vertical direction and the wavecycle function for that layer and wave type will be purely imaginary. In these situations the sines and cosines of imaginary arguments will become hyperbolic sines and cosines of real arguments.

$$\sin(\theta_{\alpha\beta}) = i \sinh(\bar{\theta}_{\alpha\beta}) \quad (\text{A.1})$$

$$\cos(\theta_{\alpha\beta}) = \cosh(\bar{\theta}_{\alpha\beta})$$

$$\text{where } \theta_{\alpha\beta} = i \bar{\theta}_{\alpha\beta}$$

I am using the notation  $\alpha\beta$  to simply mean  $\alpha$  or  $\beta$ . The hyperbolic sines and cosines grow exponentially with  $\bar{\theta}_{\alpha\beta}$  which is the cause of the dynamic range problem.

Another less obvious problem which comes about when the horizontal phase velocity is less than a layer P or S wave velocity is that, if the [R] matrix elements are computed directly from equations (3.1.20), then the computations must be done using complex arithmetic which can significantly degrade the performance of the computer code however, assuming the frequency, horizontal phase velocity, and layer P and S wave velocities are all real, all of the numbers in the [R] matrix element computations are either purely real or purely imaginary. In order to avoid complex arithmetic on the computer we redefine the functions  $\phi_\alpha$ ,  $\phi_\beta$ ,  $\theta_\alpha$ , and  $\theta_\beta$  given by equations (2.4.42) and (2.4.45) by the following.

$$\hat{\phi}_\alpha = \begin{cases} \phi_\alpha & \text{for } c > \alpha \\ i \phi_\alpha & \text{for } c < \alpha \end{cases} \quad (\text{A.2})$$

$$\hat{\phi}_\beta = \begin{cases} \phi_\beta & \text{for } c > \beta \\ i \phi_\beta & \text{for } c < \beta \end{cases}$$

$$\hat{\theta}_\alpha = \begin{cases} \theta_\alpha & \text{for } c > \alpha \\ i \theta_\alpha & \text{for } c < \alpha \end{cases} \quad (\text{A.3})$$

$$\hat{\theta}_\beta = \begin{cases} \theta_\beta & \text{for } c > \beta \\ i \theta_\beta & \text{for } c < \beta \end{cases}$$

It is obvious that the redefined functions are always real. Also note that when a redefined function is greater than or equal to zero than the original function was real and if the redefined function is less than zero then the ori-

ginal function was imaginary.

We next need to modify the trigonometric functions in the  $[R]$  matrix elements in order to avoid the dynamic range problem. We can do this by dividing the trigonometric functions by a normalizing function which is equal to the hyperbolic cosine when  $\theta_\alpha$  or  $\theta_\beta$  is imaginary and unity when  $\theta_\alpha$  or  $\theta_\beta$  is real. This normalizing function is always positive and never less than one and we drop it in the characteristic function computation since it does not effect the zeroes of the characteristic function. The normalized trigonometric functions are given below.

$$\left. \begin{aligned} \text{SN}(\hat{\theta}_\alpha) &= \sin(\hat{\theta}_\alpha) \\ \text{CS}(\hat{\theta}_\alpha) &= \cos(\hat{\theta}_\alpha) \\ \text{NORM}_\alpha &= 1 \end{aligned} \right\}, \text{ for } \hat{\theta}_\alpha > 0 \quad (\text{A.4})$$

$$\left. \begin{aligned} \text{SN}(\hat{\theta}_\alpha) &= -\tanh(\hat{\theta}_\alpha) \\ \text{CS}(\hat{\theta}_\alpha) &= 1 \\ \text{NORM}_\alpha &= \cosh(\hat{\theta}_\alpha) \end{aligned} \right\}, \text{ for } \hat{\theta}_\alpha < 0$$

$$\left. \begin{aligned} \text{SN}(\hat{\theta}_\beta) &= \sin(\hat{\theta}_\beta) \\ \text{CS}(\hat{\theta}_\beta) &= \cos(\hat{\theta}_\beta) \\ \text{NORM}_\beta &= 1 \end{aligned} \right\}, \text{ for } \hat{\theta}_\beta > 0$$

$$\left. \begin{aligned} \text{SN}(\hat{\theta}_\beta) &= -\tanh(\hat{\theta}_\beta) \\ \text{CS}(\hat{\theta}_\beta) &= 1 \\ \text{NORM}_\beta &= \cosh(\hat{\theta}_\beta) \end{aligned} \right\}, \text{ for } \hat{\theta}_\beta < 0$$

We can now write down a scaled version of the original  $[R]$  matrix which we refer to as  $[\hat{R}]$  and the elements of  $[\hat{R}]$  are given as follows.

$$\begin{aligned} {}_R\hat{R}_{11}(z, z_0) = & -2\gamma(\gamma-1)N + (\gamma^2 + (\gamma-1)^2)CS(\hat{\theta}_\alpha)CS(\hat{\theta}_\beta) \\ & + (\gamma^2\hat{\phi}_\alpha\hat{\phi}_\beta - \frac{(\gamma-1)^2}{|\hat{\phi}_\alpha\hat{\phi}_\beta|})SN(\hat{\theta}_\alpha)SN(\hat{\theta}_\beta) \end{aligned} \quad (A.5)$$

$$\begin{aligned} {}_R\hat{R}_{12}(z, z_0) = & 2\rho c^2[-\gamma(\gamma-1)(2\gamma-1)(N-CS(\hat{\theta}_\alpha)CS(\hat{\theta}_\beta)) \\ & + (\gamma^3\hat{\phi}_\alpha\hat{\phi}_\beta - \frac{(\gamma-1)^3}{|\hat{\phi}_\alpha\hat{\phi}_\beta|})SN(\hat{\theta}_\alpha)SN(\hat{\theta}_\beta)] \end{aligned}$$

$${}_R\hat{R}_{13}(z, z_0) = \rho c^2[-\gamma^2\hat{\phi}_\alpha SN(\hat{\theta}_\alpha)CS(\hat{\theta}_\beta) - \frac{(\gamma-1)^2}{|\hat{\phi}_\beta|}SN(\hat{\theta}_\beta)CS(\hat{\theta}_\alpha)]$$

$${}_R\hat{R}_{14}(z, z_0) = \rho c^2[+\frac{(\gamma-1)^2}{|\hat{\phi}_\alpha|}SN(\hat{\theta}_\alpha)CS(\hat{\theta}_\beta) + \gamma^2\hat{\phi}_\beta SN(\hat{\theta}_\beta)CS(\hat{\theta}_\alpha)]$$

$$\begin{aligned} {}_R\hat{R}_{15}(z, z_0) = & \rho^2 c^4[2\gamma^2(\gamma-1)^2(N-CS(\hat{\theta}_\alpha)CS(\hat{\theta}_\beta)) \\ & - (\gamma^4\hat{\phi}_\alpha\hat{\phi}_\beta - \frac{(\gamma-1)^4}{|\hat{\phi}_\alpha\hat{\phi}_\beta|})SN(\hat{\theta}_\alpha)SN(\hat{\theta}_\beta)] \end{aligned}$$

$$\begin{aligned} {}_R\hat{R}_{21}(z, z_0) = & \frac{1}{\rho c^2}[(2\gamma-1)(N-CS(\hat{\theta}_\alpha)CS(\hat{\theta}_\beta)) \\ & - (\gamma\hat{\phi}_\alpha\hat{\phi}_\beta - \frac{(\gamma-1)}{|\hat{\phi}_\alpha\hat{\phi}_\beta|})SN(\hat{\theta}_\alpha)SN(\hat{\theta}_\beta)] \end{aligned}$$

$$\begin{aligned} {}_R\hat{R}_{22}(z, z_0) = & N + 2[2\gamma(\gamma-1)(N-CS(\hat{\theta}_\alpha)CS(\hat{\theta}_\beta)) \\ & - (\gamma^2\hat{\phi}_\alpha\hat{\phi}_\beta - \frac{(\gamma-1)^2}{|\hat{\phi}_\alpha\hat{\phi}_\beta|})SN(\hat{\theta}_\alpha)SN(\hat{\theta}_\beta)] \end{aligned}$$

$${}_R\hat{R}_{23}(z, z_0) = +\gamma\hat{\phi}_\alpha SN(\hat{\theta}_\alpha)CS(\hat{\theta}_\beta) + \frac{(\gamma-1)}{|\hat{\phi}_\beta|}SN(\hat{\theta}_\beta)CS(\hat{\theta}_\alpha)$$

$${}_R\hat{R}_{24}(z, z_0) = -\frac{(\gamma-1)}{|\hat{\phi}_\alpha|}SN(\hat{\theta}_\alpha)CS(\hat{\theta}_\beta) - \gamma\hat{\phi}_\beta SN(\hat{\theta}_\beta)CS(\hat{\theta}_\alpha)$$

$${}_R\hat{R}_{25}(z, z_0) = \frac{1}{2} {}_R\hat{R}_{12}(z, z_0)$$

$${}_R\hat{R}_{31}(z, z_0) = \frac{1}{\rho c^2} \left[ + \frac{1}{|\dot{\phi}_\alpha|} \text{SN}(\dot{\theta}_\alpha) \text{CS}(\dot{\theta}_\beta) + \dot{\phi}_\beta \text{SN}(\dot{\theta}_\beta) \text{CS}(\dot{\theta}_\alpha) \right]$$

$${}_R\hat{R}_{32}(z, z_0) = -2 {}_R\hat{R}_{24}(z, z_0)$$

$${}_R\hat{R}_{33}(z, z_0) = \text{CS}(\dot{\theta}_\alpha) \text{CS}(\dot{\theta}_\beta)$$

$${}_R\hat{R}_{34}(z, z_0) = \frac{\dot{\phi}_\beta}{|\dot{\phi}_\alpha|} \text{SN}(\dot{\theta}_\alpha) \text{SN}(\dot{\theta}_\beta)$$

$${}_R\hat{R}_{35}(z, z_0) = -{}_R\hat{R}_{14}(z, z_0)$$

$${}_R\hat{R}_{41}(z, z_0) = \frac{1}{\rho c^2} \left[ -\dot{\phi}_\alpha \text{SN}(\dot{\theta}_\alpha) \text{CS}(\dot{\theta}_\beta) - \frac{1}{|\dot{\phi}_\beta|} \text{SN}(\dot{\theta}_\beta) \text{CS}(\dot{\theta}_\alpha) \right]$$

$${}_R\hat{R}_{42}(z, z_0) = -2 {}_R\hat{R}_{23}(z, z_0)$$

$${}_R\hat{R}_{43}(z, z_0) = \frac{\dot{\phi}_\alpha}{|\dot{\phi}_\beta|} \text{SN}(\dot{\theta}_\alpha) \text{SN}(\dot{\theta}_\beta)$$

$${}_R\hat{R}_{44}(z, z_0) = \text{CS}(\dot{\theta}_\alpha) \text{CS}(\dot{\theta}_\beta)$$

$${}_R\hat{R}_{45}(z, z_0) = -{}_R\hat{R}_{13}(z, z_0)$$

$$\begin{aligned} {}_R\hat{R}_{51}(z, z_0) = & \frac{1}{\rho^2 c^4} [2(N - \text{CS}(\dot{\theta}_\alpha) \text{CS}(\dot{\theta}_\beta)) \\ & - (\dot{\phi}_\alpha \dot{\phi}_\beta - \frac{1}{|\dot{\phi}_\alpha \dot{\phi}_\beta|}) \text{SN}(\dot{\theta}_\alpha) \text{SN}(\dot{\theta}_\beta)] \end{aligned}$$

$${}_R\hat{R}_{52}(z, z_0) = +2 {}_R\hat{R}_{21}(z, z_0)$$

$${}_R\hat{R}_{53}(z, z_0) = -{}_R\hat{R}_{41}(z, z_0)$$

$${}_R\hat{R}_{54}(z, z_0) = - {}_R\hat{R}_{31}(z, z_0)$$

$${}_R\hat{R}_{55}(z, z_0) = + {}_R\hat{R}_{11}(z, z_0)$$

$$\text{where } N = 1 / (\text{NORM}_\alpha \cdot \text{NORM}_\beta) \quad (\text{A.6})$$

The layer index has not been used for equations (A.1) through (A.6) but one should remember that all of the functions used in and given by these equations are layer dependent and the layer index has been omitted simply to minimize notational clutter.

Equations (A.5) allow us to compute scaled versions of the  $[R]$  matrix elements using real arithmetic and these scaled elements will have a much reduced dynamic range. By scaling the  $[R]$  matrix we are in fact also scaling the elements of the anti-symmetric minor matrix which is what we wanted since it is these quantities which actually determine the characteristic function and the normalized eigenfunctions. We can thus define a scaled version of the minor matrix vector given by equations (3.1.18) and (3.1.19) as follows.

$$\{\dot{M}(z_2)\} = [\hat{R}(z_1, z_2)] \{\dot{M}(z_1)\} \quad (\text{A.7})$$

We will initialize the  $\{\dot{M}\}$  vector at the top and bottom of the structure with the normal unscaled values of the  $\{M\}$  vector at the two boundaries and use equation (A.7) to compute scaled minor matrix elements within the structure. All of the elements of the  $\{\dot{M}\}$  vector are related to the  $\{M\}$  vector at any depth by a real and positive function of phase velocity and depth.

$$\{^B M(z)\} = B_{N_{\text{tot}}(c, z)} \{\dot{M}(z)\} \quad (\text{A.8})$$

$$\{^T M(z)\} = T_{N_{\text{tot}}(c, z)} \{\dot{M}(z)\}$$

The scaling functions  $B_{N_{tot}}$  and  $T_{N_{tot}}$  are computed from the product of all of the single layer scalars,  $N^{(p)}$ , given by equations (A.4) and (A.6) from the bottom boundary to depth  $z$  for  $B_{N_{tot}}$  and from the top boundary to depth  $z$  for  $T_{N_{tot}}$ . The following properties of the scaling functions can be shown.

$$\begin{aligned} B_{N_{tot}}(c, z_T) &= T_{N_{tot}}(c, z_B) = B_{N_{tot}}(c, z) T_{N_{tot}}(c, z) \\ &= NTOT(\omega, c) \end{aligned} \quad (A.9)$$

where  $z_T$  = depth of top boundary  
 $z_B$  = depth of bottom boundary  
 and  $z_T < z < z_B$

The scaler function  $NTOT(\omega, c)$  is the total product of all layer scaler functions  $N^{(p)}$  and is only dependent on the horizontal phase velocity. From equations (A.8) and (A.9) it is easy to show the following.

$$B_{M_i}(z) T_{M_j}(z) = NTOT(\omega, c) B_{M_i}(z) T_{M_j}(z) \quad (A.10)$$

where  $i, j = 1, 2, 3, 4, 5$

The normalized characteristic function given by equation (3.3.47) only involves  $B_M T_M$  products and so we can write a scaled version of the characteristic function as follows.

$${}_R \hat{\Delta} = T_{M_1} B_{M_5} + B_{M_1} T_{M_5} + 2 T_{M_2} B_{M_2} + T_{M_3} B_{M_4} + B_{M_3} T_{M_4} \quad (A.11)$$

$${}_R \bar{\Delta} = NTOT(\omega, c) {}_R \hat{\Delta} \quad (A.12)$$

Since  ${}_R \hat{\Delta}$  is zero at the eigenwavenumbers we can write down the partial



derivative of the characteristic function with respect to wavenumber as follows.

$$\left. \partial_R \bar{\Delta}(\omega, k) / \partial k \right|_{k=R K(n, \omega)} = \text{NTOT}(\omega, c) \left. \partial_R \dot{\Delta}(\omega, k) / \partial k \right|_{k=R K(n, \omega)} \quad (\text{A.13})$$

We can now see from equation (A.13) and equations (3.3.53) and (3.3.54) along with equation (A.10) that the  $\text{NTOT}(\omega, c)$  scalar function cancels out by division when the normalized eigenfunctions are computed and that the  $\{\dot{M}\}$  scaled minor matrix elements can be used in place of the normal unscaled minor matrix elements without effecting the final results.

## APPENDIX B

### THE COMPUTATIONS OF THE CHARACTERISTIC FUNCTION PARTIAL DERIVATIVES

In order to compute the normalized eigenfunctions, the group velocity and to compute a first order perturbation approximation of the shift in eigen phase velocities due to frequency dependent anelastic attenuation, it is necessary to compute a number of partial derivatives of the characteristic function. As I proved in section 3.3, the characteristic function is independent of depth and so I always compute the characteristic function using the top boundary values of the  $\{^T M\}$  and  $\{^B M\}$  vectors. Assuming the top boundary is a free surface and using equations (3.1.10) we arrive at the following.

$$\partial_R \bar{\Delta}(\omega, c) / \partial v = \partial_R ^B M_1(\omega, c, 0) / \partial v \quad (B.1)$$

where  $v$  is any of the variables frequency, horizontal phase velocity, or layer P and S wave velocities and zero depth is assumed to be the depth of the free surface. In order to compute  $\{^B M(\omega, c, 0)\}$  we start with the value of  $\{^B M\}$  defined at the bottom boundary using equations (3.1.10) through (3.1.14) based upon the bottom boundary condition. We then apply the following equation recursively (from equation (3.1.18)) at each layer interface until we reach the surface.

$$\{^B M(\omega, c, h^{(i-1)})\} = [^B R^{(i)}(\omega, c)] \{^B M(\omega, c, h^{(i)})\} \quad (B.2)$$

where  $i = n-1, n-2, \dots, 2, 1$

and  $h^{(n-1)}$  is the bottom boundary,  $h^{(0)} = 0$  is the top boundary,  $[{}^B R^{(i)}(\omega, c)]$  is the layer  $[R]$  matrix which propagates the  $\{{}^B M\}$  vector from the bottom of the layer to the top of the layer so that the following is true.

$$[{}^B R^{(i)}(\omega, c)] = [R(\omega, c, h^{(i)}, h^{(i-1)})] \quad (B.3)$$

We can apply the derivative chain rule directly to equation (B.2) to compute partial derivatives of the  $\{{}^B M\}$  vector.

$$\begin{aligned} \partial \{{}^B M(h^{(i-1)})\} / \partial v &= [{}^B R^{(i)}] \partial \{{}^B M(h^{(i)})\} / \partial v + \\ &+ \left( \partial [{}^B R^{(i)}] / \partial v \right) \{{}^B M(h^{(i)})\} \end{aligned} \quad (B.4)$$

For cases where  $v$  is either frequency or horizontal phase velocity we can compute equation (B.4) in parallel with equation (B.2) starting at the bottom boundary and recursively propagating both the  $\{{}^B M\}$  vector and the  $\partial \{{}^B M\} / \partial v$  vector upward to the surface. The problem now reduces to computing partial derivatives of the  $[{}^B R^{(i)}]$  matrix elements for each layer and the initializing derivatives of the  $\{{}^B M\}$  vector at the bottom boundary.

We can see from equations (3.1.10) to (3.1.14) that the frequency does not appear in any of the boundary  $\{M\}$  vector elements so that the following is true for all boundary conditions.

$$\partial \{{}^B M(z_B)\} / \partial \omega = \{0\} \quad (B.5)$$

where  $z_B = h^{(n-1)}$  is the bottom boundary depth

The initializing phase velocity derivatives of the  $\{{}^B M(z_B)\}$  vector elements

are given as follows.

1. A traction free surface,

$$\partial \{^B M(z_B)\} / \partial c = \{0\} \quad (B.6)$$

2. A rigid surface,

$$\partial \{^B M(z_B)\} / \partial c = \{0\} \quad (B.7)$$

3. Zero shear tractions and zero vertical displacement,

$$\partial \{^B M(z_B)\} / \partial c = \{0\} \quad (B.8)$$

4. No upward propagating P or S wave radiation,

$$\begin{aligned} \partial ^B M_1(z_B) / \partial c &= + \frac{(\gamma-1)}{\phi_\alpha \phi_\beta} \left( \frac{\gamma}{c} + \frac{(\gamma-1)}{4} \left( \frac{c}{\alpha^2 \phi_\alpha^2} + \frac{c}{\beta^2 \phi_\beta^2} \right) \right) + \frac{\gamma^2}{c} \quad (B.9) \\ \partial ^B M_2(z_B) / \partial c &= - \frac{1}{4\rho c^2 \phi_\alpha \phi_\beta} \left( \frac{2}{c} (2\gamma-1) - (\gamma-1) \left( \frac{c}{\alpha^2 \phi_\alpha^2} + \frac{c}{\beta^2 \phi_\beta^2} \right) \right) - \frac{\gamma}{\rho c^3} \\ \partial ^B M_3(z_B) / \partial c &= + \frac{1}{4\rho c^2 i \phi_\alpha} \left( \frac{2}{c} + \frac{c}{\alpha^2 \phi_\alpha^2} \right) \\ \partial ^B M_4(z_B) / \partial c &= - \frac{1}{4\rho c^2 i \phi_\beta} \left( \frac{2}{c} + \frac{c}{\beta^2 \phi_\beta^2} \right) \\ \partial ^B M_5(z_B) / \partial c &= - \frac{1}{4\rho^2 c^4 \phi_\alpha \phi_\beta} \left( \frac{4}{c} - \frac{c}{\alpha^2 \phi_\alpha^2} - \frac{c}{\beta^2 \phi_\beta^2} \right) - \frac{1}{\rho^2 c^5} \end{aligned}$$

We now need to compute the partial derivatives of the  $[^B R]$  matrix elements and then use equation (B.4) to compute the  $\{^B M\}$  vector partial derivatives at each layer interface. Unfortunately equation (B.4) suffers from the same dynamic range problems as equation (B.2) which is used to compute the characteristic function and so we need to apply a scaling function to equation (B.4). In appendix A I showed how equation (B.2) could be scaled to produce a scaled version of the  $[R]$  matrix elements. We could scale equation (B.4) by computing derivatives of the scaled  $\{^B M\}$  vec-

tor and the scaled  $[R]$  matrix elements however such derivative computations are complicated by the scaling function which itself is dependent on frequency, phase velocity and the layer P and S wave velocities. I chose to use a simpler method which involves scaling equation (B.4) in the same manner as I used to scale equation (B.2). Notice that scaled versions of the partial derivatives of the  $\{B_M\}$  vector and  $[R]$  matrix elements are not equal to the partial derivatives of the scaled versions of the same elements. I use a  $\hat{\cdot}$  notation to distinguish scaled versions of the derivatives from derivatives of the scaled functions as follows.

$$\partial\{B_M(h^{(i)})\}/\partial v = B_{N_{tot}(c,h^{(i)})} \partial\{B_{\hat{M}}(h^{(i)})\}/\partial v \quad (B.10)$$

$$\partial[B_R^{(i)}]/\partial v = N^{(i)} \partial[B_{\hat{R}}^{(i)}]/\partial v \quad (B.11)$$

where  $N^{(i)}$  is the layer scaling function given by equation (A.6) and  $B_{N_{tot}(c,h^{(i)})}$  is the total scaling function from the bottom boundary to depth  $h^{(i)}$  given in equation (A.8). The scaling functions are identical to the ones used to scale equation (B.2) for each layer and at each depth. We can apply scaling functions to each layer and write equation (B.4) as follows.

$$\begin{aligned} \partial\{B_{\hat{M}}(h^{(i-1)})\}/\partial v &= [B_{\hat{R}}^{(i)}] \partial\{B_{\hat{M}}(h^{(i)})\}/\partial v + \\ &+ \left( \partial[B_{\hat{R}}^{(i)}]/\partial v \right) \{B_{\hat{M}}(h^{(i)})\} \end{aligned} \quad (B.12)$$

As with the scaling of equation (B.2) we initialize the  $\partial\{B_{\hat{M}}\}/\partial v$  vector directly from equations (B.5) through (B.9).

The scaled versions of the partial derivatives of the  $[R]$  matrix elements are given as follows. These equations use the same functions  $\phi_\alpha$ ,  $\dot{\phi}_\beta$ ,  $\dot{\theta}_\alpha$ ,  $\dot{\theta}_\beta$ , SN, CS, and N which are all defined in appendix A. I have expressed

the  $[R]$  matrix partial derivatives in terms of a number of intermediate variables which are also defined. The partial derivatives with respect to frequency are given first.

$$\partial_R \dot{\hat{R}}_{11}(z, z_0)/\partial \omega = G_{11} \text{CACB}_{,\omega} + H_{11} \text{SASB}_{,\omega} \quad (\text{B.13})$$

$$\partial_R \dot{\hat{R}}_{12}(z, z_0)/\partial \omega = G_{12} \text{CACB}_{,\omega} + H_{12} \text{SASB}_{,\omega}$$

$$\partial_R \dot{\hat{R}}_{13}(z, z_0)/\partial \omega = S_{13} \text{SACB}_{,\omega} + T_{13} \text{SBCA}_{,\omega}$$

$$\partial_R \dot{\hat{R}}_{14}(z, z_0)/\partial \omega = S_{14} \text{SACB}_{,\omega} + T_{14} \text{SBCA}_{,\omega}$$

$$\partial_R \dot{\hat{R}}_{15}(z, z_0)/\partial \omega = G_{15} \text{CACB}_{,\omega} + H_{15} \text{SASB}_{,\omega}$$

$$\partial_R \dot{\hat{R}}_{21}(z, z_0)/\partial \omega = G_{21} \text{CACB}_{,\omega} + H_{21} \text{SASB}_{,\omega}$$

$$\partial_R \dot{\hat{R}}_{22}(z, z_0)/\partial \omega = G_{22} \text{CACB}_{,\omega} + H_{22} \text{SASB}_{,\omega}$$

$$\partial_R \dot{\hat{R}}_{23}(z, z_0)/\partial \omega = S_{23} \text{SACB}_{,\omega} + T_{23} \text{SBCA}_{,\omega}$$

$$\partial_R \dot{\hat{R}}_{24}(z, z_0)/\partial \omega = S_{24} \text{SACB}_{,\omega} + T_{24} \text{SBCA}_{,\omega}$$

$$\partial_R \dot{\hat{R}}_{25}(z, z_0)/\partial \omega = + \frac{1}{2} \partial_R \dot{\hat{R}}_{12}(z, z_0)/\partial \omega$$

$$\partial_R \dot{\hat{R}}_{31}(z, z_0)/\partial \omega = S_{31} \text{SACB}_{,\omega} + T_{31} \text{SBCA}_{,\omega}$$

$$\partial_R \dot{\hat{R}}_{32}(z, z_0)/\partial \omega = - 2 \partial_R \dot{\hat{R}}_{24}(z, z_0)/\partial \omega$$

$$\partial_R \dot{\hat{R}}_{33}(z, z_0)/\partial \omega = \text{CACB}_{,\omega}$$

$$\partial_R \dot{\hat{R}}_{34}(z, z_0)/\partial \omega = H_{34} \text{SASB}_{,\omega}$$

$$\partial_R \dot{\hat{R}}_{35}(z, z_0)/\partial \omega = - \partial_R \dot{\hat{R}}_{14}(z, z_0)/\partial \omega$$

$$\partial_R \dot{\hat{R}}_{41}(z, z_0)/\partial \omega = S_{41} \text{SACB}_{,\omega} + T_{41} \text{SBCA}_{,\omega}$$

$$\partial_R \dot{\hat{R}}_{42}(z, z_0)/\partial \omega = - 2 \partial_R \dot{\hat{R}}_{23}(z, z_0)/\partial \omega$$

$$\partial_R \dot{\hat{R}}_{43}(z, z_0)/\partial \omega = H_{43} \text{SASB}_{,\omega}$$

$$\partial_R \dot{\hat{R}}_{44}(z, z_0)/\partial \omega = \text{CACB}_{,\omega}$$

$$\partial_R \dot{\hat{R}}_{45}(z, z_0)/\partial \omega = - \partial_R \dot{\hat{R}}_{13}(z, z_0)/\partial \omega$$

$$\partial_R \dot{\hat{R}}_{51}(z, z_0)/\partial \omega = G_{51} \text{CACB}_{,\omega} + H_{51} \text{SASB}_{,\omega}$$

$$\partial_R \dot{\hat{R}}_{52}(z, z_0)/\partial \omega = + 2 \partial_R \dot{\hat{R}}_{21}(z, z_0)/\partial \omega$$

$$\partial_R \dot{\hat{R}}_{53}(z, z_0)/\partial \omega = - \partial_R \dot{\hat{R}}_{41}(z, z_0)/\partial \omega$$

$$\partial_R \dot{\hat{R}}_{54}(z, z_0)/\partial \omega = - \partial_R \dot{\hat{R}}_{31}(z, z_0)/\partial \omega$$

$$\partial_R \dot{\hat{R}}_{55}(z, z_0)/\partial \omega = + \partial_R \dot{\hat{R}}_{11}(z, z_0)/\partial \omega$$

where

$$G_{11} = \gamma^2 + (\gamma - 1)^2 \quad (\text{B.14})$$

$$H_{11} = \gamma^2 \dot{\phi}_\alpha \dot{\phi}_\beta - \frac{(\gamma - 1)^2}{|\dot{\phi}_\alpha \dot{\phi}_\beta|}$$

$$G_{12} = + 2\rho c^2 \gamma (\gamma - 1) (2\gamma - 1)$$

$$H_{12} = + 2\rho c^2 (\gamma^3 \dot{\phi}_\alpha \dot{\phi}_\beta - \frac{(\gamma - 1)^3}{|\dot{\phi}_\alpha \dot{\phi}_\beta|})$$

$$S_{13} = - \rho c^2 \gamma^2 \dot{\phi}_\alpha$$

$$T_{13} = - \rho c^2 \frac{(\gamma - 1)^2}{|\dot{\phi}_\beta|}$$

$$S_{14} = + \rho c^2 \frac{(\gamma - 1)^2}{|\dot{\phi}_\alpha|}$$

$$T_{14} = + \rho c^2 \gamma^2 \dot{\phi}_\beta$$

$$G_{15} = - 2\rho^2 c^4 \gamma^2 (\gamma - 1)^2$$

$$H_{15} = - \rho^2 c^4 (\gamma^4 \dot{\phi}_\alpha \dot{\phi}_\beta - \frac{(\gamma - 1)^4}{|\dot{\phi}_\alpha \dot{\phi}_\beta|})$$

$$G_{21} = - \frac{1}{\rho c^2} (2\gamma - 1)$$

$$H_{21} = - \frac{1}{\rho c^2} (\gamma \dot{\phi}_\alpha \dot{\phi}_\beta - \frac{(\gamma - 1)}{|\dot{\phi}_\alpha \dot{\phi}_\beta|})$$

$$G_{22} = - 4\gamma (\gamma - 1)$$

$$H_{22} = - 2(\gamma^2 \dot{\phi}_\alpha \dot{\phi}_\beta - \frac{(\gamma - 1)^2}{|\dot{\phi}_\alpha \dot{\phi}_\beta|})$$

$$S_{23} = + \gamma \dot{\phi}_\alpha$$

$$T_{23} = + \frac{(\gamma - 1)}{|\dot{\phi}_\beta|}$$

$$S_{24} = - \frac{(\gamma - 1)}{|\dot{\phi}_\alpha|}$$

$$T_{24} = - \gamma \dot{\phi}_\beta$$

$$S_{31} = + \frac{1}{\rho c^2 |\dot{\phi}_\alpha|}$$

$$T_{31} = + \frac{\dot{\phi}_\beta}{\rho c^2}$$

$$\begin{aligned}
H_{34} &= \frac{\dot{\phi}_\beta}{|\dot{\phi}_\alpha|} \\
S_{41} &= -\frac{\dot{\phi}_\alpha}{\rho c^2} \\
T_{41} &= -\frac{1}{\rho c^2 |\dot{\phi}_\beta|} \\
H_{43} &= \frac{\dot{\phi}_\alpha}{|\dot{\phi}_\beta|} \\
G_{51} &= -\frac{2}{\rho^2 c^4} \\
H_{51} &= -\frac{1}{\rho^2 c^4} (\dot{\phi}_\alpha \dot{\phi}_\beta + \frac{1}{|\dot{\phi}_\alpha \dot{\phi}_\beta|})
\end{aligned}$$

and

$$\begin{aligned}
CACB_{,\omega} &= -\frac{\dot{\theta}_\alpha}{\omega} SN(\dot{\theta}_\alpha) CS(\dot{\theta}_\beta) - \frac{\dot{\theta}_\beta}{\omega} CS(\dot{\theta}_\alpha) SN(\dot{\theta}_\beta) \\
SASB_{,\omega} &= +\frac{\dot{\theta}_\alpha}{\omega} CS(\dot{\theta}_\alpha) SN(\dot{\theta}_\beta) + \frac{\dot{\theta}_\beta}{\omega} SN(\dot{\theta}_\alpha) CS(\dot{\theta}_\beta) \\
SACB_{,\omega} &= +\frac{\dot{\theta}_\alpha}{\omega} CS(\dot{\theta}_\alpha) CS(\dot{\theta}_\beta) - \frac{\dot{\theta}_\beta}{\omega} SN(\dot{\theta}_\alpha) SN(\dot{\theta}_\beta) \\
SBCA_{,\omega} &= -\frac{\dot{\theta}_\alpha}{\omega} SN(\dot{\theta}_\alpha) SN(\dot{\theta}_\beta) + \frac{\dot{\theta}_\beta}{\omega} CS(\dot{\theta}_\alpha) CS(\dot{\theta}_\beta)
\end{aligned} \tag{B.15}$$

The scaled partial derivatives of the [R] matrix elements with respect to horizontal phase velocity are more complicated than the frequency derivatives due to the functions G, H, S, and T which depend on phase velocity. The [R] matrix phase velocity derivatives are given as follows.

$$\begin{aligned}
\partial_R \hat{R}_{11}(z, z_0) / \partial c &= -G_{11,c} + G_{11,c} CACB + G_{11} CACB_{,c} + \\
&\quad + H_{11,c} SASB + H_{11} SASB_{,c} \\
\partial_R \hat{R}_{12}(z, z_0) / \partial c &= -G_{12,c} + G_{12,c} CACB + G_{12} CACB_{,c} + \\
&\quad + H_{12,c} SASB + H_{12} SASB_{,c} \\
\partial_R \hat{R}_{13}(z, z_0) / \partial c &= S_{13,c} SACB + S_{13} SACB_{,c} + T_{13,c} SBCA + T_{13} SBCA_{,c}
\end{aligned} \tag{B.16}$$



$$\begin{aligned}
\partial_R \hat{R}_{14}(z, z_0)/\partial c &= S_{14,c} \text{SACB} + S_{14} \text{SACB}_{,c} + T_{14,c} \text{SBCA} + T_{14} \text{SBCA}_{,c} \\
\partial_R \hat{R}_{15}(z, z_0)/\partial c &= -G_{15,c} + G_{15,c} \text{CACB} + G_{15} \text{CACB}_{,c} + \\
&\quad + H_{15,c} \text{SASB} + H_{15} \text{SASB}_{,c} \\
\partial_R \hat{R}_{21}(z, z_0)/\partial c &= -G_{21,c} + G_{21,c} \text{CACB} + G_{21} \text{CACB}_{,c} + \\
&\quad + H_{21,c} \text{SASB} + H_{21} \text{SASB}_{,c} \\
\partial_R \hat{R}_{22}(z, z_0)/\partial c &= -G_{22,c} + G_{22,c} \text{CACB} + G_{22} \text{CACB}_{,c} + \\
&\quad + H_{22,c} \text{SASB} + H_{22} \text{SASB}_{,c} \\
\partial_R \hat{R}_{23}(z, z_0)/\partial c &= S_{23,c} \text{SACB} + S_{23} \text{SACB}_{,c} + T_{23,c} \text{SBCA} + T_{23} \text{SBCA}_{,c} \\
\partial_R \hat{R}_{24}(z, z_0)/\partial c &= S_{24,c} \text{SACB} + S_{24} \text{SACB}_{,c} + T_{24,c} \text{SBCA} + T_{24} \text{SBCA}_{,c} \\
\partial_R \hat{R}_{25}(z, z_0)/\partial c &= + \frac{1}{2} \partial_R \hat{R}_{12}(z, z_0)/\partial c \\
\partial_R \hat{R}_{31}(z, z_0)/\partial c &= S_{31,c} \text{SACB} + S_{31} \text{SACB}_{,c} + T_{31,c} \text{SBCA} + T_{31} \text{SBCA}_{,c} \\
\partial_R \hat{R}_{32}(z, z_0)/\partial c &= -2 \partial_R \hat{R}_{24}(z, z_0)/\partial c \\
\partial_R \hat{R}_{33}(z, z_0)/\partial c &= \text{CACB}_{,c} \\
\partial_R \hat{R}_{34}(z, z_0)/\partial c &= H_{34,c} \text{SASB} + H_{34} \text{SASB}_{,c} \\
\partial_R \hat{R}_{35}(z, z_0)/\partial c &= -\partial_R \hat{R}_{14}(z, z_0)/\partial c \\
\partial_R \hat{R}_{41}(z, z_0)/\partial c &= S_{41,c} \text{SACB} + S_{41} \text{SACB}_{,c} + T_{41,c} \text{SBCA} + T_{41} \text{SBCA}_{,c} \\
\partial_R \hat{R}_{42}(z, z_0)/\partial c &= -2 \partial_R \hat{R}_{23}(z, z_0)/\partial c \\
\partial_R \hat{R}_{43}(z, z_0)/\partial c &= H_{43,c} \text{SASB} + H_{43} \text{SASB}_{,c} \\
\partial_R \hat{R}_{44}(z, z_0)/\partial c &= \text{CACB}_{,c} \\
\partial_R \hat{R}_{45}(z, z_0)/\partial c &= -\partial_R \hat{R}_{13}(z, z_0)/\partial c \\
\partial_R \hat{R}_{51}(z, z_0)/\partial c &= -G_{51,c} + G_{51,c} \text{CACB} + G_{51} \text{CACB}_{,c} + \\
&\quad + H_{51,c} \text{SASB} + H_{51} \text{SASB}_{,c} \\
\partial_R \hat{R}_{52}(z, z_0)/\partial c &= +2 \partial_R \hat{R}_{21}(z, z_0)/\partial c \\
\partial_R \hat{R}_{53}(z, z_0)/\partial c &= -\partial_R \hat{R}_{41}(z, z_0)/\partial c \\
\partial_R \hat{R}_{54}(z, z_0)/\partial c &= -\partial_R \hat{R}_{31}(z, z_0)/\partial c \\
\partial_R \hat{R}_{55}(z, z_0)/\partial c &= +\partial_R \hat{R}_{11}(z, z_0)/\partial c
\end{aligned}$$

where

$$\delta_\alpha = \frac{c}{\alpha^2 \dot{\phi}_\alpha |\dot{\phi}_\alpha|}, \quad \delta_\beta = \frac{c}{\beta^2 \dot{\phi}_\beta |\dot{\phi}_\beta|} \quad (\text{B.17})$$

$$G_{11,c} = -\frac{4}{c}\gamma(2\gamma-1)$$

$$H_{11,c} = +4\rho c\gamma H_{21} + (\delta_\alpha + \delta_\beta) \left( \gamma^2 \dot{\phi}_\alpha \dot{\phi}_\beta + \frac{(\gamma-1)^2}{|\dot{\phi}_\alpha \dot{\phi}_\beta|} \right)$$

$$G_{12,c} = +\frac{2}{c}G_{12} - 4\rho c\gamma(6\gamma(\gamma-1)+1)$$

$$H_{12,c} = +\frac{2}{c}H_{12} - 12\rho c\gamma H_{11} + 2\rho c^2(\delta_\alpha + \delta_\beta) \left( \gamma^3 \dot{\phi}_\alpha \dot{\phi}_\beta + \frac{(\gamma-1)^3}{|\dot{\phi}_\alpha \dot{\phi}_\beta|} \right)$$

$$S_{13,c} = \left( -\frac{2}{c} + \delta_\alpha \right) S_{13}$$

$$T_{13,c} = \left( +\frac{2}{c} - \delta_\beta \right) T_{13} + 4\rho c\gamma T_{23}$$

$$S_{14,c} = \left( +\frac{2}{c} - \delta_\alpha \right) S_{14} + 4\rho c\gamma S_{24}$$

$$T_{14,c} = \left( -\frac{2}{c} + \delta_\beta \right) T_{14}$$

$$G_{15,c} = +\frac{4}{c}G_{15} + 4\rho c\gamma G_{12}$$

$$H_{15,c} = +\frac{4}{c}H_{15} + 4\rho c\gamma H_{12} - \rho^2 c^4 (\delta_\alpha + \delta_\beta) \left( \gamma^4 \dot{\phi}_\alpha \dot{\phi}_\beta + \frac{(\gamma-1)^4}{|\dot{\phi}_\alpha \dot{\phi}_\beta|} \right)$$

$$G_{21,c} = -\frac{2}{c}G_{21} + \frac{4\gamma}{\rho c^3}$$

$$H_{21,c} = -\frac{2}{c}H_{21} - 2\rho c\gamma H_{51} - \frac{1}{\rho c^2}(\delta_\alpha + \delta_\beta) \left( \gamma \dot{\phi}_\alpha \dot{\phi}_\beta + \frac{(\gamma-1)}{|\dot{\phi}_\alpha \dot{\phi}_\beta|} \right)$$

$$G_{22,c} = -2G_{11,c}$$

$$H_{22,c} = -2H_{11,c}$$

$$S_{23,c} = \left( -\frac{2}{c} + \delta_\alpha \right) S_{23}$$

$$T_{23,c} = -\delta_\beta T_{23} + 2\rho c\gamma T_{41}$$

$$S_{24,c} = -\delta_\alpha S_{24} + 2\rho c\gamma S_{31}$$

$$T_{24,c} = \left( -\frac{2}{c} + \delta_\beta \right) T_{24}$$

$$S_{31,c} = \left( -\frac{2}{c} - \delta_\alpha \right) S_{31}$$

$$T_{31,c} = \left( -\frac{2}{c} + \delta_\beta \right) T_{31}$$

$$\begin{aligned}
H_{34,c} &= +(\delta_\beta - \delta_\alpha) H_{34} \\
S_{41,c} &= \left( -\frac{2}{c} + \delta_\alpha \right) S_{41} \\
T_{41,c} &= \left( -\frac{2}{c} - \delta_\beta \right) T_{41} \\
H_{43,c} &= +(\delta_\alpha - \delta_\beta) H_{43} \\
G_{51,c} &= -\frac{4}{c} G_{51} \\
H_{51,c} &= -\frac{4}{c} H_{51} - \frac{1}{\rho^2 c^4} (\delta_\alpha + \delta_\beta) \left( \dot{\phi}_\alpha \dot{\phi}_\beta - \frac{1}{|\dot{\phi}_\alpha \dot{\phi}_\beta|} \right)
\end{aligned}$$

and

$$\begin{aligned}
C A C B_{,c} &= -\dot{\theta}_\alpha \left( \dot{\delta}_\alpha - \frac{1}{c} \right) S N(\dot{\theta}_\alpha) C S(\dot{\theta}_\beta) - \dot{\theta}_\beta \left( \dot{\delta}_\beta - \frac{1}{c} \right) C S(\dot{\theta}_\alpha) S N(\dot{\theta}_\beta) \\
S A S B_{,c} &= +\dot{\theta}_\alpha \left( \dot{\delta}_\alpha - \frac{1}{c} \right) C S(\dot{\theta}_\alpha) S N(\dot{\theta}_\beta) + \dot{\theta}_\beta \left( \dot{\delta}_\beta - \frac{1}{c} \right) S N(\dot{\theta}_\alpha) C S(\dot{\theta}_\beta) \\
S A C B_{,c} &= +\dot{\theta}_\alpha \left( \dot{\delta}_\alpha - \frac{1}{c} \right) C S(\dot{\theta}_\alpha) C S(\dot{\theta}_\beta) - \dot{\theta}_\beta \left( \dot{\delta}_\beta - \frac{1}{c} \right) S N(\dot{\theta}_\alpha) S N(\dot{\theta}_\beta) \\
S B C A_{,c} &= -\dot{\theta}_\alpha \left( \dot{\delta}_\alpha - \frac{1}{c} \right) S N(\dot{\theta}_\alpha) S N(\dot{\theta}_\beta) + \dot{\theta}_\beta \left( \dot{\delta}_\beta - \frac{1}{c} \right) C S(\dot{\theta}_\alpha) C S(\dot{\theta}_\beta)
\end{aligned} \tag{B.18}$$

We finally turn our attention to computing the partial derivatives of the characteristic function with respect to the layer P and S wave velocities. We could compute all of the partial derivatives separately however this would involve computing two times the number of layers derivatives which would be expensive in cases where there are a large number of layers. It is obvious that the following is true.

$$\partial_i B_R(i) / \partial \alpha^{(p)} = 0, \text{ for } i \neq p \tag{B.19}$$

$$\partial_i B_R(i) / \partial \beta^{(p)} = 0, \text{ for } i \neq p$$

We can thus express equation (B.4) as follows for cases where  $p < n$ .

$$\partial \{B_M(h^{(p-1)})\} / \partial \alpha^{(p)} = \left( \partial [B_R^{(p)}] / \partial \alpha^{(p)} \right) \{B_M(h^{(p)})\} \quad (B.20)$$

$$\partial \{B_M(h^{(p-1)})\} / \partial \beta^{(p)} = \left( \partial [B_R^{(p)}] / \partial \beta^{(p)} \right) \{B_M(h^{(p)})\}$$

and

$$\partial \{B_M(h^{(j-1)})\} / \partial \alpha^{(p)} = [B_R^{(j)}] \partial \{B_M(h^{(j)})\} / \partial \alpha^{(p)} \quad (B.21)$$

$$\partial \{B_M(h^{(j-1)})\} / \partial \beta^{(p)} = [B_R^{(j)}] \partial \{B_M(h^{(j)})\} / \partial \beta^{(p)}$$

for  $j = p-1, p-2, \dots, 2, 1$

Equations (B.20) and (B.21) can be expressed as follows.

$$\sum_{i=j}^n \frac{\partial \{B_M(h^{(i-1)})\}}{\partial \alpha^{(i)}} d\alpha^{(i)} = [B_R^{(j)}] \left( \sum_{i=j+1}^n \frac{\partial \{B_M(h^{(i-1)})\}}{\partial \alpha^{(i)}} d\alpha^{(i)} \right) + \quad (B.22)$$

$$+ \left( \partial [B_R^{(j)}] / \partial \alpha^{(j)} \right) d\alpha^{(j)} \{B_M(h^{(j)})\}$$

$$\sum_{i=j}^n \frac{\partial \{B_M(h^{(i-1)})\}}{\partial \beta^{(i)}} d\beta^{(i)} = [B_R^{(j)}] \left( \sum_{i=j+1}^n \frac{\partial \{B_M(h^{(i-1)})\}}{\partial \beta^{(i)}} d\beta^{(i)} \right)$$

$$+ \left( \partial [B_R^{(j)}] / \partial \beta^{(j)} \right) d\beta^{(j)} \{B_M(h^{(j)})\}$$

for  $j = n-1, n-2, \dots, 2, 1$

Equation (B.22) can be computed recursively in parallel with equation (B.2) to produce the numerator factors that appear in equation (4.2.15) which is used to compute the shift in eigen phase velocity due to small changes in the layer P and S wave velocities. Notice that the actual partial derivatives

with respect to each layer P and S wave velocity are not computed separately which makes this method more efficient than the direct approach. The values of  $d\alpha(i)$  and  $d\beta(i)$  are approximated by the imaginary values of the layer P and S wave velocities due to attenuation,  $\alpha_1^{(i)}$  and  $\beta_1^{(i)}$  from equations (4.2.13). The initializing values of  $\partial\{^B M(h^{(n-1)})\}/\partial\alpha^{(n)}$  and  $\partial\{^B M(h^{(n-1)})\}/\partial\beta^{(n)}$  at the bottom boundary are given as follows.

1. A traction free surface,

$$\begin{aligned}\partial\{^B M(z_B)\}/\partial\alpha &= \{0\} \\ \partial\{^B M(z_B)\}/\partial\beta &= \{0\}\end{aligned}\tag{B.23}$$

2. A rigid surface,

$$\begin{aligned}\partial\{^B M(z_B)\}/\partial\alpha &= \{0\} \\ \partial\{^B M(z_B)\}/\partial\beta &= \{0\}\end{aligned}\tag{B.24}$$

3. Zero shear tractions and zero vertical displacement,

$$\begin{aligned}\partial\{^B M(z_B)\}/\partial\alpha &= \{0\} \\ \partial\{^B M(z_B)\}/\partial\beta &= \{0\}\end{aligned}\tag{B.25}$$

4. No upward propagating P or S wave radiation,

$$\begin{aligned}\partial^B M_1(z_B)/\partial\alpha &= -\frac{1}{4}\left(\frac{c^2(\gamma-1)^2}{\phi_\alpha^3 \alpha^3 \phi_\beta}\right) \\ \partial^B M_2(z_B)/\partial\alpha &= +\frac{1}{4}\left(\frac{(\gamma-1)}{\rho \phi_\alpha^3 \alpha^3 \phi_\beta}\right) \\ \partial^B M_3(z_B)/\partial\alpha &= +\frac{1}{4\rho i \phi_\alpha^3 \alpha^3} \\ \partial^B M_4(z_B)/\partial\alpha &= 0 \\ \partial^B M_5(z_B)/\partial\alpha &= +\frac{1}{4}\left(\frac{1}{\rho^2 c^2 \phi_\alpha^3 \alpha^3 \phi_\beta}\right)\end{aligned}\tag{B.26}$$

$$\begin{aligned}
\partial^B M_1(z_B)/\partial\beta &= -\frac{1}{4} \left( \frac{c^2(\gamma-1)^2}{\phi_\alpha \phi_\beta^3 \beta^3} \right) - \frac{\gamma}{\beta} \left( \frac{(\gamma-1)}{\phi_\alpha \phi_\beta} + \gamma \right) \\
\partial^B M_2(z_B)/\partial\beta &= +\frac{1}{4} \left( \frac{(\gamma-1)}{\rho \phi_\alpha \phi_\beta^3 \beta^4} \right) + \frac{\gamma}{2\beta \rho c^2} \left( \frac{1}{\phi_\alpha \phi_\beta} + 1 \right) \\
\partial^B M_3(z_B)/\partial\beta &= 0 \\
\partial^B M_4(z_B)/\partial\beta &= -\frac{1}{4\rho i \phi_\beta^3 \beta^3} \\
\partial^B M_5(z_B)/\partial\beta &= +\frac{1}{4} \left( \frac{1}{\rho^2 c^2 \phi_\alpha \phi_\beta^3 \beta^3} \right)
\end{aligned}$$

where  $z_B = h^{(n-1)}$  and the layer index for the half space has been dropped.

Finally I give the partial derivatives of the  $[R]$  matrix elements with respect to the layer P and S wave velocities. As with the frequency and phase velocity derivatives, these derivatives are scaled to eliminate the dynamic range problem.

$$\begin{aligned}
\partial_R \hat{R}_{11}(z, z_0)/\partial\beta &= -G_{11,\beta} + G_{11,\beta} \text{CACB} + G_{11} \text{CACB}_{,\beta} + \quad (\text{B.27}) \\
&\quad + H_{11,\beta} \text{SASB} + H_{11} \text{SASB}_{,\beta} \\
\partial_R \hat{R}_{12}(z, z_0)/\partial\beta &= -G_{12,\beta} + G_{12,\beta} \text{CACB} + G_{12} \text{CACB}_{,\beta} + \\
&\quad + H_{12,\beta} \text{SASB} + H_{12} \text{SASB}_{,\beta} \\
\partial_R \hat{R}_{13}(z, z_0)/\partial\beta &= S_{13,\beta} \text{SACB} + S_{13} \text{SACB}_{,\beta} + T_{13,\beta} \text{SBCA} + T_{13} \text{SBCA}_{,\beta} \\
\partial_R \hat{R}_{14}(z, z_0)/\partial\beta &= S_{14,\beta} \text{SACB} + S_{14} \text{SACB}_{,\beta} + T_{14,\beta} \text{SBCA} + T_{14} \text{SBCA}_{,\beta} \\
\partial_R \hat{R}_{15}(z, z_0)/\partial\beta &= -G_{15,\beta} + G_{15,\beta} \text{CACB} + G_{15} \text{CACB}_{,\beta} + \\
&\quad + H_{15,\beta} \text{SASB} + H_{15} \text{SASB}_{,\beta} \\
\partial_R \hat{R}_{21}(z, z_0)/\partial\beta &= -G_{21,\beta} + G_{21,\beta} \text{CACB} + G_{21} \text{CACB}_{,\beta} + \\
&\quad + H_{21,\beta} \text{SASB} + H_{21} \text{SASB}_{,\beta} \\
\partial_R \hat{R}_{22}(z, z_0)/\partial\beta &= -G_{22,\beta} + G_{22,\beta} \text{CACB} + G_{22} \text{CACB}_{,\beta} + \\
&\quad + H_{22,\beta} \text{SASB} + H_{22} \text{SASB}_{,\beta} \\
\partial_R \hat{R}_{23}(z, z_0)/\partial\beta &= S_{23,\beta} \text{SACB} + S_{23} \text{SACB}_{,\beta} + T_{23,\beta} \text{SBCA} + T_{23} \text{SBCA}_{,\beta} \\
\partial_R \hat{R}_{24}(z, z_0)/\partial\beta &= S_{24,\beta} \text{SACB} + S_{24} \text{SACB}_{,\beta} + T_{24,\beta} \text{SBCA} + T_{24} \text{SBCA}_{,\beta}
\end{aligned}$$

$$\begin{aligned}
\partial_R \hat{R}_{25}(z, z_0) / \partial \beta &= + \frac{1}{2} \partial_R \hat{R}_{12}(z, z_0) / \partial \beta \\
\partial_R \hat{R}_{31}(z, z_0) / \partial \beta &= S_{31} \text{SACB}_{,\beta} + T_{31,\beta} \text{SBCA} + T_{31} \text{SBCA}_{,\beta} \\
\partial_R \hat{R}_{32}(z, z_0) / \partial \beta &= - 2 \partial_R \hat{R}_{24}(z, z_0) / \partial \beta \\
\partial_R \hat{R}_{33}(z, z_0) / \partial \beta &= \text{CACB}_{,\beta} \\
\partial_R \hat{R}_{34}(z, z_0) / \partial \beta &= H_{34,\beta} \text{SASB} + H_{34} \text{SASB}_{,\beta} \\
\partial_R \hat{R}_{35}(z, z_0) / \partial \beta &= - \partial_R \hat{R}_{14}(z, z_0) / \partial \beta \\
\partial_R \hat{R}_{41}(z, z_0) / \partial \beta &= S_{41} \text{SACB}_{,\beta} + T_{41,\beta} \text{SBCA} + T_{41} \text{SBCA}_{,\beta} \\
\partial_R \hat{R}_{42}(z, z_0) / \partial \beta &= - 2 \partial_R \hat{R}_{23}(z, z_0) / \partial \beta \\
\partial_R \hat{R}_{43}(z, z_0) / \partial \beta &= H_{43,\beta} \text{SASB} + H_{43} \text{SASB}_{,\beta} \\
\partial_R \hat{R}_{44}(z, z_0) / \partial \beta &= \text{CACB}_{,\beta} \\
\partial_R \hat{R}_{45}(z, z_0) / \partial \beta &= - \partial_R \hat{R}_{13}(z, z_0) / \partial \beta \\
\partial_R \hat{R}_{51}(z, z_0) / \partial \beta &= G_{51} \text{CACB}_{,\beta} + H_{51,\beta} \text{SASB} + H_{51} \text{SASB}_{,\beta} \\
\partial_R \hat{R}_{52}(z, z_0) / \partial \beta &= + 2 \partial_R \hat{R}_{21}(z, z_0) / \partial \beta \\
\partial_R \hat{R}_{53}(z, z_0) / \partial \beta &= - \partial_R \hat{R}_{41}(z, z_0) / \partial \beta \\
\partial_R \hat{R}_{54}(z, z_0) / \partial \beta &= - \partial_R \hat{R}_{31}(z, z_0) / \partial \beta \\
\partial_R \hat{R}_{55}(z, z_0) / \partial \beta &= + \partial_R \hat{R}_{11}(z, z_0) / \partial \beta
\end{aligned}$$

where

$$\begin{aligned}
\epsilon_\beta &= \frac{c^2}{\beta^3 \dot{\phi}_\beta |\dot{\phi}_\beta|} & (\text{B.28}) \\
G_{11,\beta} &= + \frac{4}{\beta} \gamma (2\gamma - 1) \\
H_{11,\beta} &= - \frac{4\rho c^2 \gamma}{\beta} H_{21} - \epsilon_\beta \left( \gamma^2 \dot{\phi}_\alpha \dot{\phi}_\beta + \frac{(\gamma-1)^2}{|\dot{\phi}_\alpha \dot{\phi}_\beta|} \right) \\
G_{12,\beta} &= + \frac{4\rho c^2 \gamma}{\beta} (6\gamma(\gamma-1) + 1) \\
H_{12,\beta} &= + \frac{12\rho c^2 \gamma}{\beta} H_{11} - 2\rho c^2 \epsilon_\beta \left( \gamma^3 \dot{\phi}_\alpha \dot{\phi}_\beta + \frac{(\gamma-1)^3}{|\dot{\phi}_\alpha \dot{\phi}_\beta|} \right) \\
S_{13,\beta} &= + \frac{4}{\beta} S_{13} \\
T_{13,\beta} &= + \epsilon_\beta T_{13} - \frac{4\rho c^2 \gamma}{\beta} T_{23}
\end{aligned}$$

$$\begin{aligned}
S_{14,\beta} &= -\frac{4\rho c^2\gamma}{\beta} S_{24} \\
T_{14,\beta} &= +\left(\frac{4}{\beta} - \epsilon_\beta\right) T_{14} \\
G_{15,\beta} &= -\frac{4\rho c^2\gamma}{\beta} G_{12} \\
H_{15,\beta} &= -\frac{4\rho c^2\gamma}{\beta} H_{12} + \rho^2 c^4 \epsilon_\beta \left( \gamma^4 \dot{\phi}_\alpha \dot{\phi}_\beta + \frac{(\gamma-1)^4}{|\dot{\phi}_\alpha \dot{\phi}_\beta|} \right) \\
G_{21,\beta} &= -\frac{4\gamma}{\rho c^2 \beta} \\
H_{21,\beta} &= +\frac{2\rho c^2\gamma}{\beta} H_{51} + \frac{\epsilon_\beta}{\rho c^2} \left( \gamma \dot{\phi}_\alpha \dot{\phi}_\beta + \frac{(\gamma-1)}{|\dot{\phi}_\alpha \dot{\phi}_\beta|} \right) \\
G_{22,\beta} &= -2 G_{11,\beta} \\
H_{22,\beta} &= -2 H_{11,\beta} \\
S_{23,\beta} &= +\frac{2}{\beta} S_{23} \\
T_{23,\beta} &= +\epsilon_\beta T_{23} - \frac{2\rho c^2\gamma}{\beta} T_{41} \\
S_{24,\beta} &= -\frac{2\rho c^2\gamma}{\beta} S_{31} \\
T_{24,\beta} &= +\left(\frac{2}{\beta} - \epsilon_\beta\right) T_{24} \\
T_{31,\beta} &= -\epsilon_\beta T_{31} \\
H_{34,\beta} &= -\epsilon_\beta H_{34} \\
T_{41,\beta} &= +\epsilon_\beta T_{41} \\
H_{43,\beta} &= +\epsilon_\beta H_{43} \\
H_{51,\beta} &= +\frac{\epsilon_\beta}{\rho^2 c^4} \left( \dot{\phi}_\alpha \dot{\phi}_\beta + \frac{1}{|\dot{\phi}_\alpha \dot{\phi}_\beta|} \right)
\end{aligned}$$

and

(B.29)

$$\begin{aligned}
C A C B_{,\beta} &= +\dot{\theta}_\beta \epsilon_\beta C S(\dot{\theta}_\alpha) S N(\dot{\theta}_\beta) \\
S A S B_{,\beta} &= -\dot{\theta}_\beta \epsilon_\beta S N(\dot{\theta}_\alpha) C S(\dot{\theta}_\beta) \\
S A C B_{,\beta} &= +\dot{\theta}_\beta \epsilon_\beta S N(\dot{\theta}_\alpha) S N(\dot{\theta}_\beta)
\end{aligned}$$



$$SBCA_{,\beta} = -\partial_{\beta} \hat{e}_{\beta} CS(\hat{\theta}_{\alpha}) CS(\hat{\theta}_{\beta})$$

and

$$\begin{aligned} \partial_R \hat{R}_{11}(z, z_0)/\partial \alpha &= G_{11} CACB_{,\alpha} + H_{11,\alpha} SASB + H_{11} SASB_{,\alpha} & (B.30) \\ \partial_R \hat{R}_{12}(z, z_0)/\partial \alpha &= G_{12} CACB_{,\alpha} + H_{12,\alpha} SASB + H_{12} SASB_{,\alpha} \\ \partial_R \hat{R}_{13}(z, z_0)/\partial \alpha &= S_{13,\alpha} SACB + S_{13} SACB_{,\alpha} + T_{13} SBCA_{,\alpha} \\ \partial_R \hat{R}_{14}(z, z_0)/\partial \alpha &= S_{14,\alpha} SACB + S_{14} SACB_{,\alpha} + T_{14} SBCA_{,\alpha} \\ \partial_R \hat{R}_{15}(z, z_0)/\partial \alpha &= G_{15} CACB_{,\alpha} + H_{15,\alpha} SASB + H_{15} SASB_{,\alpha} \\ \partial_R \hat{R}_{21}(z, z_0)/\partial \alpha &= G_{21} CACB_{,\alpha} + H_{21,\alpha} SASB + H_{21} SASB_{,\alpha} \\ \partial_R \hat{R}_{22}(z, z_0)/\partial \alpha &= G_{22} CACB_{,\alpha} + H_{22,\alpha} SASB + H_{22} SASB_{,\alpha} \\ \partial_R \hat{R}_{23}(z, z_0)/\partial \alpha &= S_{23,\alpha} SACB + S_{23} SACB_{,\alpha} + T_{23} SBCA_{,\alpha} \\ \partial_R \hat{R}_{24}(z, z_0)/\partial \alpha &= S_{24,\alpha} SACB + S_{24} SACB_{,\alpha} + T_{24} SBCA_{,\alpha} \\ \partial_R \hat{R}_{25}(z, z_0)/\partial \alpha &= + \frac{1}{2} \partial_R \hat{R}_{12}(z, z_0)/\partial \alpha \\ \partial_R \hat{R}_{31}(z, z_0)/\partial \alpha &= S_{31,\alpha} SACB + S_{31} SACB_{,\alpha} + T_{31} SBCA_{,\alpha} \\ \partial_R \hat{R}_{32}(z, z_0)/\partial \alpha &= -2 \partial_R \hat{R}_{24}(z, z_0)/\partial \alpha \\ \partial_R \hat{R}_{33}(z, z_0)/\partial \alpha &= CACB_{,\alpha} \\ \partial_R \hat{R}_{34}(z, z_0)/\partial \alpha &= H_{34,\alpha} SASB + H_{34} SASB_{,\alpha} \\ \partial_R \hat{R}_{35}(z, z_0)/\partial \alpha &= -\partial_R \hat{R}_{14}(z, z_0)/\partial \alpha \\ \partial_R \hat{R}_{41}(z, z_0)/\partial \alpha &= S_{41,\alpha} SACB + S_{41} SACB_{,\alpha} + T_{41} SBCA_{,\alpha} \\ \partial_R \hat{R}_{42}(z, z_0)/\partial \alpha &= -2 \partial_R \hat{R}_{23}(z, z_0)/\partial \alpha \\ \partial_R \hat{R}_{43}(z, z_0)/\partial \alpha &= H_{43,\alpha} SASB + H_{43} SASB_{,\alpha} \\ \partial_R \hat{R}_{44}(z, z_0)/\partial \alpha &= CACB_{,\alpha} \\ \partial_R \hat{R}_{45}(z, z_0)/\partial \alpha &= -\partial_R \hat{R}_{13}(z, z_0)/\partial \alpha \\ \partial_R \hat{R}_{51}(z, z_0)/\partial \alpha &= G_{51} CACB_{,\alpha} + H_{51,\alpha} SASB + H_{51} SASB_{,\alpha} \\ \partial_R \hat{R}_{52}(z, z_0)/\partial \alpha &= +2 \partial_R \hat{R}_{21}(z, z_0)/\partial \alpha \\ \partial_R \hat{R}_{53}(z, z_0)/\partial \alpha &= -\partial_R \hat{R}_{41}(z, z_0)/\partial \alpha \\ \partial_R \hat{R}_{54}(z, z_0)/\partial \alpha &= -\partial_R \hat{R}_{31}(z, z_0)/\partial \alpha \\ \partial_R \hat{R}_{55}(z, z_0)/\partial \alpha &= +\partial_R \hat{R}_{11}(z, z_0)/\partial \alpha \end{aligned}$$

where

$$\dot{\epsilon}_\alpha = \frac{c^2}{\alpha^3 \dot{\phi}_\alpha |\dot{\phi}_\alpha|} \quad (\text{B.31})$$

$$H_{11,\alpha} = -\dot{\epsilon}_\alpha \left( \gamma^2 \dot{\phi}_\alpha \dot{\phi}_\beta + \frac{(\gamma-1)^2}{|\dot{\phi}_\alpha \dot{\phi}_\beta|} \right)$$

$$H_{12,\alpha} = -2\rho c^2 \dot{\epsilon}_\alpha \left( \gamma^3 \dot{\phi}_\alpha \dot{\phi}_\beta + \frac{(\gamma-1)^3}{|\dot{\phi}_\alpha \dot{\phi}_\beta|} \right)$$

$$S_{13,\alpha} = -\dot{\epsilon}_\alpha S_{13}$$

$$S_{14,\alpha} = +\dot{\epsilon}_\alpha S_{14}$$

$$H_{15,\alpha} = +\rho^2 c^4 \dot{\epsilon}_\alpha \left( \gamma^4 \dot{\phi}_\alpha \dot{\phi}_\beta + \frac{(\gamma-1)^4}{|\dot{\phi}_\alpha \dot{\phi}_\beta|} \right)$$

$$H_{21,\alpha} = +\frac{\dot{\epsilon}_\alpha}{\rho c^2} \left( \gamma \dot{\phi}_\alpha \dot{\phi}_\beta + \frac{(\gamma-1)}{|\dot{\phi}_\alpha \dot{\phi}_\beta|} \right)$$

$$H_{22,\alpha} = -2 H_{11,\alpha}$$

$$S_{23,\alpha} = -\dot{\epsilon}_\alpha S_{23}$$

$$S_{24,\alpha} = +\dot{\epsilon}_\alpha S_{24}$$

$$S_{31,\alpha} = +\dot{\epsilon}_\alpha S_{31}$$

$$H_{34,\alpha} = +\dot{\epsilon}_\alpha H_{34}$$

$$S_{41,\alpha} = -\dot{\epsilon}_\alpha S_{41}$$

$$H_{43,\alpha} = -\dot{\epsilon}_\alpha H_{43}$$

$$H_{51,\alpha} = +\frac{\dot{\epsilon}_\alpha}{\rho^2 c^4} \left( \dot{\phi}_\alpha \dot{\phi}_\beta + \frac{1}{|\dot{\phi}_\alpha \dot{\phi}_\beta|} \right)$$

and

(B.32)

$$CACB_{,\alpha} = -\dot{\theta}_\alpha \dot{\epsilon}_\alpha SN(\dot{\theta}_\alpha) CS(\dot{\theta}_\beta)$$

$$SASB_{,\alpha} = -\dot{\theta}_\alpha \dot{\epsilon}_\alpha CS(\dot{\theta}_\alpha) SN(\dot{\theta}_\beta)$$

$$SACB_{,\alpha} = -\dot{\theta}_\alpha \dot{\epsilon}_\alpha CS(\dot{\theta}_\alpha) CS(\dot{\theta}_\beta)$$

$$SBCA_{,\alpha} = -\dot{\theta}_\alpha \dot{\epsilon}_\alpha SN(\dot{\theta}_\alpha) SN(\dot{\theta}_\beta)$$

AD-A187 663

A SPECTRAL METHOD FOR COMPUTING COMPLETE SYNTHETIC  
SEISMOGRAMS(U) COLORADO UNIV AT BOULDER D J HARVEY  
MAR 87 AFGL-TR-87-8238 F19628-85-K-0016

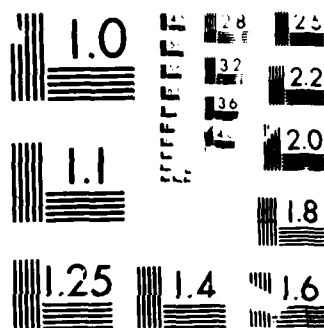
4/4

UNCLASSIFIED

F/G 8/11

ML





RESOLUTION TEST CHART

10-1

## APPENDIX C

### THE SOURCE JUMP VECTOR

The computation of the source jump vector for a variety of different source types is a subject which has received considerable attention (e.g. Harkrider (1964), Takeuchi and Saito (1972), Ben-Menahem and Singh (1971 and 1981), Bache and Harkrider (1976), Stevens (1980)). In this appendix I will briefly describe how source jump vectors are computed and I will give the source jump vectors for the most commonly used source types.

The use of a single source jump vector for a distributed source by definition implies the use of an equivalent point source. I should indicate that my definition of a simple point source is a single vector force applied at a fixed point in space and an equivalent point source is some linear combination of simple point sources. By this definition a couple source ends up being a distributed source (although the source region is infinitesimally small) since it requires two force vectors applied at an infinitesimal distance from each other. We can compute the equivalent point source jump vector from the following relations.

$$R w_1(\omega, k, m, z) = 0 \quad (C.1)$$

$$R w_2(\omega, k, m, z) = 0$$

$$R w_3(\omega, k, m, z) = \frac{1}{k} \int_0^{\infty} r dr \int_0^{2\pi} d\theta \rho f(\omega, r, \theta, z) \cdot P_l^m(r, \theta)$$

$${}_R w_4(\omega, k, m, z) = \frac{1}{k} \int_0^\infty r dr \int_0^{2\pi} d\theta \rho f(\omega, r, \theta, z) \cdot B_k^m(r, \theta)$$

$${}_L w_1(\omega, k, m, z) = 0$$

$${}_L w_2(\omega, k, m, z) = \frac{1}{k} \int_0^\infty r dr \int_0^{2\pi} d\theta \rho f(\omega, r, \theta, z) \cdot C_k^m(r, \theta)$$

and

$$\{{}_R \Sigma(\omega, k, m)\} = \int_{z_{11}}^{z_{12}} [{}_R A(z, \zeta)] \{{}_R w(\omega, k, m, \zeta)\} d\zeta \quad (C.2)$$

$$\{{}_L \Sigma(\omega, k, m)\} = \int_{z_{11}}^{z_{12}} [{}_L A(z, \zeta)] \{{}_L w(\omega, k, m, \zeta)\} d\zeta$$

where the source is distributed between depths  $z_{11}$  and  $z_{12}$  and the equivalent point source is at depth  $z_0$  which is arbitrary. Equations (C.1) and (C.2) were obtained from equations (2.4.3), (2.4.46), (2.4.13), (2.5.11) and (2.5.13).

The source jump vectors given below are from Harkrider (1964) and Kennett and Kerry (1979).

1. A center of compression explosion source produced by the application of a pressure function to the walls of a spherical cavity.

$${}_R \Sigma_1(\omega, k, 0) = S(\omega) \cdot (2\rho_0 \beta_0^2) \quad (C.3)$$

$${}_R \Sigma_2(\omega, k, 0) = 0$$

$${}_R \Sigma_3(\omega, k, 0) = 0$$

$${}_R \Sigma_4(\omega, k, 0) = S(\omega)$$

$${}_L \Sigma_1(\omega, k, 0) = 0$$

$${}_L \Sigma_2(\omega, k, 0) = 0$$

$$\{R\Sigma\} = \{L\Sigma\} = 0 \text{ for } m \neq 0$$

where

$$S(\omega) = \frac{p(\omega) a_s^3 \exp(i(\omega a_s / \alpha_s - \chi))}{\sqrt{\frac{\omega^2 a_s^2}{\alpha_s^2} + \left(1 - \frac{\omega^2 a_s^2}{4\beta_s^2}\right)^2}}$$

$$\chi = \tan^{-1} \left( \frac{\omega a_s}{\alpha_s \left(1 - \frac{\omega^2 a_s^2}{4\beta_s^2}\right)} \right)$$

$p(\omega)$  = pressure function spectrum

$a_s$  = source cavity radius

$\alpha_s$  = P wave velocity at the source

$\beta_s$  = S wave velocity at the source

$\rho_s$  = density at the source

## 2. A simple vector force point source.

$$R\Sigma_1(\omega, k, 0) = 0 \quad (C.4)$$

$$R\Sigma_2(\omega, k, 0) = 0$$

$$R\Sigma_3(\omega, k, 0) = -F_z$$

$$R\Sigma_4(\omega, k, 0) = 0$$

$$L\Sigma_1(\omega, k, 0) = 0$$

$$L\Sigma_2(\omega, k, 0) = 0$$

$$R\Sigma_1(\omega, k, \pm 1) = 0$$

$$R\Sigma_2(\omega, k, \pm 1) = 0$$

$$R\Sigma_3(\omega, k, \pm 1) = 0$$

$$R\Sigma_4(\omega, k, \pm 1) = \frac{1}{2}(\mp F_x + iF_y)$$

$$L\Sigma_1(\omega, k, \pm 1) = 0$$

$$L\Sigma_2(\omega, k, \pm 1) = \frac{1}{2}(iF_x \pm F_y)$$

$$\{R\Sigma\} = \{L\Sigma\} = 0 \text{ for } m \neq -1, 0, +1$$

where  $F_x$ ,  $F_y$  and  $F_z$  are the spectra of the components of the force vector in the 0 azimuth direction, 90 degree azimuth direction and down

direction respectively.

3. An equivalent point source which is represented by a general moment tensor.

$${}_R\Sigma_1(\omega, k, 0) = M_{xx}/(\rho_s \alpha_s^2) \quad (C.5)$$

$${}_R\Sigma_2(\omega, k, 0) = 0$$

$${}_R\Sigma_3(\omega, k, 0) = 0$$

$${}_R\Sigma_4(\omega, k, 0) = \frac{1}{2}(M_{xx} + M_{yy}) - M_{xx}(1 - 2\beta_s^2/\alpha_s^2)$$

$${}_L\Sigma_1(\omega, k, 0) = 0$$

$${}_L\Sigma_2(\omega, k, 0) = \frac{1}{2}(M_{xy} - M_{yx})$$

$${}_R\Sigma_1(\omega, k, \pm 1) = 0$$

$${}_R\Sigma_2(\omega, k, \pm 1) = \frac{1}{2}(\pm M_{xz} - iM_{yz})/(\rho_s \beta_s^2)$$

$${}_R\Sigma_3(\omega, k, \pm 1) = \frac{1}{2}i(M_{zy} - M_{yz}) \pm \frac{1}{2}(M_{xx} - M_{yy})$$

$${}_R\Sigma_4(\omega, k, \pm 1) = 0$$

$${}_L\Sigma_1(\omega, k, \pm 1) = \frac{1}{2}(\pm M_{yz} - iM_{xz})/(\rho_s \beta_s^2)$$

$${}_L\Sigma_2(\omega, k, \pm 1) = 0$$

$${}_R\Sigma_1(\omega, k, \pm 2) = 0$$

$${}_R\Sigma_2(\omega, k, \pm 2) = 0$$

$${}_R\Sigma_3(\omega, k, \pm 2) = 0$$

$${}_R\Sigma_4(\omega, k, \pm 2) = \frac{1}{4}(M_{yy} - M_{xx}) \pm \frac{1}{4}i(M_{xy} + M_{yx})$$

$${}_L\Sigma_1(\omega, k, \pm 2) = 0$$

$${}_L\Sigma_2(\omega, k, \pm 2) = \pm \frac{1}{4}i(M_{xx} - M_{yy}) + \frac{1}{4}(M_{xy} + M_{yx})$$

$$\{{}_R\Sigma\} = \{{}_L\Sigma\} = 0 \text{ for } m \neq -2, -1, 0, +1, +2$$

where  $M_{xx}$ ,  $M_{xy}$ , etc. are the spectra of the nine elements of the moment tensor and the directions are the same as those used for the vector force.



DISTRIBUTION LIST

Dr. Monem Abdel-Gawad  
Rockwell Internat'l Science Center  
1049 Camino Dos Rios  
Thousand Oaks, CA 91360

Professor Keiiti Aki  
Center for Earth Sciences  
University of Southern California  
University Park  
Los Angeles, CA 90089-0741

Dr. Ralph Alewine III  
DARPA/STO/GSD  
1400 Wilson Boulevard  
Arlington, CA 22209-2308

Professor Shelton S. Alexander  
Geosciences Department  
403 Deike Building  
The Pennsylvania State University  
University Park, PA 16802

Professor Charles B. Archambeau  
Cooperative Institute for Resch  
in Environmental Sciences  
University of Colorado  
Boulder, CO 80309

Dr. Thomas C. Bache Jr.  
Science Applications Int'l Corp.  
10210 Campus Point Drive  
San Diego, CA 92121

Dr. Robert Blandford  
DARPA/STO/GSD  
1400 Wilson Boulevard  
Arlington, CA 22209-2308

Dr. Lawrence Braile  
Department of Geosciences  
Purdue University  
West Lafayette, IN 47907

Dr. James Bulau  
Rockwell Int'l Science Center  
1049 Camino Dos Rios  
P.O. Box 1085  
Thousand Oaks, CA 91360

Dr. Douglas R. Baumgardt  
Signal Analysis & Systems Div.  
ENSQ, Inc.  
5400 Port Royal Road  
Springfield, VA 22151-2388

Dr. G. Blake  
US Dept of Energy/DP 331  
Forrestal Building  
1000 Independence Ave.  
Washington, D.C. 20585

Dr. S. Bratt  
Science Applications Int'l Corp.  
10210 Campus Point Drive  
San Diego, CA 92121

Woodward-Clyde Consultants  
ATTN: Dr. Lawrence J. Burdick  
Dr. Jeff Barker  
P.O. Box 93245  
Pasadena, CA 91109-3245 (2 copies)

Dr. Roy Burger  
1221 Serry Rd.  
Schenectady, NY 12309

Professor Robert W. Clayton  
Seismological Laboratory/Div. of  
Geological & Planetary Sciences  
California Institute of Technology  
Pasadena, CA 91125

Dr. Vernon F. Cormier/Earth Resources  
Lab, Dept of Earth, Atmospheric and  
Planetary Sciences  
MIT - 42 Carleton Street  
Cambridge, MA 02142

Professor Anton W. Dainty  
AFGL/LWH  
Hanscom AFB, MA 01731

Dr. Zoltan A. Der  
ENSQ, Inc.  
5400 Port Royal Road  
Springfield, VA 22151-2388

Professor Adam Dziewonski  
Hoffman Laboratory  
Harvard University  
20 Oxford St.  
Cambridge, MA 02138

Professor John Ebel  
Dept of Geology & Geophysics  
Boston College  
Chestnut Hill, MA 02167

Dr. Jack Evernden  
USGS-Earthquake Studies  
345 Middlefield Road  
Menlo Park, CA 94025

Professor John Ferguson  
Center for Lithospheric Studies  
The University of Texas at Dallas  
P.O. Box 830688  
Richardson, TX 75083-0688

Mr. Edward Giller  
Pacific Seirra Research Corp.  
1401 Wilson Boulevard  
Arlington, VA 22209

Dr. Jeffrey W. Given  
Sierra Geophysics  
11255 Kirkland Way  
Kirkland, WA 98033

Professor Steven Grand  
Department of Geology  
245 Natural History Building  
1301 West Green Street  
Urbana, IL 61801

Professor Roy Greenfield  
Geosciences Department  
403 Deike Building  
The Pennsylvania State University  
University Park, PA 16802

Dr. James Hannon  
Lawrence Livermore Nat'l Lab.  
P.O. Box 808  
Livermore, CA 94550

Professor David G. Harkrider  
Seismological Laboratory  
Div of Geological & Planetary Sciences  
California Institute of Technology  
Pasadena, CA 91125

Professor Donald V. Helmberger  
Seismological Laboratory  
Div of Geological & Planetary Sciences  
California Institute of Technology  
Pasadena, CA 91125

Professor Eugene Herrin  
Institute for the Study of Earth  
& Man/Geophysical Laboratory  
Southern Methodist University  
Dallas, TX 75275

Professor Robert B. Herrmann  
Department of Earth & Atmospheric  
Sciences  
Saint Louis University  
Saint Louis, MO 63156

U.S. Arms Control & Disarm. Agency  
ATTN: Mrs. M. Hoinkes  
Div. of Multilateral Affairs  
Room 5499  
Washington, D.C. 20451

Professor Lane R. Johnson  
Seismographic Station  
University of California  
Berkeley, CA 94720

Professor Thomas H. Jordan  
Department of Earth, Atmospheric  
and Planetary Sciences  
Mass Institute of Technology  
Cambridge, MA 02139

Dr. Alan Kafka  
Department of Geology &  
Geophysics  
Boston College  
Chestnut Hill, MA 02167

Ms. Ann Kerr  
DARPA/STO/GSD  
1400 Wilson Boulevard  
Arlington, VA 22209-2308

Professor Charles A. Langston  
Geosciences Department  
403 Deike Building  
The Pennsylvania State University  
University Park, PA 16802

Professor Thorne Lay  
Department of Geological Sciences  
1006 C.C. Little Building  
University of Michigan  
Ann Arbor, MI 48109-1063

Dr. Arthur Lerner-Lam  
Lamont-Doherty Geological Observatory  
of Columbia University  
Palisades, NY 10964

Dr. George R. Mellman  
Sierra Geophysics  
11255 Kirkland Way  
Kirkland, WA 98033

Professor Brian J. Mitchell  
Department of Earth & Atmospheric  
Sciences  
Saint Louis University  
Saint Louis, MO 63156

Professor Thomas V. McEvilly  
Seismographic Station  
University of California  
Berkeley, CA 94720

Dr. Keith L. McLaughlin  
Teledyne Geotech  
314 Montgomery Street  
Alexandria, VA 22314

Mr. Jack Murphy - S-CUBED  
Reston Geophysics Office  
11800 Sunrise Valley Drive  
Suite 1212  
Reston, VA 22091

Dr. Carl Newton  
Los Alamos National Lab.  
P.O. Box 1663  
Mail Stop C335, Group E553  
Los Alamos, NM 87545

Professor Otto W. Nuttli  
Department of Earth &  
Atmospheric Sciences  
Saint Louis University  
Saint Louis, MO 63156

Professor J. A. Orcutt  
Geological Sciences Div.  
Univ. of California at  
San Diego  
La Jolla, CA 92093

Dr. Frank F. Pilotte  
Director of Geophysics  
Headquarters Air Force Technical  
Applications Center  
Patrick AFB, Florida 32925-6001

Professor Keith Priestley  
University of Nevada  
Mackay School of Mines  
Reno, Nevada 89557

Mr. Jack Raclin  
USGS - Geology, Rm 3 C136  
Mail Stop 928 National Center  
Reston, VA 22092

Professor Paul G. Richards  
Lamont-Doherty Geological  
Observatory of Columbia Univ.  
Palisades, NY 10964

Dr. Norton Kimer  
S-CUBED  
A Division of Maxwell Lab  
P.O. 1620  
La Jolla, CA 92038-1620

Dr. George H. Rothe  
Chief, Research Division  
Geophysics Directorate  
HQ Air Force Technical  
Applications Center  
Patrick AFB, Florida 32925-6001

Professor Larry J. Ruff  
Department of Geological Sciences  
1006 C.C. Little Building  
University of Michigan  
Ann Arbor, MI 48109-1063

Dr. Alan S. Ryall, Jr.  
Center of Seismic Studies  
1300 North 17th Street  
Suite 1450  
Arlington, VA 22209-2308

Professor Charles G. Sammis  
Center for Earth Sciences  
University of Southern California  
University Park  
Los Angeles, CA 90089-0741

Dr. David G. Simpson  
Lamont-Doherty Geological Observ.  
of Columbia University  
Palisades, NY 10964

Dr. Jeffrey L. Stevens  
S-CUBED,  
A Division of Maxwell Laboratory  
P.O. Box 1620  
La Jolla, CA 92038-1620

Professor Brian Stump  
Institute for the Study of Earth & Man  
Geophysical Laboratory  
Southern Methodist University  
Dallas, TX 75275

Professor Ta-liang Teng  
Center for Earth Sciences  
University of Southern California  
University Park  
Los Angeles, CA 90089-0741

Dr. R. B. Tittmann  
Rockwell International Science Ctr  
1049 Camino Dos Rios  
P.O. Box 1085  
Thousand Oaks, CA 91360

Professor M. Nafi Toksoz/Earth Resources  
Lab - Dept of Earth, Atmospheric and  
Planetary Sciences  
MIT - 42 Carleton Street  
Cambridge, MA 02142

Dr. Lawrence Turnbull  
OSWR/NED  
Central Intelligence Agency  
CIA, Room 5G48  
Washington, D.C. 20505

Professor Terry C. Wallace  
Department of Geosciences  
Building #11  
University of Arizona  
Tucson, AZ 85721

Professor John H. Woodhouse  
Hoffman Laboratory  
Harvard University  
20 Oxford St.  
Cambridge, MA 02138

\*\*\*

DARPA/PM  
1400 Wilson Boulevard  
Arlington, VA 22209

Defense Technical  
Information Center  
Cameron Station  
Alexandria, VA 22314  
(12 copies)

Defense Intelligence Agency  
Directorate for Scientific &  
Technical Intelligence  
Washington, D.C. 20301

Defense Nuclear Agency/SPSS  
ATTN: Dr. Michael Shore  
6801 Telegraph Road  
Alexandria, VA 22310

AFOSR/NPG  
ATTN: Director  
Bldg 410, Room C22  
Bolling AFB, Wash D.C. 20332

AFTAC/CA (STINFO)  
Patrick AFB, FL 32925-6001

U.S. Geological Survey  
ATTN: Dr. T. Hanks  
Nat'l Earthquake Resch Center  
345 Middlefield Road  
Menlo Park, CA 94025

SRI International  
333 Ravensworth Avenue  
Menlo Park, CA 94025

Center for Seismic Studies  
ATTN: Dr. C. Romney  
1300 North 17th St., Suite 1450  
Arlington, VA 22209 (3 copies)

Science Horizons, Inc.  
ATTN: Dr. Bernard Minster  
Dr. Theodore Cherry  
710 Encinitas Blvd., Suite 101  
Encinitas, CA 92024 (2 copies)



Dr. G. A. Bollinger  
Department of Geological Sciences  
Virginia Polytechnical Institute  
21044 Derring Hall  
Blacksburg, VA 24061

Dr. L. Sykes  
Lamont Doherty Geological Observ.  
Columbia University  
Palisades, NY 10964

Dr. S. W. Smith  
Geophysics Program  
University of Washington  
Seattle, WA 98195

Dr. L. Timothy Long  
School of Geophysical Sciences  
Georgia Institute of Technology  
Atlanta, GA 30332

Dr. N. Biswas  
Geophysical Institute  
University of Alaska  
Fairbanks, AK 99701

Dr. Freeman Gilbert - Institute of  
Geophysics & Planetary Physics  
Univ. of California at San Diego  
P.O. Box 109  
La Jolla, CA 92037

Dr. Pradeep Talwani  
Department of Geological Sciences  
University of South Carolina  
Columbia, SC 29208

Dr. Donald Forsyth  
Dept. of Geological Sciences  
Brown University  
Providence, RI 02912

Dr. Jack Oliver  
Department of Geology  
Cornell University  
Ithaca, NY 14850

Dr. Muawia Barazangi  
Geological Sciences  
Cornell University  
Ithaca, NY 14853

Rondout Associates  
ATTN: Dr. George Sutton,  
Dr. Jerry Carter, Dr. Paul Pomeroy  
P.O. Box 224  
Stone Ridge, NY 12484 (3 copies)

Dr. Bob Smith  
Department of Geophysics  
University of Utah  
1400 East 2nd South  
Salt Lake City, UT 84112

Dr. Anthony Gangi  
Texas A&M University  
Department of Geophysics  
College Station, TX 77843

Dr. Gregory B. Young  
ENSØ, Inc.  
5400 Port Royal Road  
Springfield, CA 22151

Weidlinger Associates  
ATTN: Dr. Gregory Wojcik  
620 Hansen Way, Suite 100  
Palo Alto, CA 94304

Dr. Leon Knopoff  
University of California  
Institute of Geophysics  
& Planetary Physics  
Los Angeles, CA 90024

Dr. Kenneth H. Olsen  
Los Alamos Scientific Lab.  
Post Office Box 1663  
Los Alamos, NM 87545

Professor Jon F. Claerbout  
Professor Amos Nur  
Dept. of Geophysics  
Stanford University  
Stanford, CA 94305 (2 copies)

Dr. Robert Burridge  
Schlumberger-Doll Resch Cr.  
Old Quarry Road  
Ridgefield, CT 06877

Dr. Robert Phinney/Dr. F.A. Dahlen  
Dept of Geological  
Geophysical Sci. University  
Princeton University  
Princeton, NJ 08540 (2 copies)

New England Research, Inc.  
ATTN: Dr. Randolph Martin III  
P.O. Box 857  
Norwich, VT 05055

Sandia National Laboratory  
ATTN: Dr. H. B. Durham  
Albuquerque, NM 87185

AFGL/XO  
Hanscom AFB, MA 01731-5000

AFGL/LW  
Hanscom AFB, MA 01731-5000

AFGL/SULL  
Research Library  
Hanscom AFB, MA 01731-5000 (2 copies)

Secretary of the Air Force (SAFRD)  
Washington, DC 20330

Office of the Secretary Defense  
DDR & E  
Washington, DC 20330

HQ DNA  
ATTN: Technical Library  
Washington, DC 20305

Director, Technical Information  
DARPA  
1400 Wilson Blvd.  
Arlington, VA 22209

Los Alamos Scientific Laboratory  
ATTN: Report Library  
Post Office Box 1663  
Los Alamos, NM 87544

Dr. Thomas Weaver  
Los Alamos Scientific Laboratory  
Los Alamos, NM 97544

Dr. Gary McCartor  
Mission Research Corp.  
735 State Street  
P.O. Drawer 719  
Santa Barbara, CA 93102

Dr. Al Florence  
SRI International  
333 Ravenwood Avenue  
Menlo Park, CA 94025-3493

Dr. W. H. K. Lee  
USGS  
Office of Earthquakes, Volcanoes,  
& Engineering  
Branch of Seismology  
345 Middlefield Rd  
Menlo Park, CA 94025

\*\*\*

Dr. Peter Basham/Earth Physics Branch  
Department of Energy and Mines  
1 Observatory Crescent  
Ottawa, Ontario  
CANADA K1A 0Y3

Dr. Eduard Berg  
Institute of Geophysics  
University of Hawaii  
Honolulu, HI 96822

Dr. Michel Bouchon - Universite  
Scientifique et Medicale de Grenob  
Lab de Geophysique - Interne et  
Tectonophysique - I.R.I.G.M-B.P.  
38402 St. Martin D'Herès  
Cedex FRANCE

Dr. Hilmar Bungum/NTNF/NORSAR  
P.O. Box 51  
Norwegian Council of Science,  
Industry and Research, NORSAR  
N-2007 Kjeller, NORWAY

Dr. Kin-Yip Chun  
Geophysics Division  
Physics Department  
University of Toronto  
Ontario, CANADA M5S 1A7

Dr. Alan Douglas  
Ministry of Defense  
Blacknest, Brimpton,  
Reading RG7-4RS  
UNITED KINGDOM

Professor Peter Harjes  
Institute for Geophysik  
Rhur University/Bochum  
P.O. Box 102148, 4630 Bochum 1  
FEDERAL REPUBLIC OF GERMANY

Dr. E. Husebye  
NTNF/NORSAR  
P.O. Box 51  
N-2007 Kjeller, NORWAY

Mr. Peter Marshall, Procurement  
Executive, Ministry of Defense  
Blacknest, Brimpton,  
Reading RG7-4RS  
UNITED KINGDOM

Dr. B. Massinon  
Societe Radiomana  
27, Rue Claude Bernard  
75005, Paris, FRANCE

Dr. Pierre Mechler  
Societe Radiomana  
27, Rue Claude Bernard  
75005, Paris, FRANCE

Dr. Ben Menaheim  
Weizman Institute of Science  
Rehovot, ISRAEL 951729

Dr. Svein Mykkeltveit  
NTNF/NORSAR  
P.O. Box 51  
N-2007 Kjeller, NORWAY

Dr. Frode Ringdal  
NTNF/NORSAR  
P.O. Box 51  
N-2007 Kjeller, NORWAY

University of Hawaii  
Institute of Geophysics  
ATTN: Dr. Daniel Walker  
Honolulu, HI 96822

\*\*\*

END

DATE

FILMED

FEB.

1988